

High rate plasma deposition of silicon oxide like films

Citation for published version (APA):

Hest, van, M. F. A. M. (2002). *High rate plasma deposition of silicon oxide like films*. [Phd Thesis 1 (Research TU/e / Graduation TU/e), Applied Physics and Science Education]. Technische Universiteit Eindhoven.
<https://doi.org/10.6100/IR557875>

DOI:

[10.6100/IR557875](https://doi.org/10.6100/IR557875)

Document status and date:

Published: 01/01/2002

Document Version:

Publisher's PDF, also known as Version of Record (includes final page, issue and volume numbers)

Please check the document version of this publication:

- A submitted manuscript is the version of the article upon submission and before peer-review. There can be important differences between the submitted version and the official published version of record. People interested in the research are advised to contact the author for the final version of the publication, or visit the DOI to the publisher's website.
- The final author version and the galley proof are versions of the publication after peer review.
- The final published version features the final layout of the paper including the volume, issue and page numbers.

[Link to publication](#)

General rights

Copyright and moral rights for the publications made accessible in the public portal are retained by the authors and/or other copyright owners and it is a condition of accessing publications that users recognise and abide by the legal requirements associated with these rights.

- Users may download and print one copy of any publication from the public portal for the purpose of private study or research.
- You may not further distribute the material or use it for any profit-making activity or commercial gain
- You may freely distribute the URL identifying the publication in the public portal.

If the publication is distributed under the terms of Article 25fa of the Dutch Copyright Act, indicated by the "Taverne" license above, please follow below link for the End User Agreement:

www.tue.nl/taverne

Take down policy

If you believe that this document breaches copyright please contact us at:

openaccess@tue.nl

providing details and we will investigate your claim.

High Rate Plasma Deposition of Silicon Oxide Like Films

Proefschrift

ter verkrijging van de graad van doctor
aan de Technische Universiteit Eindhoven,
op gezag van de Rector Magnificus, prof.dr. R.A. van Santen,
voor een commissie aangewezen door het College
voor Promoties in het openbaar te verdedigen op
dinsdag 27 augustus 2002 om 16.00 uur

door

Marinus Franciscus Antonius Maria van Hest

geboren te Tilburg

Dit proefschrift is goedgekeurd door de promotoren:

prof.dr.ir. M.C.M. van de Sanden

en

prof.dr.ir. D.C. Schram

The work presented in this thesis is part of a collaboration between General Electric and the plasma physics group 'Equilibrium and Transport in Plasmas' at the Department of Applied physics of the Eindhoven University of Technology. The work is also financially supported by General Electric.

Printed and bound by Universiteitsdrukkerij Technische Universiteit Eindhoven
Cover realization by Jan-Willem Luiten

CIP-DATA LIBRARY TECHNISCHE UNIVERSITEIT EINDHOVEN

Hest, Marinus Franciscus Antonius Maria van

High Rate Plasma Deposition of Silicon Oxide Like Films / by Marinus Franciscus Antonius Maria van Hest. - Eindhoven: Eindhoven University of Technology, 2002. -

Proefschrift.

ISBN 90-386-2009-8

NUR 926

Trefw.: plasma / plasmadepositie / plasmadiagnostiek / plasmachemie / materiaalonderzoek / siliciumoxide

Subject headings: plasma / plasma deposition / plasma diagnostics / plasma chemistry / material characterization / silica

Contents

5. Deposition of silicon oxide like films using a remote thermal plasma.	95
5.1 Introduction	96
5.2 Experimental setup	96
5.3 Result	98
5.3.1 Silicon oxide like film deposition	98
5.3.2 Film composition	101
5.3.3 Temperature dependency	103
5.4 Discussion	105
5.5 Conclusions	108
6. Argon-Oxygen plasma treatment of deposited silicon oxide like films.	113
6.1 Introduction	114
6.2 Definitions	115
6.3 Result	117
6.3.1 Exposure time	117
6.3.2 Oxygen flow variation	120
6.4 Discussion	122
6.4.1 Exposure time	122
6.4.2 Oxygen flow variation	124
6.4.3 Reaction mechanism	127
6.5 Conclusions	129
7. The reaction mechanism of HMDSO in an expanding thermal argon plasma	133
7.1 Introduction	134
7.2 Experimental setup	137
7.3 TMS deposition results	138
7.4 Discussion	144
7.4.1 TMS	145
7.4.2 HMDSO	148
7.5 Conclusions	151
8. ZnSn_xO_y deposition: A combinatorial approach.	155
8.1 Introduction	156
8.2 Experimental setup	157
8.3 Results	159
8.3.1 ZnSn _x O _y combinatorial libraries	159
8.3.2 Anneal temperature	163
8.3.3 ZnSn _x In _y O _z combinatorial libraries	164
8.4 Conclusions	165
9. General conclusions	167
Summary.	171
Samenvatting	173
Dankwoord/Acknowledgement.	175
Curriculum vitea	176

Chapter 1

General introduction

1.1 Thin film deposition

Nowadays thin films play an important role in life. Although their presence is often unnoticed, without them many devices would be quite different from their present form, e.g. television, coloured windows, solar cells, and telephones; or would even not exist at all e.g. microprocessors, compact discs, and the remote control. It is therefore understandable that people are looking for new applications for the use of thin films as well as new and better ways to produce thin films.

One of the methods of producing thin films is by means of plasma technology. This is a technique by which a plasma, also known as ‘the fourth state of matter’, is used to generate ions, electrons and radicals which deposit at a surface where they will form a thin film. The source of these depositing species could be either gaseous, liquid or solid in origin. Most of the time a plasma is generated by means of an electrical discharge. The variety of application for the thin films is as numerous as the variety of plasma sources used to deposit them. Some examples of plasma sources used for deposition of thin films are: RF- and DC-sputtering [1,2], for which solid state targets are used as a source of the depositing species; parallel plate discharge [3,4], inductively coupled plasmas [5,6], microwave plasmas [7,8], and arcs [9,10] which mainly rely on gaseous monomers as a source for the depositing species.

In general the film deposition rates obtained with the conventional plasma deposition techniques are low (up to a couple of nm/s) and the deposition area is small (tens of cm²). At the Eindhoven University of Technology a plasma technique has been developed which is capable of depositing good quality film of various materials at high growth rates (over 10 nm/s) [11]. In general a high film growth rate is appreciated in industry, because it reduces the production time of devices and with that also the production cost. However for very thin films (<10 – 20 nm) it is less beneficial to have growth rates of several tens of nm/s, because the time gain does often not validate the investment needed for the equipment to obtain high growth rates.

The used plasma technique is based on an arc plasma. In general gas enters the arc on one side, then a plasma is generated inside the arc by means of a discharge and the plasma flows out of the arc on the other side. Because these thermal arc plasmas are normally used at or close to atmospheric pressure, the dimensions of the generated plasma are small. These plasmas can therefore best be compared with the flame of a welding torch. However, for the used plasma technique the outlet of the flowing arc is connected to a vacuum vessel ($p = 10 - 30$ Pa). The plasma generated in the arc will expand into this vacuum. In this way a remotely generated expanding thermal plasma is created with low electron temperature [11]. By injecting a molecular gas, also called precursor, into this expanding plasma chemical reactions between ions and electrons in the plasma and the gas molecule are initiated. Due to these chemical reactions the gas molecules are dissociated into radicals or ions which will cause deposition of a film at a surface which is located either in the plasma beam or close to it in the vacuum vessel.

The expanding thermal plasma used at the Eindhoven University of Technology has been, and in most cases still is, used for the deposition of hydrogenated amorphous silicon (a-Si:H) [12,13,14,15], hydrogenated amorphous carbon (a-C:H) [11,16,17,18,19], diamond [20,21], carbon nitride [22,23], silicon nitride [24], and zinc oxide [25,26]. The hydrogenated amorphous silicon, silicon nitride and zinc oxide work has mainly been done for application in solar cells, whereas hardness and wear-resistance have been the main reasons for the work on hydrogenated amorphous carbon, diamond, and carbon nitride.

In this thesis, as an extension to these applications, the expanding thermal plasma will be used for the deposition of silicon oxide films. Silicon oxide is a material which has many applications due to its optical, electrical and mechanical properties. It can be used as an optical coating [27], UV protection coating [28,29], electrical insulator [30,31,32], barrier film for food packaging [33,34], corrosive protection film [35,36], and even as a moisture sensor [37]. This wide range of applications immediately shows the importance of silicon oxide films as well as the large economic benefits for industry when these films can be deposited at high deposition rates.

For the deposition of silicon oxide films by conventional plasma techniques many different gaseous precursors have been used, although sputtering of a pure silicon dioxide target (Quartz) can also be applied. Gaseous precursors however have the advantage that they are in general easy to use and can be applied in large quantities. The two most often used precursors are silane [38,39] and tetraethoxysilane (TEOS) [40,41], both in combination with oxygen. A simplified image of their atomic composition has been given in Figure 1.1. As can be seen silane is a good source for silicon atoms, however due to its toxicity and its hazardous properties several precautions have to be taken before this precursor can be used. Therefore it is less applicable for industrial purposes. TEOS does not have these hazardous properties and it is less toxic, however at room temperature this precursor is liquid and needs to be evaporated before it can be injected into a depositing plasma. As can be seen in Figure 1.1 TEOS does contain a significant amount of carbon and hydrogen. Due to the combination with oxygen in the depositing plasma it is possible to produce carbon and hydrogen free films, because the oxygen forms water and carbon dioxide with the hydrogen and carbon atoms. One advantage in using TEOS rather than silane is the fact that the silicon atom in TEOS is already bonded to four oxygen atoms and therefore it is already in a configuration, which is close to the structure present in silicon dioxide films.

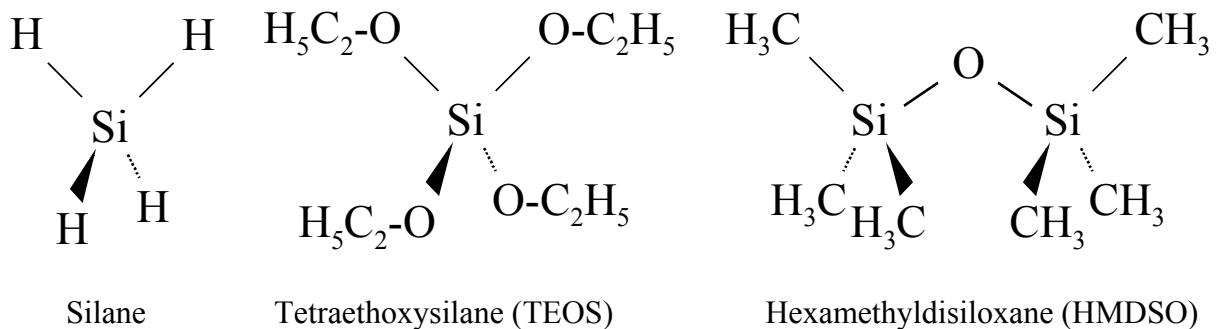


Figure 1.1: Molecular representation of silane, tetraethoxysilane and hexamethyldisiloxane.

In the last decade hexamethyldisiloxane (HMDSO) in combination with oxygen has been used more often as a precursor for the deposition of silicon oxide films [42,43]. As with TEOS, this precursor is less toxic and less hazardous than silane, although not totally harmless [44]. Also like TEOS this precursor is liquid at room temperature. The atomic configuration of HMDSO has also been shown in Figure 1.1. It can be seen that in comparison to TEOS this precursor contains less carbon and hydrogen, which need to be eliminated in the plasma by means of oxygen to form a pure silicon oxide film. Compared to TEOS this precursor has one more advantage. It contains two silicon atoms and therefore it is a better source of silicon atoms. Also the silicon is already present in a Si-O-Si configuration,

which is needed for the formation of pure silicon oxide films. Although HMDSO is a more expensive precursor than TEOS* it is still a commercially interesting precursor for application in industry due to the presence of two silicon atoms per molecule in a Si-O-Si configuration and its lower carbon content.

Although oxygen is added to the deposition plasmas using TEOS or HMDSO as precursor, in most cases the deposited film will still contain some carbon and hydrogen. Therefore the best way of chemically identifying the film is not by SiO_x as used for pure silicon oxide films, but by $\text{SiO}_x\text{C}_y\text{H}_z$. The values for x , y , and z are obviously dependent on the type of plasma used to produce the film, on the plasma parameters and the material temperature at time of deposition. Because of the presence of carbon and hydrogen in the deposited films, the silicon oxide films in this thesis will be addressed as silicon oxide like films†.

Because of the benefits of HMDSO above TEOS, in this thesis HMDSO has been used as a precursor gas for the deposition of silicon oxide like films. As mentioned HMDSO is a liquid precursor and needs to be evaporated before it can be injected into the expanding thermal plasma. Controlling and evaporating the liquid precursors is often a delicate matter. The classical method is the well known ‘bubbler’ system, with its inherent problems: poor stability and poor reproducibility, due to the extremely high sensitivity to changes in temperature. Therefore in this work another, fairly new, system has been used for the control and evaporation of the liquid precursor. For the evaporation of the precursor a Bronckhorst controlled evaporation module (CEM, type W-202) in combination with a Bronckhorst Liqui-Flow® meter (type L2C2) has been used. This is a closed system, which controls the liquid flow rate and evaporates the liquid. This system is more reliable and stable than the more conventionally used bubbler systems [45,46].

The interest of the research done in the plasma physics group at the Eindhoven University of Technology lies not only in the production of films with specific properties. At the same time the overall process of film deposition is also of interest. In this the interest is very broad and can be distinguished in three main areas. The first one concerns the plasma gas phase, for which questions arise like; How is the precursor dissociated?; What are the main dissociation products? How do these products depend on the plasma parameters? The second area relates to the deposited film, for which question arise like; What are the optical, mechanical, or electrical properties of the deposited film?; What is the film composition?; How does this depend on the plasma composition? The third and probably most difficult area concerns the deposition process itself, for which questions arise like: What is the dominant deposition particle?; Which reactions occur at the film surface? Each of these three areas require their own techniques to analyse the parameters needed for answering the various questions.

In this thesis not all the questions stated for the three fields will be answered, but serious effort has been made to get as many answers as possible. For the first area the answers concerning the thin film deposition from HMDSO and oxygen in an expanding thermal plasma are mainly obtained indirectly and from the properties of the deposited films. These properties have been measured with the aim of answering the questions in the second area, but provide enough information to also gain a good insight in the plasma chemistry.

* Price TEOS: € 30,00 per liter, HMDSO € 108.00 per liter [47].

† In literature these kind of films are also referred to as silicone like films.

The last area, the plasma film interaction, contains elements of the first and the second area. Although in the first and second area respectively the plasma and the film can be studied separately, the third area makes the use of *in situ* diagnostic techniques obligatory. *In situ* diagnostics to monitor the evolution of the different bond types in the film in time do already exist. Fourier transform infrared reflection absorption spectroscopy [48,49] is one of the more widely used techniques, but due to the high deposition rates obtained when using the expanding thermal plasma this diagnostic is pushed beyond its limits. Therefore in this work a new and fast infrared reflection absorption spectroscopy setup has been designed which enables the monitoring of the evolution of the different bond types present in the film at high film growth rates. Aside from this new setup *in situ* single wavelength ellipsometry has also been used.

1.2 Aim of this thesis

The aim of the project has been the production of silicon oxide like thin films from HMDSO and oxygen at high growth rates by means of an expanding thermal argon plasma. The main task has however not been to optimise the deposition plasma parameters in such a way that pure silicon oxide is produced. The main task has been to get more insight in the correlation between the plasma parameter on one hand and the film properties as well as the plasma properties on the other hand. This has been achieved by studying the expanding thermal plasma with only the addition of oxygen without the deposition precursor and by studying the depositing plasma with and without the addition of oxygen. Also more than one precursor has been used to get a better understanding of the plasma and surface chemistry of the silicon oxide like film deposition process using HMDSO and oxygen as a precursor. Finally a second goal of this work has been the development of a new and fast diagnostic for the *in situ* monitoring of the film growth.

1.3 Outline of this thesis

In chapter 2 the deposition setup as well as the liquid precursor evaporation system are first discussed. Second a description is given of the various diagnostics used in this work, including the various applications of infrared spectroscopy.

Chapter 3 deals with the design and testing of the new and fast infrared reflection absorption spectroscope, which is designed for the *in situ* analysis of the film growth at high deposition rates. In chapter 3 the design specifications and a theoretical study of this spectroscope as well as an initial experimental study to demonstrate the spectroscope's abilities are described.

In chapter 4 a study of the expanding thermal plasma into which oxygen is injected is presented. In this chapter the ion density and temperature profiles of the expanding thermal plasma, with and without the addition of oxygen, are presented. This data has been obtained from Langmuir double probe experiments. Pitot probe measurements are used to obtain a better understanding of the flow pattern of the gasses in the plasma reactor. The combination of Langmuir probe and Pitot Probe measurements is used to calculate the total ion flux generated by the arc plasma source.

In chapter 5 to 7 the results of the study on the deposition plasma are given. In chapter 5 a deposition study is presented which results in more understanding in the silicon oxide like

film properties as a function of various deposition parameters. In chapter 6 an oxygen treatment study of the deposited silicon oxide like films is presented. In this study deposited silicon oxide like films are exposed to the expanding thermal plasma into which only oxygen is injected. This to get a better insight into the reactivity between oxygen and the deposited films. In chapter 7 an attempt is made to unravel the reaction mechanism of the silicon oxide like film deposition from HMDSO and oxygen. Both gas phase reactions as well as surface reactions are addressed. In addition to the data shown in chapter 5 and chapter 6 a deposition study using tetramethylsilane (TMS) as a precursor is presented in chapter 7. This in order to get more understanding in the sticking probabilities of the various deposition species responsible for silicon oxide like film growth.

In chapter 8 some of the results obtained during a two month visit to the National Renewable Energy Laboratory in Golden, Colorado (USA) are presented. This work involves the deposition of combinatorial libraries of $ZnSn_xO_y$ by means of co-sputtering of solid state targets. These kind of films are used as transparent conductive oxides (TCO) in e.g. solar cells. The libraries are analysed for their conductivity and their composition in order to find the stoichiometry at which the best conductivity is obtained.

The main conclusion of the work presented in this thesis are summarized in chapter 9.

References

- [1] R.E. Stauber, J.D. Perkins, P.A. Parilla, and D.S. Ginley, *Electrochem. Solid State Lett.* **2** (1999) 654
- [2] N. Mizutani, N. Wakiya, M. Yoshida, K. Hijikata, and K. Shinozaki, *Ferroelectrics* **260** (2001) 249
- [3] S. Croci, A. Pecheur, J.L. Autran, A. Vedda, F. Cacavale, M. Martine, and G. Spinolo, *J. Vac. Sci. Technol. A* **19** (2001) 2670
- [4] O.V. Balachova, M.A.R. Alves, J.W. Swart, E.S. Braga, and L. Cescato, *J. Appl. Phys.* **85** (1999) 3345
- [5] M. Schaepkens, G.S. Oehrlein, and J.M. Cook, *J. Vac. Sci. Technol. B* **18** (2000) 848
- [6] Y. C. Liang, C.N.H. Franklin, *Diamond Relat. Mater.* **10** (2001) 1058
- [7] G.S. Oehrlein, Y. Zhang, D. Vender, and M. Haverlag, *J. Vac. Sci. Technol. A* **12** (1994)
- [8] A. Barranco, F. Yubero, J.P. Espinos, J. Benitez, A.R. Gonzales-Elipe, J. Cotrino, J. Allain, T. Girardeau, and J.P. Riviere, *Surf. Coat. Technol.* **142-144** (2001) 856
- [9] J. Laimer, H. Pauser, H. Störi, R. Haubner, and B. Lux, *Diamond Relat. Mater.* **6** (1997) 406
- [10] M. Rahmane, G. Soucy, and M.I. Boulos, *Rev. Sci. Instrum.* **66** (1995) 3424
- [11] G.M.W. Kroesen, D.C. Schram, and M.J.F. van de Sande, *Plasma Chem. Plasma Proc.* **10** (1990) 49
- [12] W.M.M. Kessels, M.C.M. van de Sanden, R.J. Severens, and D.C. Schram, *J. Appl. Phys.* **87** (2000) 3313
- [13] W.M.M. Kessels, M.C.M. van de Sanden, and D.C. Schram, *J. Vac. Sci. Technol. A* **18** (2000) 2153
- [14] B.A. Korevaar, G.J. Adriaenssens, A.H.M. Smets, W.M.M. Kessels, H.-Z. Song, M.C.M. van de Sanden, and D.C. Schram, *J. Non-Cryst. Solids* **266-269** (2000) 380

- [15] G.J. Meeusen, *Plasma Beam Deposition of Amorphous Hydrogenated Silicon*, Ph.D. Thesis, Eindhoven University of Technology (1994); W.M.M. Kessels, *Remote Plasma Deposition of Hydrogenated Amorphous Silicon- Plasma Processes, Film Growth, and Material Properties*, Ph.D. Thesis Eindhoven University of Technology (2000); B.A. Korevaar, *Integration of Expanding Thermal Plasma Deposited Hydrogenated Amorphous Silicon in Solar Cells*, Ph.D. Thesis Eindhoven University of Technology (2002); A.H.M. Smets, *Growth Related Material Properties of Hydrogenated Amorphous Silicon*, Ph.D. Thesis Eindhoven University of Technology (2002)
- [16] J.W.A.M. Gielen, P.R.M. Kleuskens, M.C.M. van de Sanden, L.J. van IJzendoorn, D.C. Schram, E.H.A. Dekempeneer, and J. Meneve, *J. Appl. Phys.* **80** (1996) 5986
- [17] J.W.A.M. Gielen, W.M.M. Kessels, M.C.M. van de Sanden, and D.C. Schram, *J. Appl. Phys.* **82** (1997) 2643
- [18] J.W.A.M. Gielen, M.C.M. van de Sanden, P.R.M. Kleuskens, and D.C. Schram, *Plasma Sources Sci. Technol.* **5** (1996) 492
- [19] J.W.A.M. Gielen, M.C.M. van de Sanden, and D.C. Schram, *Thin Solid Films* **271** (1995) 56
- [20] J.J. Beulens, A.J.M. Buuron, and D.C. Schram, *Surf. Coat. Technol.* **47** (1991) 401
- [21] A.J.M. Buuron, *Plasma Deposition of Carbon Materials*, Ph.D. Thesis, Eindhoven University of Technology (1993)
- [22] A. de Graaf, G. Dinescu, J.L. Longueville, M.C.M. van de Sanden, D.C. Schram, E.H.A. Dekempeneer, and L.J. van IJzendoorn, *Thin Solid Films* **333** (1998) 29
- [23] A. de Graaf, *Deposition of CNH Materials; Plasma and Film Characterization*, Ph.D. Thesis, Eindhoven University of Technology (2000)
- [24] W.M.M. Kessels, F.J.H. van Assche, J. Hong, J.D. Moschner, T. Lauinger, D.C. Schram, and M.C.M. van de Sanden, *Mater. Res. Soc. Symp. Proc.* **664**, A.8.6.1. (2001).
- [25] R. Groenen, J. Loffler, P.M. Sommeling, J.L. Linden, E.A.G. Hamers, R.E.I. Schropp, and M.C.M. van de Sanden, *Thin Solid Films* **392** (2001) 226
- [26] J. Loffler, R. Groenen, J.L. Linden, M.C.M. van de Sanden, and R.E.I. Schropp, *Thin Solid Films* **392** (2001) 315
- [27] P. Tien, G. Smolinsky, and R. Martin, *J. Appl. Opt.* **11** (1972) 637
- [28] J. Leiber and W. Michaeli, *Proc. ANTEC Society on Plastics Engineers*, Detroit (1992) 2583
- [29] G. Wahl, M. Pulver, W. Decker, And L. Klippe, *Surf. Coat. Technol.* **100-101** (1998) 132
- [30] T. Templer, L. Vallier, R. Madar, J.C. Oberlin, and R.A.B. Devine, *Thin Solid Films* **241** (1994) 251
- [31] C. Falcony, A. Ortiz,, S. Lopez, J.C. Alonso, and S. Muhl, *Thin Solid Films* **199** (1991) 269
- [32] J. Sielski and M. Kryszewski, *IEEE Trans. Electr. Insul.* **27** (1992) 687
- [33] N. Inagaki, S. Kondo, M. Hirata, and H. Urushibata, *J. Appl. Polym. Sci.* **30** (1989) 3385
- [34] P. Fayer, C. Holland, B. Jaccoud, and A. Roulin, *Proc. 38th SVC conf.* (1995) 15
- [35] H.P. Schreiber, M.R. Wertheimer, and A.M. Wróbel, *Thin Solid Films* **72** (1980) 487
- [36] T. Okuhare and J.M. White, *Appl. Surf. Sci.* **29** (1987) 223
- [37] R.K. Sathir and Z.N. Sanjana, *J. Mater. Sci.* **26** (1991) 4261

- [38] S.M. Han and E.S. Eydil, *J. Vac. Sci. Technol.* **A 14** (1996) 2062
- [39] L.-N. He, S. Hasagwa, *Thin Solid Films* **384** (2001) 195
- [40] K.H.A. Bogart, S.K. Ramirez, L.A. Gonzales, G.R. Bogart, and E.R. Fisher, *J. Vac. Sci. Technol.* **A 16** (1998) 3175
- [41] A. Granier, F. Nicolazo, C. Vallee, A. Goullet, G. Turban, and B. Grolleau, *Plasma Sources Sci. Technol.* **6** (1997) 147s
- [42] N. Benissad, C. Boisse-Laporte, C. Vallee, A. Granier, and A. Goullet, *Surf. Coat. Technol.* **116-119** (1999) 868
- [43] M. Walker, K.M. Baumgärtner, J. Fiechtinger, M. Kaiser, A. Schulz, and E. Rächle, *Vacuum* **57** (2000) 387
- [44] Sigma Chemical Inc. Material Safety Data Sheet H3762 Hexamethyldisiloxane
- [45] H.J. Boer, *Journal de Physique IV* **5** (1995) C5-961
- [46] H.J. Boer, *Solid State Technology* (March 1996) 149
- [47] Merck Chemicaliën Catalogus (Dutch) 1998-1999
- [48] N.J. Harrick, *Internal Reflection Spectroscopy*, John Wiley & Sons Inc., New York (1967)
- [49] J.R. During, *Applications of FT-IR Spectroscopy*, Elsevier, Amsterdam (1990)

Chapter 2

Setup and diagnostics

2.1 Deposition setup

The used deposition setup has been described extensively before [1,2,3]. The setup can be splitted in five main parts which will shortly be discussed hereafter. An overview of the setup is given in Figure 2.1.

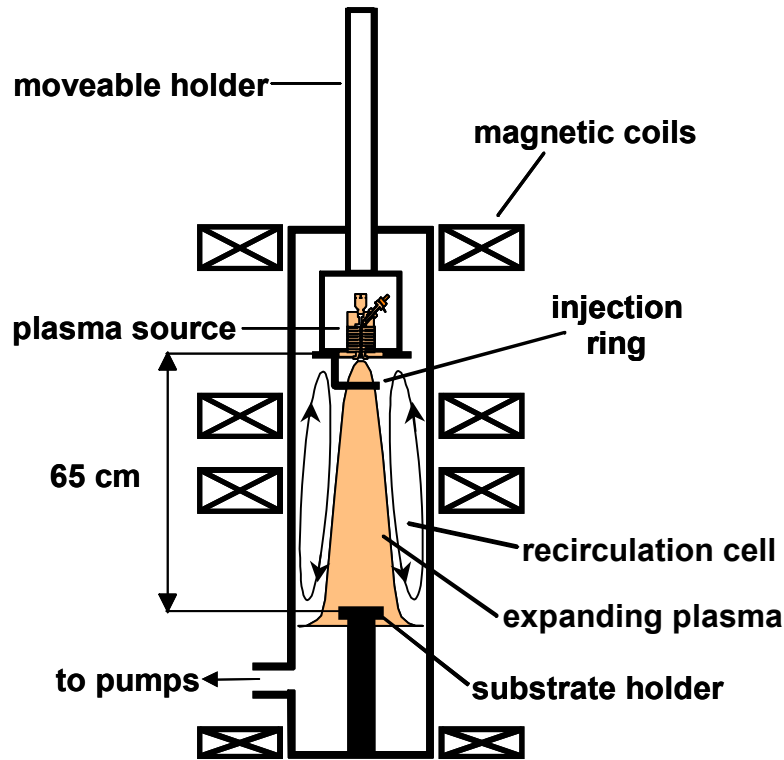


Figure 2.1: *The expanding thermal plasma deposition setup.*

- Plasma source*

The plasma source is a wall-stabilised cascaded arc [4], which is shown in Figure 2.2. The arc consists of three cathodes, four cascade plates and one anode plate. The cathodes are located symmetrically in the cathode housing (top). The cathode housing, plates and anode are insulated by means of boron nitride rings. All parts are made of copper except for the cathode tips, which are made of tungsten with 2 % of lanthanum to reduce the work function. The arc channel has a diameter of 4 mm. The cascaded arc is operated using argon gas (purity grade 5.0), with typical flows between 25 sccs and 100 sccs, which is injected through a hole in the top off the cathode housing. Typical arc currents are between 25 A and 90 A and typical operating pressures in the cathode house under these conditions vary from 0.2 bar to 0.5 bar.

* Beside the plasma source mentioned here there is also a second plasma source present. To the substrate holder an RF bias can be applied. This plasma source has however not been used in this work and therefore will not be discussed.

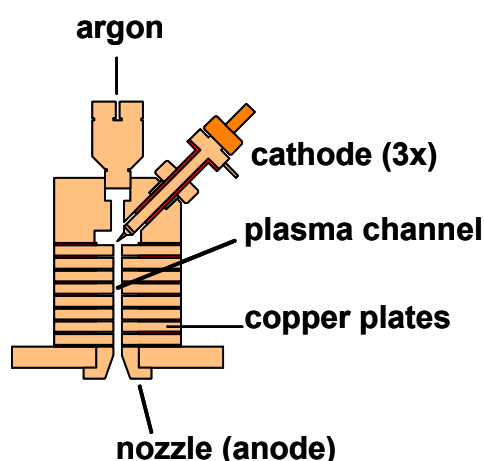


Figure 2.2: *The cascaded arc.*

- Expansion vessel

The expansion vessel is a stainless steel cylindrical vessel (diameter 32 cm, length approximately 100 cm) which is positioned vertically[†]. On top of the expansion vessel the plasma source has been mounted in a stainless steel container which is mounted on a moveable arm, which gives the possibility to change the vertical position of the plasma source in the vessel. The expansion vessel has been equipped with several ports for mounting analysis tools. Under typical operation conditions in combination with the used pumping system typically downstream pressures in the range from 0.1 mbar and 0.5 mbar are obtained. Due to the large difference in pressure between the arc and the expansion vessel, the plasma will flow out of the arc at supersonic velocity [5,6,7]. In the expansion the velocity will first increase and then decrease until a shock front will be formed after which the plasma flows at subsonic velocities towards the substrate holder. The position of this shock front depends on the plasma conditions.

- Substrate holder

The substrate holder, on which the substrates are mounted, is situated at the bottom of the vessel. The distance between the arc exit (nozzle) and the top of the substrate holder is equal to 65 cm, but as mentioned can be varied by means of a moveable arm. The substrate holder is mounted on top of a temperature controlled chuck due to which the temperature of the substrate holder can be varied in a range of - 50 °C to 300 °C with a temperature accuracy at the substrate surface of $\Delta T \approx 10$ °C [8]. For the temperature control a combination of ohmic heating and liquid nitrogen cooling is used. For a good heat contact between the substrate holder and the chuck a small flow of helium gas is used (couple of sccs). A load lock system is used to change the substrate holder without pressurising the expansion vessel. The base pressure of the load lock system is approximately 10^{-6} mbar.

[†] The reactor vessel is circumvented by several magnetic coils, which can be used to confine the plasma. These have not been used in this work and are therefore not discussed.

- Pumping system

The reactor vessel is connected to a pump stack with one rotary piston pump (Edwards: 240 m³/hr) and two mechanical booster pumps (Edwards EH2600: 2600 m³/hr; Edwards EH500A: 500 m³/hr) which generate a base pressure of 10⁻⁴ mbar. Overnight the reactor is pumped by a turbo molecular pump (Leybold Turbovac 1500: 90 m³/hr) which keeps the reactor pressure at 10⁻⁶ mbar.

- Gas handling system

Into the expanding argon plasma, precursors are injected to obtain deposition on top of the substrates. There are two different precursor injection positions. The precursor can be injected through the nozzle of the cascaded arc as well as through a punctured ring situated approximately 5 cm from the arc exit. For the injection of the precursor through the nozzle a special nozzle has been used, as shown in Figure 2.3. This nozzle makes it possible to inject the oxygen symmetrically into the plasma beam. Also the precursor is injected before the plasma shock and therefore the mixing of the precursor and the argon plasma is very good.

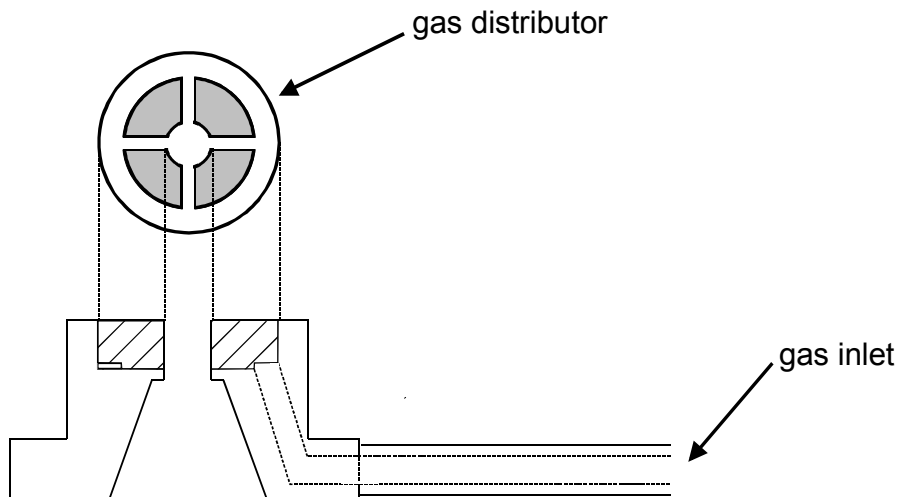


Figure 2.3: Schematic of the injection nozzle.

In general these precursors are gaseous and are controlled by means of regular mass flow controllers. However in this work organosilicon precursors are used which at room temperature are in a liquid phase. Therefore these kind of precursors first need to be evaporated, which can be done by so called bubbler systems. A disadvantage of these kind of systems is that they do not produce a very stable vapour flow and therefore another system for the evaporation of liquid precursors has been chosen.

For the evaporation of the precursor a Bronckhorst controlled evaporation module (CEM, type W-202) in combination with a Bronckhorst Liqui-Flow® meter (type L2C2) has been used. This is a closed system, which controls the liquid flow rate and evaporates the liquid fully. This system is more reliable and stable than the more conventionally used bubbler systems [9,10]. Just as in the case of a bubbler system a carrier gas for the vapour is needed, which is supplied to the CEM system by means of a regular gas flow controller.

Because the gas used for the plasma is argon also argon has been selected as the carrier gas. An schematic overview of the complete liquid evaporation module is given in Figure 2.4.

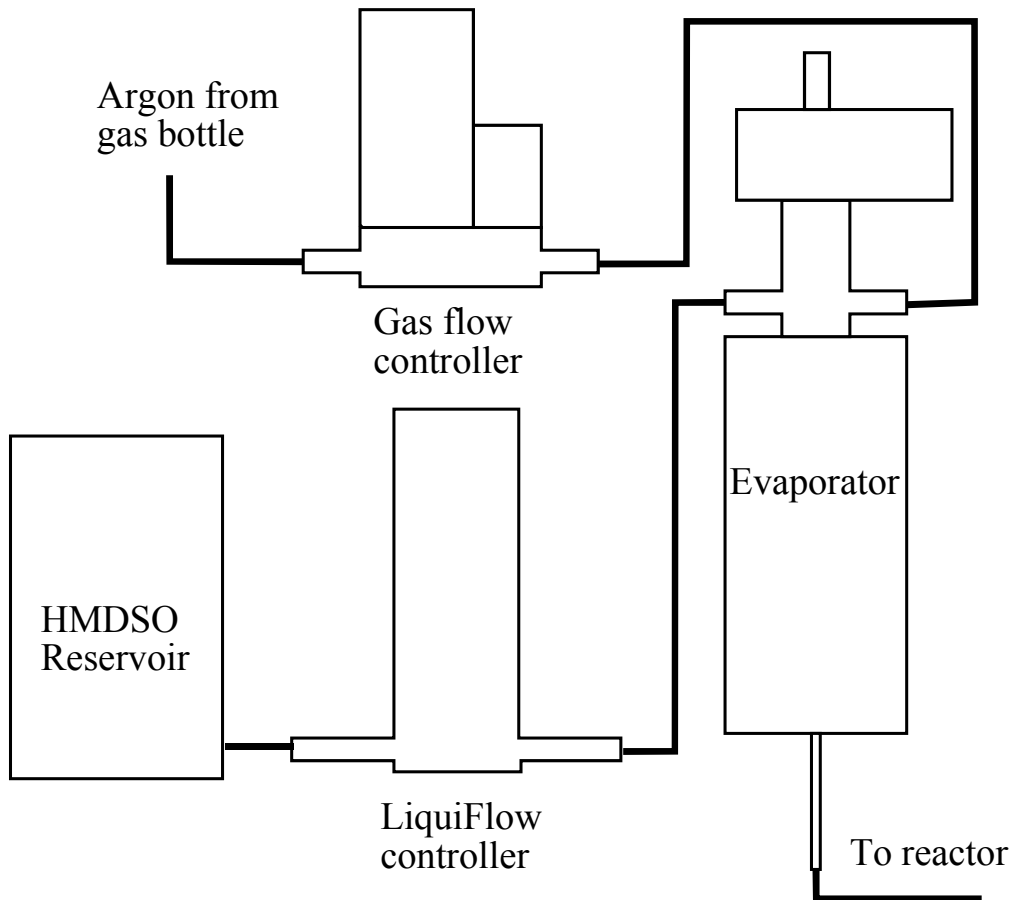


Figure 2.4: Schematic of the liquid evaporation system.

2.2 Diagnostics

2.2.1 Ellipsometry

Ellipsometry is an optical diagnostic which can be used to determine the complex refractive index and thickness of a film material which is deposited on top of a known substrate material. The main principle of this optical technique is based on the difference in reflection coefficient for perpendicular (s-direction[‡]) and parallel polarized (p-direction) light (cf. Figure 2.5). This means that at reflection at a surface the polarisation direction of polarized light will change. The change itself is dependent on the optical properties of the material at which the reflection takes place.

[‡] 's' is of the german word 'senkrecht' which means perpendicular.

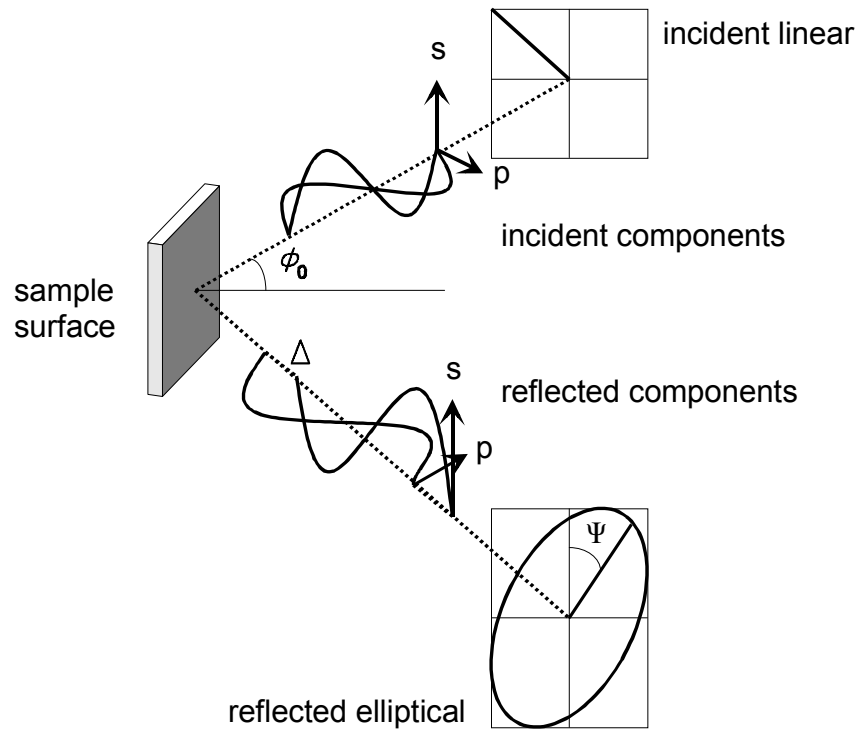


Figure 2.5: Schematic overview of the meaning of the ellipsometric parameter Ψ and Δ .

The complex reflection ratio (ρ) of the parallel and perpendicular reflection coefficient, r_p and r_s respectively, is given by:

$$\rho = \frac{r_p}{r_s} = \frac{|r_p|}{|r_s|} \exp[i(\delta_p - \delta_s)] = \tan(\Psi) \exp(i\Delta) \quad (2.1)$$

where δ_p and δ_s are the individual phase shifts at reflection for the parallel and perpendicular component respectively. In general the values of the ellipsometric parameters Ψ and Δ are measured by an ellipsometer. When the material at which the light is reflected is assumed to be a semi infinite material then it is easy to calculate the complex refractive index from these parameters. In that case the so called two phase model can be used, which is mostly used for bulk materials. The Fresnel equations for optical isotropic materials, obtained from boundary conditions for the electric field components at the surface are given by [11,12]:

$$r_p = \frac{n_0 \cos \phi_0 - n_1 \cos \phi_1}{n_0 \cos \phi_0 + n_1 \cos \phi_1} \quad (2.2)$$

$$r_s = \frac{n_1 \cos \phi_0 - n_0 \cos \phi_1}{n_1 \cos \phi_0 + n_0 \cos \phi_1} \quad (2.3)$$

Here n_1 and n_2 are the complex refractive indices of respectively ambient and the sample and ϕ_0 and ϕ_1 are the angle of incidence and the angle of refraction respectively as indicated in Figure 2.6.

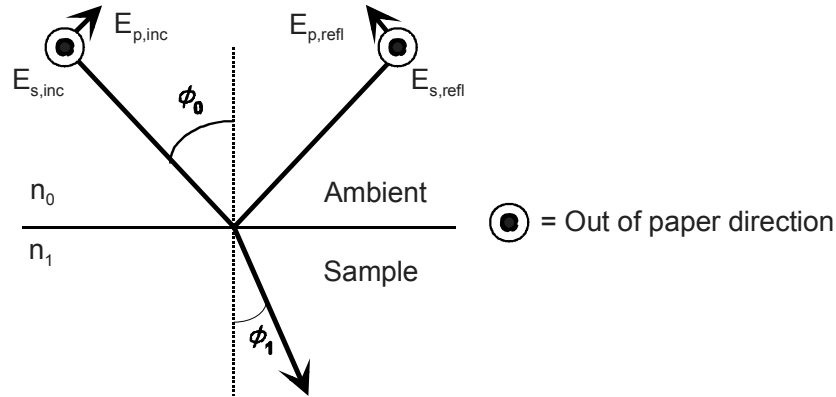


Figure 2.6: Reflection on a semi infinite sample.

By combining the Fresnel equations and the complex reflection ratio (Eq. (2.1)) an equation for the complex refractive index can be derived:

$$n_1 = n_0 \sin \phi_0 \sqrt{1 + \left(\frac{1 - \rho}{1 + \rho} \right) \tan^2 \phi_0} \quad (2.4)$$

This equation can also be used more generally for substrates with one or more films on top of it. However the refractive index obtained in that way for these kind of systems will be a refractive index for the whole system and no information about the refractive index of the individual films is obtained.

The two phase model is only valid for ideal surfaces with optical properties that do not vary from the bulk properties. If the optical properties of the bulk material do differ from the surface properties then a three or more phase model needs to be applied. For the films deposited in this work the film can always be assumed as a homogeneous film and therefore a three phase model is sufficient. A global representation of the deposited samples is given in Figure 2.7. The reflection coefficients for this system of film and substrate are given by:

$$r_\alpha = \frac{r_{02}^\alpha + r_{21}^\alpha e^{-2i\beta}}{1 + r_{02}^\alpha r_{21}^\alpha e^{-2i\beta}} \quad (2.5)$$

where r_{lm}^α is the Fresnel coefficient for α -polarised (p or s) light at the interface from l to m and

$$\beta = \frac{2\pi d_2 n_2 \cos \phi_2}{\lambda} \quad (2.6)$$

the phase thickness, with λ the wavelength of the used light and d_2 the thickness of the film.

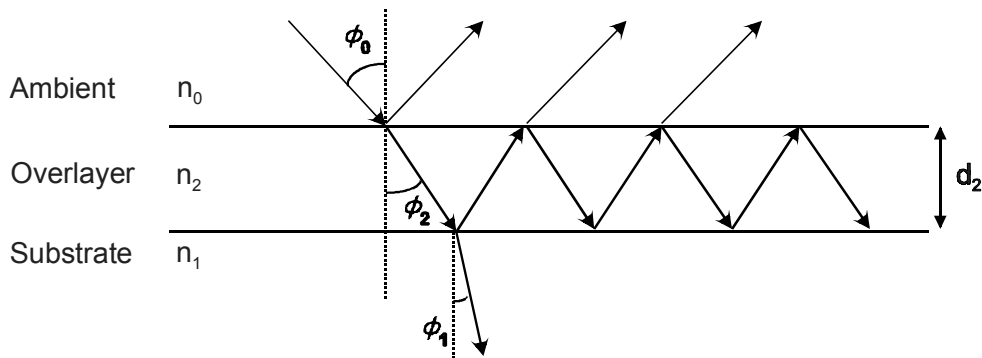


Figure 2.7: Schematic overview of a sample with a thin homogeneous film on top.

For multiple films also reflection coefficients can be derived, but for simulation purposes it is often easier to use the so called impedance formalism. This is easy to use because it makes it possible to add and subtract thin film effects on the ellipsometric parameters. More details on this impedance formalism can be found in literature [13].

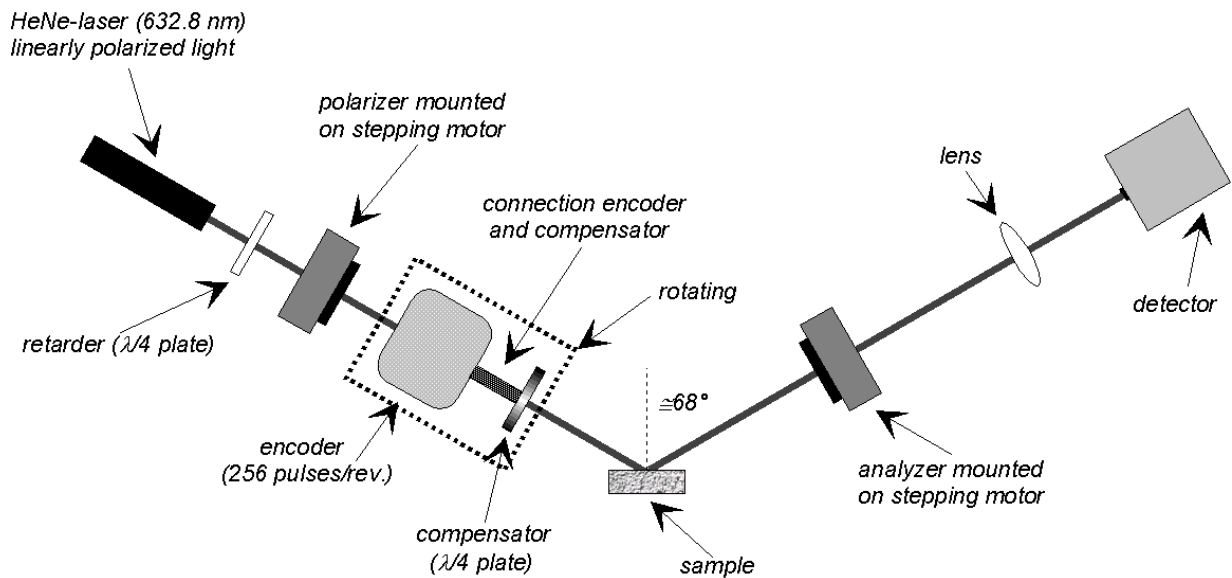


Figure 2.8: Schematic representation of the used *in situ* rotating compensator ellipsometer.

In this work an *in situ* rotating compensator ellipsometer has been used to perform the actual measurements. A schematic representation of the used ellipsometer is shown in Figure 2.8. As a light source a He-Ne laser ($\lambda = 632.8$ nm) is used, which is polarised circularly by a $\lambda/4$ plate. By means of a polariser this light is linearly polarized after which the light passes through a second $\lambda/4$ plate (compensator) which is rotating. This results in time dependent polarised light which enters the reactor by means of a quartz window and it is reflected at the sample surface. The reflection changes the polarisation of the incident light. The reflected light exits the reactor through another quartz window after which it passes through another polariser (analyser) before being focused onto a photodiode detector. The detector signal as well as the rotating compensator position are measured by a computer by means of an ADC. From the registered detector signal as function of the compensator position, the ellipsometric parameters Ψ and Δ can be calculated. Dedicated software is used to simulate the

ellipsometric parameters as function of time. By comparing these simulations with the measured Ψ - Δ trajectories as function of time, the complex refractive index, the film growth rate and the final film thickness can be derived. A typical example of a Ψ - Δ trajectory obtained during the deposition of a silicon oxide like film is shown in Figure 2.9. When the Ψ - Δ trajectory does not show a spiral shape, the imaginary part of the refractive index is close to zero.

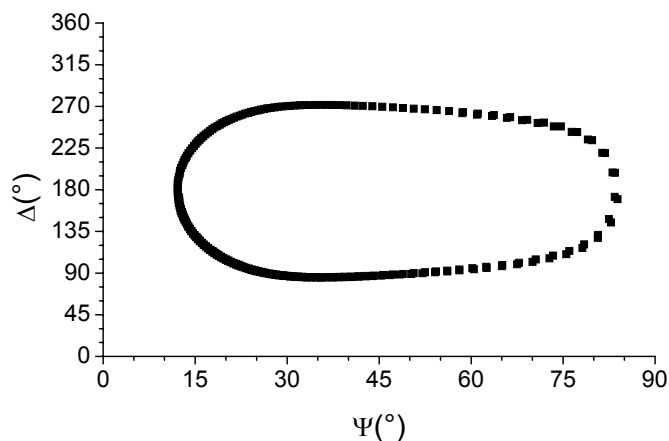


Figure 2.9: Typical Ψ - Δ trajectory obtained during the deposition of a silicon oxide like film from hexamethyldisiloxane and oxygen.

2.2.2 Infrared absorption spectroscopy

Infrared absorption spectroscopy is a very powerful tool. It can be used for many purposes in multiple configurations. It can be used for film analysis as well as for the sampling of gasses, because many vibrational bonding frequencies in solid and gaseous materials are in the infrared part of the electromagnetic spectrum. In this section an overview will be given of the various fields for which infrared absorption spectroscopy can be used. This overview is not a complete overview and it is mainly focussed on the varieties used in this thesis work.

Infrared transmission absorption spectroscopy can be used to analyse the gas phase of a plasma as well as the solid state phase of deposited films. Work on gas phase transmission absorption spectroscopy has been published in literature by means of a paper [14] which is attached to this chapter in published form as an appendix. This paper demonstrates the power of infrared transmission absorption spectroscopy in combination with mass spectroscopy in the gas phase of a plasma. This paper also shows what kind of additional information can be obtained from gas phase infrared transmission absorption spectroscopy with respect to mass spectrometry.

Here in short the method for infrared transmission absorption spectroscopy on deposited films is treated. This is the method which is frequently used for data shown in the rest of this work. After this a discussion is given on infrared reflection absorption spectroscopy, which includes simple reflection as well as special substrates which enhance the absorption signal.

2.2.2.1 Infrared transmission absorption spectroscopy for film analysis

As described in the appendix, infrared gas phase absorption spectroscopy is a powerful analysis technique. Although it provides useful information about the gas phase of the plasma it does not give any information on the film deposition mechanism. For this infrared absorption spectroscopy needs to be applied to the surface. This can either be done in transmission or reflection.

Infrared transmission absorption spectroscopy for analysis of the deposited films is almost identical to infrared gas phase absorption spectroscopy. Here instead of the absorbing gas the sample is placed in the infrared beam. By measuring the transmission of the sample with and without the deposited film it is possible to derive the film absorption. The transmission spectrum will have an interference background aside from the resonant absorptions, which can be assigned to specific bonds. The interference is caused by multiple reflections in the deposited film. It is possible to use this background to calculate the infrared refractive index and the thickness of the deposited film [15,16]. By simulation of the interference background the transmission spectrum without this interference can be constructed from which the absorption can be calculated. In general the absorbance[§] ($A(x)$) is calculated by:

$$A(x) = -^{10}\log(Tr(x)) \tag{2.7}$$

with $Tr(x)$ is the film transmission after removal of the interference pattern at spectral position x , where x can either be in wavelength, wavenumber, energy, etc.

In general it is fairly easy do identify the absorptions caused by the various bonds present in the deposited film when the spectral positions of the various absorption bands are know. In this work infrared transmission absorption spectroscopy will be used as a main tool for the analysis of silicon oxide like films. In these type of films a limited number of bond types will be present. In Table 2.1 an overview is given of the various absorbing bonds including their absorbing wavenumber range as they have been reported in literature. The table is limited to the bonds that have been used for analysis in this thesis.

Table 2.1: Overview of the various film absorbing bonds and their absorbing wavenumber range.

Bond type	Wavenumber (cm ⁻¹)	Reference
Si-O	430-450	[17,18,19,20]
Si-O ₂	430-450	[17,18]
Si-O-Si	1020-1090	[18,19,20,21]
Si-O-C	1020-1090	[18,20]
Si-CH ₃	1260	[18,19,21]
CH _x	2960	[18,22]
Si-OH	3000-3600	[17,19,20]
Si-H	2100-2300	[18,19]

[§] In this thesis this parameter is also addressed as ‘absorption’.

For the actual measurement of the infrared transmission spectra of the deposited films, a Bruker Vector 22 Fourier transform infrared spectroscope has been used. For reaching a good signal to noise level, 100 measured spectra are averaged. The measuring resolution of 4 cm^{-1} is used, which is sufficient because the solid state absorption peaks have in general a width that is several times this resolution [23].

2.2.2.2 Infrared reflection absorption spectroscopy

Where infrared transmission absorption is mostly used as an *ex situ* analysis tool, infrared reflection absorption spectroscopy is often used as an *in situ* analysis tool [e.g. 24,25,26]. This means that in the case of transmission absorption measurements the sample with the deposited film is often transported through and exposed to air, which can change the film properties. In the case of *in situ* infrared spectroscopy this influence is avoided. In general samples in a deposition reactor are mounted on a substrate holder through which *in situ* infrared transmission absorption spectroscopy is most likely not possible. Therefore, *in situ* infrared reflection absorption is often used in that situation [24]. In Figure 2.10 an example of a *in situ* infrared reflection spectroscopy setup, based on a FTIR spectroscope, is shown. The infrared beam emitted by the FTIR spectroscope is focussed on the sample by means of a 90° off axis parabolic mirror and after reflection the beam is focussed on an MCT infrared detector.

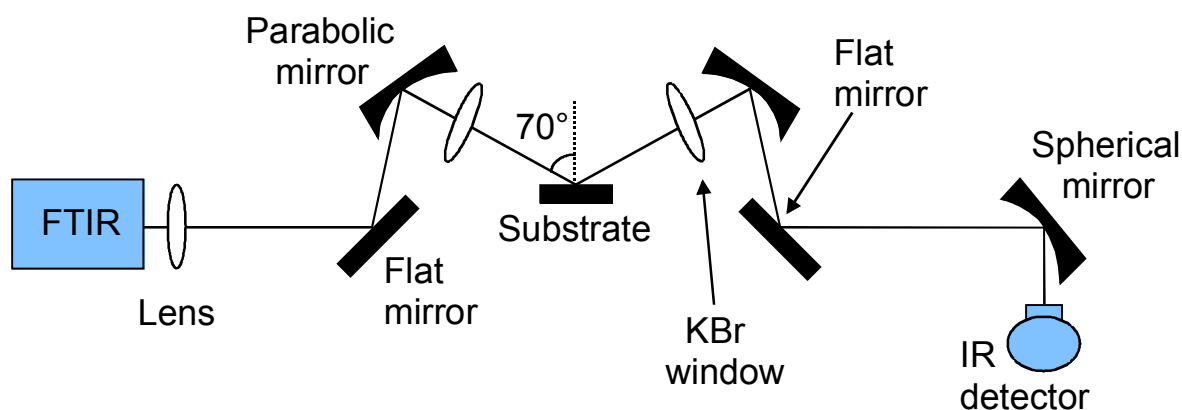


Figure 2.10: A typical infrared reflection absorption spectroscopy setup.

Another advantage from using *in situ* reflection absorption spectroscopy is that it is possible to study the actual film growth. However to do so, the sensitivity of the used device needs to be sufficient. When the film is in a static situation, the sensitivity of a reflection absorption spectroscopy can be enhanced quite easily by measuring the infrared reflection spectrum several times and averaging them. However, a single reflection at the sample surface is in general not sufficient to reach monolayer sensitivity when the measurements have to be done in real-time, i.e. at the same time scale as the deposition of one monolayer. Several techniques are available to enhance the absorption signal above the detection limit of the infrared reflection absorption spectroscopy, due to which the measuring time can be reduced. However the measuring time cannot be reduced indefinitely because of the instruments limitations. Therefore, the typical measuring time for a single scan of a typical FTIR spectroscopy is higher than the time needed to deposit one monolayer, in particular at very high growth rates (several tens of nm per second). For the deposition process studied in this

work this is the case and therefore a new infrared spectroscope has been developed which is described extensively in chapter 3.

In this work attenuated total reflection (ATR) [27,28] will be used for the enhancement of the absorption signal. This is only one of the several techniques that can enhance the absorption signal. An extensive discussion of several techniques to enhance the absorption signal has been given by de Graaf [3]. In that work he demonstrates the use of e.g. optical cavity substrates [29] and metal substrates [30,31]. These techniques in general only provide enhancement in a limited wavelength interval. This however does not apply to the ATR technique. A detailed description of the ATR theory has been given by Harrick [28]. Here only a short general description will be given and some important details will be stressed.

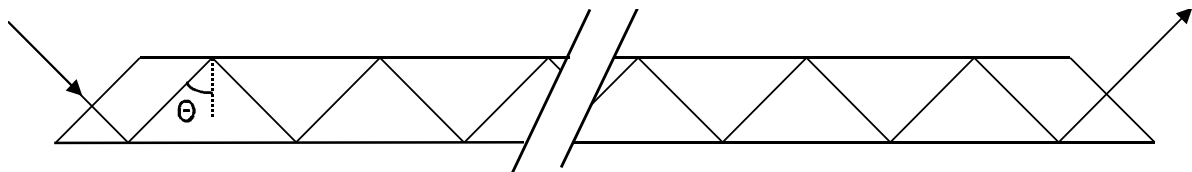


Figure 2.11: Trapezium shaped ATR crystal.

When using the ATR technique a crystal is used, which can have several shapes, e.g. a parallelogram or a trapezium shape. In Figure 2.11 an example is given of a trapezium shaped ATR crystal, which is also the shape used for the *in situ* infrared measurements in this work. Light enters the ATR crystal on one side, then several internal reflection follow, after which the light leaves the substrate at the other side. When there is an absorbing medium on top of the crystal the light beam will interact with this film several times and therefore the absorption is enhanced. The number of reflections is dependent on the length of the ATR crystal and on the angle of the light beam and the initial surface. Whether the reflections at the surface of the ATR crystal are total internal reflections is dependent on the angle of the light in the crystal and on the refractive index change at the boundary of the crystal and its surrounding. Total internal reflection occurs when both the parallel and the perpendicular reflection coefficient are equal to 1. In the case of total internal reflection no energy is lost due to reflection, only due to absorption in the crystal medium. The minimum angle at which this occurs is known as the critical angle (θ_c), given by:

$$\theta_c = \sin^{-1} \frac{n_2}{n_1} \quad (2.8)$$

where n_1 is the refractive index of the medium in which the light propagates, and n_2 is the refractive index of the medium at which the light is reflected. Total internal reflection occurs at angles (θ) between the critical angle and grazing angle ($\theta_c \leq \theta < 90^\circ$). From Eq. (2.8) it can be seen that for total internal reflection to occur the refractive index of the medium in which the light propagates needs to be larger than that of the medium at which the light is reflected.

When total internal reflection occurs an evanescent wave will be created which reaches into the medium at which the light is reflected. The amplitude of the electric field of this evanescent wave falls off exponentially with the distance from the reflecting surface. When there is no absorption, the distance which is needed to reduce the electric field

amplitude to e^{-1} of its original value at the surface is called the depth of penetration (d_p), which is given by:

$$d_p = \frac{\lambda / n_1}{2\pi \sqrt{\sin^2 \theta - (n_2 / n_1)^2}} < \frac{\lambda}{2\pi n_1}. \quad (2.9)$$

Here λ is the wavelength of the light which is reflected. It can be derived that with the presence of an evanescent wave there is no net flow of energy out of the surface [28].

When a film is deposited on top of an ATR crystal then, dependent on the refractive index of the deposited film, two different processes can occur. When the refractive index of the film is too high, i.e. no total internal reflection occurs anymore at the interface of the crystal and the deposited film, the light beam will partially propagate into the film and undergo a total internal reflection at the film surface and an evanescent wave reaches into the ambient of the film. This is the case if the reflection angle is still above the critical angle. When the refractive index of the deposited film is low enough and total internal reflection does still occur at the interface of the crystal and the deposited film, then an evanescent wave will penetrate in the deposited film. From Eq. (2.9) it can be seen that in case of infrared light ($\lambda=10 \mu\text{m}$) the depth of penetration will still be in the order of micrometers. When the deposited film is absorbing, part of the energy in the evanescent wave is absorbed and therefore the total energy throughput of the ATR crystal is reduced. Independent of the refractive index of the film deposited on top of the ATR crystal a part of the light that enters the crystal is being absorbed either directly or indirectly by the film.

The absorption enhancement with respect to single reflection is caused by the multiple interactions of the light with the film when an ATR crystal is used. The number of interactions is independent of the refractive index of the crystal when the light enters perpendicular to the initial bevel of the crystal and therefore also the enhancement is independent of the wavelength of the light. Obviously the wavelength interval for which the ATR crystal can be used is limited by the transmission properties of the ATR crystal material.

Changing from transmission absorption spectroscopy to reflection absorption spectroscopy is less straightforward as has been mentioned. By changing from transmission to reflection also some complications are generated. The most important complication is a change of spectral absorption peak position and of the peak shape with respect to transmission absorption spectroscopy (cf. Figure 2.12). The absorption peak change is dependent on the reflection angle and has been described by Harrick [28] for both internal and external reflection. Here the presence of the change and the explanation will be discussed briefly for external reflection only. However, for internal reflection a similar effect occurs as has been shown by Harrick [28].

The change of position and shape is caused due to the change of the real part of the refractive index at a spectral position at which an absorption takes place. The absorption scales with the imaginary part of the refractive index. By means of the Kramers-Kronig relation [32,33] it is possible to use a transmission absorption spectrum to derive the films complex refractive index. In Figure 2.13 the complex refractive index as derived from the transmission absorption spectrum shown in Figure 2.12 is shown. Form this in combination with the Fresnel reflection coefficients [11,12] the reflection absorption spectrum can be calculated. In Figure 2.12 the calculated reflection absorption spectrum and measured

reflection absorption spectrum are shown besides the transmission spectrum^{**}. It can be seen clearly that in the part of the spectrum where there is absorption the calculated and measured reflection absorption spectra are quite similar although the match is not 100% perfect. This proves that the change in the real part of the refractive index as a result of absorption is causing the absorption peaks to change shape and position. The difference observed outside the absorption zone and the small difference observed in the absorption zone is mainly caused by assumptions that had to be made for the refractive index of the substrate material in order to perform the calculation.

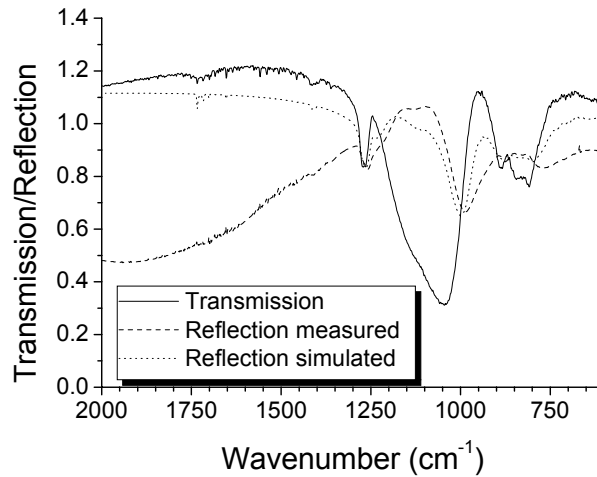


Figure 2.12: Measured transmission and reflection absorption spectrum of a typical deposited $\text{SiO}_x\text{C}_y\text{H}_z$ film on silicon as well as the simulated reflection absorption spectrum.

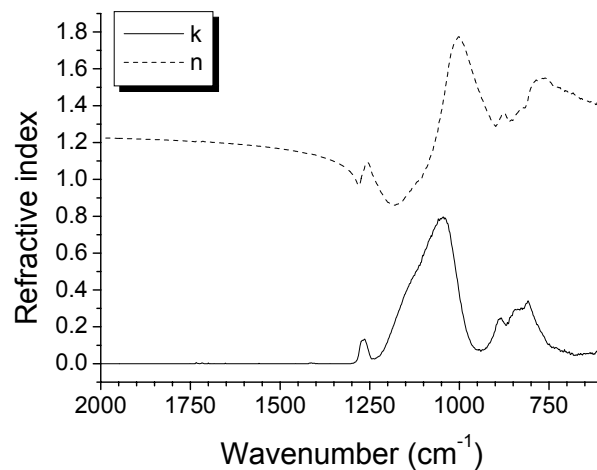


Figure 2.13: Calculated complex refractive index. Calculated from the measured transmission absorption spectrum shown in Figure 2.12. n and k are Kramers-Kronig consistent.

^{**} Thanks to Dr. Achim von Keudel for supplying his program for the calculation of the reflection spectrum and the refractive index.

References

- [1] J.W.A.M. Gielen, M.C.M. van de Sanden, P.R.M. Kleuskens, and D.C. Schram, *Plasma Sources Sci. Technol.* **5** (1996) 492
- [2] J.W.A.M. Gielen, W.M.M. Kessels, M.C.M. van de Sanden, and D.C. Schram, *J. Appl. Phys.* **82** (1997) 2643
- [3] A. de Graaf, *Deposition of CNH Materials; Plasma and Film Characterization*, Ph.D. Thesis, Eindhoven University of Technology (2000)
- [4] H. Mäcker, *Z. Naturforsch.* **11** (1956) 457
- [5] M.C.M. van de Sanden, J.M. de Regt and D.C. Schram, *Plasma Sources Sci. Technol.* **3** (1994) 501
- [6] R.Engeln, S. Mazzouffre, P. Vankan, D.C. Schram, and N. Sadeghi, *Plasma Sources Sci. Technol.* **10** (2001) 595
- [7] S. Mazouffre, M.G.H. Boogaarts, J.A.M. van der Mullen, and D.C. Schram, *Phys. Rev. Lett.* **84** (2000) 2622
- [8] J.W.A.M. Gielen, *Plasma Beam Deposition of Amorphous Hydrogenated Carbon*, Ph.D. Thesis, Eindhoven University of Technology (1996)
- [9] H.J. Boer, *Journal de Physique IV* **5** (1995) C5-961
- [10] H.J. Boer, *Solid State Technology* (March 1996) 149
- [11] R.M.A. Azzam and N.M. Bashara, *Ellipsometry and Polarized Light*, North-Holland Publishing Co., Amsterdam (1977)
- [12] F.L. Pedrotti and L.S. Pedrotti, *Introduction to Optics*, Prentice-Hall Inc., New Jersey (1993)
- [13] G.M.W. Kroesen, *Ellipsometry*, Course Notes (nr. 3P200), VDF/NG 96-01, Eindhoven University of Technology (1996)
- [14] M.F.A.M. van Hest, A. de Graaf, M.C.M. van de Sanden, and D.C. Schram, *Plasma Sources Sci. Technol.* **9** (2000) 615; Appendix A of this Chapter.
- [15] A.J.M. Buuron, M.C.M. van de Sanden, W.J. van Ooij, R.M.A. Driessens, and D.C. Schram, *J. Appl. Phys.* **78** (1995) 528
- [16] J.W.A.M. Gielen, M.C.M. van de Sanden, and D.C. Schram, *Thin Solid Films* **271** (1995) 56
- [17] M. Nakamura, Y. Mochizuki, and K. Usima, *Solid State Comm.* **50** (1984) 1079
- [18] K. Kashiwagi, Y. Yoshida, and Y. Murayama, *Jap. J. Appl. Phys.* **30** (1991) 1803
- [19] J.A. Thiel, J.G. Brace, and R.W. Knoll, *J. Vac. Sci. Technol. A* **12** (1994) 1365
- [20] K. Sano, S. Hayashi, S. Wickramanayaka, and Y. Hatanaka, *Thin Solid Films* **281-282** (1996) 397
- [21] S.H. Lee and D.C. Lee, *Thin Solid Films* **325** (1998) 83
- [22] B. Dischler, A. Bubenzer, and P. Koidl, *Solid State Comm.* **48** (1983) 105
- [23] J.R. During, *Applications of FT-IR Spectroscopy*, Elsevier, Amsterdam (1990)
- [24] M. Meier and A. von Keudell, *J. Appl. Phys.* **90** (2001) 3585
- [25] H. Ohta, M. Hori, and T. Goto, *J. Appl. Phys.* **90** (2001) 1955
- [26] P. Scheible and A. Lunk, *Thin Solid Films* **364** (2000) 40
- [27] N.J. Harrick, *Phys. Rev. Lett.* **4** (1960) 224
- [28] N.J. Harrick, *Internal Reflection Spectroscopy*, John Wiley & Sons Inc., New York (1967)
- [29] N. Maley, I. Szafranek, L. Mandrell, M. Katiyar, J.R. Abelson, and J.R. Thornton, *J. Non-Cryst. Solids* **114** (1989) 163

Chapter 2

- [30] S.A. Francis and A.H. Ellison, *J. Opt. Soc. Am.* **49** (1959) 131
- [31] Y. Toyoshima, K. Arai, A. Matsuda, and K. Tanaka, *Appl. Phys. Lett.* **56** (1990) 1540
- [32] D.W. Johnson, *J. Phys. A.* **8** (1975) 490
- [33] M.A. Turowski and T.F Kelly, *Ultramicroscopy* **41** (1992) 41

Appendix A

Use of *in situ* FTIR spectroscopy and mass spectrometry in an expanding hydrocarbon plasma

M.F.A.M. van Hest, A. de Graaf, M.C.M. van de Sanden, and D.C. Schram

Published in Plasma Sources Sci. Technol. **9** (2000) 615

Abstract

In situ Fourier transform infrared (FTIR) spectroscopy and mass spectrometry have been used to investigate the gas phase of an expanding thermal argon plasma into which hydrocarbons are injected. With both techniques it is possible to determine the depletion of the precursor gas and the densities of new species formed in the plasma, each of the techniques with its own advantages and disadvantages. To determine absolute densities of different species in the plasma by means of mass spectrometry it is necessary to deconvolute the obtained mass spectra, whereas by means of FTIR spectroscopy different species are easily recognized by their infrared absorption at specific positions in the absorption spectrum. With mass spectrometry the gas composition is measured locally, i.e. close to the gas extraction point. On the other hand with FTIR spectroscopy all particles in the infrared beam are included in the measurement. When both techniques are combined most of the individual disadvantages cancel, leading to a very powerful plasma diagnostic tool. Aside from the power resulting from the combination of both techniques, FTIR spectroscopy data also contains information on the temperature of the stable species inside the plasma. A method to extract the rotational particle temperature (within 100 K) by means of infrared absorption spectra simulation is presented.

A.1 Introduction

In depositing plasmas all kind of chemical reactions do occur. An example of a depositing plasma is an expanding argon plasma into which acetylene (C_2H_2) is injected for deposition of a-C:H and DLC materials [1,2,3]. After injection the acetylene molecules will react with the argon ions and the electrons in the expanding argon plasma, resulting in the production of radicals such as C_2H and H [4]. When methane (CH_4) is injected in an expanding argon plasma, the methane will also be dissociated by interaction with the argon ions and the electrons. The radicals produced in this way are able to react further and new stable gases, such as acetylene, will be produced (see Figure A.1). This production of new gases is also observed in an rf glow discharge in which methane is used as a feed gas [5]. Measurement of this production of new gases will lead to a better understanding of the reaction mechanisms taking place in the plasma as well as the mechanism responsible for film growth.

An easy way to investigate the plasma composition is by the use of a mass spectrometer. Mass spectrometry is widely used as a plasma diagnostic tool and much is known about the characteristics of this technique [6]. There are many different kind of methods to use mass spectrometry, e.g. appearance potential mass spectrometry, residual gas analysis (RGA), positive and negative ion mass spectrometry. In this paper an RGA will be used as a mass spectrometer. Using an RGA however has some advantages and disadvantages. An advantage is that an RGA is easy to use. One disadvantage of the use of an RGA is that measurements on molecules will always lead to a cracking pattern. One specific molecule does not lead to a signal at one specific mass. Another disadvantage is the fact that the measurement is not a direct measurement of the plasma composition, this is because an RGA is situated remote of the plasma.

A second way to measure molecules is infrared absorption spectroscopy. Due to the fact that this is an optical technique the method is non-intrusive. Just as with mass spectrometry also different methods of infrared absorption spectroscopy are available, e.g. Fourier transform infrared absorption spectroscopy (FTIRAS) used here [7,8,9] and infrared laser absorption spectroscopy (radical detection). Just as the use of an RGA, a FTIRAS setup has advantages and disadvantages. One advantage is that it is easy to distinguish different particles in the plasma, because infrared absorption is at different characteristic wavelengths. Another advantage of FTIRAS is that FTIRAS data also contains information on the temperature of the absorbing species. In this paper a method to derive the rotational particle temperature from the infrared absorption spectrum will be presented. A disadvantage is that the detection limit of FTIRAS is approximately one order of magnitude higher than that of mass spectrometry.

The major advantage of mass spectrometry and infrared absorption spectroscopy is that both techniques can be used to measure *in situ* the stable gases composition of a plasma without influencing the plasma. Another advantage is obtained from the combination of both techniques. With FTIRAS it is possible to determine easily which stable monomers are present in the plasma, because the absorbance of different species occurs at characteristic energies. This is exactly the point at which mass spectrometry fails, because the mass spectra obtained for different species often overlap, e.g. acetylene (C_2H_2), ethene (C_2H_4), and ethane (C_2H_6), each having mass peaks in the range from 24 to 30 amu. In this paper therefore both techniques will be used for the same purpose. So far the combination of both techniques has not been used very often. Hollenstein et al. [10] for example used infrared spectroscopy and

mass spectrometry but no comparison was made between results from the two techniques. In this paper FTIRAS has been used only to determine which particles are present in the plasma and not as a quantitative tool.

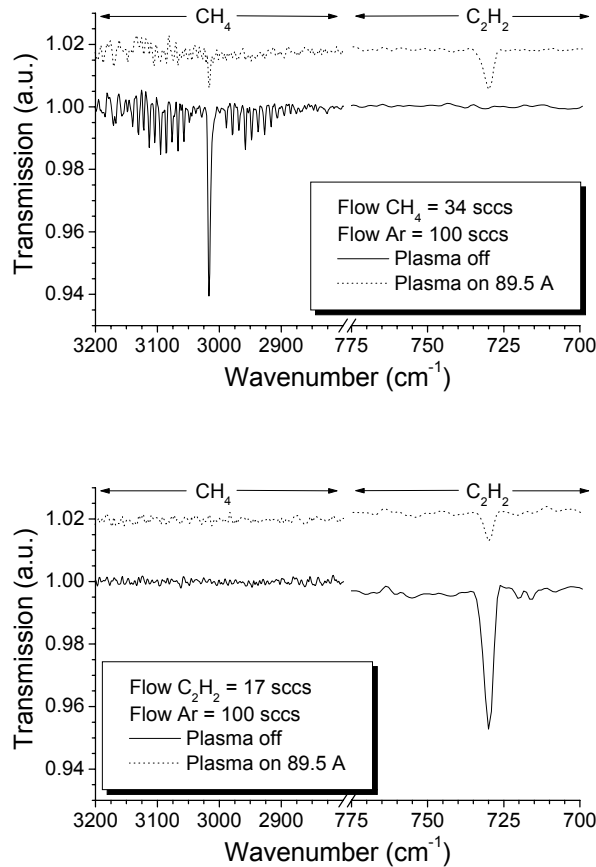


Figure A.1: Infrared transmission spectra of CH_4 and C_2H_2 in the plasma on and the plasma off situation. The baseline for the plasma on case had been shifted for the sake of clarity.

The aim of this paper is to demonstrate the power of the combination of mass spectrometry and FTIRAS. The results shown in this paper will be based on measurements performed on an expanding thermal argon/acetylene ($\text{Ar}/\text{C}_2\text{H}_2$) plasma. This paper is focussed on the diagnostic aspect of the instrumentation. A more detailed discussion concerning further interpretation of the data shown has been given by de Graaf *et al.* [11]

In the first part of the paper the experimental setup will be described, including a brief description of the used mass spectrometer and the theory of deconvolution of mass spectra. After this a short description of the Fourier transform spectrometer will be given as well as the theory of the non-linearity and temperature dependency of the absorption. In the second part of this paper experimental data will be shown and discussed. These data consists of two parts, the depletion of the precursor and the determination of the rotational particle temperature in the plasma by means of infrared absorption spectroscopy.

A.2 Experimental setup

In figure A.2 the plasma deposition setup is shown. The setup is described extensively before [1,12,13,14], therefore a short description of the setup suffices here. The setup consists of a cylindrical expansion vessel (diameter 36 cm, length 90 cm) at a base pressure of less than 10^{-5} mbar. As a plasma source a cascaded arc is used [15,16]. With this cascaded arc an expanding thermal argon plasma is created, into which a precursor gas (acetylene C_2H_2 or methane CH_4) is injected downstream at approximately 5 cm from the arc exit, by means of a punctured gas injection ring with a diameter of 10 cm. The typical deposition operating conditions are given in Table A.1. For all measurements shown an argon flow of 100 sccs and an arc to substrate distance of 60 cm has been used.

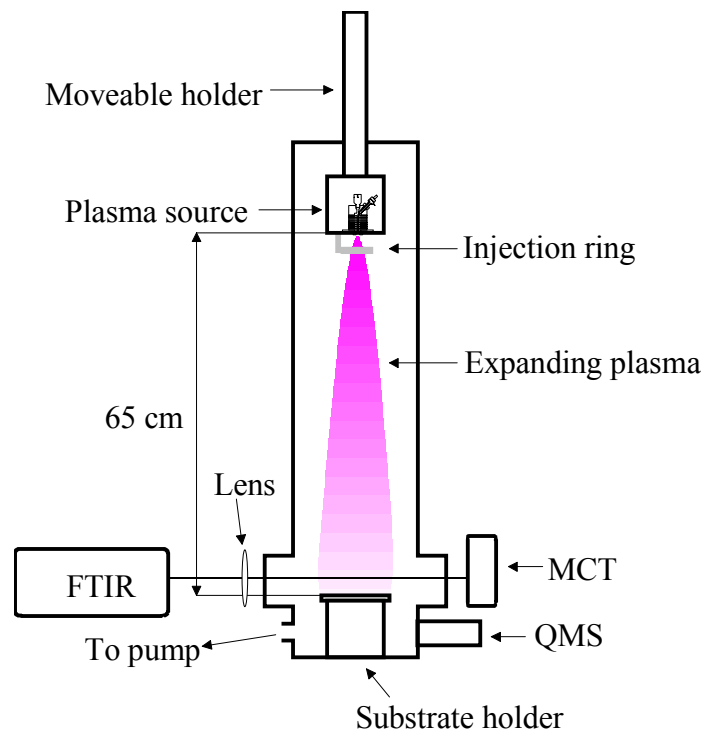


Figure A.2: Overview of the experimental setup.

Table A.1: Typical deposition setup parameters.

Parameter	Processing values
Ar Flow	25 -100 sccs
C_2H_2 Flow	0-20 sccs
Arc Current I_{arc}	30-90 A
Arc Voltage V_{arc}	50-80 V
Arc Power P_{arc}	1.5-7 kW
Arc Pressure p_{arc}	0.2-0.6 bar
Vessel Pressure p_{vessel}	0.1-1.0 mbar
Distance Arc-Substrate	30-60cm

A.3 Mass spectrometry

A Kurt J. Lesker Company AccuQuad™ 200D residual gas analyser is used to sample the background gas at a position just below the substrate holder (QMS in Figure A.2). This is done by means of a bypass valve, with a cylindrical U-shaped channel that has a diameter of 30 μm , positioned in the wall of the reactor. The mass spectrometer measures the composition of the gas in front of the gas extraction point. The plasma however is not homogeneous, due to which the composition of the gas at the wall will be different from the composition in the center of the plasma. Due to the fact that the gas extraction pinhole is situated below the substrate level, where the gas is homogeneous due to full mixing [4,17] of the gas in the expanding plasma beam and the background, the measured mass spectra will be a fingerprint of the gas in the whole vessel. So they will contain data on the expanding plasma beam as well as the background gas. Due to the U-shape of the pinhole and the absence of an ion lens it is not possible for ions or radicals to enter the mass spectrometer. The radicals will stick to, or recombine at the wall of the pinhole, whereas the ions will be neutralized on interaction with the wall of the pinhole. Therefore the mass spectra obtained will only be due to the stable molecular and atomic species present in front of the mass spectrometer's gas extraction pinhole. There will be a small contribution due to neutralised and recombined particles, however this will be negligible because the density of radicals in the plasma is low in comparison to the stable particle density.

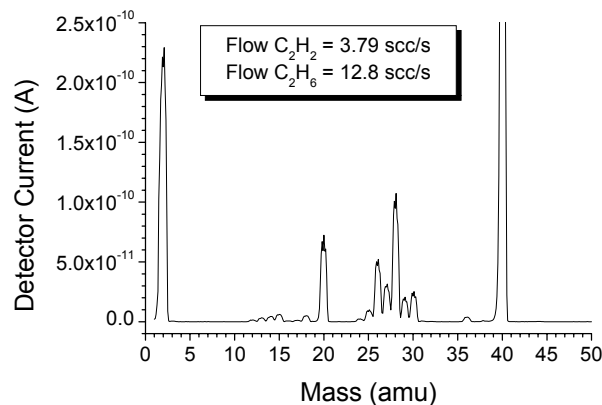


Figure A.3: Measured mass spectrum of a mixture of C_2H_2 (3.79 sccs) and C_2H_6 (12.8 sccs).

To analyse hydrocarbon species (C_nH_{2m}) present in the gas phase of the plasma, the mass spectrometry signals in the range of 12-16 amu (C to CH_4) and in the range of 24-30 amu (C_2 to C_2H_6) have been used. Analysis of the mass spectrometry signal in these ranges for four different gases (methane (CH_4), acetylene (C_2H_2), ethene (C_2H_4), and ethane (C_2H_6)) shows that there is a weak non-linear behaviour between the signal, at each individual mass, and the amount of gas present in the reactor. This non-linear behaviour is due to the non molecular flow through the pinhole. Therefore it is necessary to calibrate the mass spectrometer before measured mass spectra of unknown compound can be quantified. Contributions due to isotopes, which are present naturally in the precursor gas, are included in this calibration. When a mixture of gases is injected into the reactor, the measured mass spectrum (see Figure A.3) is equal to the sum of the mass spectra of the individual gas

species. This makes deconvolution of the mass spectra possible. For the deconvolution of the mass spectra only the calibrated cracking patterns of CH_4 , C_2H_2 , C_2H_4 , and C_2H_6 have been used. Deconvolution of mass spectrometry measurements on known mixtures of these gases result in a particle density of the individual gases that is within 5 % of the real value, which indicates that deconvolution of mass spectra works accurately. The calibration of the mass spectrometer has been performed in the situation that no plasma was present in the reactor, only argon (100 sccs) and the hydrocarbon species were present. When the plasma is ignited, some of the molecules present in the reactor will be dissociated and the temperature of the species will change. The dissociation and consecutive consumption of the hydrocarbon particles in the reactor will lead to a decrease of the measured mass spectrometer signals.

To make the deconvolution of measured mass spectra work in a situation when the plasma is on, two conditions have to be met. First the measured mass spectra should be independent of the gas temperature or the dependency on the gas temperature should be known. Second, the contribution of species other than the four used for deconvolution (i.e. C_xH_y with $x \geq 3$) in the ranges where the mass spectra are analysed should be negligible. The first condition is automatically met, because due to the combination of the mass spectrometry pinhole, the mass spectrometer, and the location at which the gas in the reactor is sampled, a change in particle density as a result of a change in particle temperature does not affect the mass spectrometry signal. This has been verified by measurements at a mass to charge ratio equal to 40 in a pure argon plasma. The mass spectrometry signal in the case the plasma is on is the same as in the case that the plasma is off, which indicates that a change in temperature does not affect the mass spectrometry signal intensity. This makes it straightforward to calculate the precursor consumption from the plasma on and plasma off signals. The second condition is in general met when there is no polymerisation in the plasma, i.e. production of C_xH_y with $x \geq 3$ in a C_2H_2 plasma. It has been shown by de Graaf et al. [11] that an Ar/ C_2H_2 cascaded arc plasma has little or no polymerisation.

A.4 Fourier transform infrared spectroscopy

A Bruker Vector 22 Fourier transform infrared spectroscope is used to sample the plasma at approximately 5 cm above the substrate holder (FTIR in Figure A.2) at one lateral position. An infrared beam (circular, approximately 5 cm in diameter) leaving the FTIR spectroscope passes through a NaCl lens ($f = 35$ cm). After this the beam is passing through the plasma reactor through two KBr windows (optical diameter 18 mm, thickness 4 mm) in the walls of the reactor. Finally the infrared beam is focused by a spherical mirror on to a nitrogen cooled Graseby D315 infrared MCT detector. The best resolution possible is 1 cm^{-1} , however all the measurements shown have been performed at a resolution of 2 cm^{-1} , which is done for the sake of speed. For each measurement 100 scans are averaged, which takes approximately 1 minute.

The absorption measured by means of infrared absorption spectroscopy is the result of a line-of-sight measurement. This means that the absorption measured is the sum of the absorption from all the species present in the infrared beam passing through the plasma. For the gases used in this study the infrared absorption spectra do not overlap. This means that it is very easy to distinguish the different species in the infrared absorption spectra. Only molecular particles can be measured, because the density of the radicals and the cross section of absorption of the atomic species are too low to be detected. The measured infrared spectrum is a convolution of the real spectrum and the apparatus profile of the FTIR

spectroscope. For the gases used the absorption line width (assumed to be only Doppler broadened) is much smaller than the apparatus profile width ($\sim 0.01 \text{ cm}^{-1}$ and 2 cm^{-1} respectively). For molecular gases the infrared absorption is not limited to one single line, but the absorption consists of many absorption lines close together (within the apparatus profile width). The absolute absorption intensity of the individual lines in the absorption band depends on the population distribution of the quantum states of the molecule. Due to the fact that the individual line width is much smaller than the apparatus profile width, the measured absorption band-head intensity ($A_{meas}(\tilde{\nu}')$) as function of the particle density has a non-linear behaviour, which is shown in Figure A.4. The band-head intensity is the difference between the maximum of the absorption peak (Q-branch) and the base line. This non-linear behaviour has also been observed by many others [7,18]. The measured non-linear behaviour can be derived mathematically from the FTIR spectroscopy and the absorption theory by assuming a Gaussian absorption line profile and a Gaussian apparatus profile. A Gaussian apparatus profile is obtained when a 3- or 4-term Blackmann-Harris apodization function is used during Fourier transformation. The measured absorption intensity at frequency $\tilde{\nu}'$ ($A_{meas}(\tilde{\nu}')$), is given by (see Appendix B):

$$A_{meas}(\tilde{\nu}') = -^{10}\log \left[1 + \sum_{qp} \frac{\Delta \nu_\ell}{\Delta \nu_a} \exp \left[-\frac{(\tilde{\nu}' - \tilde{\nu}_{qp})^2}{\Delta \nu_a^2} \right] \cdot \sum_{n=1}^{\infty} \frac{1}{n! \sqrt{n}} \left(-\frac{\alpha}{\Delta \nu_\ell \sqrt{\pi}} \right)^n \right] \quad (\text{A.1})$$

where $\tilde{\nu}_{qp}$ is the absorption frequency of a single absorption line, $\Delta \nu_\ell$ is the absorption line width, $\Delta \nu_a$ is the apparatus profile width, the sum over qp indicates a sum of all individual absorption lines. The quantity α is equal to:

$$\alpha = \frac{h \tilde{\nu}_{qp}}{c} B_{qp} N_q L \quad (\text{A.2})$$

where B_{qp} is the transition probability for a transition from state p to state q , N_q is the density of the particles in state q , L is the absorption path length, c is the speed of light, and h is the Planck constant. $N_q L$ is equal to the number of absorbing particles in the state q in the infrared beam ($\int N_q dl$).

From the right hand side of Eq. (A.1) (the sum over n) it can be seen that the absorption intensity has a non-linear behaviour on the particle density N_q and consequently also on the total particle density. This non-linear behaviour of the measured infrared absorption intensity as expressed by Eq. (A.1) and Eq. (A.2) is temperature dependent, because of one direct and two indirect effects. The direct effect is the particle density being inversely proportional to the particle temperature at constant pressure (ideal gas law). The first indirect effect is the change of the absorption line profile with a change in the particle temperature due to Doppler broadening (Eq. (A.3)). The second indirect effect is the change in the distribution of the rotational quantum states of the absorbing molecules, which leads to a change in the shape of the absorption profile measured. This distribution is dependent on the particle temperature by the Boltzmann law (Eq. (A.4)). The direct effect is automatically

accounted for in Eq. (A.2) by means of the particle density (N_q). The indirect effects can easily be implemented by using

$$\Delta v_l = \tilde{v}_{qp} \sqrt{\frac{8kT \ln 2}{mc^2}} \quad (\text{A.3})$$

for the Doppler width and

$$N_q = (2q + 1) N_0 e^{-Bq(q+1)/kT} = (2q + 1) N_{\text{tot}} \frac{B}{kT} e^{-Bq(q+1)/kT} \quad (\text{A.4})$$

for the rotational quantum state distribution. In Eq. (A.3) k is the Boltzmann constant, m is the mass of the absorbing particle, and T is the absolute temperature. In Eq. (A.4) N_{tot} is the total particle density, N_0 is the density of the particles in the quantum state $q = 0$, and B is the rotational constant of the specific particle. Implementation of the two indirect temperature effects makes it possible to derive the temperature of an absorbing gas from its infrared absorption spectrum.

Summarizing it can be said that the main difference between mass spectrometry and Fourier transform infrared gas phase absorption spectroscopy is situated in the overlapping of the signal correlated with different particles. Both techniques do not give any information on radicals present in the plasma reactor. Only information on stable molecular and atomic species is obtained. The detection limit of mass spectrometry is however almost one order of magnitude lower than that of Fourier transform infrared gas phase absorption spectroscopy.

Another mathematical description of the measured absorption intensity has been given by Cleland *et al.* [8]. However in their study a triangular apodization function was used for the Fourier transformation. The use of this apodization function results in a different mathematical expression for the measured absorption intensity. Cleland *et al.* studied N_2O , which has the advantage that the absorption lines have bigger spacing ($0.9\text{-}1.2 \text{ cm}^{-1}$) in comparison with C_2H_2 ($0.01\text{-}0.03 \text{ cm}^{-1}$). Due to the bigger spacing the individual absorption lines can still be distinguished, which is not the case for the C_2H_2 absorption band studied in this work. The mathematical expression showed in this paper can be generally used for any absorption measured as long as the apparatus profile is Gaussian.

A.5 Results and discussion

Mass spectrometry and Fourier transform infrared gas phase absorption spectroscopy are used to analyse the gas phase of an argon/acetylene ($\text{Ar}/\text{C}_2\text{H}_2$) plasma. First the mass spectrometer and the infrared spectrometry setup have been calibrated. To do this, only the precursor gas is injected into the reactor and no plasma is ignited. Meanwhile the mass spectrometry signal and the infrared absorption intensity have been measured. The measured signals are correlated to the precursor gas flow, which leads in its turn to a certain partial pressure [17]. With the use of the so obtained calibration curves (e.g. Figure A.4) it is easy to convert any measured signal to a equivalent flow. This flow is called 'equivalent', because the flow calculated is equivalent to the one if that molecule would have been injected in the absence of the plasma. Due to the fact that the calibration curves are used to derive the

equivalent flow, the assumption is made that the temperature of the particles is equal to room temperature. As will be shown further on this is close to the real temperature. The detection limit for C_2H_2 of mass spectrometry and FTIRAS in flows are 0.06 sccs and 0.5 sccs respectively. The method of using a calibration curve is the method that is generally applied to infrared absorption data [7,18].

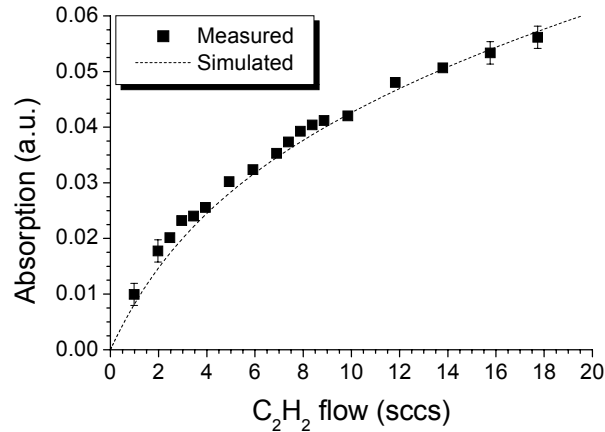
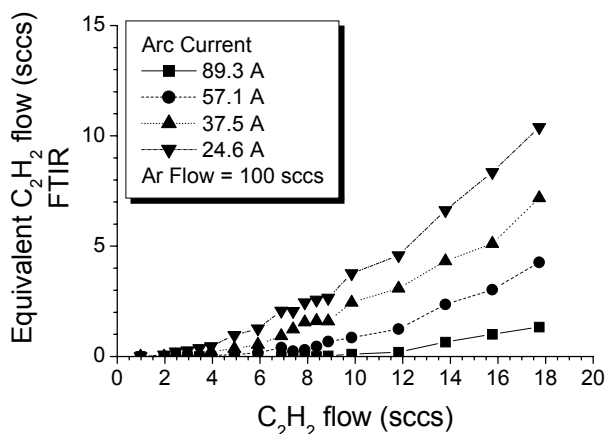


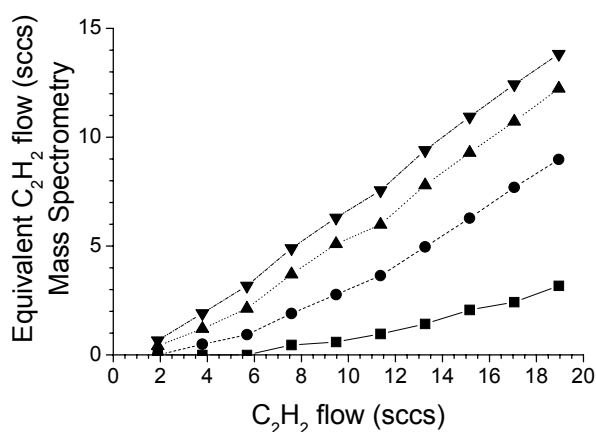
Figure A.4: Measured and simulated absorption band-head intensity for the $\nu_5(\pi_u)$ absorption band of C_2H_2 as function of the precursor gas flow.

Figure A.1 shows the infrared spectra of CH_4 and C_2H_2 for the plasma off and plasma on situation. This figure shows the strongest CH_4 and C_2H_2 absorption bands. The absorption due to C_2H_4 and C_2H_6 stay below the detection limit for the Ar/ CH_4 as well as for the Ar/ C_2H_2 plasma. From Figure A.1 it can be seen that there is a conversion of CH_4 into C_2H_2 in an Ar/ CH_4 plasma, whereas there is no conversion of C_2H_2 into C_xH_y with $x=1$ or 2 and $y=4$ or 6 in an Ar/ C_2H_2 plasma. Since there is little or no polymerisation in an Ar/ C_2H_2 plasma the mass spectra in the ranges which are analysed are not influenced by the cracking patterns of C_xH_y with $x \geq 3$. Therefore the equivalent C_2H_2 flow derived from deconvolution of the mass spectra is equal to the actual C_2H_2 flow. Figure A.5 shows the equivalent flow of C_2H_2 in an Ar/ C_2H_2 plasma as function of the C_2H_2 precursor gas flow for different arc currents as obtained from both infrared absorption spectroscopy data and mass spectrometry data. From Figure A.5 it can be seen that the equivalent flow of C_2H_2 as calculated from mass spectrometry data shows the same behaviour as the equivalent flow of C_2H_2 as calculated from infrared absorption spectroscopy data, which indicates that mass spectrometry and infrared absorption spectroscopy are compatible. However a difference in the absolute values of the equivalent flow can be observed. This difference is due to the fact that the particle density and temperature in the reactor are not constant along the line-of-sight of the infrared absorption setup. For the calibration however the particle density and temperature are constant along the line-of-sight, because the gas is distributed homogeneously when no plasma is present. When the plasma is ignited, most of the precursor gas that is not dissociated in the plasma beam will end up in the background of the plasma (see Figure A.2), resulting in a presumably hollow radial profile of the precursor particle density. Another reason for the difference between mass spectrometry and infrared absorption spectrometry is that the temperature in the plasma beam is different from room temperature, which is the temperature used to calculate the equivalent flows with. Due to the two indirect temperature

effects on the absorption and the fact that the plasma is not homogeneous, the quantitative data obtained by mass spectrometry is more accurate for calculation of the gas composition in the plasma reactor than the infrared spectroscopy data. This is mainly because mass spectrometry measures the fully mixed gas mixture and mass spectrometry data does not require any correction for the particle temperature. Further interpretation of the data shown has been given by de Graaf *et al.* [11].



(a)



(b)

Figure A.5: Measured equivalent flows of C_2H_2 as function of the C_2H_2 precursor flow for different arc currents, obtained from FTIR spectroscopy data (a) and from mass spectrometry data (b).

A.6 Temperature measurements

To get a better understanding of the processes taking place inside the expanding plasma beam, it is useful to know the particle temperature. Knowing the particle temperature can help to eliminate certain reaction mechanisms and is able to give an indication of the location (gas phase or wall) where reactions are taking place. When e.g. the temperature is low, approximately room temperature, spontaneous dissociation reaction of the precursor can be neglected. To determine the plasma temperature, an infrared spectrum simulation and

fitting program has been written for the $\nu_5(\pi_u)$ infrared absorption band of C_2H_2 (729 cm^{-1}). This infrared absorption band has been selected, because it has the highest absorption intensity (due to the presence of a Q-branch) and it is the only absorption band which, although the depletion of the precursor is high, can in most cases still be observed in the plasma on situation. The program simulates the infrared spectrum around 729 cm^{-1} using Eq. (A.1) and Eq. (A.2). To generate a spectrum by means of Eq. (A.1) and Eq. (A.2), it is necessary to know the wavelength position and transition probability of all the individual absorption lines. The Hitran 1996 molecular database [19,20] provides these data for the $\nu_5(\pi_u)$ infrared absorption band of C_2H_2 . To demonstrate the temperature effect on the absorption line profile the normalized simulated Q-branch infrared absorption spectra at different temperatures and constant particle density are shown in Figure A.6. From this figure it can be clearly seen that the width and shape of the measured absorption profile is dependent on the temperature. The higher the temperature the broader the measured absorption band. Although the natural line width (Doppler) is much smaller than the apparatus profile width, Figure A.6 clearly shows that changes can be observed in the infrared absorption spectrum due to changes in the C_2H_2 particle temperature. This is a result of changes in the particle quantum state distribution.

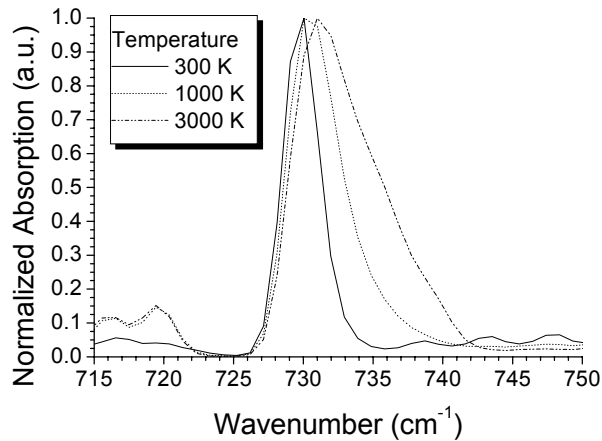


Figure A.6: Normalized Q-branch absorption intensity of the $\nu_5(\pi_u)$ absorption band of C_2H_2 for three different temperatures as derived from C_2H_2 spectrum simulation.

To check if the temperature dependency of the absorption intensity is also correct a gas cell has been built. The gas cell is an aluminum tube, which is placed inside the reactor in such a way that the infrared beam passes through it. The aluminum tube temperature, and with it the temperature of the gas in the tube, can be changed by a heating wire which is located on the outside of the aluminum tube. A thermocouple (Chromel/Alumel type K) has been used to measure the temperature of the aluminum tube. Infrared absorption spectra have been obtained at different gas cell temperatures. The obtained infrared absorption spectra have been fitted by the simulation and fitting program. In Figure A.7 a measured and a simulated spectrum, for the temperature and density found by fitting the measured data, are shown. The two small absorption peaks on the left side of Figure A.7 ($715\text{--}720\text{ cm}^{-1}$) are hot bands of the C_2H_2 molecule [21]. Analysis of these hot bands falls outside the scope of this paper. From Figure A.7 it can be seen that there is a good agreement between the measured and the simulated spectrum. The fitted temperature is close to the measured temperature of the gas cell. It can therefore be concluded that fitting of the measured infrared absorption

spectrum is possible. In Figure A.4 besides the measured absorption band-head intensity the simulated absorption band-head intensity of the infrared absorption band at 729 cm^{-1} is shown as function of the precursor gas flow. From comparison of the measured and the simulated absorption band-head intensity it can be seen that the measured band-head intensity is in good agreement with the simulated band-head intensity. From this it can be concluded that Eq. (A.1) is a good model to describe the measured non-linearity of the absorption band-head intensity.

In Figure A.8 the fitted temperature from infrared absorption data as obtained from gas cell measurements as function of the gas cell temperature is shown. During the gas cell measurements the acetylene pressure in the gas cell was approximately 0.85 mbar. In Figure A.8 it can be seen that the fitted temperature is within 100 K of the gas cell temperature, which is sufficiently accurate to determine the rotational temperature of the molecules inside a plasma. The deviation of the fitted temperature and the gas cell temperature is mainly caused by the inhomogeneity of the temperature in the gas cell. This is because the ends of the gas cell are close to the reactor wall, which has a temperature close to room temperature. It can therefore be concluded that it is possible to derive the particle temperature from an infrared absorption spectrum. It however has to be noted that in the infrared spectrum simulation and fitting program the density and temperature have been assumed to be constant along the line-of-sight of the infrared beam, which is most likely to be not the case.

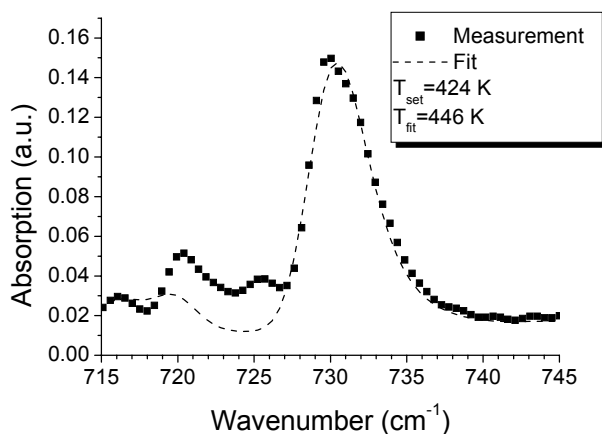


Figure A.7: Measured and simulated absorption spectrum for C_2H_2 at a pressure of 0.875 mbar.

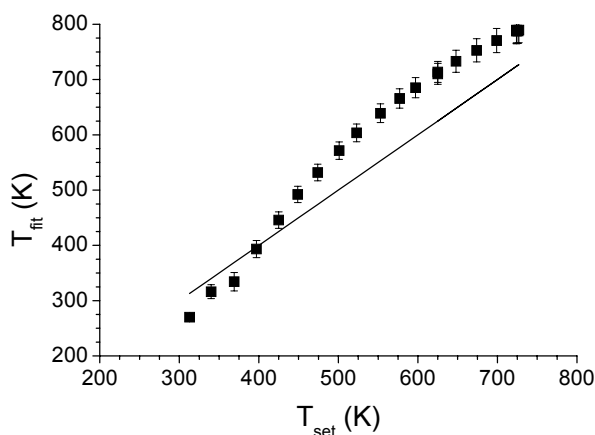


Figure A.8: Fitted temperature for C_2H_2 as function of the gas cell temperature set point.

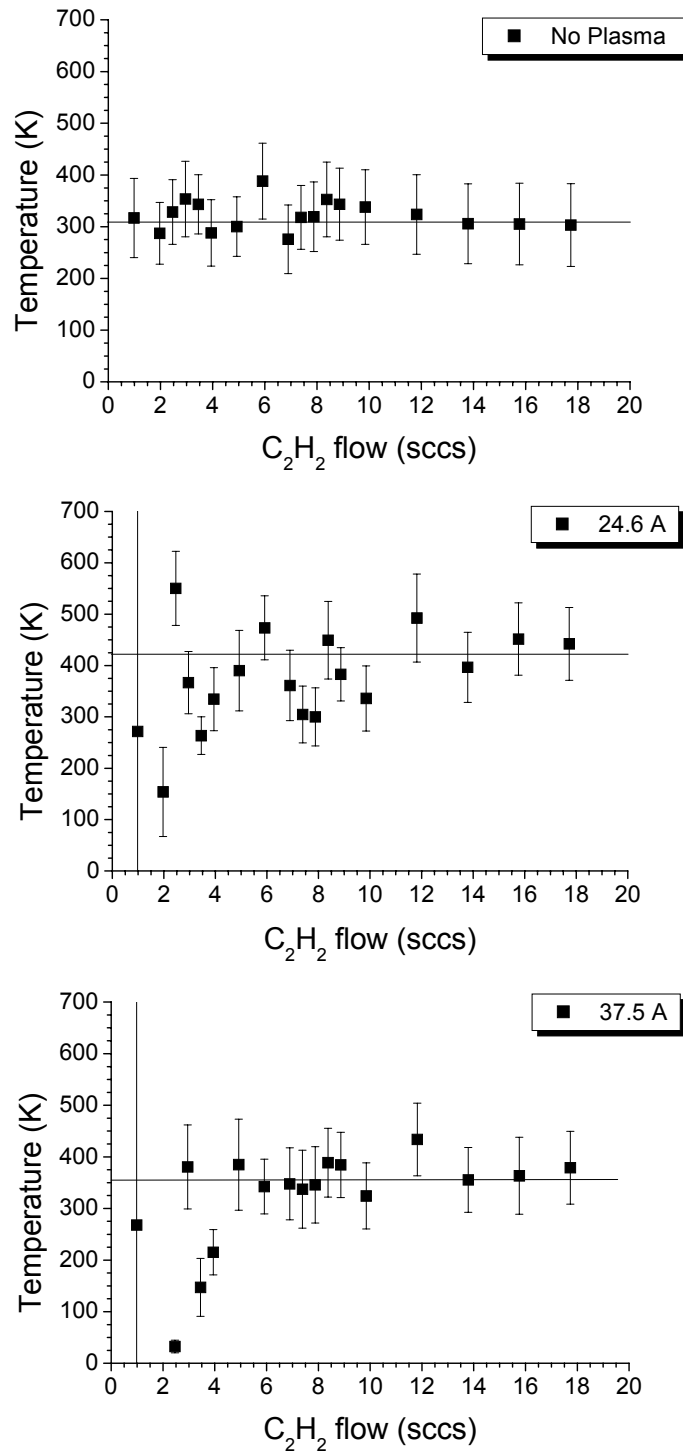


Figure A.9: Fitted rotational temperature of the C_2H_2 gas as function of the C_2H_2 precursor gas flow for the plasma off (top) and the plasma on situation with an arc current of 24.6 A (middle) and 37.5 A (bottom).

In Figure A.9 the fitted temperature of an Ar/ C_2H_2 plasma as function of the precursor gas flow is shown for the plasma off and the plasma on situation (for two different arc currents). From this figure two conclusions can be made. First it can be seen that the plasma

temperature is independent of the C_2H_2 precursor gas flow. For the plasma on situation the fitted temperature at flows below 6 sccs has a large deviation from the constant temperature. This is because for these flows, the precursor consumption is very high (>80%) and therefore the absorption signal is too low to determine the temperature accurately. Second it can be seen that the fitted C_2H_2 particle temperature in the plasma on situation is close to the C_2H_2 particle temperature in the plasma off situation. Both phenomena can be explained by the fact that the C_2H_2 which is not consumed is dominantly situated in the background and not in the expanding plasma. In the expanding plasma beam the temperature will be higher (2 to 3 times) than outside the plasma beam, but also the particle density in the plasma beam will be lower (2 to 3 times) than outside the plasma beam. So the measured absorption will be mainly due to the particles in the background. The precursor particles that get into the background did not interact with the ions in the plasma, because then the particles would be dissociated [12], so their temperature will not change. The temperature therefore will be close to room temperature, and independent of the precursor gas flow. The temperature of the gas could be a little above room temperature, due to interaction with the reactor wall, which is above room temperature. As mentioned before the plasma inhomogeneity is also causing the difference between the equivalent flows measured by means of mass spectrometry and FTIRAS. From the knowledge that the gas in the background has a temperature close to room temperature it can be concluded that no spontaneous dissociation processes can take place in the background of the plasma.

A.7 Conclusions

Mass spectrometry and infrared absorption spectroscopy are two compatible tools. Infrared absorption spectroscopy has the advantage above mass spectrometry that the measured data contains more information (temperature) and that, in most of the cases, it is not necessary to deconvolute the measured absorption spectra. Mass spectrometry however has, due to the used configuration, the advantage that it is very easy to obtain quantitative information, because temperature does not affect the measured values. Infrared absorption spectra easily provide the information on which stable particles are present in the reactor, whereas mass spectrometry easily provides the information on how much of these species are present in the reactor. Mass spectrometry, due to the configuration used, measures the composition of the gas in the plasma reactor, whereas infrared absorption spectroscopy measures the composition of the gas along a line-of-sight of the infrared absorption setup. This makes mass spectrometry more useful to measure the gas composition of an inhomogeneous gas. Quantitative comparison of both techniques will be most efficient when the plasma is a homogenous plasma. For an inhomogenous plasma still a qualitative comparison of both techniques can be made accurately.

From infrared absorption spectra it is possible to obtain the rotational particle temperature, with an accuracy of 100 K, along the line-of-sight of the infrared absorption beam due to the dependency of $\Delta\nu_l$ and N_q on temperature. When the temperature of the plasma is not homogeneous the measured temperature will be close to the temperature of the particles from which the absolute number of particles in the absorbing infrared beam is the highest. In an homogeneous plasma the accuracy of the temperature determination will be better.

Acknowledgements

The skillful technical assistance of M.J.F. van de Sande, A.B.M. Hüsken and H.M.M. de Jong is greatly appreciated. The financial support from the foundation of Fundamental Research on Matter (Projects FOM-RG and 95BR1406) and from the EC (INCO-Copernicus project IC15-CT96-0730) is thankfully acknowledged.

Appendix B

Transmission is described by the following differential equation

$$\frac{dI}{dx} = -h\tilde{\nu}_{qp} B_{qp} N_q P(\tilde{\nu} - \tilde{\nu}_{qp}) \frac{I}{c} \Rightarrow \frac{1}{I} dI = \frac{-h\tilde{\nu}_{qp}}{c} B_{qp} N_q P(\tilde{\nu} - \tilde{\nu}_{qp}) dx$$

Here $\frac{dI}{dx}$ is the change in intensity of the light (I) in a displacement dx through the absorbing medium, h is the Planck constant, $\tilde{\nu}_{qp}$ is the frequency of the absorbed light, N_q the density of the particles in the $J=q$ state, $P(\tilde{\nu} - \tilde{\nu}_{qp})$ is the absorption line profile, c the speed of light, and B_{qp} the absorption coefficient for absorption from state $J=q$ to $J=p$.

If the absorbing medium is considered homogeneous (N constant) of length L and the apparatus line profile is neglected, the solution of this differential equation is given by:

$$\ln \frac{I}{I_0} = \frac{-h\tilde{\nu}_{qp}}{c} B_{qp} N_q P(\tilde{\nu} - \tilde{\nu}_{qp}) L = -\alpha P(\tilde{\nu} - \tilde{\nu}_{qp})$$

and thus the transmission Tr becomes

$$Tr = \frac{I}{I_0} = \exp[-\alpha P(\tilde{\nu} - \tilde{\nu}_{qp})] = 1 + \sum_{n=1}^{\infty} \frac{(-\alpha)^n}{n!} P^n(\tilde{\nu} - \tilde{\nu}_{qp})$$

This is the transmission when only one absorption line is present. For multiple absorption lines the transmission is given by:

$$Tr = 1 + \sum_J \sum_{n=1}^{\infty} \frac{(-\alpha)^n}{n!} P^n(\tilde{\nu} - \tilde{\nu}_{qp})$$

where \sum_J indicates a sum over all absorption lines with their own absorption frequency.

When the absorption is being measured, the measured absorption line will be a convolution of the absorption line profile $P(\tilde{\nu} - \tilde{\nu}_{qp})$ and the apparatus profile $W(\tilde{\nu} - \tilde{\nu})$. In the case of the Fourier transform infrared spectroscope the apparatus profile width ($\Delta\nu_a$) is much broader than the absorption line width ($\Delta\nu_l$). Due to this it becomes impossible to resolve individual absorption lines which are close together (within the apparatus profile width). According to

Chapter 2

the theory of convolution, the convolution of multiple absorption lines is equal to the sum of the convolutions of the individual absorption lines. The absorption, which is given by $A = -^{10} \log(Tr)$ thus becomes:

$$\begin{aligned}
 A &= -\log \left[\frac{\int_0^{\infty} I W(\tilde{\nu} - \tilde{\nu}') d\tilde{\nu}}{\int_0^{\infty} I_0 W(\tilde{\nu} - \tilde{\nu}') d\tilde{\nu}} \right] \\
 &= -\log \left[\frac{\int_0^{\infty} I_0 \left(1 + \sum_J \sum_{n=1}^{\infty} \frac{(-\alpha)^n}{n!} P^n(\tilde{\nu} - \tilde{\nu}_{qp}) \right) \cdot W(\tilde{\nu} - \tilde{\nu}') d\tilde{\nu}}{\int_0^{\infty} I_0 W(\tilde{\nu} - \tilde{\nu}') d\tilde{\nu}} \right] \\
 &= -\log \left[\frac{\int_0^{\infty} \left(1 + \sum_J \sum_{n=1}^{\infty} \frac{(-\alpha)^n}{n!} P^n(\tilde{\nu} - \tilde{\nu}_{qp}) \right) \cdot W(\tilde{\nu} - \tilde{\nu}') d\tilde{\nu}}{\int_0^{\infty} W(\tilde{\nu} - \tilde{\nu}') d\tilde{\nu}} \right] \\
 &= -\log \left[1 + \int_0^{\infty} \sum_J \sum_{n=1}^{\infty} \frac{(-\alpha)^n}{n!} P^n(\tilde{\nu} - \tilde{\nu}_{qp}) \cdot W(\tilde{\nu} - \tilde{\nu}') d\tilde{\nu} \right] \\
 &= -\log \left[1 + \sum_J \sum_{n=1}^{\infty} \int_0^{\infty} \frac{(-\alpha)^n}{n!} P^n(\tilde{\nu} - \tilde{\nu}_{qp}) W(\tilde{\nu} - \tilde{\nu}') d\tilde{\nu} \right]
 \end{aligned}$$

Now consider $P(\tilde{\nu} - \tilde{\nu}_{qp})$ and $W(\tilde{\nu} - \tilde{\nu}')$ Gaussian. Then the absorption A is given by:

$$A = -\log \left[1 + \sum_J \sum_{n=1}^{\infty} \int_0^{\infty} \frac{(-\alpha)^n}{n!} \left(\frac{1}{\sqrt{\pi} \Delta \nu_{\ell}} \right)^n \left(\exp \left[\frac{-(\tilde{\nu} - \tilde{\nu}_{qp})^2}{\Delta \nu_{\ell}^2} \right] \right)^n \frac{1}{\sqrt{\pi} \Delta \nu_a} \exp \left[\frac{-(\tilde{\nu} - \tilde{\nu}')^2}{\Delta \nu_a^2} \right] d\tilde{\nu} \right]$$

Which can be simplified to* :

*

$$\begin{aligned}
 \int_0^y \exp[-(ax^2 + bx + c)] dx &= \frac{1}{2} \sqrt{\frac{\pi}{a}} \exp \left[\frac{b^2 - 4ac}{4a} \right] \operatorname{erf} \left(y\sqrt{a} + \frac{b}{2\sqrt{a}} \right) \\
 \Rightarrow \int_0^{\infty} \exp \left[\frac{-(x-\alpha)^2}{\beta^2} - \frac{(x-\gamma)^2}{\delta^2} \right] dx &= \frac{1}{2} \sqrt{\pi} \frac{\beta\delta}{\sqrt{\beta^2 + \delta^2}} \exp \left[\frac{-(\alpha-\gamma)^2}{\beta^2 + \delta^2} \right]
 \end{aligned}$$

$$\begin{aligned}
 A &= -\log \left[1 + \sum_J \sum_{n=1}^{\infty} \frac{(-\alpha)^n}{n!} \frac{1}{\pi^{\frac{n+1}{2}}} \frac{1}{\Delta v_\ell^n} \frac{1}{\Delta v_a} \frac{\sqrt{\pi} \frac{\Delta v_\ell}{\sqrt{n}} \Delta v_a}{\sqrt{\left(\frac{\Delta v_\ell}{\sqrt{n}}\right)^2 + \Delta v_a^2}} \exp \left[-\frac{(\tilde{v}' - \tilde{v}_{qp})^2}{\left(\frac{\Delta v_\ell}{\sqrt{n}}\right)^2 + \Delta v_a^2} \right] \right] \\
 &= -\log \left[1 + \sum_J \sum_{n=1}^{\infty} \frac{(-\alpha)^n}{n!} \frac{1}{\pi^{\frac{n}{2}}} \frac{1}{\Delta v_\ell^n} \frac{1}{\sqrt{1+nq^2}} \exp \left[-\frac{(\tilde{v} - \tilde{v}_{qp})^2}{\left(\frac{\Delta v_\ell}{\sqrt{n}}\right)^2 + \Delta v_a^2} \right] \right] \quad \text{with } q = \frac{\Delta v_a}{\Delta v_\ell} \gg 1 \\
 &= -\log \left[1 + \sum_J \frac{\Delta v_\ell}{\Delta v_a} \exp \left[-\frac{(\tilde{v}' - \tilde{v}_{qp})^2}{\Delta v_a^2} \right] \cdot \sum_{n=1}^{\infty} \frac{1}{n! \sqrt{n}} \left(-\frac{\alpha}{\Delta v_\ell \sqrt{\pi}} \right)^n \right]
 \end{aligned}$$

References Appendix A

- [1] J.W.A.M. Gielen, M.C.M. van de Sanden, P.R.M. Kleuskens, and D.C. Schram, *Plasma Sources Sci. Technol.* **5** (1996) 492
- [2] M.W. Weiler, S. Sattel, T. Giessen, K. Jung, H. Ehrhardt, V.S. Veerasamy, and J. Robertson, *Phys. Rev.* **B 53** (1994) 1594
- [3] J. Robertson, *Pure Appl. Chem.* **66** (1994) 1789
- [4] A. de Graaf, M.F.A.M. van Hest, M.C.M. van de Sanden, K.G.Y. Letourneur, and D.C. Schram, *Appl. Phys. Lett.* **74** (1999) 2927
- [5] D.J. Dagel, C.M. Mallouris, and J.R. Doyle, *J. Appl. Phys.* **79**, 8735 (1996)
- [6] O. Auciello and D.L. Flamm, *Plasma diagnostics*, volume 1, Academic press Inc., San diego (1989)
- [7] L. Sansonnens, A.A. Howling, and Ch. Hollenstein, *Plasma Sources Sci. Technol.* **7** (1998) 114
- [8] T.A. Cleland and D.W. Hess, *J. App. Phys.* **64** (1988) 1068
- [9] M.Haverlag, E. Stoffels, W.W. Stoffels, G.M.W. Kroesen, and F.J. de Hoog, *J. Vac. Sci. Technol.* **A 12** (1994) 3102
- [10] Ch. Hollenstein, A.A. Howling, C. Courteille, D. Magni, S.M. Scholtz, G.M.W. Kroesen, N. Simons, W. de Zeeuw, and W. Schwarzenbach, *J. Phys. D* **31** (1998) 74
- [11] A. de Graaf, M.F.A.M. van Hest, M.C.M. van de Sanden, K.G.Y. Letourneur and D.C. Schram, *Proceedings of the 14th International Symposium on Plasma Chemistry (ISPC-14)*, Vol. I (1999) 1755
- [12] J.W.A.M. Gielen, W.M.M. Kessels, M.C.M. van de Sanden, and D.C. Schram, *J. Appl. Phys.* **82** (1997) 2643
- [13] J.W.A.M. Gielen, P.R.M. Kleuskens, M.C.M. van de Sanden, L.J. van IJendoorn, D.C. Schram, E.H.A. Dekempeneer, and J. Meneve, *J. Appl. Phys.* **80** (1996) 5986
- [14] J.W.A.M. Gielen, M.C.M. van de Sanden, and D.C. Schram, *Appl. Phys. Lett.* **69** (1996) 152
- [15] H. Mäcker, *Z. Naturforsch.* **11** (1956) 457

- [16] G.M.W. Kroesen, D.C. Schram, and J.M. de Haas, *Plasma Chem. Plasma Proc.* **10** (1990) 531
- [17] M.C.M. van de Sanden, R.J. Severens, W.M.M. Kessels, R.F.G. Meulenbroeks, and D.C. Schram, *J. Appl. Phys.* **84** (1998) 2426
- [18] M. Haverlag, F.J. de Hoog, and G.M.W. Kroesen, *J. Vac. Sci. Technol.* **A 9** (1991) 327
- [19] Hitran 1996 molecular database on CD-ROM, Related to *The Atlas of Absorption lines from 0 to 17.900 cm⁻¹*, Nasa Reference Publication 1188 (1987)
- [20] L.S. Rothman, R.R. Gamache, A. Goldman, L.R. Brown, R.A. Toth, H.M. Pickett, R.L. Poynter, J.M. Flaud, C. Camy-Peyret, A. Barbe, N. Husson, C.P. Rinsland, and M.A.H. Smit, *Appl. Optics* **26** (1987) 4058
- [21] Y.Kabbadj, M. Herman, G. Di Lonardo, L. Fusina, and J.W.C. Johns, *J. Mol. Spec.* **150** (1991) 535

Chapter 3

Design of a fast *in situ* infrared diagnostic tool

M.F.A.M. van Hest, A. Klaver, D.C. Schram, and M.C.M. van de Sanden

Abstract

Conventional Fourier transform infrared (FTIR) spectrometers cannot be used to perform real time *in situ* infrared reflection absorption spectroscopy at monolayer sensitivity for high deposition rates (couple of tens to hundreds of nm/s) which can be obtained when using an expanding thermal deposition plasma. Therefore a new analysis tool has been developed. The tool is based on a fast optical scanner in combination with conventional grating technology. This results in a loss of spectral range with respect to FTIR spectrometers, but a significant gain is obtained in time resolution. For the used combination this makes it possible to measure at a time resolution as low as 1.3 ms and a resolution of 24 cm^{-1} at 1000 cm^{-1} . The absorption sensitivity for single reflection at the best time resolution is approximately 10^{-2} , but can be improved by using signal enhancement techniques. Here attenuated total reflection (ATR) has been used and the best sensitivity obtained is approximately 10^{-3} . Which is close to monolayer sensitivity for various absorption bands in the infrared spectrum of silicon oxide films. Monolayer sensitivity can be obtained by averaging multiple spectra, however this will cause the time resolution to decrease.

3.1 Introduction

A commonly used method for the analysis of thin film materials is Fourier transform infrared (FTIR) reflection absorption spectroscopy [e.g. 1,2,3]. This technique can be used *in situ* and in order to obtain monolayer sensitivity the absorption signal needs to be enhanced. Enhancement of the absorption signal can be obtained by implementing an Attenuated Total Reflection (ATR) crystal [e.g. 4,5]. Due to this crystal the reflected infrared light will have multiple interactions with the deposited thin film, instead of just one in single reflection mode. The absorption signal enhancement can be up to a factor of 100 and is dependent on the dimensions of the ATR crystal and the angle of reflection within the crystal. With this technique it is possible to measure absorptions of very thin films, down to less than one monolayer, dependent on the type and strength of the absorption. The absorption signal can also be enhanced by means of using a metal substrate or an optical cavity substrate [6,7,8]. However, optical cavity substrates only enhance the absorption in a limited wavelength interval, which is dependent on the chosen substrate. For every wavelength interval another substrate is needed and therefore these kind of substrates are less easy to use than an ATR crystal. With the use of metal substrates the enhancement of the signal is smaller than with optical cavity substrates or ATR crystals, which makes these kind of substrates less suitable for obtaining enhancements large enough for obtaining monolayer sensitivity.

Due to the common low deposition rates of various thin film materials (up to 1 nm/s) *in situ* FTIR reflection absorption spectroscopy, had enough time resolution. With fast sampling (rapid scan) the interval 500 cm^{-1} - 7500 cm^{-1} can be measured with reasonable signal to noise ratio in about 0.1 s. With the improvement of the deposition methods and resulting higher deposition rates conventional FTIR reflection absorption spectroscopy as a real time *in situ* diagnostic is pushed to its limits. Especially at deposition rates obtained with the use of an expanding thermal plasma (ETP) deposition method, as used e.g. at the Eindhoven university of technology [9,10,11,12,13], this conventional FTIR reflection absorption spectroscopy analysis method can not be used as an *in situ* tool anymore if one wants to study the film growth *in situ* with monolayer sensitivity. A simple calculation shows that the deposition of one single monolayer takes less than 10 ms at a deposition rate of 30 nm/s and less than 1 ms at a deposition rate of 300 nm/s. These are rates that can be obtained with the ETP deposition method.

To improve the time resolution during infrared reflection absorption experiments it has been necessary to develop a new and faster *in situ* diagnostic tool. The minimum specifications of this new setup together with the specifications of the conventional FTIR setup are given in Table 3.1. In this table it can be seen that only two parameters have to be improved and in the others there is some degree of freedom which can be offered. The new setup is a compromise between offering some of the strong properties of FTIR spectroscopy and gaining time resolution. The heart of the new setup has been found in a grating which is mounted on a high speed optical scanner. In this way a high speed monochromator has been constructed. The largest negative effect of introducing the grating will be on the spectral range of the fast infrared reflection absorption setup with respect to the conventional FTIR reflection absorption spectroscopy as will be explained in this chapter.

In the remainder of this chapter the new setup will be described extensively. A detailed description of the individual components of the setup will be given, as well as a motivation why these specific components have been chosen. Based on the specifications of the different components an estimation of the expected signal to noise ratio will be given.

This is followed by experimental results to demonstrate that the new method is operational and is conform its design specifications. The use of the fast infrared reflection absorption spectroscopy will be illustrated by means of fast deposition of silicon oxide like films from hexamethyldisiloxane (HMDSO) and oxygen on silicon substrates and ZnSe ATR crystals.

Table 3.1: Overview of minimum specifications and FTIR equivalents.

Parameter	Minimum	FTIR (typical)
Spectral range	Dependent on absorption*	$500\text{ cm}^{-1} - 7500\text{ cm}^{-1}$
Time resolution	1.0 – 2.0 ms	0.1-1.0 s
Resolution	25 cm^{-1}	$8\text{ cm}^{-1} - 16\text{ cm}^{-1}$
Sensitivity	$2 \cdot 10^{-4}$ (monolayer, Si-O-Si)	10^{-2} with averaging

3.2 The fast infrared spectroscopy

A schematic overview of the optics of the fast infrared reflection spectroscopy is shown in Figure 3.1. The light emitted by a cascaded arc light source (1) is converted into a parallel beam (2) and is guided through a reflection absorption spectroscopy setup (3-9) after which the exiting parallel beam is reflected on the surface of a grating (10) and focused (11) onto an infrared detector (13). Just before the detector the light beam passes through a filter (12), which suppresses second and higher order diffractions of the grating.

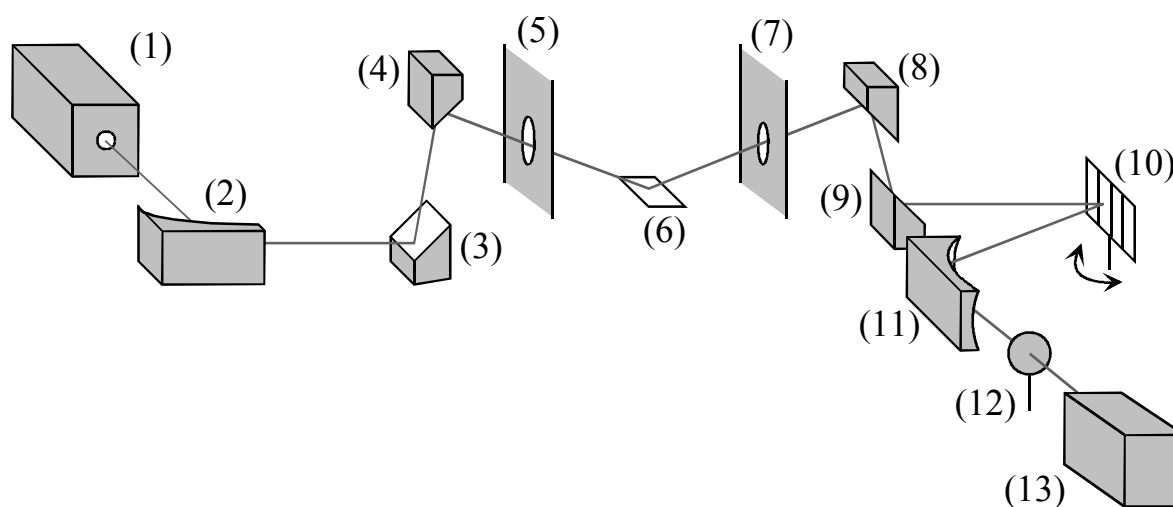


Figure 3.1: Schematic overview of the fast infrared reflection absorption setup: (1) light source, (2) 90° off axis parabolic mirror ($f=19\text{ cm}$), (3) flat gold coated mirror, (4), 90° off axis parabolic mirror ($f=36\text{ cm}$), (5) KBr window in vessel wall, (6) substrate, (7) KBr window in vessel wall, (8) 90° off axis parabolic mirror ($f=36\text{ cm}$), (9) flat gold coated mirror, (10) grating on optical scanner, (11) 90° off axis parabolic mirror ($f=7.5\text{ cm}$), (12) filter, and (13) detector.

* For the setup used in this publication the spectral range $700\text{ cm}^{-1} - 1400\text{ cm}^{-1}$ is used

Light source

A cascaded arc is used as a light source (1), because it has a higher infrared light intensity than the more commonly used globars in FTIR spectrometers [14,15,16]. A detailed description of the light source has been given by Wilbers *et. al.* [15,16] and Raghavan *et. al.* [14]. The used light source has been operated with argon at a pressure of 1.8 bar and an argon flow of 10 sccm. The operating current was set to 25 A and the light exiting window of the arc is made of KBr and has a thickness of 4 mm. Measurements on the light beam emitted by the arc show that the divergence of the beam exiting the arc is 75 mrad and the radiating surface is $3 \cdot 10^{-4} \text{ m}^2$. The light output of the light source, in the spectral range used in the rest of this publication, can be mainly influenced by the arc operating current and the gas pressure[†]. Increasing the arc current has a strong influence on the light intensity, an increase of 10 % in the current results in an increase of 10 % in the emitted light intensity. A 10 % increase of the gas pressure however results in only a 5 % increase of the emitted light intensity. Limitations imposed by the window thickness (pressure) and the power supply (current) resulted in the used operating conditions.

Grating on optical scanner

In conventional FTIR spectroscopy a broadband spectrum (typical spectral range 500 cm^{-1} to 7500 cm^{-1}) is measured by a scanning mirror interferometer, which is the heart of a FTIR spectrometer. Due to the movement of one of the two mirrors in the interferometer the Fourier transform of the light spectrum is generated. By measuring the light intensity as function of the mirror position and by Fourier transforming the so obtained interferogram a broadband light intensity spectrum is obtained. Notice that the resolution of this kind of spectrometers is dependent on the displacement of the scanning mirror [5,17]. A larger displacement results in a higher resolution. The interferometer speed is the main reason the time resolution is not high. In short it is fair to say that in a FTIR spectrometer the interferometer works as the medium to identify the separate wavelengths.

In the fast infrared reflection absorption spectroscopy setup a dispersive medium is used to separate the light into its individual components. As a result of this only a limited wavelength interval will be detected by the detector at any time, whereas in FTIR spectroscopy all the light is detected by the detector at the same time [5,17]. This results in a lower absolute detector signal intensity in the new situation compared to FTIR spectroscopy, due to which noise induced by a background signal will become relatively more important in the new situation.

As a dispersive medium a grating is used. For calculating the dispersion the grating equation is used [18,19]:

$$a(\sin \theta_i + \sin \theta_m) = m\lambda, \quad (3.1)$$

where a is the groove spacing, m the order of diffraction, λ the wavelength, θ_i and θ_m the angle of incidence and the angle of diffraction respectively. By rotating the grating and keeping the detector at a fixed position, both the incident and diffraction angle are changed simultaneously, which is identical to the procedure used in most monochromators [19,20,21].

[†] It is known that changing the gas from argon to xenon has a positive influence on the light intensity [15].

As stated before the use of the fast infrared absorption reflection spectroscopy will be shown by means of fast deposition of silicon oxide like films. Therefore the grating has been chosen such that it is possible to measure in the wavelength interval from 700 cm^{-1} to 1400 cm^{-1} . In this interval both the absorption of Si-O and Si-CH_x bonds are present which have an absorption width of several tens of wavenumbers. Using the grating equation (Eq. (3.1)) with normal incidence (0.0 rad) and a refraction angle of approximately 0.5 rad at 1050 cm^{-1} (center of interval), it can be calculated that it is best to use a grating of 53 grooves/mm. This exact grating is not commercially available and therefore a blazed grating of 50 grooves/mm has been used. Changing the setup for other wavelengths can be done by changing the grating, filter, and/or detector.

The grating is positioned on top of an optical scanner (Cambridge Technology Inc. model 6650) which is capable of oscillating the used grating at a frequency of up to 300 Hz (sinusoidal) with an angle large enough to pass the desired wavelength interval along the detector. This wavelength interval is smaller than the interval that can be measured with the FTIR spectroscopy, because of the limited rotational angle of the optical scanner at such high oscillation frequencies. Therefore it will not be possible to monitor film absorptions at positions in the absorption spectrum which are not within the range scanned by the grating at the same time. Notice that the maximum rotational angle is dependent on the mass of the grating and the frequency. Increasing the oscillating frequency or the grating mass results in a decrease of the maximum rotational angle.

Due to the fact that the grating is oscillating on top of the optical scanner it is possible to measure the spectrum in both the forward and backward motion of the oscillation. Therefore the acquisition speed of the spectra will be twice the oscillation frequency. So at an oscillating frequency of 300 Hz the spectra are obtained at 600 Hz, and the measuring timescale is equal to 1.3 ms, which is equal to the timescale needed for monitoring monolayer film growth at a growth rate of approximately 230 nm/s. For monitoring even higher film growth rates another optical scanner will be needed. The reproducibility of the angle of the optical scanner is within 6 μrad . This is accurate enough to be negligible with respect to the measuring interval of the detector signal and the scanner position signal. Note that in the grating equation the change in the incident and diffracted angle is the same as the rotational angle of the scanner. Furthermore the maximum rotational angle of the scanner is twice the oscillation amplitude.

Mirrors

In total the setup consists of six mirrors. For the mirrors that focus (4 and 11) and defocus (2 and 8) the light beam 90° off axis parabolic mirrors have been used. This has been done to reduce the aberrations which are obtained by using spherical mirrors. The disadvantage of using 90° off axis parabolic mirrors is that they are less easy to align than spherical mirrors due to their strict 90° positioning [22].

In order not to lose too much intensity due to reflection on the mirrors, four of the six mirrors have been coated with a thin gold coating. The other two (4 and 5) are not coated. This is because these two 90° off axis parabolic mirrors had to be custom made because they have a focal length (36 cm) which is not commercially available.

Windows

The infrared reflection absorption spectroscopy is used to monitor *in situ* the film deposition and therefore two windows have to be mounted in the deposition reactor wall. As window material KBr has been chosen, just as for the light source, because it has a good transparency in the wavelength range of interest. A disadvantage of using KBr windows is that they are hygroscopic, and therefore less useful when someone wants to measure a water absorption signal.

Filter

The main part of the fast reflection absorption spectroscopy is a grating. A disadvantage of using a grating is that instead of only getting a first order diffraction also second and higher order diffractions appear. These higher orders interfere with the first order and therefore have to be filtered. The interfering wavelength (λ_{int}) can be given by:

$$\lambda_{\text{int}} = \frac{\lambda_1}{m} \quad m \geq 2, \quad (3.2)$$

where λ_1 is the first order wavelength and m the order of the interfering light. The light which is interfering with the first order light is always smaller in wavelength. Therefore for removing the higher orders a filter is needed, that transmits the desired wavelength and absorbs the lower wavelengths. The cut off needs to be somewhere between the lowest wavelength desired and half of the highest wavelength desired. The transmission profile of the used filter is given in Figure 3.2. As can be seen the used filter does transmit the light in the desired range (700 cm^{-1} to 1400 cm^{-1}) up to 70 % of its original intensity. The cut off at 1400 cm^{-1} is in agreement with the desired wavelength band. Notice that the filter has to be changed when the grating is changed for measurements in another wavelength interval.

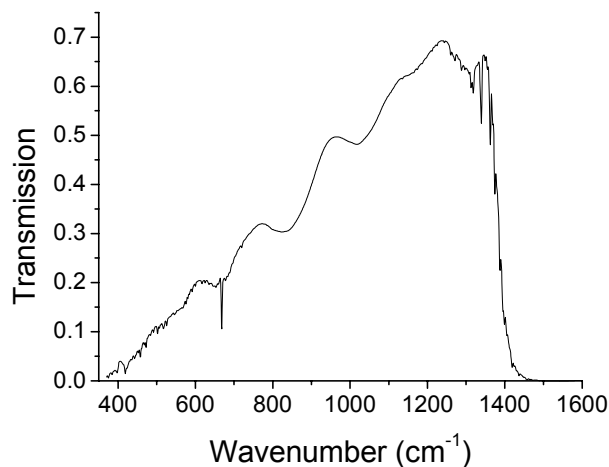


Figure 3.2: Cut off filter transmission profile.

Detector

To detect the infrared light a MCT detector (type D316) has been used. Due to its high sensitivity for infrared light the MCT detectors have a fairly high dark current induced by background radiation [e.g. 23]. For this reason in general MCT detectors are equipped with a double amplifier, i.e. a DC amplifier followed by an AC amplifier, with fixed amplification factors. However, for the new infrared reflection absorption spectroscope it is better to only DC amplify the detector signal. This in order to have a direct correlation between the detector signal and the infrared light intensity on the detector. By installing a variable resistors to the amplifier it has been made possible to subtract the dark current signal from the detector signal and by installing a second variable resistor also the amplification factor of the amplifier has been changed to maximize the detector output voltage. The detector response time, including amplifier, is equal to 5 μ s.

Data acquisition and control

The signal of the detector as well as the signal that indicates the position of the optical scanner is measured by means of a 16-bit 200 kSamples/s ADC card (National Instruments 6035E) inside a PC. The measurements are controlled by means of the same computer by dedicated software which has been programmed in National Instruments CVI labwindows. In the software code a part has been integrated which can be used to analyse the measured data.

The number of data points measured to record one single spectra (N) is given by:

$$N = \frac{1}{2f_{osc}} \frac{f_{sample}}{N_{channels}}, \quad (3.3)$$

where f_{osc} is the optical scanner oscillation frequency, f_{sample} is the ADC sampling rate. $N_{channels}$ is equal to the number of channels used for measuring, which is fixed to two, one for the detector and one for the optical scanner position. In the case the setup is used at 300 Hz and the ADC sampling frequency is set to its maximum value the number of data points for one single spectrum will be equal to 167. Roughly it can be said that approximately every 4 cm^{-1} a data point is obtained, which is enough to have several data points within one single solid state absorption band (typical width 10 cm^{-1} to 50 cm^{-1}). When the setup is operated at a lower oscillating frequency the number of data points per spectra will increase and the spectral measuring interval will decrease. At the maximum ADC sampling frequency the detector signal is measured every 10 μ s which is twice the response time of the detector.

The detector position signal is also measured every 10 μ s. The total rotational angle of the scanner is 0.1 rad and therefore the position is measured every 0.6 mrad when the scanner is assumed to scan with a constant velocity. This 0.6 mrad is much larger than the 6 μ rad positioning accuracy of the optical scanner, and therefore the error due to positioning of the scanner can be neglected.

3.3 Theory

3.3.1 Spectral resolution

When the detector area would be infinitesimal small, the light source would be a point source and the optics would be aligned perfectly, the wavelength interval detected at any time would be unique for every measuring time. However, due to the dimensions of the detecting area of the detector a small wavelength interval will be detected. The grating is responsible for the dispersion of the light and therefore the grating determines the wavelength interval on the detector. In Figure 3.3 a schematic representation of the grating, focusing mirror, and detector part is given ($L_1=20$ cm). In this figure the final focusing mirror (cf. Figure 3.1) is represented as a lens. From this plot it can be seen that indeed a small wavelength interval is focused onto the active detector area. Although the focusing mirror is represented as a lens, this has no consequences for the shown effect. Using the grating equation (Eq. (3.1)) and the lens theory[‡], it follows that the wavelength interval on the detector, and thus the resolution, is about 24 cm^{-1} at 1000 cm^{-1} . This width is less than the absorption peak separation of the various absorption peaks of the silicon oxide like film absorption spectrum in the range from 700 cm^{-1} to 1400 cm^{-1} . Therefore the individual absorption bands in the silicon oxide like film absorption spectrum can be identified in the reflection absorption spectrum. Also the calculated resolution is better than the minimum value given in Table 3.1.

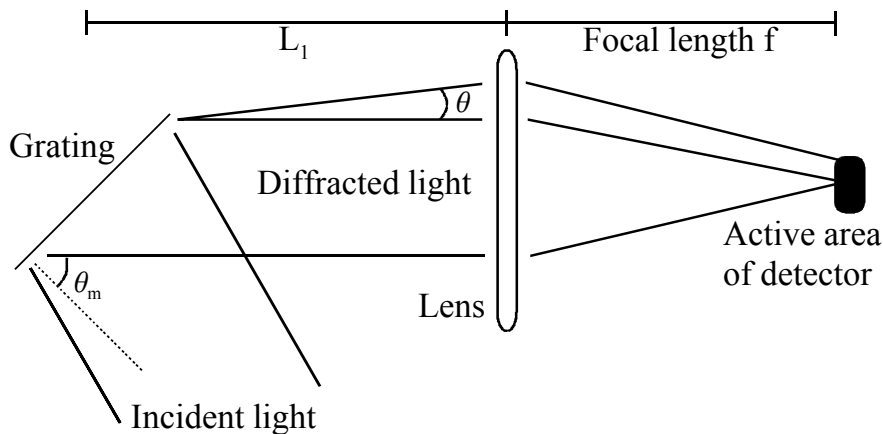


Figure 3.3: Schematic presentation of light path from grating to detector.

3.3.2 Signal intensity

To be able to estimate the number of photons which will be collected by the detector, and the resulting detector signal, the number of photons emitted by the light source as well as the geometrical and optical losses need to be known. In this section this estimation will be made, in a worst case approach, from light source to detector.

[‡] The angle of θ is determined by the focal length (f) and the size of the detector area (a). $\theta = \tan^{-1} (0.5 * a/f)$

3.3.2.1 Source intensity

Raghavan et. al. [14] showed that the cascaded arc light source in the infrared can be modeled as a blackbody radiator with a temperature (T) of 12000 K and an emissivity of 20%. The number of photons emitted per second per solid angle of the blackbody radiator as function of the wavelength ($N(\lambda)$ [$\text{s}^{-1}\text{sr}^{-1}$]) is given by Planck's blackbody radiation equation:

$$N(\lambda) = \frac{c}{\lambda^4} \frac{1}{\exp(hc / \lambda kT) - 1}, \quad (3.4)$$

with c the speed of light, h the Planck constant, and k the Boltzmann factor. It has been shown that always a small wavelength interval (24 cm^{-1}) is on the detector. So by integrating Eq. (3.4) over this wavelength interval the number of photons emitted by the light source can be calculated. Including the opening angle, the emitting surface area and the emissivity efficiency it is found that the light source emits a minimum of $2.0 \cdot 10^{17}$ photons/s in any wavelength interval detected by the detector in the desired spectral range. Not all photons emitted by the light source will reach the detector. Photons will be lost by two reasons. Firstly by means of geometrical losses on the various optical elements and secondly by optical losses during reflection and transmission at and through the various optical elements.

3.3.2.2 Geometrical losses

To calculate the geometrical losses of the setup a ray trace simulation of the setup has been performed. For this calculation the setup has been slightly simplified. First all 90° off axis parabolic mirror have been modeled as ideal infinitesimal thin lenses. This will have no effect on the final result as long as the opening angle is the same. Second all flat mirrors have been left out of the simulation, which is allowed because due to their size no light will fall outside the mirror surface and thus there is no geometrical loss. The total geometrical loss of the setup is dependent on the kind of sample used. In case the setup is used in the single reflection mode, the sample will be large in comparison to the spot size on the sample and therefore there will be no geometrical loss at the sample. In contrast when the setup is used in ATR mode the spot size on the initial bevel surface of the ATR crystal will be larger than this surface and therefore a significant loss will result at this bevel surface. In Figure 3.4 the light spot on the initial bevel surface of the ATR crystal is shown. It can be seen clearly that a large amount of the light is lost at this initial bevel surface. The spot size is approximately 6 mm in diameter and the ATR crystal has a width of 20 mm and a height 0.7 mm. Therefore approximately 80% of the light on the initial surface of the ATR crystal does not enter the crystal and is lost. The spot size of 6 mm at the initial bevel surface of the ATR crystal is due to an inaccurate focal length of the 90° off axis parabolic mirror that focuses the light onto the initial bevel surface. The focal length is 36 cm whereas a focal length of 45 cm would have been better, but as mentioned these 90° off axis parabolic mirrors had to be custom made and 36 cm was the largest focal length that could be manufactured.

From the simulation it can be concluded that when the setup is used in single reflection mode, the total geometrical transmission is equal to 70%. The main geometric losses are on the first KBr window (15%) and on the detector (10%). When using the setup in ATR mode, the geometrical setup transmission drops to a mere 15%.

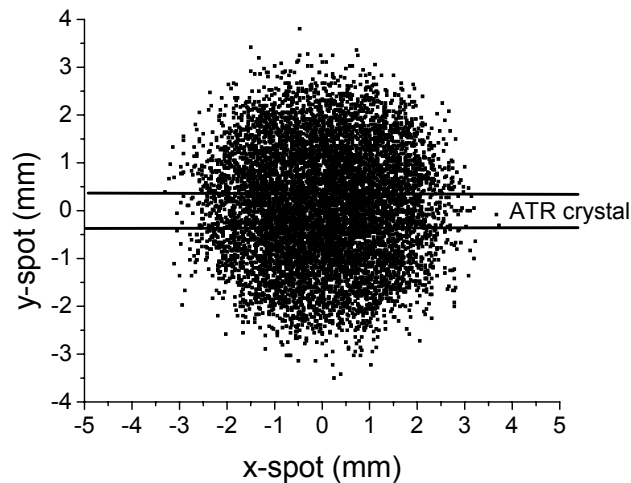


Figure 3.4: Spot on the initial bevel surface of ATR crystal obtained from ray trace simulations.

3.3.2.3 Optical losses

The different elements in the setup will all have a non-perfect transmission or reflection, due to which a part of the light will be lost on interaction of the light with the various elements. This loss can be calculated by means of simple calculation. In Table 3.2 the reflection and transmission coefficients of the various elements in the setup are given. For the grating not only the reflection coefficient is important, but also the efficiency has to be known. The efficiency is equal to the fraction of the total incident light which will be reflected into the first order. This efficiency is at least 30 % [24]

Table 3.2: Reflection and transmission coefficients for the various elements of the setup.

Element	Trans/Refl coefficient
Gold coated mirror	98% reflection
Aluminum mirror	70% reflection
KBr window	80% reflection
Grating	70% reflection
Filter	70% transmission
Substrate	70% reflection
ZnSe ATR crystal	70% transmission

When considering all the elements in the setup, the total optical losses can be calculated. These are found to be equal to 96.8% and practically independent of the setup operation mode. This is because the ZnSe ATR crystal transmission loss is approximately equal to the silicon substrate reflection loss. The main loss is on the grating and on the custom made aluminum 90° off axis parabolic mirrors.

3.3.2.4 Detector

Considering the amount of photons emitted by the light source and the geometrical and optical losses of the setup elements, it is found that about $5 \cdot 10^{15}$ photons per second per detected wavelength interval (24 cm^{-1}) will arrive on the detector surface when the system is used in single reflection mode. In the spectral range for which the setup has initially been designed the used detector has a minimum detection efficiency of 60%, and the energy flux detected by the detector will be at least $7.3 \cdot 10^{-5} \text{ W}$. Dependent on the detector amplifier settings this energy flux will result in a lower limit for the maximum detector signal of 2.2 V. The noise in the detector signal is approximately 20 mV and therefore a theoretical signal to noise ratio of 10^2 can be obtained. With this signal to noise ratio it is possible to measure absorption intensities of 1 % and higher when the system is used in single reflection mode and no spectra are averaged. In the case the setup is used in ATR mode without anything else changed, the measured detector signal will go down by approximately one order of magnitude, but nevertheless the minimum detectable absorption intensity will increase.

Notice that in the calculation of the light intensity a worst case scenario has been used and therefore the maximum signal measured is higher than this calculated value. The intensity calculation has been done in the wavelength interval having the lowest light intensity and the lowest detector sensitivity has been used. However, in the range used the detector has the highest sensitivity in the wavelength interval in which the emitted light intensity by the light source is the lowest. Therefore the maximum signal measured by the detector will be higher than its calculated value and thus the best signal to noise ratio will be higher than its calculated value. A rough estimation shows that this value will be 50 % to 100 % higher.

Aside from the photons emitted by the light source which end up on the detector surface also photons emitted by various elements in the direct vicinity of the detector will emit photons which end up on the detector surface causing the measured signal to increase with an offset. A significant part of this offset can be subtracted from the measured signal electronically, but still the value will be dependent on the angle of the grating because the number of background photons collected by the detector will be different for a different grating position. In section 3.4 it will be shown how to eliminate the total background signal.

In conclusion a summary of the various parameters of the fast infrared reflection absorption spectroscopy setup is given in Table 3.3. As can be seen the time resolution of 1.3 ms is obtained for which still a signal to noise ratio of 10^2 is obtained in single reflection. Nevertheless, to do this spectral range and resolution had to be offered with respect to FTIR reflection absorption spectroscopy.

Table 3.3: Summary of various parameters of the fast infrared reflection absorption spectroscopy setup.

Parameter	Fast grating spectroscope
Spectral range	700 – 1400 cm^{-1}
Time resolution	$\geq 1.3 \text{ ms}$
Resolution	24 cm^{-1}
Sensitivity at best time resolution	$1 \cdot 10^{-2}$ single reflection $1 \cdot 10^{-3}$ ATR crystal

3.4 Reflection absorption spectra

To obtain a reflection absorption spectrum with the fast infrared reflection absorption spectroscope a couple of steps have to be made. First a background spectrum and a reference spectrum have to be obtained as shown in Figure 3.5. The background spectrum is the spectrum as function of the optical scanner angle obtained in the case that the light source is turned off. It can be seen in Figure 3.5 that the detector intensity is not constant as function of the optical scanner position. This is due to the infrared light emitted by various objects in the direct vicinity of the infrared reflection absorption spectroscopy setup.

Absorption is measured relative to a reference. The reference is obtained by measuring the light intensity as function of the optical scanner angle when the light source is turned on. For the reference spectrum shown in Figure 3.5 a bare silicon sample has been used as a reflector. Notice that the reference spectrum has a good resemblance with the filter profile (cf. Figure 3.2), from which it can be concluded that the light source is continuous with nearly constant intensity in the measuring range.

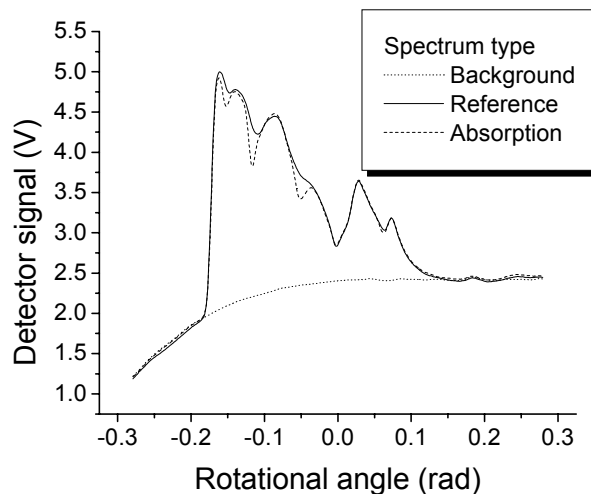


Figure 3.5: Raw signal from the infrared reflection absorption spectroscope.

It can also be seen in Figure 3.5 that the reference spectrum consists of two parts. A sudden increase in intensity is observed at 0.0 rad after which the remaining part of the measured spectrum resembles the first part of the spectrum. The intensity however is less than that of the first part of the spectrum. This is not a real intensity change for the wavelengths corresponding to the angle indicated, but this is a second order diffraction of the grating for the wavelengths which are transmitted by the filter. Because it is a second order diffraction, according to the grating equation (Eq. (3.1)), it needs to have double the width of the other part of the spectrum. Therefore the part seen is the second order of the part of the spectrum observed between -0.175 rad and -0.125 rad and not of the whole spectrum observed between -0.175 rad and 0 rad. The reason for not observing the whole second order spectrum of the transmitted light is because of to the blaze angle of the grating. This causes the intensity of the light diffracted at angles larger than 0.100 rad to decrease rapidly.

To calculate the reflection absorption spectrum also a measured intensity spectrum ($I(\varphi)$), in which part of the intensity is absorbed, is needed. The reflection absorption spectrum ($R(\varphi)$) can be calculated by:

$$R(\varphi) = \frac{I(\varphi) - I_{back}(\varphi)}{I_0(\varphi) - I_{back}(\varphi)}, \quad (3.5)$$

where $I_0(\varphi)$ is the reference spectrum obtained without absorption and $I_{back}(\varphi)$ is the background spectrum obtained when the light source has been turned off. In Figure 3.5 an absorption spectrum is shown obtained by introducing an absorber in the reflecting light beam. By means of Eq. (3.5) the absorption spectrum as function of the optical scanner position of the measured intensity data is calculated and the result of this calculation is shown in the image on the left side of Figure 3.6.

3.5 Wavelength calibration

In general it will be rather difficult to measure the angle of incidence and the angle of diffraction at the grating accurate enough to use the grating equation for calculating the wavelength as function of the optical scanner position. Therefore a wavelength calibration has to be performed. The easiest way to perform a wavelength calibration is by means of gas phase absorption. First because in general the spectral position of gas phase absorptions is known very well and second because gas phase absorption bands have a small width compared to solid state absorption bands. So as an extra from gas phase absorption measurements also some information about the apparatus profile (resolution) of the fast infrared reflection absorption spectroscopy setup is obtained. To calibrate the setup in the range from 700 cm^{-1} to 1400 cm^{-1} HMDSO gas has been used. In the given range this molecule has four absorption bands as shown in Table 3.4.

With the aligned fast infrared reflection absorption spectroscopy setup the gas phase absorption can be measured. A blank silicon substrate is used as a reflector, the pump line is closed and 50 Pa HMDSO is let into the reactor. In both the incident light beam to the sample as the reflected infrared beam from the sample gas phase absorption will take place. By measuring the infrared spectrum with and without the HMDSO gas present it is possible to calculate the absorption spectrum as function of the optical scanner position.

Table 3.4: Overview of different gas absorption bands of HMDSO in the range 700 cm^{-1} to 1400 cm^{-1} [25,26].

Bond	Vibration type	Wavenumber
Si-CH ₃	Sym. Bending	1260 cm^{-1}
Si-O-Si	Asym. stretching	1070 cm^{-1}
Si-CH ₃	Asym rocking	850 cm^{-1}
Si-CH ₃	Asym. Bending	758 cm^{-1}

In Figure 3.6 an absorption spectrum measured by means of the fast infrared reflection absorption spectroscopy is given. This spectrum has been calculated using the measurements shown in Figure 3.5. Notice that there is no difference between calculating a reflection

absorption spectrum and a gas phase absorption spectrum. The shown absorption spectrum has been calculated by means of Eq. (3.5).

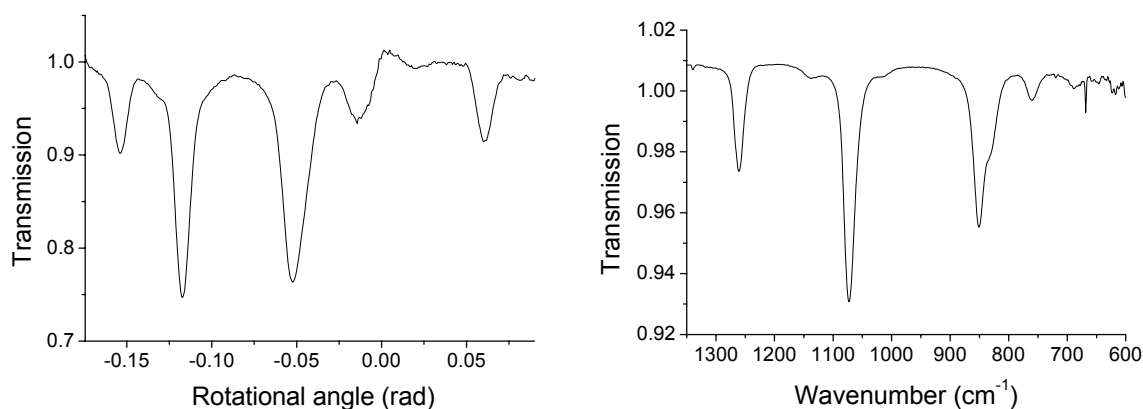


Figure 3.6: Measured HMDSO gas phase absorption with fast infrared reflection absorption spectroscopy (left) and with FTIR gas phase absorption spectroscopy (right).

In Figure 3.6 also the absorption spectrum obtained by means of the more conventional FTIR gas phase absorption spectroscopy technique is shown. Comparison of the two absorption spectra immediately shows that there are five absorption peaks in the fast infrared reflection absorption spectrum and there are only four absorption peaks in the FTIR gas phase absorption spectrum. This difference is due to the fact that the absorption peaks in the fast infrared reflection absorption setup can also be seen in their second order diffraction from the grating. So the first absorption peak (shown on the left) has the same origin as the last absorption peak (shown on the right). When the absorption intensity of these two absorption peaks are compared it can be seen that the absorption intensity is the same.

Note that there is a difference between the absorption intensity measured with the fast infrared reflection absorption setup and the FTIR gas phase absorption setup. This is mainly due to a difference in used gas pressure in both cases, but it is also due to a difference in resolution. Comparison of the noise level of both methods by means of the spectra shown in Figure 3.6 is not valid because for the FTIR spectroscopy measurements 100 spectra have been averaged and for the fast infrared reflection spectroscopy no spectra have been averaged. Also the path length between the two methods is different because the FTIR spectroscopy measurement is a straight through measurement (5 cm above and parallel to the substrate) and in the case of the fast infrared reflection spectroscopy the infrared light beam passes through the reactor at an angle and is reflected at a surface causing the path length to be longer.

By means of the absorption peak positions a conversion of the optical scanner angle position to wavenumbers can be made using eq. (3.1). For the absorption spectrum shown in Figure 3.6 this has been done and the result of this conversion is shown in Figure 3.7. Comparing this absorption spectrum with the spectrum measured by means of FTIR gas phase absorption spectroscopy shows that in FTIR spectroscopy the resolution is independent of the position in the spectrum whereas this is not the case for the fast infrared reflection absorption spectroscopy. Due to the use of a grating the resolution as measured in wavelength is close to constant, but due to the fact that the conversion of wavelength to wavenumber has to be made a $1/\lambda$ dependency is introduced. The difference does not have an effect on the development of the different absorption peaks in time dependent measurements, which is the main reason for

which the new setup has been developed. In the rest of this chapter, for the sake of clarity the optical scanner position will be converted to wavelength instead of wavenumbers.

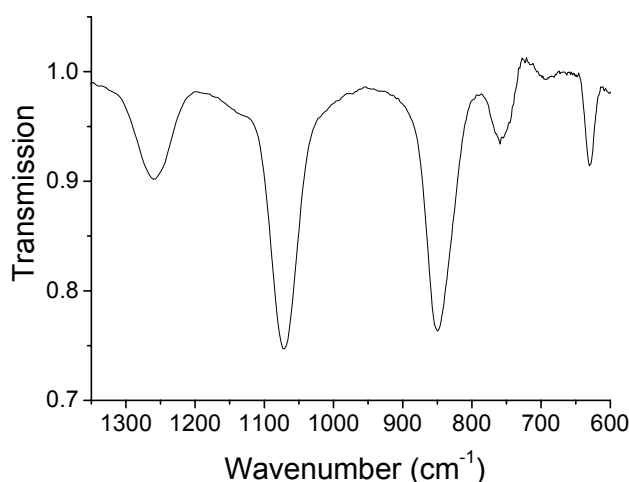


Figure 3.7: HMDSO gas phase absorption spectrum with converted optical scanner position.

The calibration, which is easy to perform has to be made every time when a small change to the alignment of the setup is made, e.g. when the sample is changed or the detector signal is optimized. This is because a slight movement of the detector or of a mirror will lead to a slight change of the wavelength measured at the detector at a specific angle of the optical scanner.

3.6 Sensitivity

Various substrate types can be used as has been shown in the introduction. There it has been shown that it is the easiest to use the setup in two different modes. First the setup is used in single reflection mode and second in ATR mode. The absorption sensitivity is obviously different for these two modes.

To demonstrate the sensitivity and time resolution of the fast reflection absorption setup an expanding thermal plasma deposition setup is used. This deposition setup has been depicted in literature before extensively and therefore only a short description of the setup suffices [27,28,29]. A thermal argon plasma is generated by a cascaded arc and expands into a vacuum vessel with a typical pressure of 10 Pa to 30 Pa. Into this expanding argon plasma deposition precursor gases are injected by means of a punctured injection ring situated at 5 cm from the arc exit or by means of an injection nozzle [13]. The injected precursor will be dissociated by interaction with the argon plasma. The dissociated species will cause film deposition to occur at the substrate which is situated on top of a thermostated chuck 65 cm from the arc exit. The deposition is monitored by means of the fast infrared reflection absorption spectroscopy setup and the film thickness is monitored by means of *in situ* ellipsometry. For the demonstration hexamethyldisiloxane (HMDSO) and oxygen are used as film deposition precursors.

3.6.1 Single reflection

In Figure 3.8 the evolving detector signal, corrected for the background signal, as function of the wavelength at various times during a HMDSO/oxygen deposition are shown (deposition rate 10.0 nm/s). It can be seen that the maximum value of the detector signal is approximately 3.2 V which is, as expected, above the predicted 2.2 V. In Figure 3.8 also the reflection absorption spectra at various times during film growth are shown. It can be seen that there are various absorption peaks appearing and growing during the deposition process. Notice that the spectra shown are single spectra, each obtained in 2.5 ms, and that they have not been averaged. For the sake of clarity only a couple of spectra are shown.

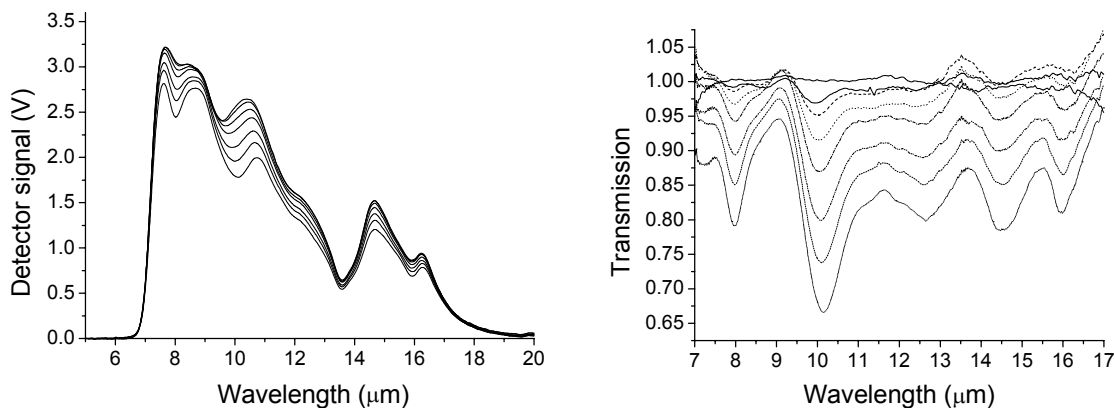


Figure 3.8: Corrected detector signal and calculated reflection spectra at various times during silicon oxide like film deposition obtained in single reflection mode; time interval between shown measurements = 6.6 s.

The noise level can also be observed in Figure 3.8 when the first reflection spectrum is studied in more detail. This first spectrum is obtained when there was still no deposition on top of the sample and therefore it is a good indication of the noise level. For the longer wavelengths the noise present in this reflection spectrum is larger than for the shorter wavelengths. This is in agreement with the measured detector signal, the higher the detector signal the lower the relative noise in the detector signal and the lower the noise in the calculated reflection spectrum. The absolute value of the noise level measured is in agreement with the expected noise level (10^{-2}). It is not possible to measure the absorption of any absorption peak, not even the strongest one, at monolayer sensitivity ($2 \cdot 10^{-4}$).

A better way to present the absorption peak evolution as function of time, without skipping measured spectra, is by integrating the various absorption peaks in every individual absorption spectrum obtained. Integration has been done by fitting a baseline to every absorption peak and integrating the area between the absorption and its baseline. An example of the integrated absorption intensity as function of time is given in Figure 3.9. It can be seen that the integrated absorption has a noise level which is different for the different absorption peaks. This difference in absorption is caused by the spectral detector signal, which causes the noise on the calculated reflection absorption spectrum to be dependent on the position in the spectrum.

The scanning time and time resolution of the data shown in Figure 3.8 and Figure 3.9 has been chosen 2.5 ms as mentioned before. This time scale is not the fastest possible, but at

this time scale the scanning angle could be higher and therefore the second order diffraction of the first absorption peak (at 16.05 μm) could also be measured. This reflection absorption intensity has also been integrated and is also shown in Figure 3.9. It can be seen that the evolution of this peak as function of time is similar to the evolution for this reflection absorption peak observed in its first order as to be expected. The integrated absolute absorption intensity is different but that is due to fact that the absorption has been treated in the same way as the other absorption peaks in first order. To convert the scanner angle to wavelengths it has been assumed that all data were first order and therefore the width of the second order peaks in the wavelength spectrum is different from the one measured in the first order. The peak absolute absorption intensity is however the same and thus the integrated absorption intensity is different. The physical interpretation of the data shown in Figure 3.8 and Figure 3.9 will not be discussed in this publication. Notice that *in situ* measurements of the same deposition at a faster time scale speed would have resulted in the same signal to noise ratio for the integrated absorption intensity.

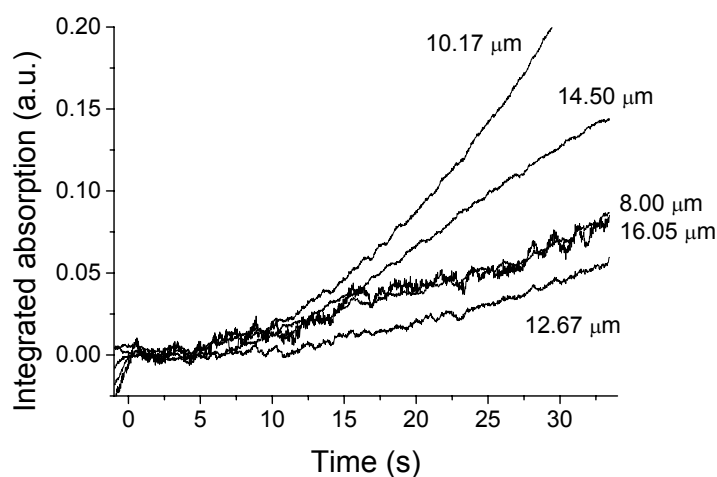


Figure 3.9: Integrated absorption intensity for the various absorption peaks observed during silicon oxide like film deposition as function of time in single reflection mode.

The integrated absorption intensity can be smoothed by adjacent averaging. This will show the evolution of the absorption intensity more clearly, but it will lead to loss of detail of the deposition processes which take place on a shorter timescale than the timescale represented by the averaging interval. So when studying the initial growth process of a film only processes slower than the measuring timescale can be observed. For steady state film growth adjacent averaging will not influence the results. For the data shown in Figure 3.9 five point adjacent averaging has been used.

Notice that for the conditions used the fast *in situ* infrared reflection absorption spectroscope will not detect the HMDSO gas phase absorption during deposition. This is because during deposition the absolute density of HMDSO in the gas phase is too low to be detected. During deposition the pressure in the plasma reactor is 10 Pa and less than 5 % of the gas is the deposition precursor gas. During a deposition experiment the precursor is injected into the plasma and a large amount (approximately 70 %) of it is consumed by the plasma. So less than 1.5% of 10 Pa is HMDSO gas and thus the HMDSO partial pressure is less than 0.15 Pa, which is only 1/333 part of the pressure used for gas phase calibration

measurements (cf. Figure 3.7). Therefore the absorption intensity of the strongest absorber of this small amount of HMDSO ($0.25/333=7.5\cdot 10^{-4}$) will be below the sensitivity of the spectroscope (10^{-2}). Notice that the gas phase absorption intensity is of the same order as the monolayer absorption intensity. When increasing the sensitivity it is therefore possible that the contribution due to the gas phase cannot be neglected and a correction needs to be made. Eliminating the gas phase contribution can be done with the use of a polariser and performing the experiment twice at different polarisation angles.

3.6.2 ATR

To get an enhancement of the absorption signal an ATR crystal can be used [4,5,30,31]. In the crystal the light will have multiple internal reflections, due to which the light will also have multiple interactions with the deposited film on top of the ATR crystal. In these experiments ZnSe ATR crystals have been chosen. ZnSe has a good transparency for the infrared, and also a reasonable transparency for the visible, which makes the aligning procedure of the setup easier because the path of the light can be observed without the means of any infrared light detecting device.

The refractive index of ZnSe in the range 5-10 μm is approximately equal to 2.4. The refractive index of the deposited silicon oxide film is about 1.4 and the angle of the light, with respect to the ATR crystal surface, in the ATR crystal is approximately 55° . This is above the critical angle [4] for total internal reflection which is approximately 35° and therefore the light will not propagate into the film deposited on top of the crystal. The absorption will occur in the evanescent wave that occurs at the surface at which total internal reflection takes place [4]. Notice that the light will pass through the film twice, once on entering the crystal and once on leaving the crystal. This will also cause transmission absorption, which is different from reflection absorption. However, this will only be a small fraction of the total absorption, e.g. with 35 reflections this fraction will be $2/37$.

In Figure 3.10 the infrared reflection absorption spectra obtained with the use of an ATR crystal are shown, for similar HMDSO/oxygen deposition as shown for single reflection mode. Again, only a selection of spectra are shown for the sake of clarity and no spectra averaging has been used. The infrared absorptions are more intense than in the case of single reflection. In Figure 3.10 also the corrected detector signal as function of the wavelength is shown. Comparison of the maximum detector signal with the maximum signal obtained in single reflection mode (see Figure 3.8) shows that the signal decreased one order of magnitude, where a reduction with a factor of 5 was expected. This difference is probably due to the alignment of the setup, which is more critical in the case of ATR mode than in the case of single reflection mode. This is due to the focusing on the initial bevel of the ATR crystal.

Comparison of the reflection absorption spectra obtained in ATR mode with the reflection absorption spectra obtained in single reflection mode shows some differences. Notice that in the case of the ATR mode a smaller part of the spectrum is plotted due to which two reflection absorption peaks are not plotted. In the omitted part the noise level is too high to get any clear picture, which can already be observed on the higher wavelength side of the reflection absorption spectrum shown in Figure 3.10. The first difference is that the peak at 8 μm is much smaller with respect to the peak with biggest reflection absorption intensity in the ATR mode than in the single reflection mode. The second difference that can be seen is that the shape of the various absorption peaks is different and that the position of the maximum

reflection absorption intensity is slightly shifted. Both differences are due to the change of substrate material when changing from single reflection mode to ATR mode.

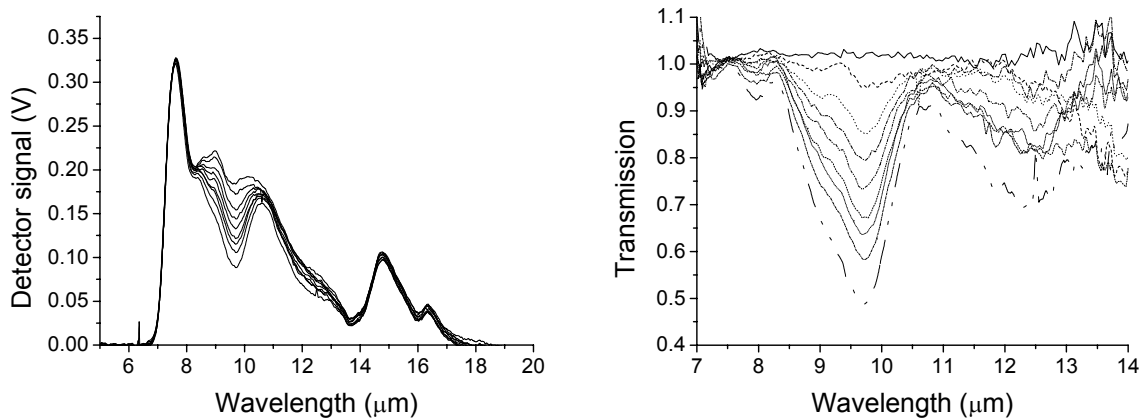


Figure 3.10: Measured detector signal and calculated reflection spectra at various times during silicon oxide like film deposition obtained in ATR mode; time interval between shown measurements = 0.45 s.

A similar difference is observed between a reflection absorption spectrum and the transmission absorption spectrum on the same substrate material [4]. Due to the absorption the imaginary part of the refractive index as function of wavelength is not equal to zero at the wavelength of an absorption. Therefore the Fresnel coefficients for reflection as function of wavelength will have a change locally which results in a change in the reflection. The Fresnel coefficients are also dependent on the refractive index of the substrate material and because the film deposited on top of the silicon substrate is similar to the film deposited on top of the ZnSe ATR crystal the change in the reflection absorption spectrum can only be due to the difference in substrate material. A calculation using the Fresnel equations fully supports this theory [32].

To get a better insight in the development of the various absorption peaks, the absorption peaks are integrated and plotted as function of time. The result is shown in Figure 3.11. Five point adjacent averaging has been used to smooth the integrated absorption data. The data in Figure 3.11 indicates that the absorption intensity is much stronger than in the case of single reflection (cf. Figure 3.9). However, it is not possible to give an exact value for the absorption intensity increase, because the substrate material is different for the two modes. An increase with a factor of 35 was expected, and looking at the strongest absorption peak it can be seen that indeed an increase close to this value is reached. However, the sensitivity of the ATR setup is not 35 times as high as in the case of single reflection. This can be seen in the noise level of the ATR absorption spectra taken before the deposition started. In this spectra the absolute noise level ($4 \cdot 10^{-2}$) is higher than in the single reflection absorption spectrum ($1 \cdot 10^{-2}$). This is due to the fact that the absolute infrared intensity on the detector is decreased by installing an ATR crystal in the setup. This lower intensity will lead to a higher relative noise level in the detected signal and therefore a higher absolute noise in the ATR absorption spectra with respect to the single reflection absorption spectra. Although the absolute noise level is higher still the absorption sensitivity is increased and therefore the absorption of thinner films can be measured *in situ* with a high time resolution. Taking the absorption intensity to be 35 times that of the single reflection mode than a single reflection

equivalent absorption of approximately $1 \cdot 10^{-3}$ can be measured, which is in agreement with the predictions.

The sensitivity can be increased even more by averaging multiple spectra, but it should be realized that this will result in a lower time resolution. For deposition rates of only a couple of nanometers per second this does not have to be a problem, because within the deposition of one monolayer up to one hundred spectra can be obtained. Averaging one hundred spectra will result in an increase in sensitivity by a factor 10. In the case the setup is used for the analysis of silicon oxide like film deposition this would improve the sensitivity to monolayer sensitivity. In the use of the setup it is best to find a balance between time scale, sensitivity and averaging.

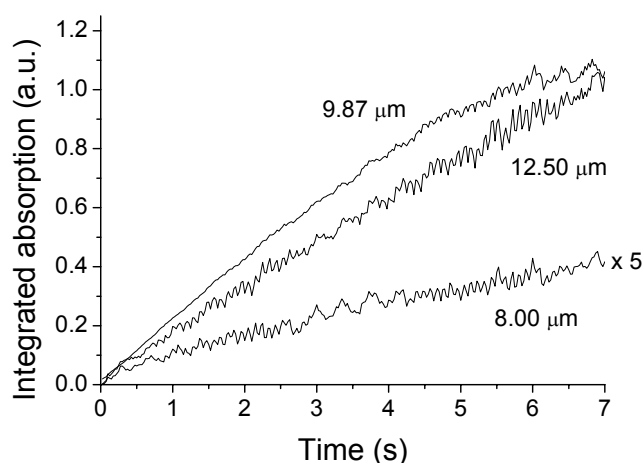


Figure 3.11: *Integrated absorption intensity for the various absorption peaks observed during silicon oxide like film deposition as function of time in ATR mode.*

3.7 Conclusions

A fast *in situ* infrared reflection absorption spectroscopy setup has been designed and constructed. With this new setup it has been demonstrated that *in situ* film growth can be monitored in real time at high deposition rates (up to several hundreds of nm/s). It has been demonstrated that the setup is capable of detecting absorptions of thin films that calibrating the setup is easy by means of gas phase absorption.

The minimum corresponding film thickness which can be measured is however dependent on the absorption intensity of the different bonds present in the deposited film. The sensitivity of the new setup is dependent on the amount of light collected by the detector and on the interaction length of the light with the absorbing medium. When using the setup in single reflection mode absorptions of $1 \cdot 10^{-2}$ and up can be detected and for the ATR mode the minimum absorption needs to be above $1 \cdot 10^{-3}$. For the ZnSe ATR crystal used the sensitivity should be increased by a factor of 35, but installing an ATR crystal reduces the detector signal and therefore the increase of the sensitivity is only a factor 10. The absorption sensitivity with ATR crystal is not enough to make the setup monolayer sensitive. This is even true for the Si-O-Si bond which is the strongest, when depositing silicon oxide like films by means of a HMDSO/oxygen plasma. To reach monolayer sensitivity for the strongest bond a minimum sensitivity of $2 \cdot 10^{-4}$ is needed. To reach the monolayer sensitivity a longer ATR crystal has to

be used or multiple reflection absorption spectra have to be averaged. However, the latter influences the measurement time scale in a negative sense.

Another way to increase sensitivity is by intensifying the light source and by reducing the light intensity losses in the setup. The former can be done by increasing the operation pressure and arc current of the arc [14,15] and the latter can be done by using only gold coated mirrors or adapting the setup in such a way that less optical components are needed.

The fast moving grating principle can also be used for gas phase absorptions measurements. The setup for this would be fairly easy. The light of the light source is made parallel by means of a 90° off axis parabolic mirror and is send straight through the vessel onto the grating after which it is focused on the detector. In this case less mirrors are used and there is no reflection at a substrate and thus more light will reach the detector and with this the sensitivity is increased. However, in general the species density in the gas phase will be low, especially when the plasma is on, and therefore still only the stronger absorbing species can be detected. Alternatively the sensitivity can be increased by making an optical cavity which enlarges the absorption path length [33,34]. Applying the fast moving grating principle to gas phase absorption might make a study of the gas phase possible on the timescale of milliseconds.

References

- [1] M. Meier and A. von Keudell, *J. Appl. Phys.* **90** (2001) 3585
- [2] H. Ohta, M. Hori, and T. Goto, *J. Appl. Phys.* **90** (2001) 1955
- [3] P. Scheible and A. Lunk, *Thin Solid Films* **364** (2000) 40
- [4] N.J. Harrick, *Internal Reflection Spectroscopy*, John Wiley & Sons Inc., New York (1967)
- [5] J.R. During, *Applications of FT-IR Spectroscopy*, Elsevier, Amsterdam (1990)
- [6] S.A. Francis and A.H. Ellison, *J. Opt. Soc. Am.* **49** (1959) 131
- [7] Y. Toyoshima, K. Arai, A. Matsuda, and K. Tanaka, *Appl. Phys. Lett.* **56** (1990) 1540
- [8] N. Maley, I. Szafranek, L. Mandrell, M. Katiyar, J.R. Abelson, and J.R. Thornton, *J. Non-Cryst. Solids* **114** (1989) 163
- [9] J.W.A.M. Gielen, P.R.M. Kleuskens, M.C.M. van de Sanden, L.J. van IJzendoorn, D.C. Schram, E.H.A. Dekempeneer, and J. Meneve, *J. Appl. Phys.* **80** (1996) 5986
- [10] W.M.M. Kessels, A.H.M. Smets, B.A. Korevaar, G.J. Adriaenssens, M.C.M. van de Sanden, and D.C. Schram, *Mater. Res. Soc. Symp. Proc.* **557** (1999) 25
- [11] A. de Graaf, G. Dinescu, J.L. Longueville, M.C.M. van de Sanden, D.C. Schram, E.H.A. Dekempeneer, and L.J. van IJzendoorn, *Thin Solid Films* **333** (1998) 29
- [12] J.W.A.M. Gielen, M.C.M. van de Sanden, P.R.M. Kleuskens, and D.C. Schram, *Plasma Sources Sci. Technol.* **5** (1996) 492
- [13] M.F.A.M. van Hest, B. Mitu, D.C. Schram, and M.C.M. van de Sanden, *Deposition of silicon oxide like films using a remote thermal plasma*, to be published; Chapter 5 of this thesis
- [14] R. Raghavan and P.W. Morrison Jr., *J. Quant. Spectroscopy Radiative Transfer* **69** (2001) 605
- [15] A.T.M. Wilbers, G.M.W. Kroesen, C.J. Timmermans, and D.C. Schram, *Meas. Sci. Technol.* **1** (1990) 1326
- [16] A.T.M. Wilbers, G.M.W. Kroesen, C.J. Timmermans, and D.C. Schram, *J. Quant. Spectroscopy & Radiative Transfer* **45** (1991) 1

- [17] J.T. Houghton and S.D. Smith, *Infrared Physics*, Oxford University Press, Oxford (1966)
- [18] F.L. Pedrotti and L.S. Pedrotti, *Introduction to Optics*, Prentice-Hall Inc., New Jersey (1993)
- [19] C. Palmer, *Diffraction Grating Handbook*, Richardson Grating Laboratory, Rochester New York (2000)
- [20] S.P. Davis, *Diffraction Grating Spectrographs*, Holt, Rinehart and Winston, New York (1970)
- [21] G.A. Vanasse, Editor, *Spectrometric Techniques IV*, Academic Press, New York (1985)
- [22] M.M. Hemerik, *Design of a Mid-infrared Cavity Ring Down Spectrometer*, Ph.D. Thesis, Eindhoven University of Technology (2001)
- [23] Y. Segui and P. Raynaud, in *Plasma Processing of Polymers*, Ed. R. d'Agostino, P. Favia, and F. Fracassi, Nato ASI series **346** (1997) 81
- [24] M.C. Hutley, *Diffraction Gratings*, Academic Press, London (1982)
- [25] H.G. Pryce Lewis, T.B. Casserly, and K.K. Gleason, *J. Electrochem. Soc.* **148** (2001) F212
- [26] D. Magni, Ch. Deschenaux, Ch. Hollenstein, A. Creatore, and P. Fayet, *J. Phys. D* **34** (2001) 87
- [27] J.W.A.M. Gielen, M.C.M. van de Sanden, P.R.M. Kleuskens, and D.C. Schram, *Plasma Sources Sci. Technol.* **5** (1996) 492
- [28] J.W.A.M. Gielen, W.M.M. Kessels, M.C.M. van de Sanden, and D.C. Schram, *J. Appl. Phys.* **82** (1997) 2643
- [29] A. de Graaf, *Deposition of CNH Materials; Plasma and Film Characterization*, Ph.D. Thesis, Eindhoven University of Technology (2000)
- [30] N.J. Harrick, *Phys. Rev. Lett.* **4** (1960) 224
- [31] E.S. Aydil, R.A. Gottscho, and Y.J. Chabal, *Pure & Appl. Chem.* **66** (1994) 1381
- [32] M.F.A.M. van Hest, *High Rate Plasma Deposition of Silicon Oxide Like Films*, Ph.D. Thesis, Eindhoven University of Technology (2002), Chapter 2 of this thesis.
- [33] V. Nagali, S.I. Chou, D.S. Baer, and R.K. Hanson, *J. Quant. Spectroscopy and Radiative Transfer* **57** (1997) 795
- [34] R. Engeln, K.G.Y. Letourneur, M.G.H. Boogaarts, M.C.M. van de Sanden, and D.C. Schram, *Chem. Phys. Lett.* **310** (1999) 405

Chapter 4

Analysis of the argon-oxygen plasma gas phase

M.F.A.M. van Hest, J.R. Haartsen, M.H.M. van Weert, D.C. Schram,
and M.C.M. van de Sanden

Abstract

An expanding thermal argon plasma into which oxygen is injected has been analysed by means of Langmuir probe and Pitot probe. Information is obtained on the ion density in and the flow pattern of the downstream plasma. Combination of the Langmuir probe and Pitot probe measurements provide information on the total ion flux generated by the plasma source (cascaded arc). It has been found that the ion diffusion is mainly determined by the background pressure in the expansion vessel and the used arc current. The ion density is determined by the total power input into the plasma as well as the gas flow in the plasma source. There is an optimum in the power transfer used for ionisation from plasma source to the feed gas. Interaction of oxygen with the plasma results in a decrease of the argon ion density and a decrease of the plasma beam radius. By means of Pitot probe the recirculation pattern of the downstream plasma has been investigated experimentally. Due to the low downstream pressure (10-30 Pa) the conventional compressible Pitot probe theory does not apply anymore. At these low pressures viscous effect start to play an important role when measuring the stagnation pressure and can therefore not be neglected.

4.1 Introduction

There are many different methods to analyse various plasma parameters, e.g. ion and electron density, ion and electron temperature and particle drift velocity. Due to the diversity in plasma sources also the range in which the various plasma parameters vary is large (several orders of magnitude). In general the analysis methods can be divided into two different groups. The first group contains the non intrusive methods, i.e. methods which do not influence the plasma; e.g. optical emission spectroscopy [1,2], laser induced fluorescence [3,4], Thomson scattering [5,6], etc. The second group contains the intrusive methods, i.e. methods which do influence the plasma; e.g. Langmuir probe [7,8], Pitot probe* [9,10], etc. For the methods mentioned in the second group the influence is unavoidable, and the aim is usually to minimize the perturbing character as much as possible. To make a correct interpretation of the measured data by means of these intrusive methods the disturbance needs to be known so that possible changes caused due to the analysis tool can be corrected for.

In this chapter a study will be presented of an expanding thermal argon plasma, generated by means of a cascaded arc [11,12], into which oxygen is injected. This plasma will be analysed by means of Langmuir probe measurements and Pitot probe measurements. By means of Langmuir probe measurements the local ion density and the local ion and electron temperature is measured. From these measurements it is possible to derive the geometrical reaction profile of argon ions, electrons and the injected oxygen molecules. By means of the Pitot probe the local particle drift velocity is measured, which will give information about the flow pattern in the plasma reactor. To calculate the ionisation degree of the plasma the total ion flux from the cascaded arc plasma source needs to be measured. For this the particle drift velocity is needed. Therefore a combination of Langmuir probe measurements and Pitot probe measurements will make it possible to calculate the ionisation degree of the plasma source accurately. Although the two methods of measurement are intrusive, they are easy to use and low cost.

Langmuir probes are used to analyse plasmas for many decades and they can have all kinds of shapes and sizes. In principle a Langmuir probe is no more than a conducting plate or wire which is positioned inside the plasma. By applying a voltage to the probe a current is generated which gives information about the charged particles in the plasma. By changing the position in the plasma the spatial variation of the different parameters can be measured. The conventional Langmuir probe (single probe), consists of one conductor which is connected to a power supply which generates a voltage relative to ground. Applying a positive voltage to the probe results in a current which is induced by the electrons and applying a negative voltage results in a current which is induced by the ions. Due to the fact that the mobility of electrons is larger than that of ions, the measured current due to the electrons will be several orders of magnitude larger than the current due to the ions. Depending on the plasma to which the Langmuir probe is applied and on the probe size, electron currents of the order of 1 A can be measured. The current is limited by the probe size in combination with heating of the probe, for significant heating the probe will start to emit electrons and for even higher heating the probe may melt. In the case the probe is applied to an argon-oxygen plasma, the probe could burn due to presence of oxygen. This burning will already occur at less severe plasma conditions than that are needed to melt the probe.

* Also referred to as Pitot tube.

A double Langmuir probe can be used to prevent the probe from burning. A double Langmuir probe consist is in essence of two single Langmuir probes where instead of connecting the power supply between the probe and ground the two probes are connected to the power supply. By doing this the current to both probes needs to be the same, but of opposite sign, and will therefore be equal to the ion current. For many plasmas the ion current has such a low value that, even with the presence of oxygen, the probes do not burn or melt in this situation.

A Pitot probe is a tube which in general has a tip with a 90° angle. One side of the tube is open and the other side is connected to a pressure gauge. By inserting the open end of the tube into a flow the pressure in the tube will become equal to the local stagnation pressure of the flow. From the stagnation pressure the local average particle drift velocity of the flow can be derived. By measuring the stagnation pressure at various positions in the flow, it is possible to derive the particle drift velocity profile

4.2 Analysis method

4.2.1 Langmuir probe

A detailed study of various Langmuir probes and their theory has been given by e.g. Peterson and Talbot [13], which was applied for an expanding thermal plasma by Brussaard [14]. As only a double Langmuir probe will be used a description of the double Langmuir probe theory suffices here. The theory will be focussed on the use of a double cylindrical probe of which both probe tips have the same size.

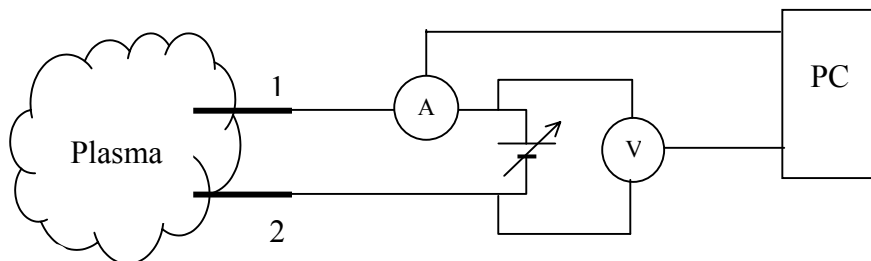


Figure 4.1: Schematic of a double Langmuir probe and its electronics.

Double cylindrical Langmuir probe

In Figure 4.1 a schematic is given of the used double Langmuir probe and its electronics. When no voltage is applied to the two probe tips while they are in the plasma, both probe tips will have the same potential[†], the floating potential. When the voltage to probe 1 is lowered with respect to probe 2, the number of ions attracted by probe 1 will increase, which is compensated by probe 2 by repelling less electrons because the net current needs to remain zero. When the potential applied between the two probes is not extremely high, the probe with the lowest voltage will have a voltage which is below plasma potential.

[†] Unless there is a significant difference in the local electron density at both probe positions.

Chapter 4

When the mean free path of the particles in the plasma is much larger than the Debye length[‡] of the plasma the repelled (electron) current to each probe is given by:

$$I = I_0 \cdot e^{-\chi} \quad (4.1)$$

where χ is the nondimensional potential expressed in terms of the probe potential (V_{probe} relative to the plasma potential), particle temperature (T) and attracted particle charge (q):

$$\chi = \frac{qV_{probe}}{k_B T} . \quad (4.2)$$

I_0 is equal to the random (Maxwellian) current to a probe at the plasma potential and is given by [15]:

$$I_0 = \frac{1}{4} n_0 q \left(\frac{8k_B T}{\pi m} \right)^{1/2} A_p, \quad (4.3)$$

with n_0 the number density of the charged particles in the undisturbed plasma, m the mass of the charged particle, and A_p the surface area of the probe.

Beside the repelled current there is also an attracted current. Peterson and Talbot [13] semi-empirically found a function for the current provided by the attracted particles, which is given by:

$$I = I_0 \cdot (\beta + |\chi|)^\alpha, \quad (4.4)$$

where χ is again the nondimensional potential as given by Eq. (4.2). α and β depend on the ratio of the temperature of the attracted and repelled particles and on the ratio of the probe radius (R_p) to the Debye length ($\lambda_D = \sqrt{\varepsilon_0 k_B T_e / e^2 n_e}$). In the case that the electron temperature is equal to the ion temperature[§] the dependency of α and β on R_p / λ_D is given by:

$$\alpha = \frac{2.9}{\ln(R_p / \lambda_D) + 2.3} - 0.27 \quad (4.5)$$

$$\beta = 2.35 + 0.135 \cdot [\ln(R_p / \lambda_D)]^3$$

The total current through the probes (I) is given by:

[‡] “The Debye length is the screening distance over which charge separation takes place and thus gives the distance over which an electrical field may exist in the plasma” [14]

[§] For the used expanding thermal plasma source it has been shown that this is actually the case [14,44].

$$I = I_{e1} + I_{i1} = -I_{e2} - I_{i2}, \quad (4.6)$$

with the subscripts 1 and 2 indicating the two probes and the subscripts e and i indicating electron and ion respectively. When the applied potential difference (V_a) is given by:

$$V_a = V_2 - V_1, \quad (4.7)$$

then

$$\begin{aligned} V_1 &= V_f - V_1' \\ V_2 &= V_f - V_2' \end{aligned} \quad (4.8)$$

with V_1' and V_2' are the potentials with respect to the floating potential V_f . The current through the double cylindrical probe with equal tip surfaces can now be derived from Eqs. (4.1), (4.2), (4.4), and (4.6) and is given by:

$$I = \frac{I_{i1} e^{\frac{eV_a}{k_B T}} - I_{i2}}{1 + e^{\frac{eV_a}{k_B T}}}. \quad (4.9)$$

The individual ion currents can be derived from Eq. (4.4) and Eq. (4.8) and are given by:

$$\begin{aligned} I_{i1} &= I_{i0} \left(\beta + \frac{e(V_f - V_1')}{k_B T} \right)^\alpha \\ I_{i2} &= I_{i0} \left(\beta + \frac{e(V_f + V_2')}{k_B T} \right)^\alpha \end{aligned} \quad (4.10)$$

A difficulty in the interpretation of the double probe characteristics comes from the fact that only the applied potential is known and not the individual potential of each probe with respect to the plasma potential. Expressions for the potentials V' and V_f can be derived in an implicit form and are given by:

$$\frac{eV_1'}{k_B T} = -\ln \left\{ \left[1 + \frac{eV_1'/k_B T}{\beta - eV_f/k_B T} \right]^\alpha + \left[1 + \frac{eV_1'/k_B T}{\beta - eV_f/k_B T} - \frac{eV_a/k_B T}{\beta - eV_f/k_B T} \right]^\alpha \right\} + \ln(1 + e^{eV_a/k_B T}) \quad (4.11)$$

and

$$\frac{eV_f}{k_B T} = -\frac{1}{2} \ln \left(\frac{m_i}{m_e} \right) + \alpha \ln \left(\beta - \frac{eV_f}{k_B T} \right) \quad (4.12)$$

Chapter 4

It can be seen clearly that these equations are not easy to apply for the evaluation of a measured I-V characteristic (cf. Figure 4.2) and therefore Peterson and Talbot [13] developed a procedure for the evaluation of the double probe characteristic.

The temperature can be calculated using the derivative of the I-V characteristic while both probes are at floating potential ($V_a = 0$). Then the following equation holds:

$$\frac{k_B T}{e} \frac{1}{\xi} = \left\{ \frac{I_{i1} I_{i2}}{I_{i1} + I_{i2}} \left(\frac{\partial I}{\partial V_a} \right)^{-1} \right\}_{V_a=0} \quad (4.13)$$

with

$$\xi = 1 + \frac{\alpha}{\beta + |eV_f / k_B T|}. \quad (4.14)$$

When both probe areas are equal, the ion currents at floating potential become equal for both probes and Eq. (4.13) can be simplified even further. The factor ξ is only slightly dependent on the particle temperature and density. It varies from 1.1 to 1.0 when the ratio R_p / λ_D varies between 1 and 100, therefore the factor can be approximated by 1. At very large applied potentials, the current to one of the probes will consist only of the ion current to that probe. It has been found by Peterson and Talbot [13] that the best potential to evaluate the ion current is approximately equal to $10.8 k_B T / e$.

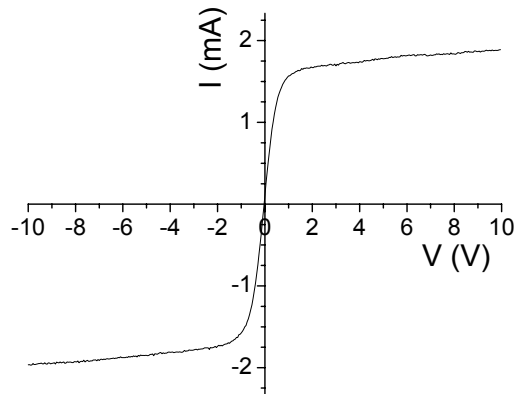


Figure 4.2: Typical symmetric double probe I-V characteristic.

According to Peterson and Talbot [13] the following recipe can be used to calculate the ion density and the ion/electron temperature from a symmetrical double probe I-V characteristic (cf. Figure 4.2):

1. Estimate the ion saturation current at the floating potential by (non-linear) extrapolation.
2. Estimate the temperature by using Eq. (4.13) with ξ equal to unity.
3. Determine the value of the currents at $V_a = \pm 10.8 k_B T / e$.

4. Calculate V_f using Eq. (4.12). A first estimate of α and β may be obtained from the extrapolated saturation currents at floating potential.
5. Calculate I_0 from Eq. (4.10) with $V' = 10k_bT/e$.
6. Calculate the ion density by Eq. (4.3) and use that to determine α and β .
7. Calculate the currents at the floating potential from Eq. (4.10), with $V' = 0$.
8. Calculate the ion temperature from Eq. (4.13).

Step 3 through 8 may have to be repeated once or twice before the recursive equations Eq. (4.11) and Eq. (4.12) are satisfied. Applying the recipe to the I-V characteristic shown in Figure 4.2 results in an ion density of $1.0 \cdot 10^{19} \text{ m}^{-3}$ and an electron temperature of 0.29 eV.

4.2.2 Pitot probe

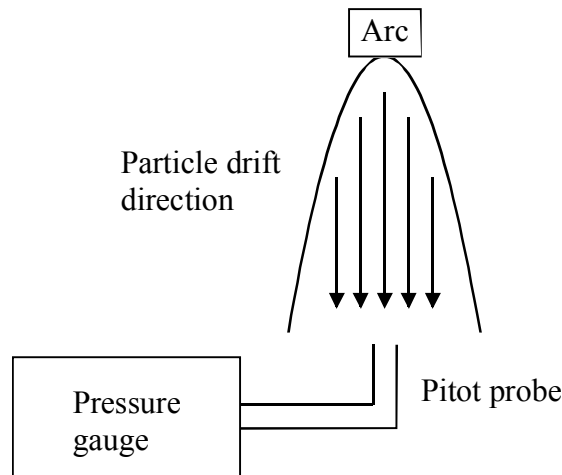


Figure 4.3: Schematic drawing of a Pitot probe in the plasma beam.

Pitot probes can be used in many different kind of flows and it has been a proven technique for measuring the velocity profile of plasma jets [16,17]. In general a Pitot probe is a tube which has a 90° angle with at one end an open tip and at the other end a pressure gauge connected, as shown in Figure 4.3. The opening at the end is directed such that the gas flow is into the direction of the opening. The pressure gauge will prevent the gas from flowing through the tube and therefore a stagnation pressure is built up in the tube. The stagnation pressure is mainly dependent on the velocity of the particles. There are two regimes for the measurement of the stagnation pressure. The first regime is in the case that the particle drift velocity is smaller than the sound velocity (subsonic) and thus the mach number (M) is smaller than 1. The second regime is when the particle drift velocity is larger than the sound velocity (supersonic, $M > 1$). In this case in front of the Pitot probe a bow shock is formed and the stagnation pressure is influenced. The expressions for the stagnation pressure (p_s) relative to the background pressure (p_o) for a compressible gas in the two different regimes are given by [18,19,20]:

$$M < 1 \quad \frac{p_s}{p_o} = \left(1 + \frac{\gamma - 1}{2} M^2 \right)^{\frac{\gamma}{\gamma - 1}} \quad (4.15)$$

$$M > 1 \quad \frac{p_s}{p_o} = \frac{\left(\frac{\gamma + 1}{2} M^2 \right)^{\frac{\gamma}{\gamma - 1}}}{\left(\frac{2\gamma}{\gamma + 1} M^2 - \frac{\gamma - 1}{\gamma + 1} \right)^{\frac{1}{\gamma - 1}}} \quad (4.16)$$

where γ is the ratio of the specific heats (C_p / C_v). For the expanding thermal plasma it has been found by modelling that $\gamma = 1.2$ for a pure argon plasma [21]. To calculate the actual velocity the mach number needs to be multiplied with the sound velocity which is given by:

$$v_s = \sqrt{\frac{\gamma k_B T}{m}} \quad (4.17)$$

where m is the effective mass of the particles, k_B the Boltzmann constant and T the particle temperature.

Pitot probes are in general used for measurements in flowing gases and liquids. When using it in a plasma ions and electrons might influence the behaviour of the probe by means of e.g. recombination of ions and electrons on the wall of the probe. For the use of Pitot probes in a plasma reported in literature in general this is not taken into account because the effects are small and negligible because of the limited ionisation degree of the plasma. Beside this there are other phenomena, such as viscosity and temperature, which have a larger influence to the measured stagnation pressure as will be shown later.

During decades of Pitot probe utilisation, many different Pitot probes have been created, all with their specific goal. Besides the Pitot probes to measure only the velocity also enthalpy probes have been developed, which are similar to Pitot probes with one addition which makes it possible to also obtain information about the temperature of the particles. This is done by adding a cooling device in the wall of the probe which also prevents the probe from becoming too hot when exposed to hot gasses. In this chapter a regular (uncooled) Pitot probe is used.

4.2.3 Total ion flux

By means of the Langmuir probe measurements it is possible to measure the ion density at various positions in the plasma. In this case an expanding thermal plasma (cascaded arc) is being investigated. The plasma is expanding in a cylindrical vessel at low pressure (up to 30 Pa). By measuring across a radial line in this plasma, the radial ion density can be measured. Because the gas enters at the arc exit situated on one end of the reactor and the pumps are situated at the other end, the plasma is a flowing plasma. The ions and electrons of the plasma will therefore be transported from the arc exit to the pump entrance. The amount of gas entering the reactor is known and by means of Langmuir probe measurements it is now possible to calculate the amount of ions and electrons entering the reactor. To do so in a

cylindrical reactor the radial ion density profile ($n_i(r)$) and the radial drift velocity profile** ($v(r)$) are needed. When assuming cylindrical symmetry the ion flux (ϕ_i) is given by:

$$\phi_i = 2\pi \int_0^{R'(v=0)} n_i(r) \cdot v(r) \cdot r dr \quad (4.18)$$

where r is the radial position. Notice that the flux is not integrated to the reactor wall, but only to the point at which the particle velocity is equal to zero ($R'(v=0)$). This is done because in the reactor a recirculation cell (cf. Figure 4.4) is formed and the origin of the ions in the recirculation part of the recirculation cell as well as their velocity is uncertain. Moreover, the ion density in the recirculation part of the recirculation cell is relatively small in comparison to density in the plasma beam and therefore the number of ions which are not included in the integration will be negligible to the number that are included.

4.3 Experimental setup

The plasma setup is shown in Figure 4.4 and has been described before extensively [22,23,24] and therefore a brief description of the main characteristics of the setup suffices here. The reactor consists of a stainless steel cylindrical vessel (diameter 320 mm, length 100 cm) which is positioned vertically. On top of the vessel a cascaded arc [25,26] has been mounted onto a moveable holder. The cascaded arc is operated using pure argon gas (grade 5.0). For the injection of oxygen gas (grade 5.0) a punctured ring (diameter 10 cm) is present which is situated at approximately 5 cm from the arc exit. A temperature controlled substrate holder is situated at the bottom of the vessel. The distance between the arc exit and the top of the substrate holder is equal to 65 cm, but can be varied. The temperature of the substrate holder can be varied in a range of - 50 °C to 300 °C. The reactor vessel is connected to a pump stack with one rotary piston pump (Edwards 240 m³/hr) and two mechanical booster pumps (Edwards EH2600: 2600 m³/hr; Edwards EH500A: 500 m³/hr) which generates a base pressure of 10⁻⁴ mbar. Overnight the reactor is pumped by a turbo molecular pump (Leybold Turbovac 1500: 90 m³/hr) which keeps the reactor pressure at 10⁻⁶ mbar. For the transfer of samples a load lock system (10⁻⁶ mbar) is connected to the plasma reactor. In Table 4.1 an overview is given of the various plasma parameters with their typical ranges in which they are varied.

Table 4.1: Overview of the plasma parameters and their ranges.

Parameter	Range
Ar flow	15 – 120 sccs
O ₂ flow	0 – 17 sccs
Arc current	25 – 75 A
Arc pressure	0.2 – 0.6 bar
Vessel pressure	10 – 35 Pa

** positive is defined as flowing from source exit to pump entrance

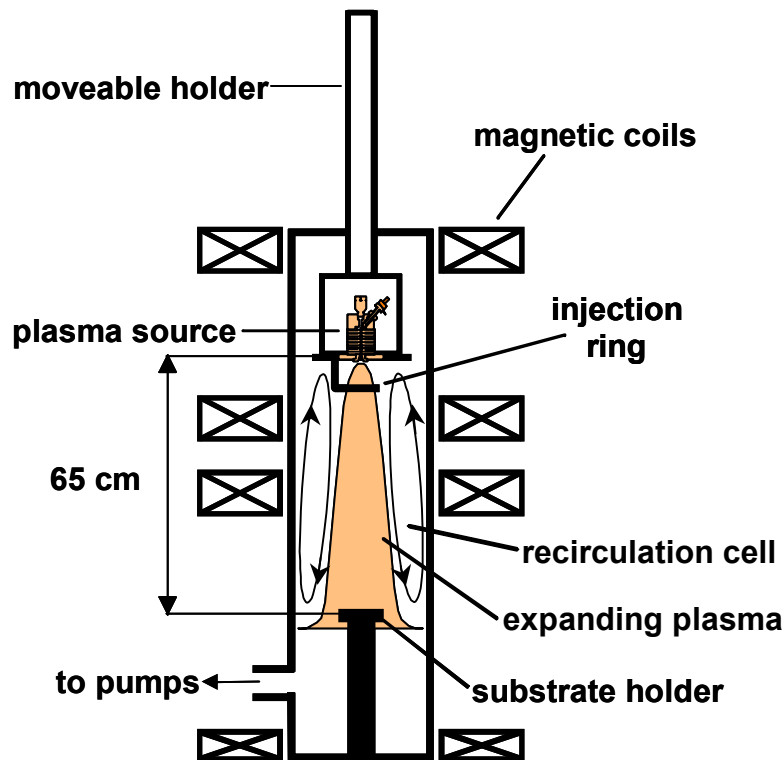


Figure 4.4: *The expanding thermal plasma setup.*

The Langmuir probe as well as the Pitot probe have been mounted on a manually moveable holder (cf. Figure 4.5), which makes it possible to position the measuring device at an axial position close to the wall of the plasma reactor as well as in the centre of the plasma. The maximum translation of the holder is 180 mm which is enough to scan the whole radius of 160 mm. The same holder has been used for both the Langmuir probe as the Pitot probe measurements and therefore the holder had to be changed when switching from one measurement to the other. Both measurements have therefore been performed at different times. The double Langmuir probe consists of two platinum wires with a diameter of 0.250 mm and an exposed length of 5.0 mm which are mounted at the end of the moveable holder. By means of an electrical feed through these wires were connected to a Keithley 2400 SourceMeter which was used to apply a voltage to the probes and simultaneously measure the current. The sourcemeter has been connected to a computer by which it is operated by means of a Labview program. The measured I-V characteristics are stored and automatically analysed by a C++ program. The Pitot probe consisted of a glass tube with an outer diameter of 5.0 mm and an inner diameter of 4.0 mm which is mounted at the end of the holder (cf. Figure 4.5). At the outside of the reactor a MKS pressure gauge (type 626AX01MDE) is mounted which has a range from 0.1 Pa to 100 Pa and an accuracy of 0.1 Pa. The pressure readout of this pressure gauge is also connected to a computer by which it is also operated by means of a Labview program. The pressure data is stored to files for post measurement data analysis. For all data shown the distance between the probe and the arc exit is chosen at 30 cm, unless otherwise stated.

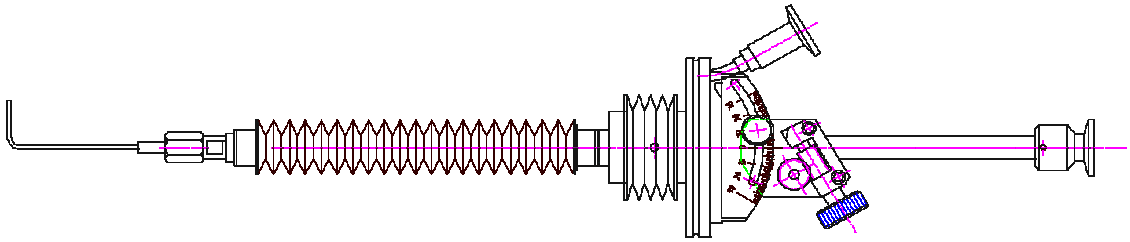


Figure 4.5: Schematic overview of the moveable vacuum holder with Pitot probe attached.

4.4 Results and discussion

First the double Langmuir probe results will be discussed after which a discussion of the Pitot probe results will be given. In the end there will be a discussion about the combination of both measurement techniques for the calculation of the ion flux.

4.4.1 Langmuir probe

The ion density and temperature can most easily be measured in the case of a pure argon plasma. In that case the effective mass of the ions is known and is equal to 40 amu. For the analysis of the double Langmuir probe measurement data it has been assumed that no argon ions have been double ionised. In Figure 4.6 an example is given of the ion density and temperature, which are considered to be equal to the electron density and temperature, of a pure argon plasma (50 sccs) for various arc current as function of the Langmuir probe position^{††}. Note that the measurements have been performed at a probe to arc exit distance which is equal to 30 cm. In Figure 4.6 it can be seen that the ion density shows a maximum in the centre of the plasma which has the highest value for the highest arc current, as expected. As can be seen ion densities of more than 10^{19} m^{-3} are obtained for this pure argon plasma. It can also be seen that at the edge of the reactor ($r=0 \text{ mm}$) there is still a considerable ion density, especially for the highest arc current. The radius of the beam does increase with increasing arc current, which can clearly be seen from the position at which the ion density is half of the maximum ion density. This is caused by the increasing ionisation degree at increasing arc currents, due to which the ambipolar diffusion coefficient of the ions in the expansion does increase. Note that in the expanding thermal plasma the ambipolar diffusion of the ions is driven by the radial gradient in the ion and electron concentrations, but that also the particle drift velocity determines the beam radius of the ions and electrons at an axial position.

The temperature as function of the probe position shows a maximum value in the centre for the lowest arc current and shows an almost constant temperature for the highest arc current. This is caused by the fact that the ions do collide with the background gas. In the case of the lowest arc current the ion density is very low close to the reactor wall, where the gas temperature is the lowest. Therefore the ion temperature will be low too. In the case of the highest arc current there is still a significant amount of ions present close to the reactor wall, which will have a higher temperature because the total power input into the reactor is higher than in the case of the lowest arc current. The temperature in the centre of the plasma beam is

^{††} Position 0 mm is at the edge of the reactor and position 160 mm is the centre of the reactor.

almost independent of the arc current, which indicates that the temperature of the ions is determined by the plasma source and not by the total power input. More power results in more ions not in another temperature. The value of the temperature is small (<0.3 eV) and therefore the dissociative power of the electrons will be small in the case that any molecular gas is injected into the pure argon plasma.

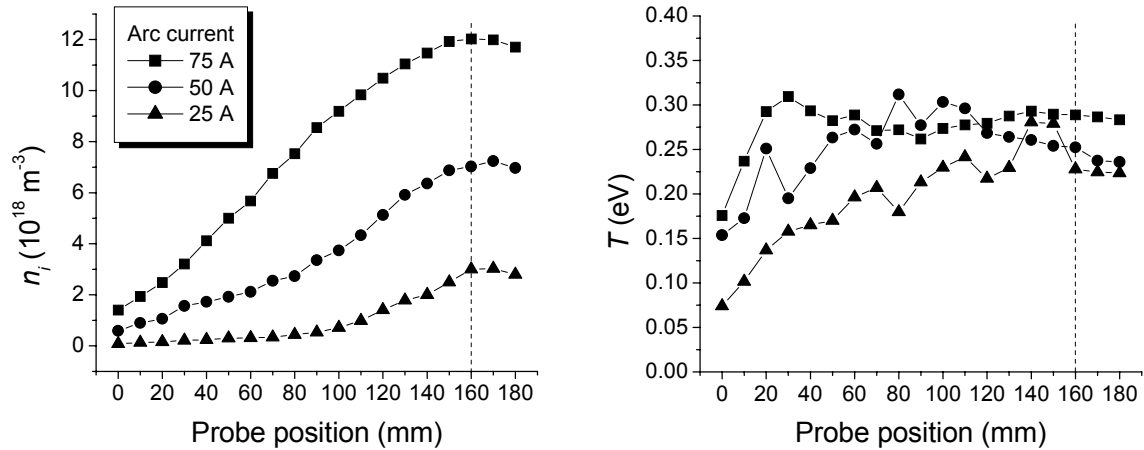


Figure 4.6: Ion density and temperature as function of the probe position for various arc currents; argon flow = 50 sccs.

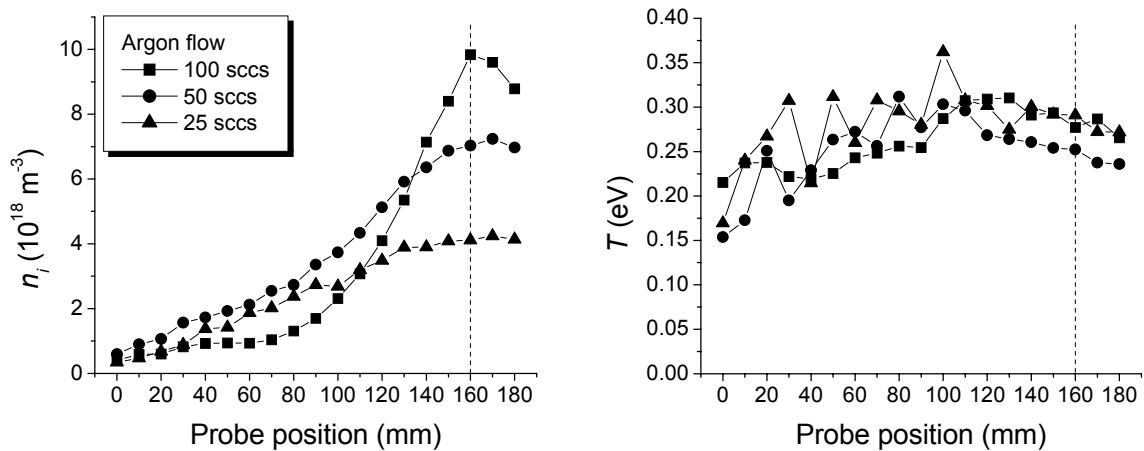


Figure 4.7: Ion density and temperature as function of the probe position for various argon flows; arc current = 50 A, fixed pumping capacity.

In Figure 4.7 the ion density and temperature are given for a pure argon plasma at fixed arc current (50 A) for various argon flows. First it can be seen that the temperature profile in the reactor is weakly dependent on the argon flow, which again indicates that the temperature is dominated by the plasma source and not by the total power input. Secondly, it can be seen in Figure 4.7 that the highest value for the ion density in the centre of the plasma is obtained at the highest value of the argon flow. This is caused by two mechanisms. First, due to the increased argon flow and a fixed pumping capacity, the pressure inside the plasma reactor does increase, which reduces the ambipolar diffusion of the ions in the expansion. Second, the ionisation efficiency in the arc will become better at higher argon flows, because

then the pressure in the arc is higher. Due to this the transfer efficiency of energy from the arc to the plasma is higher too. The first mechanism also results in a different plasma beam diameter for the various flows.

In Figure 4.8 the ion density and temperature are given for a pure argon plasma at fixed arc current (50 A) for various argon flows, but at a fixed background pressure (32 Pa). Again it can be seen that the temperature is almost independent of the argon gas flow. For the ion density as function of the probe position it can be seen clearly that the ion beam radius is independent of the argon flow, which shows that the ambipolar diffusion is, aside from the total number of ions, mainly determined by the background pressure. Comparison of the ion density profile for the various argon flows shows that the profiles obtained at 50 sccs, 75 sccs and 100 sccs are almost identical but different from the profile obtained at 25 sccs. This illustrates that the energy transfer efficiency, used for ionisation, between the arc cathodes and the plasma in the arc is dependent on the argon flow, but when increasing the argon flow above a certain level this ionisation transfer efficiency becomes independent of the argon flow.

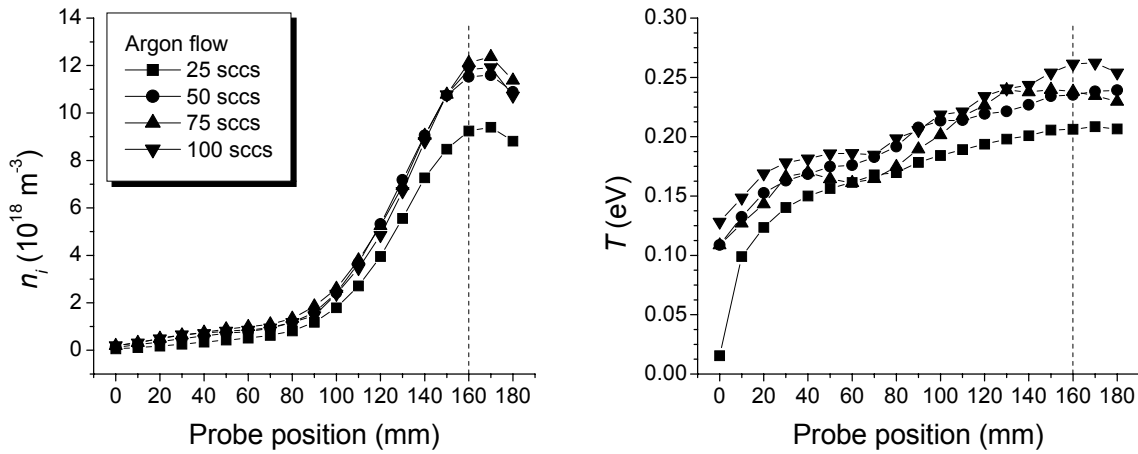
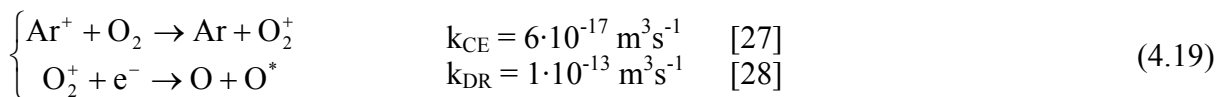


Figure 4.8: Ion density and temperature as function of the probe position for various argon flows at fixed background pressure; arc current = 50 A, $p_{\text{reactor}} = 32 \text{ Pa}$.

Now that the ion density profile of the pure argon plasma is known, oxygen has been injected into the argon plasma by the punctured ring at 5 cm from the arc exit. Addition of oxygen could cause a change in the effective ion mass, which is needed for calculation of the ion density (cf. Eq. (4.3)). It has been shown that the temperature of the pure argon plasma is too low to cause electron impact dissociation of the oxygen molecules. The dissociation of oxygen has to be by means of a charge exchange reaction and a dissociative recombination reaction with an argon ion and an electron respectively. This results dominantly in the following reaction mechanism [14]:



where O^* indicates an oxygen metastable. It can be seen that the reaction mechanism results in the dissociation of molecular oxygen into two oxygen radicals. The reaction rate for

dissociative recombination is orders of magnitude higher than that of the charge exchange reactions, therefore the density of the O_2^+ ion will be low with respect to the argon ion density for significant argon ion densities ($\geq 10^{18} \text{ m}^{-3}$). When also assuming that no O^+ ions are created by means of e.g. charge exchange of an argon ion and an oxygen radical, it is valid to take the effective mass of the ion equal to the mass of the argon ion (40 amu).

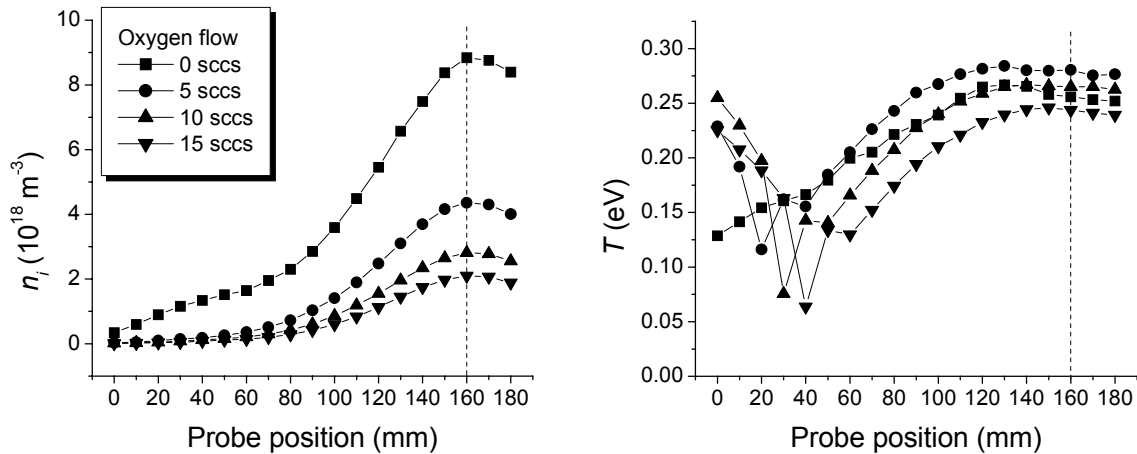


Figure 4.9: Ion density and temperature as function of the probe position for various oxygen flows at fixed background pressure; arc current = 50 A, argon flow = 50 sccs, $p_{\text{reactor}} = 23 \text{ Pa}$.

It has been shown that changing the background pressure changes the diffusion profile of the argon plasma, therefore addition of oxygen has been done at constant background pressure. In Figure 4.9 the ion density and temperature profile are given for various oxygen flows injected into a pure argon plasma (50 sccs, 50 A). It can be seen that the ion density does decrease with an increase in the injected oxygen flow. This is as expected by the fact that argon ions and electrons react with the molecular oxygen. Looking more closely at Figure 4.9 it can be seen that the ion beam radius does decrease with increasing oxygen flow, which suggests that the oxygen mainly reacts with ions that are situated at the outside of the plasma beam. This makes perfect sense because the molecular oxygen is injected by means of a ring and therefore the ions on the outside of the beam will be the first to encounter the injected oxygen. Molecular oxygen present in the background gas can also only react on the outside of the argon plasma beam. Similar observations have been made by Meulenbroeks [29] and Mazouffre [30] for hydrogen.

The temperature profile is slightly affected by the injection of oxygen. The higher temperature measured close to the wall of the reactor are due to the small ion density at this position which makes it impossible to calculate the temperature accurately from the measured Langmuir probe I-V characteristic, although the ion density itself can be calculated accurately. This is because the calculated temperature is based mainly on the derivative of the I-V curve at $V=0$ (cf. (4.13)) and the ion density is based mainly on the current at high voltage (cf. (4.3)). For the used Langmuir probe accurate temperature measurements can be done only when the ion density is higher than $3 \cdot 10^{17} \text{ m}^{-3}$. The shape of the temperature profile does not change dramatically, however it does shift in absolute value. When only looking at the temperature in the centre of the plasma beam as function of the oxygen flow (cf. Figure 4.10), it can be seen that the highest temperature is obtained at an injected oxygen flow of 5 sccs. A similar maximum has been observed before in the etch rate while etching photoresist [14] and

the post treatment of carbon containing silicon oxide film using an argon-oxygen plasma in the same reactor [31]. However it has been shown that the change in temperature is not the cause of the maximum observed with the treatment of films by means of an argon-oxygen plasma.

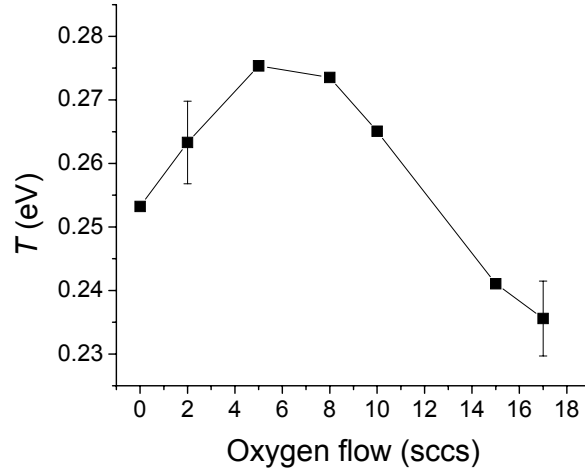


Figure 4.10: The ion temperature at the central axis as function of oxygen flow at fixed background pressure; arc current = 50 A, argon flow = 50 sccs, $p_{reactor} = 23$ Pa.

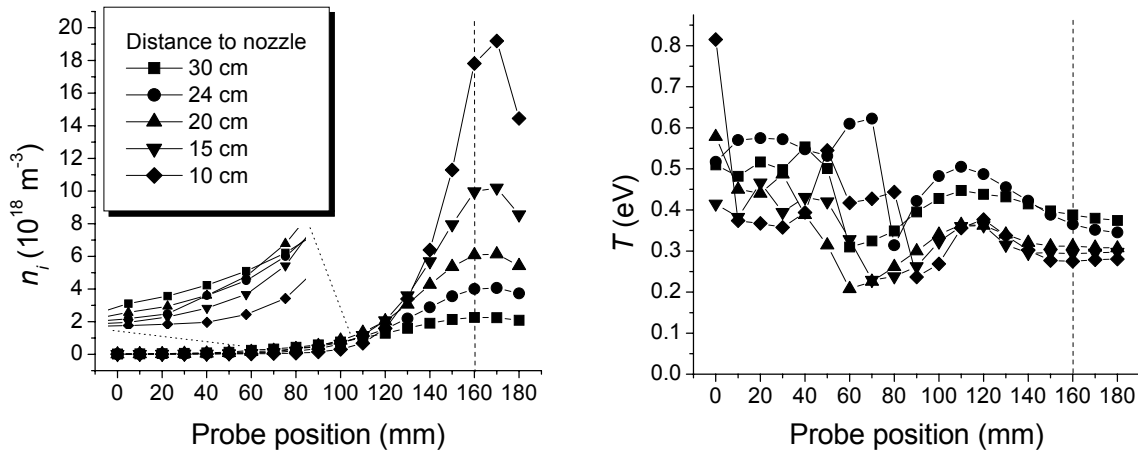


Figure 4.11: The ion density and temperature as function of the probe position for various distances to the arc exit; arc current = 50 A, argon flow = 50 sccs, oxygen flow = 10 sccs, $p_{reactor} = 20$ Pa.

To obtain a more clear picture of the interaction of molecular oxygen with the argon plasma, it is useful to investigate the ion profile as function of the distance to the plasma source exit. In Figure 4.11 the ion density and temperature have been given at various distances from the arc exit. In Figure 4.11 it can be seen that the ion density is decreasing as function of the distance to the arc exit. Two mechanisms are responsible for the loss of the ions and electrons. Firstly because the argon plasma is expanding, the plasma beam diameter is increasing. Secondly because the argon ions and electrons are reacting with the injected molecular oxygen. The first mechanism is best illustrated at the edge of the plasma beam

(probe position 60 – 100 mm), which has the highest ion density for the largest distance. The reaction with oxygen can best be observed in the temperature profile. Here again the temperatures calculated for ion densities below $3 \cdot 10^{17} \text{ m}^{-3}$ are inaccurate and should not be considered as the real temperature. It can be seen clearly that the temperature shows a maximum not on the central axis of the plasma beam, but at the edge of the plasma beam. The maximum is moving towards the reactor wall when the distance between the arc exit and the measuring position is increased. The fact that the temperature increases when the argon plasma is reacting with molecular ions indicates that the reaction mechanism is exothermic. Comparing the temperature profile obtained at 24 cm with the one obtained at 30 cm shows that the temperature in the centre of the plasma beam is increasing whereas the temperature at the edge of the plasma beam is decreasing. This means that the heat produced in the reactions with oxygen is distributed evenly in the plasma beam by heat transfer. This explains why the temperature does increase on the central axis at 30 cm, however it does not explain the maximum yet.

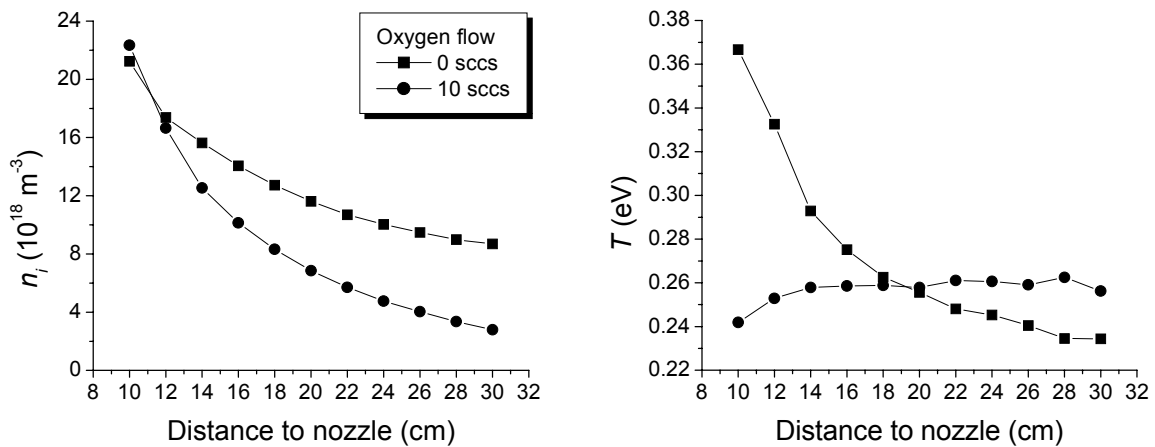


Figure 4.12: The ion density and temperature on the central axis with and without the addition of oxygen for various distances to the arc exit; arc current = 50 A, argon flow = 50 sccs, $p_{\text{reactor}} = 22.5 \text{ Pa}$.

To get more understanding in why the maximum is there, a more detailed study of the ion density and temperature at the central axis as function of the distance between arc exit and measuring position is needed. The ion density and temperature as function of distance to the arc exit with and without addition of oxygen are shown in Figure 4.12. In this figure it can be seen that the ion density in the case that oxygen is added to the plasma decreases more rapidly than in a pure argon plasma. This is due to the reactions of molecular oxygen with the argon ions and electrons. Even more interesting are the temperature measurements. For the pure argon plasma the temperature does decrease as function of the distance to the arc exit. Just as is expected from central energy input and heat conduction to the wall. However when oxygen is added to the plasma the temperature becomes almost independent of the distance to the arc exit. The temperature with addition of oxygen has a lower value compared to the pure argon situation up to a distance of 18 cm, whereas the temperature has a higher value for a distance higher than 18 cm. This indicates that the injection of oxygen, which is at room temperature, does cool the plasma. Reaction of oxygen with argon ions and electrons cause the temperature of the plasma to increase with respect to the adiabatic cooling observed in a pure argon

plasma. Eventually the temperature reaches a value above the pure argon plasma temperature. The maximum observed in the temperature, on the central axis, as function of the added oxygen flow is therefore caused by a mixture of cooling due to the addition of the cold gas and heating due to the interaction of oxygen molecules with the argon ions and electrons. The fact that the temperature, for the case shown, is almost independent of the distance to the arc exit is merely based on coincidence. Notice that the heat conductivity of pure argon is worse than that of an argon-oxygen mixture, which will also play a role in the observed trend.

4.4.2 Pitot probe

By means of Eq. (4.18) the total ion flux can be calculated when the ion density and the particle drift velocity is known. In the previous part the ion density has been derived from Langmuir probe measurements. Now the particle drift velocity will be derived from Pitot probe measurements. Although the main purpose of the Pitot probe measurements is to calculate the particle drift velocity profile also some phenomenon which are caused by the Pitot probe will be discussed.

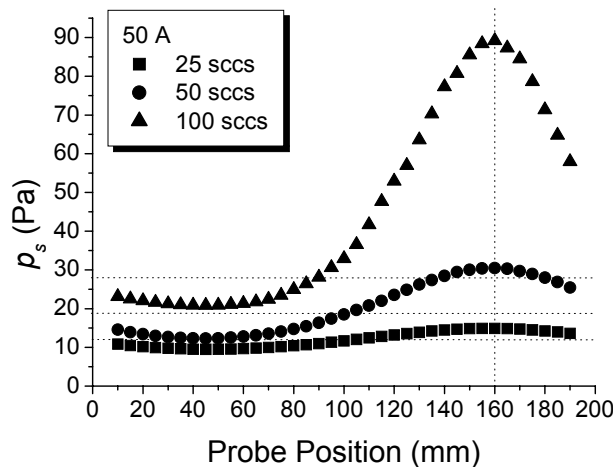


Figure 4.13: Stagnation pressure as function of probe position for various argon flows.

In Figure 4.13 some typical stagnation pressures (p_s) as function of the Pitot probe position for various argon flows are given. The Pitot probe opening is directed towards the plasma source exit. The background pressure (p_o), measured in the pump line, is 10.7, 17.0, and 27.5 Pa for an argon flow of 25, 50, and 100 sccs respectively. It can be seen in Figure 4.13 that as function of the probe position stagnation pressures are measured which are above and below the background pressure. According to Eq. (4.15) and Eq. (4.16) the measured stagnation pressure will always be higher than the background pressure, but the Pitot probe theory is only valid when the opening in the Pitot probe is directed towards the flow. Therefore the measured stagnation pressure below the background pressure can only be due to a particle drift velocity which is not in the direction of the Pitot probe opening but in the opposite direction. The fact that the particles close to the wall have a velocity opposite to the particles in the centre of the plasma is because a recirculation cell is formed on the outside of the plasma beam (cf. Figure 4.4), which is a known phenomenon [32,33]. Because the Pitot probe theory is not valid for flows which are not in the direction of the opening of the Pitot

probe, the tube needs to be rotated in such a way that the flow is in the direction of the opening again before the stagnation pressure can be measured accurately. Since the Pitot probe measurements are performed halfway between the arc exit and the substrate holder, the flow will be mainly in forward or in reverse direction and no substantial radial component will be present. Therefore the Pitot probe rotation angle has been taken equal to 180° .

In Figure 4.14 the stagnation pressure measured with a rotated Pitot probe is shown (reverse). Also in Figure 4.14 the stagnation pressure measured with the normal (forward) Pitot probe and a straight probe (straight) are shown. A straight probe is no more than a normal Pitot probe which has been cut just before the 90° angle, which will cause the opening of the tube to be perpendicular to the flow direction. For low particle drift velocities ($M < 0.1$) this will measure the local background pressure. For high particle drift velocities the flow along the opening of the tube could cause a pressure decrease in the straight probe.

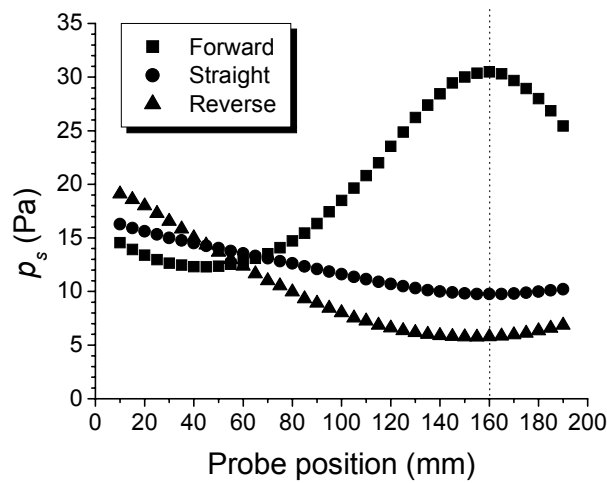


Figure 4.14: Stagnation pressure as function of probe position for forward and reverse probe positioning and the measured pressure using a straight probe; argon flow = 50 sccs and arc current = 50 A.

In Figure 4.14 it can be seen that the stagnation pressure for the forward Pitot probe and the reverse Pitot probe do have a common point. This common point is where the particles will have no velocity. According to the theory the stagnation pressure will be equal to the background pressure when the particles have no velocity and therefore also the straight probe should measure the same pressure at that position. This is however not the case, which is caused by the fact that the position in the plasma, with respect to the arc exit, is not the same in the forward, reverse and straight case. The difference in distance from the arc exit between the forward and reverse Pitot probe is approximately 6 cm and the straight probe is positioned halfway the forward and the reverse Pitot probe. As the plasma beam is expanding, the diameter of the plasma beam will increase as function of the distance from the arc exit and therefore the position at which the particles will have no drift velocity will move further away from the centre of the reactor with increasing distance from the arc exit. So the probe position at which the particle drift velocity is equal to zero in the case of the reverse Pitot probe will be further away from the centre of the plasma beam than in the case of the forward Pitot probe. It is therefore better to take the intersection of the measured pressure with the straight probe and

the stagnation pressure as the position where there is no velocity, although here also a small error will be made due to the difference in measuring position.

The Pitot probe measurements show the highest stagnation pressure in the centre of the plasma beam. From laser induced fluorescence (LIF) experiments the particle drift velocity in the centre of the plasma beam is known to be subsonic at the axial measuring position [34,35,36]. Therefore according to Eq. (4.15) the maximum stagnation pressure possible is approximately two times the background pressure ($M=1, \gamma=5/3$). In Figure 4.13 for an argon flow of 100 sccs a stagnation pressure of approximately 80 Pa is measured at a background pressure of only 27.5 Pa, which makes the stagnation pressure almost three times the background pressure. According to the theory this indicates that the velocity should be supersonic which is in contradiction with the LIF experiments. This means that either the LIF experiments are incorrect, or the Pitot probe causes an effect which is not accounted for in the Pitot probe theory. LIF experiments are very accurate and there is no doubt on the values obtained, furthermore in the past the velocities obtained by LIF experiments were verified by modelling of the plasma [37]. Therefore the high value of the measured stagnation pressure should be due to an unaccounted effect in the Pitot probe theory.

It should be noted that the Pitot probe theory is only valid when the gas comes to a standstill in an isentropic manner. When this is not the case, various effects are known to influence the measured stagnation pressure by means of Pitot probes. Barker [38] was one of the first to discover that for low Reynolds numbers ($Re < 100$) viscous effects increase the impact pressure above its expected value (cf. Eq. (4.15) and Eq. (4.16)). For hot gases this effect has been observed experimentally [39]. A second effect that makes the measured stagnation pressure deviate from the Pitot probe theory is heat transfer from the plasma to the probe or otherwise. Because the Pitot probe is connected to the outside of the plasma reactor it will in general have a lower temperature than the plasma and therefore a strong temperature gradient will exist close to the Pitot probe. According to Barkan and Whitman [40] these temperature effects start to play a role in similar conditions as where the viscous effects start to become non-negligible. In the plasma used the Reynolds number is low and therefore both these effects cannot be neglected. A third effect is known to cause wrong velocities to occur when bluntly using the Pitot probe theory to calculate the velocity. This effect is caused by the assumptions made for the background pressure. In general it is assumed that the plasma reactor is isobaric, which is not always the case. Therefore measuring the background pressure through a hole in the wall of the reactor or in the pump line does not give the local background pressure. In Figure 4.14 it can be seen that when using a straight probe a non constant pressure is measured as function of the probe position, even in the regime where $M < 0.1$, which indicates that the pressure inside the reactor is non isobaric. However from experiments by Meulenbroeks [32], using a similar reactor, it is known that the pressure is only slightly non-isobaric (<5 %), due to which this effect does not apply for the used setup.

Simulations by Magin *et al.* [41] showed that the viscosity and temperature effect have a positive influence on the measured stagnation pressure. Magin *et al.* also showed that the temperature effect becomes less when the temperature difference between the plasma and the Pitot probe becomes less. In Figure 4.15 the measured stagnation pressure in the centre of the plasma as function of time for changing plasma conditions (argon flow and arc current) is shown. It can be seen that the stagnation pressure does decrease when the arc current is increased at fixed argon flow. This means that when the arc current is increased the temperature difference between the plasma and the Pitot probe will decrease which is possible because the Pitot probe is uncooled. A quick measurement of the Pitot probe temperature by

means of a thermocouple showed that the temperature of the Pitot probe does increase when increasing the arc current due to which the temperature difference does decrease. The experiment shown in Figure 4.15 therefore reveals that in the plasma studied this temperature effect can not be neglected.

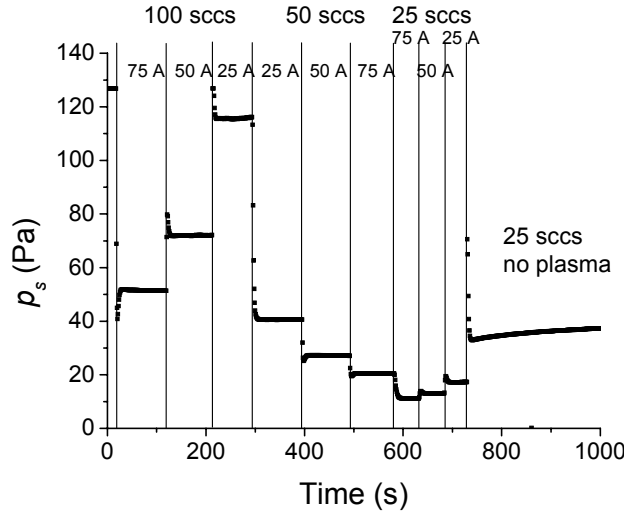


Figure 4.15: Stagnation pressure at fixed position as function of time for changing plasma parameters.

In the appendix of this chapter a rough estimation of the pressure change (Δp) due to insertion of a Pitot probe into the flow, present in the plasma reactor, has been made using the momentum balance for the neutral argon gas, i.e. ionisation is considered to be low. This estimation has been made neglecting any temperature gradients and any effects caused by the charged particles. The result of the estimation is given by:

$$\frac{\Delta p}{p_o} \propto \frac{1}{2} \left(\frac{v_z}{v_{th}} \right)^2 + \frac{\lambda^2}{R_p^2} \frac{v_z}{v_{th}} \quad (4.20)$$

where v_z is the particle drift velocity in the axial direction, v_{th} is the thermal velocity, λ is the mean free path, and R_p is the Pitot probe radius. For background pressures used in the plasma reactor (10 to 30 Pa) the mean free path of the particles in the plasma is of the same order or larger than the probe radius. This causes the viscous term (second term) to become non-negligible, which is in agreement with the measurements. According to Eq. (4.20) the pressure change will increase when the probe radius is decreased. Nevertheless experiments however show that the pressure change decreases with decreasing probe radius. A decrease in probe radius however, also results in an increase in the temperature of the probe tip and thus a decrease in temperature difference between plasma and probe tip. Therefore the temperature effect decreases which could cancel the effect shown by Eq. (4.20).

It has been shown that in the plasma studied, simply calculating the particle drift velocity from the measured stagnation pressure is not possible. However, the Pitot probe measurements can still be useful. First of all the position at which the particles have no velocity can easily be determined as already has been shown. Second the velocity can still be

calculated using the reverse Pitot probe, because a useable value is obtained between the reactor wall and the position where the particles have zero drift velocity. In this region the particle density is relatively high and therefore the viscous effects will be minimal. Also in this region the gas temperature will be relative low and therefore the temperature difference will be small. It is therefore safe to assume that the temperature effect on the stagnation pressure, in this outer region of the reactor, will be small.

4.4.2.1 Recirculating flow

As observed by means of Pitot Probe measurements, a recirculation cell exists in the flow pattern of the expanding thermal plasma. This recirculation cell has a interaction with the plasma beam in the centre. Therefore species injected into the beam by means of the injection ring (e.g. deposition precursors) will diffuse into the recirculation cell. This will cause these particles to recirculate to the point where the plasma expands into the plasma reactor. Particles present in the recirculation cell can also diffuse into the expanding plasma beam, and therefore the total amount of gas which enters the plasma beam is not equal to the amount injected by means of the injection ring, but there will also be a contribution by precursor species present in the recirculation cell.

Combination of the velocity profile measured at the edge of the reactor obtained from Pitot probe measurements with the LIF measurements performed by various people [34,35,36] in the centre of the plasma it is possible to generate the velocity profile when some assumptions are made. In the case of the expanding thermal plasma source the forward velocity profile can be assumed to be parabolic in shape up to the point at which the velocity is equal to zero. For the outer part of the velocity profile the Pitot probe data can be used. The velocity profile ($v(r)$) obtained by doing this is shown in Figure 4.16. Notice that using the Pitot probe data results in a velocity which is not equal to zero at the reactor wall. By making a reasonable assumption of the temperature profile^{‡‡} ($T(r)$), from which the total particle density profile ($n(r)$) follows, the forward flow fraction (κ_{for}) can be calculated. $T(r)$ and $n(r)$ are shown in Figure 4.16. The forward flow fraction is the total forward particle flow (ϕ_{for}) relative to the total injected particle flow (ϕ_{inj}) and is given by:

$$\kappa_{for} = \frac{\phi_{for}}{\phi_{inj}}, \quad (4.21)$$

with:

$$\phi_{for} = 2\pi \int_0^{R'(v=0)} n(r) \cdot v(r) \cdot r dr . \quad (4.22)$$

In Figure 4.16, T_{max} and v_{max} are the particle temperature and velocity in the centre of the plasma as derived from LIF experiments. Because of the setup used, gas injection at the top and pumping at the bottom, the reverse particle flow is always equal to the forward particle

^{‡‡} The temperature profile is also assumed to be parabolic, which is in good agreement with temperatures measured using a free floating thermocouple.

flow minus the injected flow. Note that when there would be no recirculation the forward flow fraction is equal to unity.

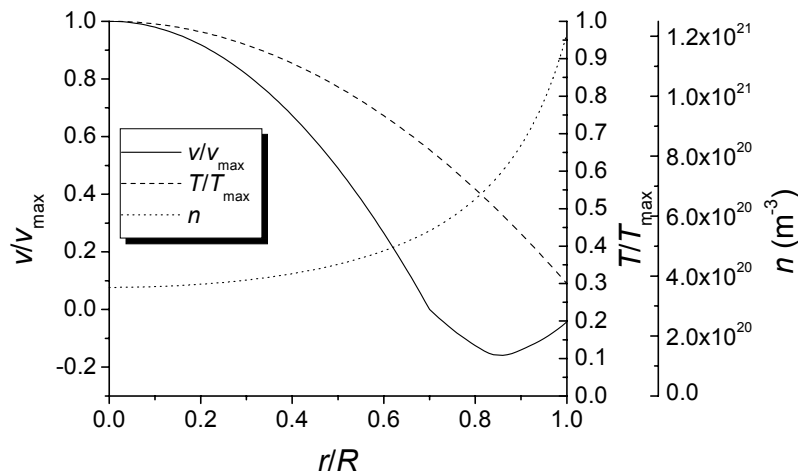


Figure 4.16: Model density, temperature and velocity as function of the relative radius (r/R). Density for $T_{max} = 2000$ K and $p = 10$ Pa.

In Table 4.2 the forward flow fraction for various plasma conditions is given. It can be observed that the forward flow fraction is significantly different from unity and depends strongly on the argon flow. Because the measurements at different argon flows are performed at different background pressures, the dependency of the forward flow fraction on the argon flow is probably mainly determined by this difference. Increasing the argon flow increases the background pressure, but doubling the argon flow does not double the background pressure, and therefore the flow beam radius decreases with increasing argon flow. As a result, the contact surface between the main beam and the recirculation cell will decrease with increasing argon flow. This will cause the particles in the recirculation cell to move slower and therefore the effective forward flow in the recirculation cell, and with this the forward flow fraction, will be smaller.

Table 4.2: Forward flow fraction for various argon flows in the arc (ϕ_{Ar}) and arc currents (I_{arc}).

I_{arc} \ ϕ_{Ar}	25 sccs	50 sccs	100 sccs
0 A	2.13	1.65	1.21
25 A	4.73	2.57	1.59
50 A	3.59	2.33	1.52
75 A	2.56	2.14	1.42

It is clear from Table 4.2 that starting the plasma increases the forward flow fraction significantly. The observed increase is probably due to a better coupling between the injected particle beam and the background gas in the case that ions are present in the beam. However, the highest forward flow fraction is observed at the lowest arc current. This can be explained by the fact that at the lowest arc current the ion beam radius is the smallest (cf. Figure 4.6) and therefore the smallest amount of ions diffuse into the recirculation part of the recirculation cell. At higher arc currents, the plasma beam radius is larger and more ions and

electrons will diffuse into the recirculation part of the flow pattern. These ions and electrons slow down the gas in the recirculation cell and therefore the total gas flow in the recirculation part of the recirculation cell is reduced and consequently also the forward flow fraction is decreased.

It has been shown that the amount of gas present in the recirculation cell is of the order of the used argon gas flow in the arc. Therefore when injecting a precursor into the plasma beam by means of the injection ring, a significant amount will recirculate. This means that when new stable species are generated in the plasma beam [42] these will also recirculate and enter the plasma beam upstream where they can react with the argon plasma. However a significant part of the new stable species will be pumped away and the species that did recirculate by means of the recirculation cell still need to enter the plasma beam by means of diffusion. Therefore the total amount of stable species which enter the plasma beam will most probably still be small with respect to the amount of precursor injected by means of the injection ring.

4.5 Combination of Langmuir probe and Pitot probe measurements

Combining the Langmuir probe measurement and the Pitot probe measurements the ion flux can be calculated by means of Eq. (4.18). The ion flux as function of the argon gas flow in the arc for various arc currents at constant background pressure is shown in Figure 4.17. An interesting phenomenon which can be seen in Figure 4.17 is that the total ion flux from the arc is increasing with an increase in the total argon flow used in the arc up to a certain level and above this level the ion flux does not change significantly anymore with a change in the total argon flow. This can be explained by the arc efficiency [37,43]. With an increase in the argon flow through the arc also the pressure inside the cathode housing of the arc increases. At a higher pressure in the cathode housing the energy transfer coefficient from the cathodes to the argon gas will be better with respect to a lower pressure. For flows up to 40 sccs this energy transfer efficiency still increases, however for an additional increase of the argon flow there will be no more increase in the efficiency, causing the ion flux to saturate.

Another trend which can be seen in Figure 4.17 is that the ion flux increases with increasing arc current, which is logical because at higher arc current more power is put into the arc plasma and therefore more ions and electrons are created. From only the ion density in the centre of the beam (cf. Figure 4.6) this trend was already observed. Looking more careful at the ion flux as function of the arc current at a fixed argon flow above the saturation level (cf. Figure 4.17), it can be seen that the ion flux seems to have a quadratic behaviour. Because the ion flux is only derived at three different arc currents no certainty about a real quadratic behaviour can be given. When this result is compared to the result obtained by Gielen [44] with the same plasma source, a clear distinction can be seen. In his case the ion flux had a linear trend with the arc current. Gielen, however, never used the particle drift velocity to calculate the ion flux but only the ion density and an assumption for the ion flux at a specific arc current and argon flow. Moreover Gielen did not measure the ion density profile up to the wall of the reactor, but only a small fraction of it close to the centre of the plasma. Doing the same with the measurements shown in Figure 4.6 would also lead to a linear behaviour, explaining the conclusion found by Gielen. The total ion flux found by Gielen, 10 sccs of argon ions at 48 A arc current and 100 sccs of argon gas in the arc, is much higher than found

in this work. Here the value for the same plasma settings is less than a quarter of that value, however still the ionisation degree is high (0.5 % and higher). Taking into account the total ion and the velocity profile gives more accurate results even though a part of the velocity profile had to be assumed.

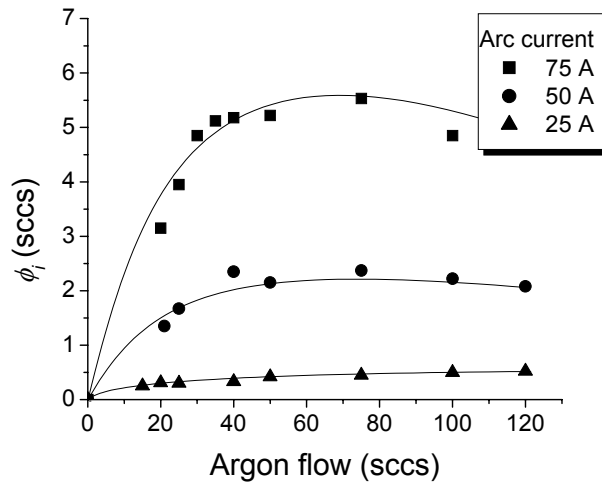


Figure 4.17: Ion flux as function of argon flow for various arc current at fixed background pressure ($p_{reactor}=32 Pa$).

Addition of oxygen to the argon plasma does not change the total ion flux which is emanated by the arc, but it does change the ion flux at the position where the ion density profiles have been obtained. In Figure 4.18 the ion flux at 30 cm from the arc exit as function of the injected oxygen flow is shown. From this figure it can be seen clearly that the ion flux decreases with increasing oxygen flow. Addition of oxygen flows equal to several times the ion flux does not lead to the full depletion of all ions, which could be an indication that oxygen mainly reacts at the edge of the plasma beam and that in the centre of the beam mainly argon is present and no oxygen. Close to the substrate, oxygen can be diffused up to the centre of the plasma beam, also consuming the argon ions present there.

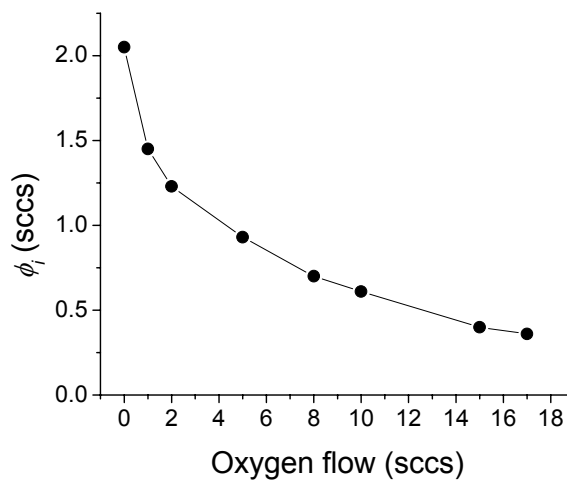


Figure 4.18: Ion flux at fixed argon flow as function of oxygen addition; argon flow = 50 sccs, arc current = 50 A.

In Figure 4.19 the ion flux as function of the distance to the arc exit is shown in the case with and without addition of oxygen. It can be seen that in the case that oxygen is added to the plasma the ion flux decreases as function of the distance to the arc exit, as expected. Although the oxygen is injected by a ring which is located at 5 cm from the arc exit, extrapolation of the ion flux with addition of oxygen indicates that the ion flux starts to decrease at 8 cm from the arc exit. This indicates that the oxygen probably enters the plasma no sooner than 8 cm from the arc exit. The ion flux when no oxygen is added to the plasma is independent of the distance to the arc exit, which indicates that there is no recombination between argon ions and electrons in the plasma beam. This has already been observed before by van de Sanden [45]. The ion flux obtained at 30 cm is slightly lower than the ion flux obtained closer to the exit of the arc. This is probably due to loss of argon ions and electrons at the wall of the reactor. In Figure 4.19 also the plasma beam radius is shown. The plasma beam radius presented is the radius at which the ion density is e^{-1} times the ion density in the centre of the plasma. It can be seen that the radius increases with distance to the arc exit and that the radius is smaller in the case oxygen is added to the plasma with respect to the case that no oxygen is added. Notice that the ion beam radius is independent of the radius in which the gas flows in the forward direction and thus the flow pattern does not need to be affected by addition of oxygen.

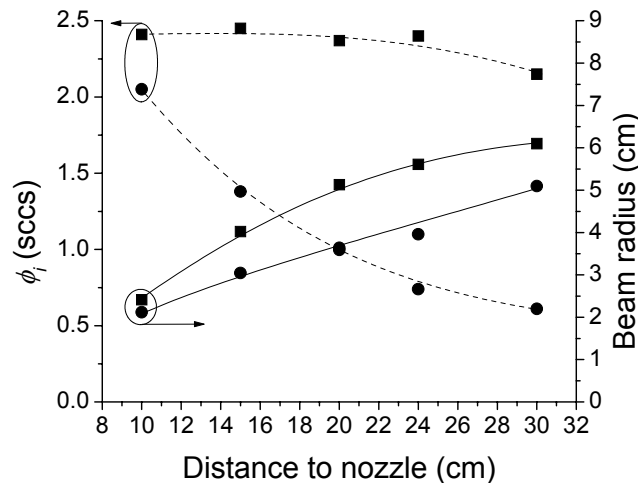


Figure 4.19: Ion flux as function of the distance to the nozzle with (10 sccs) and without addition of oxygen; argon flow = 50 sccs, arc current = 50 A.

4.6 Conclusions

- Langmuir probe

From the Langmuir probe measurements it can be concluded that the expanding thermal plasma generated by means of a cascaded arc generates high ion densities ($>1 \cdot 10^{19} \text{ m}^{-3}$) and low ion and electron temperature (couple of tenths of eV). Detailed profiles are now available which confirm results shown before by various authors [14,26,45,46]. A new observation from the Langmuir probe measurements is that addition of oxygen causes the

ion and electron temperature of the plasma to increase by exothermic reactions, but it also causes the ion and electron temperature to decrease by the addition of cold gas. From the combination of both effects it can clearly be seen in Langmuir probe measurements that the reaction between oxygen molecules and argon ions mainly occurs at the edge of the expanding argon plasma beam.

The ion diffusion profile is mainly dependent on the background pressure in the expansion vessel and the arc current. Increasing the arc current will cause the ion diffusion to occur faster and increasing the background pressure will reduce the plasma beam diameter. Changing the argon gas flow in the arc does not change the diffusion profile when the background pressure is kept constant.

- **Pitot probe**

From Pitot probe measurements it can be seen clearly that there is a recirculation cell in the flow pattern of the expanding thermal plasma. This recirculation cell probably extends along the full length of the reactor. Pitot probe measurements are an easy method to make the flow pattern visible qualitatively. Quantitatively Pitot probe measurements in an expanding thermal plasma are less straightforward. Due to various effects, the measured stagnation pressure is higher than the value expected on basis of the conventional Pitot probe theory. These effects have been identified qualitatively, however it has not been possible to quantify them. Nevertheless the data obtained by means of Pitot probe measurements can be used to calculate the velocity in the regime where the gas temperature is close the Pitot probe temperature and where the particle density is relatively high. This is close to the reactor wall in the recirculating part of the recirculation cell. For the other part of the velocity profile an estimation of the velocity has to be made based on velocity data obtained by other means. With this velocity profile it is possible to calculate the forward flow fraction. This quantity has been found to be significantly different from unity and mainly dependent on argon flow because that determines the flow pattern. The presence of ions causes the forward flow fraction to increase significantly which is caused by the coupling between ions and neutral gas.

- **Combination of Langmuir probe and Pitot probe measurements**

With the derived velocity profile and ion density profile the ion flux emitted by the arc source can be calculated. The ion flux is dependent on both arc current and argon flow. The energy transfer efficiency of the arc to the gas is increasing with increasing argon flow, but reaches a maximum for an argon gas flow of approximately 40 sccs. Above this no more ions are generated by the cascaded arc and thus the plasma ionisation degree does decrease with increasing argon flow. In the range from 25 A to 75 A the ion flux has a quadratic behaviour on the arc current and not a linear one as was shown by Gielen [44]. However Gielen did not use the velocity profile and therefore the measurements presented here are more accurate.

Addition of oxygen to a pure argon plasma does not decrease the ion flux from the plasma source, but due to reaction of oxygen molecules with argon ions and electrons the number of ions downstream decreases. A decrease in the ion flux is not observed downstream in a pure argon plasma, from which it can be concluded that the argon ions in the expanding thermal plasma do not recombine with electrons. So in a pure argon plasma the main loss process is at the wall of the reactor. This had been shown before by van de Sanden [45]

Appendix

Consider the momentum balance for the neutral gas:

$$\nabla p = -nm(w \cdot \nabla)w - \nabla \cdot \Pi \quad (\text{A.1})$$

where m is the particle mass, n the neutral particle density, w the particle drift velocity, p the pressure, and Π the viscosity tensor. For the axial direction, in cylinder coordinates Eq. (A.1) can be written as:

$$\frac{\partial p}{\partial z} = -nmw_z \frac{\partial w_z}{\partial z} - (\nabla \cdot \Pi)_z \quad (\text{A.2})$$

with^{§§} [47]

$$(\nabla \cdot \Pi)_z = -\frac{1}{r} \frac{\partial}{\partial r} r \eta \frac{\partial w_z}{\partial r} - \frac{1}{r} \frac{\partial}{\partial r} r \eta \frac{\partial w_r}{\partial z} + \frac{2}{3} \frac{\partial}{\partial z} \eta \frac{\partial w_r}{\partial r} + \frac{2}{3} \frac{\partial}{\partial z} \eta \frac{w_z}{r} - \frac{4}{3} \frac{\partial}{\partial z} \eta \frac{\partial w_z}{\partial z} \quad (\text{A.3})$$

Here $\eta = nkT\tau$ where k is the Boltzman constant, T the temperature and τ the collision time. Because the flow is laminar halfway between the plasma source exit and the substrate holder all radial velocity components and its derivatives can be considered to be small and will be neglected. When also assuming η to be independent of r and z , and neglecting temperature gradients Eq. (A.3) can be simplified and the total momentum balance in the axial direction becomes:

$$\frac{\partial p}{\partial z} = -\frac{1}{2} nm \frac{\partial w_z^2}{\partial z} + \frac{\eta}{r} \frac{\partial}{\partial r} r \frac{\partial w_z}{\partial r} + \frac{4\eta}{3} \frac{\partial^2 w_z}{\partial z^2} \quad (\text{A.4})$$

By substituting $\tau = \lambda / v_{th}$ with λ the mean free path and taking $v_{th} \propto \sqrt{kT/m}$ Eq. (A.4) is reduced to:

$$\frac{\partial p}{\partial z} \propto -\frac{1}{2} \frac{p}{v_{th}^2} \frac{\partial w_z^2}{\partial z} + \frac{p\lambda}{v_{th}r} \frac{\partial}{\partial r} r \frac{\partial w_z}{\partial r} + \frac{4p\lambda}{3v_{th}} \frac{\partial^2 w_z}{\partial z^2} \quad (\text{A.5})$$

The velocity gradient induced by the probe tip in the radial direction will be along a distance proportional to the probe radius ($\partial r \sim R_p$) and in the axial direction along a distance several times the mean free path ($\partial z \sim \lambda$). Now assume these gradients are linear and integrate Eq. (A.5) in the axial direction over the length in which the particles come to a standstill in front of the probe. The result of this is given by:

^{§§} Azimuthal components are neglected because of symmetry.

$$\frac{\Delta p}{p_o} \propto \frac{1}{2} \left(\frac{v}{v_{th}} \right)^2 + \frac{\lambda^2}{R_p^2} \frac{v}{v_{th}} \quad (\text{A.6})$$

where v is the undisturbed particle velocity. The third term in Eq. (A.5) cancels because the second derivative is equal to zero, and the first term changes sign because the first derivative of the squared drift velocity is negative.

References

- [1] J.M. Holland, *Modern Spectroscopy*, John Wiley & Sons Inc., New York (1987)
- [2] G.S. Selwyn, *Optical Diagnostic Techniques for Plasma Processing*, ed. by W. Weed, AVS Monographs Series, AVS Education Committee, New York (1993)
- [3] H.F. Döbele, *Plasma Sources Sci. Technol.* **9** (2000) 447
- [4] J.D. Buck, D.C. Robie, A.P. Hickman, D.J. Bamford, and W.K. Bischel, *Phys. Rev. A* **39** (1989) 2932
- [5] J. Sheffield, *Plasma Scattering of Electromagnetic Radiation*, Academic Press, New York (1975)
- [6] M.J. van de Sande, *Laser Scattering on Low Temperature Plasmas, High Resolution and Stray Light Rejection*, Ph.D. Thesis, Eindhoven University of Technology (2002)
- [7] J.D. Swift and M.J.R. Schwar, *Electrical probes for Plasma Diagnostics*, Iliffe Books Ltd., London (1970)
- [8] L. Schott, *Plasma Diagnostics*, ed. W. Lochte-Holtgraven, North-Holland, Amsterdam, (1968)
- [9] S. Katta, J.A. Lewis, and W.H. Galvin, *Rev. Sci. Instrum.* **44** (1973) 1519
- [10] M. Brossa and E. Pfender, *Plasma Chem. Plasma Proc.* **8** (1988) 75
- [11] G.M.W. Kroesen, D.C. Schram, and M.J.F. van de Sande, *Plasma Chem. Plasma Proc.* **10** (1990) 49
- [12] A.J.M. Buuron, M.C.M. van de Sanden, W.J. Ooij, R.M.A. Driessens, and D.C. Schram, *J. Appl. Phys.* **78** (1995) 528
- [13] E.W. Peterson and L. Talbot, *AIAA Journal* **8** (1970) 2215
- [14] G.J.H. Brussaard, *Remote Arc Generated Plasma in Diatomic Gases*, Ph.D. Thesis, Eindhoven University of Technology (1999)
- [15] H. Mott-Smith and I. Langmuir, *Phys Rev.* **28** (1926) 727
- [16] M. Rahmane, G. Soucy, and M.I. Boulos, *Plasma Chem. Plasma Processing* **16** (1996) 196S
- [17] J.R. Fincke, S.C. Snyder, and W.D. Swank, *Rev. Sci. Instrum.* **64** (1993) 711
- [18] A.H. Shapiro, *The Dynamics and Thermodynamics of Compressible Fluid Flow*, John Wiley & Sons Inc., New York (1953)
- [19] R.M. Young and J.J. Schreurs, *Diamond Relat. Mater.* **5** (1996) 134
- [20] M. Rahmane, G. Soucy, and M.I. Boulos, *Rev. Sci. Instrum.* **66** (1995) 3424
- [21] K.T.A.L. Burm, W.J. Goedheer, and D.C. Schram, *Physics of Plasmas* **6** (1999) 2622
- [22] J.W.A.M. Gielen, M.C.M. van de Sanden, P.R.M. Kleuskens, and D.C. Schram, *Plasma Sources Sci. Technol.* **5** (1996) 492
- [23] J.W.A.M. Gielen, W.M.M. Kessels, M.C.M. van de Sanden, and D.C. Schram, *J. Appl. Phys.* **82** (1997) 2643

- [24] A. de Graaf, *Deposition of CNH Materials; Plasma and Film Characterization*, Ph.D. Thesis, Eindhoven University of Technology (2000)
- [25] H. Mäcker, *Z. Naturforsch.* **11** (1956) 457
- [26] M.C.M. van de Sanden, J.M. de Regt, G.M. Jansen, J.A.M. van der Mullen, D.C. Schram, and B. van der Sijde, *Rev. Sci. Instrum.* **63** (1992) 3369
- [27] P. Gaucherel and B. Rowe, *Int. J. of Mass Spectrometry and Ion Phys.*, **25** (1977) 211
- [28] J.B. Hasted, *Physics of Atomic Collisions* Butterworths, Washington (1964)
- [29] R.F.G. Meulenbroeks, A.J. van Beek, A.J.G. van Helvoort, M.C.M. van de Sanden, and D.C. Schram, *Phys. Rev. E.* **49** (1994) 2272
- [30] S. Mazouffre., M.G.H. Boogaarts, I.S.J. Bakker, P. Vankan, R.A.H. Engeln, and D.C. Schram, *Phys. Rev. E* **64** (2001) 016411
- [31] M.F.A.M. van Hest, A. Klaver, D.C. Schram, and M.C.M. van de Sanden, *Argon-oxygen plasma treatment of deposited silicon oxide like films*, to be published; Chapter 6 of this thesis
- [32] R.F.H. Meulenbroeks, R.A.H. Engeln, J.A.M. van der Mullen, and D.C. Schram, *Phys. Rev. E* **53** (1996) 5207
- [33] R.F.G. Meulenbroeks, D.C. Schram, M.C.M. van de Sanden, and J.A.M. van der Mullen, *Phys. Rev. Lett.* **76** (1996) 1840
- [34] M.C.M. van de Sanden, J.M. de Regt and D.C. Schram, *Plasma Sources Sci. Technol.* **3** (1994) 501
- [35] R.Engeln, S. Mazzouffre, P. Vankan, D.C. Schram, and N. Sadeghi, *Plasma Sources Sci. Technol.* **10** (2001) 595
- [36] S. Mazouffre, M.G.H. Boogaarts, J.A.M. van der Mullen, and D.C. Schram, *Phys. Rev. Lett.* **84** (2000) 2622
- [37] G.M. Janssen, *Design of a General Plasma Simulation Model*, Ph.D. Thesis, Eindhoven University of Technology (2000)
- [38] M.Barker, *Proc. Roy. Soc. A-101* (1922) 435
- [39] A.L. Hare, 3rd International Symposium on Plasma Chemistry, Limoges (1977) G.3.2.
- [40] P. Barkan and A.M. Whitman, Aerospace Research Laboratories United States Air Force (November 1964) ARL 64-192
- [41] T. Magin and G. Degrez, *Cooled Pitot Probe in inductive air plasma jet: What do we measure?*, 2nd International Symposium on Atmospheric Re-entry Vehicles and Systems, Arcachon, France (2001)
- [42] M.F.A.M. van Hest, A. de Graaf, M.C.M. van de Sanden, and D.C. Schram, *Plasma Sources Sci. Technol.* **9** (2000) 615; Appendix to chapter 2 of this thesis
- [43] K.T.A.L. Burm, W.J. Goedheer, J.A.M. van der Mullen, G.M. Janssen, and D.C. Schram, *Plasma Sources Sci. Technol.* **7** (1998) 395
- [44] J.W.A.M. Gielen, *Plasma Beam Deposition of Amorphous Hydrogenated Carbon*, Ph.D. Thesis, Eindhoven University of Technology (1996); Relevant data also published in: A. de Graaf, M.F.A.M. van Hest, M.C.M. van de Sanden, K.G.Y. Letourneur, and D.C. Schram, *Appl. Phys. Lett.* **74** (1999) 2927
- [45] M.C.M. van de Sanden, J.M. de Regt, and D.C. Schram, *Phys. Rev. E* **47** (1993) 2792
- [46] J.J. Beulens, M.J. de Graaf, G.M.W. Kroesen, and D.C. Schram, *Mater. Res. Soc. Proc.* **190** (1990) 311
- [47] H. Schellekens, *Modelling of the Diffuse Arc in a Vacuum Circuit-Breaker*, Ph.D. Thesis, Eindhoven University of Technology (1983)

Chapter 5

Deposition of silicon oxide like films using a remote thermal plasma

M.F.A.M. van Hest, B. Mitu, D.C. Schram and M.C.M. van de Sanden

Abstract

Silicon oxide like films have been deposited using a remote plasma produced from an expanding thermal plasma. Hexamethyldisiloxane (HMDSO) and oxygen have been used as precursor gases. It is shown that it is possible to deposit silicon oxide like films at high deposition rates (>60 nm/s) with good optical properties. Analysis of the deposited films by means of elastic recoil detection analysis and Fourier transform infrared spectroscopy shows that the dissociation and deposition mechanism is complex. The deposited films contain carbon which is chemically bonded in a methyl configuration. From this fact the plasma gas phase chemistry and the surface chemistry have been hypothesized. The film deposition rate increases with a decrease in substrate temperature, which is highly beneficial for deposition of silicon oxide like films on substrate materials with low melting temperature.

5.1 Introduction

Silicon dioxide films can be used for many applications, e.g. insulator films for semiconductors, optical coatings and scratch resistant coatings. Applying a silicon dioxide film on top of another bulk material can be done in many different ways. A possible method is by means of chemical vapour deposition (CVD). This is a process that is well known and is still used frequently. However, usually the silicon dioxide film deposition rate is rather low and high substrate temperatures are needed [1,2]. Another method to produce silicon dioxide films is by means of plasma enhanced CVD (PECVD). In this process a plasma is used to enhance the dissociation process of the deposition precursor, which will result in a higher deposition rate. In the past this method has been studied and good results have been achieved [3,4,5,6]. Although the deposition rate increased, still the deposition rate is small, up to several nm/s. An additional advantage of using PECVD with respect to CVD is that it enables a decrease of the substrate temperature.

A higher deposition rate of silicon dioxide is economically beneficial for some of its industrial applications. In the recent past it has been shown that high deposition rates (several tens of nm/s) can be obtained by means of an expanding thermal plasma for various type of films, e.g. hydrogenated amorphous carbon films (a-C:H) for diamond like coatings [7,8] and hydrogenated amorphous silicon films (a-Si:H) for solar cells [9,10]. It is therefore interesting to investigate if it is possible to deposit silicon dioxide or silicon oxide like films at high deposition rate by means of this technique.

A method to generate an expanding thermal plasma is by means of a cascaded arc source which has been connected to a vacuum vessel [11]. In this chapter the deposition of silicon oxide like films by means of an expanding thermal argon plasma into which hexamethyldisiloxane (HMDSO, $(\text{CH}_3)_3\text{-Si-O-Si-(CH}_3)_3$) and oxygen are injected as a precursor will be discussed. HMDSO is a precursor which is becoming more popular in the last decade. Beside this precursor also tetraethoxysilane (TEOS) [12,13] and silane [14,15] in combination with oxygen are often used as precursors. For industrial application silane is less preferable because of the safety precautions that have to be taken when using this highly reactive precursor. At room temperature both HMDSO and TEOS are liquids. The use of HMDSO is preferred in this work, because it contains more silicon atoms and less carbon atoms per molecule with respect to TEOS. Also the vapour pressure of HMDSO is higher than that of TEOS at room temperature enabling an easier precursor injection.

A disadvantage of taking an organosilicon as a precursor is the carbon content in the precursor, which will also become part of the deposited film if it is not eliminated by e.g. ion bombardment, a high substrate temperature, or oxidation. A significant carbon content of the deposited film can be detrimental to the material properties for certain applications (e.g. insulator material), whereas for other applications it might be beneficial (e.g. optical coatings).

5.2 Experimental setup

The experimental setup has been described before extensively [16,17,18]. Therefore a short description of the main characteristics will suffice here. The reactor consists of a stainless steel cylindrical vessel (diameter 36 cm, length 100 cm) which is positioned vertically. On top of the vessel a cascaded arc has been mounted. A temperature controlled

substrate holder is situated at the bottom of the vessel. The distance between the arc exit and the top of the substrate holder is equal to 65 cm, but is variable. The temperature of the substrate holder can be varied in a range of - 50 °C to 300 °C with a temperature accuracy at the substrate surface of $\Delta T \approx 10$ °C [19]. The reactor vessel is connected to a pump stack with one rotary piston pump (Edwards: 240 m³/hr) and two mechanical booster pumps (Edwards EH2600: 2600 m³/hr; Edwards EH500A: 500 m³/hr) which generates a base pressure of 10⁻⁴ mbar. Overnight the reactor is pumped by a turbo molecular pump (Leybold Turbovac 1500: 90 m³/hr) which keeps the reactor pressure at 10⁻⁶ mbar. Samples are transferred by means of a load lock system (10⁻⁶ mbar).

There are two different precursor gas injection positions. The precursor gas can be injected through the nozzle of the cascaded arc as well as through a punctured ring (diameter 10 cm) situated approximately 5 cm from the arc exit. For nozzle injection of the precursor gas a special nozzle is used (cf. Figure 5.1), through which it is possible to inject the precursor gas symmetrically into the plasma beam.

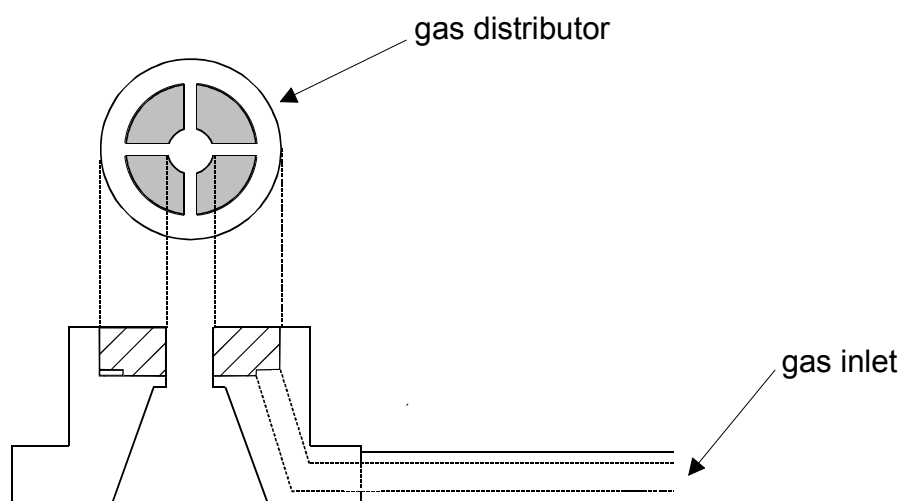


Figure 5.1: Schematic of the injection nozzle.

For the deposition of silicon dioxide two precursors are used. As the first precursor hexamethyldisiloxane (HMDSO, $(\text{CH}_3)_3\text{-Si-O-Si-(CH}_3)_3$) is used as a supplier of the silicon atoms. HMDSO is a liquid precursor with a convenient vapour pressure (2500-5000 Pa) at room temperature [20,21]. It has to be evaporated before injection into the expanding argon plasma beam. This is done using a Bronckhorst controlled evaporation module (CEM, type W-202) in combination with a Bronckhorst Liqui-Flow® meter (type L2C2). This is a closed system, which controls the liquid flow rate and evaporates the liquid. This system is more reliable and stable than the more conventionally used bubbler systems [22,23]. The second precursor is pure oxygen (purity grade 5.0), which is used as a supplier of the oxygen atoms. The oxygen flow is controlled by a regular mass flow controller. An overview of the deposition parameters and their ranges are given in Table 5.1. Also the so-called 'standard' condition is given in Table 5.1. The 'standard' condition is defined, in order to study the dependency of the film properties on the deposition parameters. Each of the parameters has been varied individually, while the other deposition parameters were kept constant, unless stated otherwise. Normally HMDSO is injected through the punctured ring at 5 cm from the arc exit and oxygen is injected through the nozzle of the arc. However, for some experiments

the injection order is reversed. The two injection sequences are indicated as O₂-HMDSO or HMDSO-O₂ injection for respectively normal and reverse injection.

Table 5.1: Overview of the plasma parameters and their ranges as well as the ‘standard’ conditions.

Parameter	Range	Standard condition
Ar flow	15 – 100 sccs	25 sccs
O ₂ flow	0 – 16 sccs	5 sccs
HMDSO flow	0.79 - 6.35 sccs	1.98 sccs
Ar flow (carrier gas in CEM)	0.8 sccs	0.8 sccs
HMDSO evaporation temperature	40 - 80 °C	65 °C
Arc current	25 – 90 A	50 A
Arc pressure	0.2 – 0.6 bar	0.2 bar
Vessel pressure	10 – 45 Pa	11.0 Pa
Substrate temperature	0 – 300 °C	50 °C

In situ analysis of the optical properties (refractive index and film thickness) of the deposited films is done by means of *in situ* ellipsometry. For this a He-Ne laser (632.8 nm) is utilized, mounted in a PCSA (polariser – compensator – sample – analyser) rotating compensator ellipsometer [24,25]. The deposited films have been analysed *ex-situ* by means of Fourier transform infrared transmission absorption spectroscopy [26,27] using a Bruker Vector 22 FTIR spectroscope. With this method the individual bonding types in the deposited films can be investigated. Elastic recoil detection analysis (ERDA) [28,29,30] measurements have been performed to determine the chemical composition of the deposited films.

5.3 Results

5.3.1 Silicon oxide like film deposition

By means of *in situ* ellipsometry it is quite easy to obtain the refractive index of the deposited film. As mentioned the silicon oxide like film deposited from HMDSO will most likely, beside silicon oxide, contain some carbon. Also voids might exist in the deposited films. Therefore the refractive index of the deposited silicon oxide like film will be a function of the silicon oxide, carbon and void content. The carbon content will have a positive and the void content a negative contribution to the refractive index. This means that a refractive index higher than that of pure silicon dioxide indicates the presence of carbon in the film and a refractive index lower than that of pure silicon dioxide indicates the presence of voids in the film. However a refractive index higher than that of pure silicon dioxide does not exclude the presence of voids and a refractive index lower than that of pure silicon dioxide does not exclude the presence of carbon. A mixture of voids and carbon in the film can result in a refractive index which is equal to that of pure silicon dioxide, although the film is far from being pure silicon dioxide.

To get an insight into the plasma chemistry leading to the dissociation of HMDSO, the dependencies on different deposition parameters (substrate temperature, HMDSO flow, and

oxygen flow) have been analysed. Figure 5.2 shows the deposition rate and refractive index as function of the HMDSO precursor gas flow at a fixed oxygen flow. First of all it can be seen in Figure 5.2 that deposition rates over 60 nm/s can be reached at a low substrate temperature (50 °C). This rate is at least one order of magnitude higher than the deposition rates obtained with the more conventional (PE)CVD technique at high temperatures [3,4,5,6]. Secondly it can be seen in Figure 5.2 that the deposition rate is increasing with increasing HMDSO flow. This is because an increase in the HMDSO precursor flow rate will increase the deposition particle flux to the substrate. The refractive index increases with increasing HMDSO flow, at a fixed oxygen flow, up to a flow rate of approximately 2 sccs. For HMDSO flows of 2 sccs and higher the refractive index of the film becomes independent of the HMDSO flow. Notice that the refractive index measured in this range is close to the refractive index of pure silicon dioxide, which is equal to 1.457 at the ellipsometry measuring wavelength (632.8 nm). As mentioned this does not exclude the presence of carbon and voids in the deposited films. The fact that the refractive index is lower than that of pure silicon dioxide for HMDSO flows below 2 sccs indicates that the deposited films in this range contain voids.

It is known that for the used plasma the electron temperature is low (approximately 0.3 eV) and that therefore no dissociation of the injected precursor can occur by means of a reaction with an electron [31,32]. The chemistry is dominated by first a charge exchange reaction of the argon ions in the plasma and the injected precursor followed by a dissociative recombination reaction of the formed ion and an electron. By means of Langmuir probe measurements it has been found that the argon ion flux, for the used plasma parameters, emitted by the arc is approximately equal to 2 sccs [31]. This means that for HMDSO flows above 2 sccs the HMDSO molecules will most likely only react once with the argon ions and electrons. For flows smaller than 2 sccs there is a surplus of argon ions and electrons and multiple interactions can occur, leading to further dissociation of the primary dissociation products. So at HMDSO flows above 2 sccs the dissociated particle flux composition to the deposition surface, assuming no polymerisation, becomes independent of the injected HMDSO flow, and with this also the film composition and thus the film refractive index.

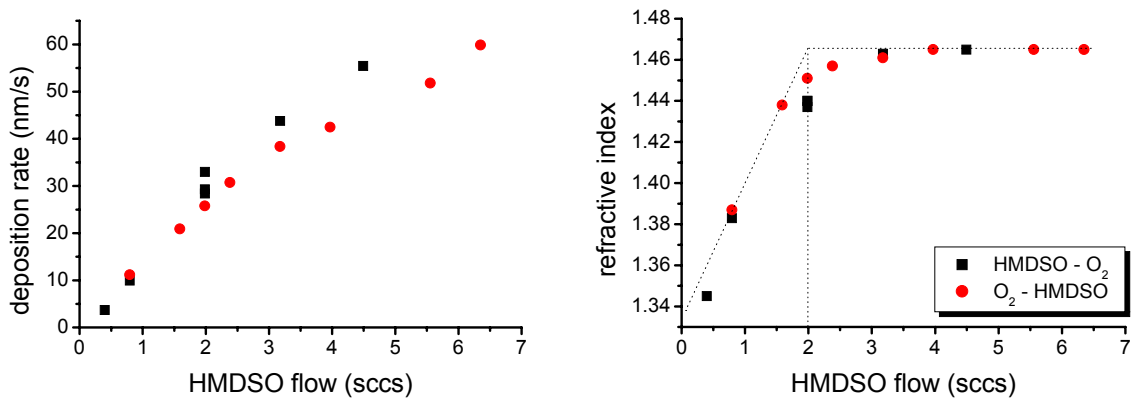


Figure 5.2: Film deposition rate and refractive index as function of the HMDSO precursor flow. Other plasma parameters at 'standard' conditions.

From Figure 5.2 it is observed that the deposition rate is slightly higher in the case when HMDSO is injected in the nozzle and oxygen in the injection ring (HMDSO-O₂). In this reversed injection case HMDSO molecules have a longer interaction length with the argon ions and electrons in the expanding plasma beam than in the other case and the interaction

with oxygen is most likely to occur after the injection ring. In the normal injection case (O_2 -HMDSO) the HMDSO will, from the time of injection, immediately react with oxygen radicals and also with argon ions and electrons.

The difference between the deposition rate for the two different injection orders is significant, and can be caused by two different ways. It is either caused by the difference in interaction between HMDSO and atomic oxygen on one side or argon ions and electrons on the other side. Both interactions will result in different dissociation product which will have their own interaction process at the surface. The presence of oxygen causes a difference in deposition rate because when atomic oxygen arrives at the surface it has an interaction that reduces the amount of carbon and hydrogen present in the deposited film [33,34]. When oxygen is injected further downstream the creation of oxygen radicals occurs later in the downstream plasma and the density of oxygen radicals at the surface is likely to be higher. This will result in a higher carbon and hydrogen etch rate and thus a lower deposition rate. In addition oxygen does not only etch but can also be incorporated into the film [33,34], which might result into a higher deposition rate. Of these two processes the abstraction of methyl groups by atomic oxygen is probably the most likely one. However, this is in contradiction with the observed deposition rates. Therefore a difference in sticking probability of the different reaction products formed in the two different interaction processes should be responsible for the observed difference.

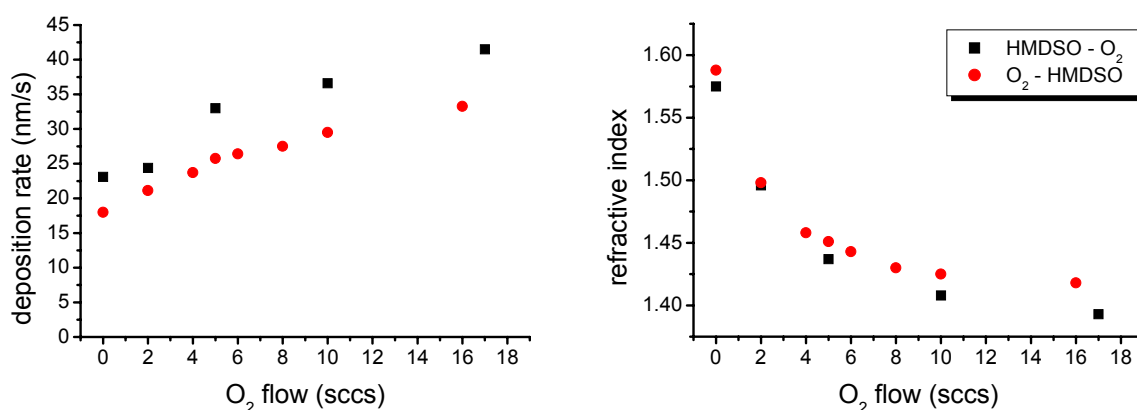


Figure 5.3: Film deposition rate and refractive index as function of the oxygen precursor gas flow. Other plasma parameters at 'standard' conditions.

In Figure 5.3 the film deposition rate and refractive index as function of the oxygen flow, for a fixed HMDSO flow, are shown. Figure 5.3 reveals that the deposition rate is increasing with increasing oxygen flow. It is however difficult to analyse the process that is causing the increase in the deposition rate, because the depositions have been performed using the full pumping capacity. This leads to an increase of the pressure inside the deposition reactor when the total gas flow is increased. As a result the diameter of the plasma beam becomes smaller and the deposition species are concentrated in a smaller volume. This results in a smaller deposition area and therefore a higher deposition rate. The observed deposition rate is proportional to the reactor pressure, which supports this explanation. However, besides from this effect, the increase can also be caused by a change in the dissociation products of the precursor, which might have a higher sticking probability or generate a film with a higher void concentration. On the other hand, more oxygen in the plasma will also cause more

carbon and hydrogen to be eliminated from the film which would result in a decrease of the deposition rate. As can be seen the number of processes is too large to identify the process which causes the increase of the deposition rate.

In Figure 5.3 it can also be seen that the refractive index of the deposited film is decreasing with increasing oxygen flow. When no oxygen is added to the deposition plasma the refractive index is higher than the refractive index of pure silicon dioxide and therefore carbon is present in the film. At the maximum oxygen flow the refractive index is lower than that of pure silicon dioxide and therefore voids need to be present in the deposited film. Notice, that for the case when no oxygen is added, the refractive index has almost the same value as when CH_4 would have been used for deposition of the film [18,35], which is an indication that the deposited film is most likely carbon rich.

Figure 5.3 shows a higher deposition rate for the case HMDSO is injected in the nozzle (HMDSO- O_2) than for the case when HMDSO is injected in the ring (O_2 -HMDSO). This is similar to the deposition rate as function of the HMDSO flow for the two different injection methods (see Figure 5.2). When no oxygen is added, the growth rate is the highest when the HMDSO is injected in the nozzle, indicating that a longer interaction length of HMDSO with the argon plasma results in more dissociation of the injected precursor.

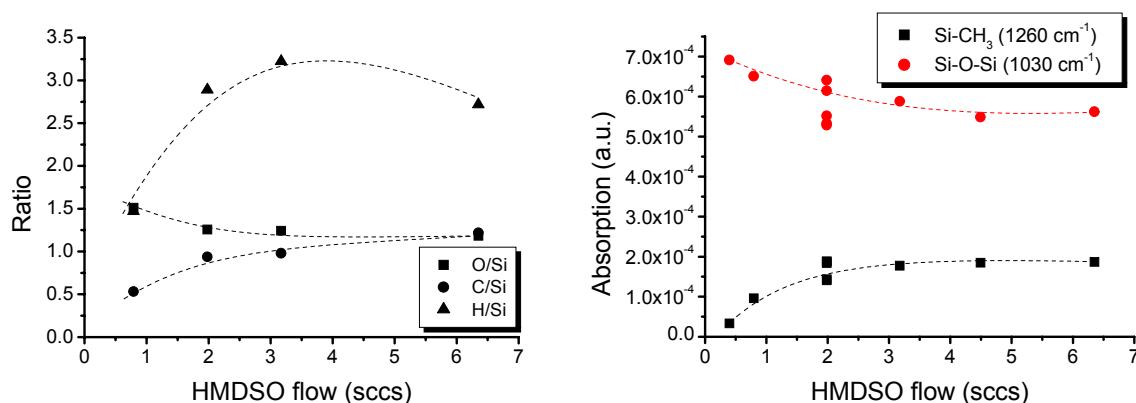


Figure 5.4: Carbon to silicon, hydrogen to silicon, and oxygen to silicon ratio of the deposited films derived from ERDA measurements and absorption intensity of two different bonds in the film as measured by means of infrared absorption spectroscopy as function of the HMDSO precursor gas flow. Other plasma parameters at ‘standard’ conditions.

5.3.2 Film composition

To detect the carbon content of the films, ERDA measurements have been performed on some of the deposited films. With this technique the concentration of different atoms in the film can be measured. In this case the carbon, oxygen, silicon and hydrogen contents have been analysed. In Figure 5.4 the results of these measurements in terms of carbon to silicon, oxygen to silicon and hydrogen to silicon ratios are shown as function of the HMDSO precursor gas flow. When the data shown in Figure 5.4 is compared to the refractive index data shown in Figure 5.2, it can be seen that the carbon to silicon and the hydrogen to silicon ratio show the same trend as the refractive index. This shows that there is a strong correlation between the carbon fraction of the deposited film and the refractive index of the film. Another observation which can be made from Figure 5.4 is that the hydrogen to silicon ratio is

approximately 3 times higher than the carbon to silicon ratio. Therefore the hydrogen to carbon ratio is approximately equal to 3, just as in the precursor itself. This indicates that in the gas phase or at the substrate surface the precursor is depleted and methyl groups are removed from the precursor as complete groups. This is corroborated by recent cavity ring down spectroscopy measurements which only showed CH production under extreme low HMDSO conditions [36].

ERDA measurements can only show the number density of the particles and no information is obtained on the various bond types present in the deposited films. This information can however easily be obtained by means of infrared transmission absorption spectroscopy. In Figure 5.4 the absorption intensity as function of the HMDSO flow is shown for two different bond types (Si-CH₃ and Si-O-Si). The absorption intensity is corrected for film thickness. In Figure 5.4 it can be seen that as function of the HMDSO flow the Si-CH₃ absorption is increasing with increasing HMDSO flow. This is consistent with the ERDA measurement, where an increase, with respect to silicon, of carbon and hydrogen is observed in the film. In conclusion, it can be said that when carbon is present in the deposited films it will be present as a methyl group which is bonded to a silicon atom. This is exactly the same configuration as in the precursor.

Further analysis of the ERDA data in Figure 5.4 reveals that for HMDSO flows above 2 sccs the film composition is independent of the HMDSO flow, which is similar to the behaviour of the refractive index (see Figure 5.2). The values of the shown ratios (O/Si=1, C/Si=1, and H/Si=3) approach the ratios in CH₃-Si-O, which is present as part of the precursor. As mentioned at HMDSO flows larger than 2 sccs the HMDSO molecule only has one interaction with an argon ion or oxygen atom before reaching the substrates surface, therefore the obtained stoichiometry can only be reached by one gas phase interaction and one surface interaction. This is an indication that the HMDSO molecule has a preference for breaking at the Si-O bond on interaction with an argon ion and an electron (charge exchange and dissociative recombination) or on interaction with an oxygen radical. This is not what is expected on basis of bond strengths. Si-CH₃ is the weakest bond when considering a complete removal of methyl groups. When using other plasma deposition techniques, such as RF-plasma (capacitively coupled), it has been shown that there the Si-CH₃ bond is the preferred bond to be dissociated [37,38]. Breaking of the HMDSO on the Si-O bond on interaction with an argon ion and an electron is energetically possible because the ionisation energy is higher than the bonding energy of this bond. To obtain the measured film stoichiometry the O-Si-(CH₃)_x radicals need to have a significantly higher sticking probability than the Si-(CH₃)_x radicals. The fact that the film composition is not changing anymore for HMDSO flows above 2 sccs is a good indication that polymerisation of the precursor under these plasma conditions is not very likely, because when polymerisation would occur a change in film stoichiometry is expected.

In Figure 5.5 the ratio of the carbon to silicon, oxygen to silicon and hydrogen to silicon as obtained from ERDA measurements are shown as function of the oxygen precursor gas flow. When no oxygen is added to the deposition plasma the ratio of oxygen and silicon in the deposited film is equal to 1, which is another indication that HMDSO on interaction with argon ions and electrons (charge exchange and dissociative recombination) is dissociated on the Si-O bond. When the shown ratios and the refractive index as shown in Figure 5.3 are being compared, it can be seen that there is again a good correlation between the refractive index and the carbon to silicon ratio as well as with the hydrogen to silicon ratio, which shows once more the correlation between the refractive index and the carbon content of the film.

Figure 5.5 reveals a clear decrease of the carbon content with increasing oxygen precursor gas flow. Therefore oxygen is the dominant species responsible for removal of methyl groups from HMDSO. It can, as in Figure 5.4, also be seen in Figure 5.5 that the ratio of hydrogen to carbon is equal to 3 for low oxygen flow (<5 sccs). For higher oxygen flows this ratio decreases to approximately 2, indicating that methyl groups can also be removed partially or that carbon containing species, other than methyl, are formed in the gas phase which contribute to film growth.

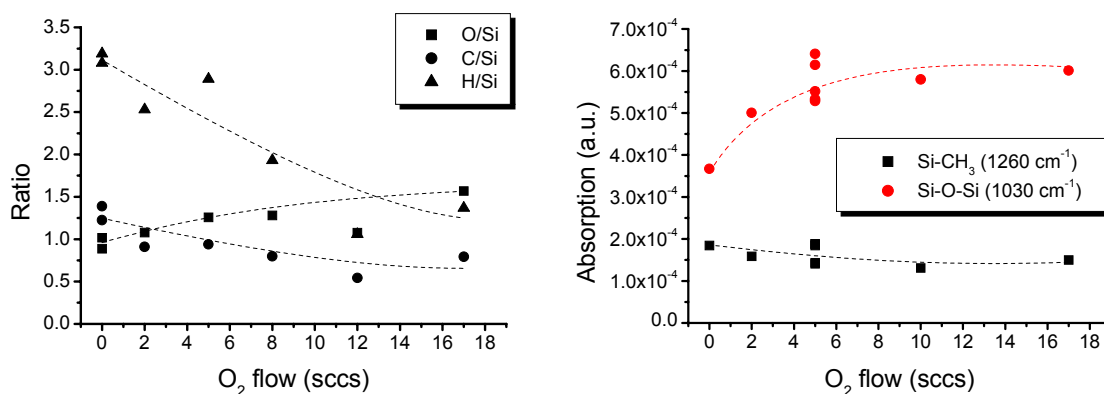


Figure 5.5: Carbon to silicon, hydrogen to silicon, and oxygen to silicon ratio of the deposited films derived from ERDA measurements and absorption intensity of two different bonds in the film as measured by means of infrared absorption spectroscopy as function of the oxygen precursor gas flow. Other plasma parameters at 'standard' conditions.

In literature it has been reported that at higher oxygen flows also silanol bonds (Si-OH) are incorporated into the deposited film [39,40]. If that would be the case here the hydrogen to carbon ratio should increase and not decrease as has been measured. Infrared measurements corroborate the absence of silanol groups and therefore this process is negligible for deposition using an expanding thermal plasma.

In Figure 5.5 also the infrared absorption intensity, corrected for film thickness, for two different bonds is shown as function of the oxygen precursor gas flow. When these are compared with the ERDA data a correlation between the Si-O-Si bond intensity and the oxygen to silicon ratio can be observed. When the oxygen content of the film decreases, the number of Si-O-Si bonds will automatically decrease. This is due to the fact that a decrease in oxygen content is correlated with an increase of the carbon content in the deposited film. More carbon will generate more Si-CH₃ bonds and therefore less bonds are available to form Si-O-Si bonds. Because most likely a Si-O bond is broken in the dissociation process in the gas phase of the plasma the presence of Si-O-Si in the film has to be a result of surface reactions.

5.3.3 Temperature dependency

In Figure 5.6 the deposition rate as function of the substrate temperature is shown. Besides the high deposition rate, it can be seen in Figure 5.6 that the deposition rate decreases with increasing substrate temperature. In comparison to CVD this is exactly the opposite behaviour since in this case temperature is needed to achieve precursor dissociation [1,2]. This is an interesting property of using this plasma source, i.e. the substrate does not have to

be heated to obtain high deposition rates, which is good for deposition on materials with a low melting temperature, e.g. aluminium or plastics. Figure 5.6 also shows the refractive index of the deposited films as function of the deposition temperature. It can be seen that the refractive index is slightly increasing with increasing temperature. The refractive index of the films has been measured *in situ* during deposition. It is known that the refractive index of silicon dioxide increases with increasing temperature by $1.2 \cdot 10^{-5}/^{\circ}\text{C}$ [41], but the observed change is slightly larger than this value. The value of the refractive index rises above the refractive index of pure silicon dioxide, which is due to the presence of carbon in the deposited films.

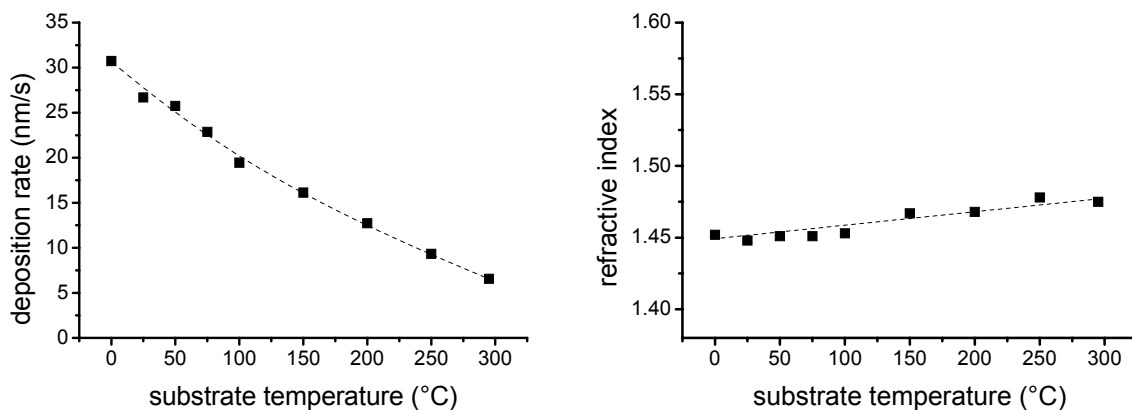


Figure 5.6: Film deposition rate and refractive index as function of the substrate temperature. Other plasma parameters at ‘standard’ conditions.

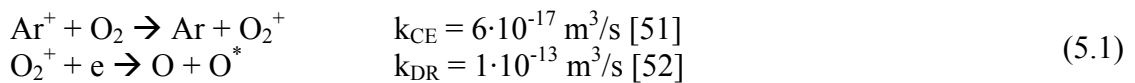
Due to the use of a remote plasma source the plasma particle flux and composition at the substrate surface is in general independent of the substrate temperature. The effective sticking probability of a species contributing to growth in the plasma however is dependent on both substrate temperature and surface composition. The sticking probability of different radicals is likely to decrease with increasing substrate temperature in the used temperature range [42]. The change of the sticking probability will be different for the different species in the plasma and therefore the composition of the film can change with a change in substrate temperature.

The composition will also change because of a second effect. It is most likely that the carbon content of the deposited film will decrease with increasing substrate temperature. A higher substrate temperature will enhance the carbon etching by the oxygen radicals present in the plasma. As a result of this higher carbon etch rate the effective deposition rate will decrease. The enhanced carbon etch rate will cause a decrease of the refractive index, which is not observed. Therefore, it is needed that the void density has to go down with increasing substrate temperature and the film will become more dense. A lower deposition rate will increase the residence time that possibly weakly adsorbed (physisorbed) particles at the substrate surface will have before forming a chemical bond [43,44]. Due to this increased residence time, the particles will have more time to fill the gaps in the film, resulting in a less rough film surface and less voids in the deposited film. Although due to enhanced etching the carbon content decreases, the densification of the film still results in an effective increase of the refractive index.

5.4 Discussion

The argon plasma generated in the cascaded arc which expands into a vacuum vessel is a remote plasma, in the sense that the plasma source is not influenced by the conditions of the expansion vessel. In the downstream expansion four different species will be present, i.e. argon atoms, argon ions, argon metastables and electrons. The metastables do not play an important role in the downstream chemistry as has been shown by Buuron *et al.* [45]. When downstream a deposition precursor is injected into the argon plasma, the precursor species will interact with the argon plasma. Due to the low electron temperature (approx. 0.3 eV [31,46]) in the expansion there will be no electron induced dissociation reactions. The argon atoms will also have no significant contribution to dissociative reactions (gas temperature is low) and therefore mainly the argon ions and electrons present in the argon plasma will be responsible for dissociation of the injected gasses (charge exchange followed by dissociative recombination). This has previously been demonstrated utilizing other different precursor gases such as acetylene [47] and silane [48,49,50].

Oxygen is injected as a precursor into the argon plasma at the nozzle position. For the deposition of silicon oxide like films the oxygen has been injected for two purposes. First it serves to remove methyl groups from the precursor in the gas phase or either at the surface of the deposited film. Secondly it is needed to obtain the silicon dioxide stoichiometry. The injected oxygen will react with the argon ions and the electrons according to the following reaction mechanism:



First the oxygen molecules will charge exchange with the argon ions produced in the arc, leading to the production of oxygen molecular ions [53]. These ions will dissociatively recombine with an electron and form two oxygen radicals, of which at least one might be electronically excited leading to optical emission of oxygen excited states. The dissociative recombination reaction is much faster than the charge exchange reaction, therefore the charge exchange reaction is the rate-limiting step. As a result the molecular oxygen ion density will be small and negligible in comparison to the argon ion density. Notice, that argon ions and electrons are consumed and thus their density decreases from the arc exit to the substrate surface.

Langmuir double probe measurements show that the argon ion density decreases with increasing oxygen flow in an argon/oxygen plasma as is shown in Figure 5.7. A more detailed analysis of the argon-oxygen plasma is given in reference [31]. In Figure 5.7 the ion density as measured in the centre of the plasma beam at an axial position of 30 cm from the exit of the cascaded arc is depicted. Addition of only 2 sccs of molecular oxygen to the 25 sccs argon plasma already reduces the ion density by more than 50 %. The measurements have been performed at 30 cm from the arc exit, and therefore the plasma at the injection ring (at 5 cm) will still be dominated by argon ions. Notice that the argon ions have a small kinetic energy. The self-bias is low (<1 V) [54] due to the low electron temperature and therefore there will be no ion bombardment of the substrate. In combination with the low substrate temperatures used this excludes an elimination of carbon containing groups or any other groups of atoms from the surface by this process.

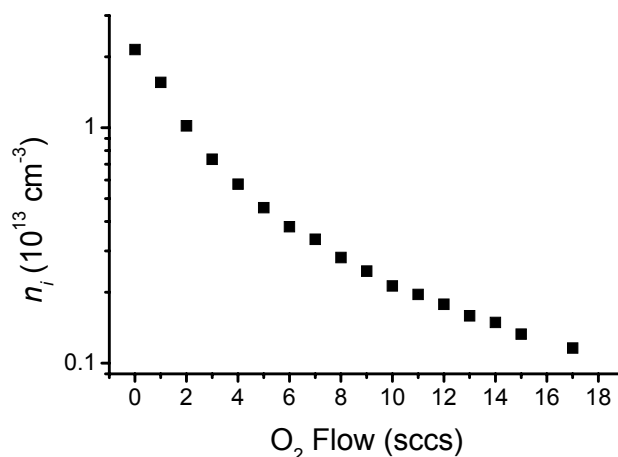
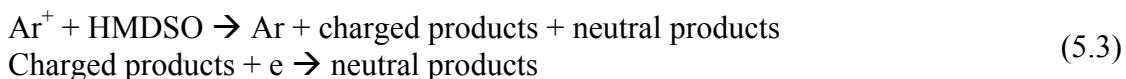


Figure 5.7: Ion density as function of the oxygen flow for different arc currents measured at a distance of 30 cm from the arc exit. Argon flow=25 sccs, Arc current = 50 A.

Besides reactions of argon ions with oxygen also the HMDSO will react when injected into the plasma beam. This can occur in two different ways. It can react with the argon ions in a similar way as molecular oxygen does, or it can react with the oxygen radicals that are created in the expanding argon plasma. The most likely reaction with oxygen radicals is given by:



Neutral products created in this reaction will be radical and/or molecules which consist of precursor gas atoms e.g. radicals; $(\text{CH}_3)_3\text{-Si-O-Si-(CH}_3)_2$, $(\text{CH}_3)_3\text{-Si-O}$, CO, CH₃, H, molecules; H₂, C₂H₂. The reaction mechanism with argon ions is given by:



On the charge exchange between an argon ion and an HMDSO molecule, the HMDSO molecule will already dissociate because the ionic molecule is instable [55,56]. The most likely charged particle is therefore the $(\text{CH}_3)_3\text{-Si-O-Si-(CH}_3)_2^+$. The charged products will dissociate further when they dissociatively recombine with an electron. The dissociation of HMDSO by an argon ion is more efficient than dissociation by an oxygen radical because the ion is more energetic, which leads to more internal energy in the resulting dissociation products. However, every argon ion can produce two oxygen radicals, and every oxygen radical can dissociate one HMDSO molecule, whereas one argon ion can only dissociate one HMDSO molecule. Therefore the dissociative power of the plasma is increased by introducing oxygen to the plasma. This is not corroborated by the experiments e.g. the deposition rate, which does not show a large increase when oxygen is added to the plasma (cf. Figure 5.3). This means that the reaction products produced on interaction of HMDSO with oxygen radicals need to be different from the dissociation products formed on interaction of HMDSO with argon ions and electrons or the produced oxygen radicals need to be lost at the wall at such a high rate that they will have no positive contribution.

As derived from the ERDA measurements the HMDSO molecule will most likely dominantly break on the Si-O bond on interaction with either an oxygen radical or an argon ion and electron. As shown at the HMDSO injection point the plasma is still dominated by argon ions and therefore the majority of the dissociation reactions of HMDSO will occur by means of an interaction of argon ion and electrons with HMDSO molecules. Therefore the decrease of the film carbon content with an increase of the molecular oxygen flow is most likely caused by a surface reaction or by a gas phase reaction of one of the dissociation products with an oxygen radical.

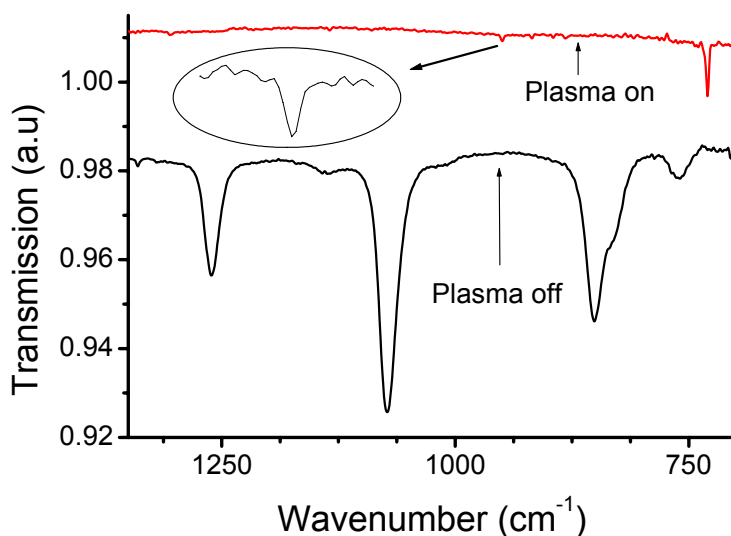


Figure 5.8: Infrared gas phase absorption spectrum. 100 sccs argon, 4 sccs HMDSO, no oxygen and 80 A. Other plasma parameters at 'standard' conditions.

In Figure 5.8 a part of the infrared gas phase absorption spectrum during deposition is shown. It can be seen that for the conditions used in the shown case the precursor is fully depleted. At 'standard' conditions the depletion is approximately 70%. It can be seen that significant amounts of C_2H_2 (729 cm^{-1}) and C_2H_4 (948 cm^{-1}) are present in the gas phase [57]. Studying the whole infrared gas phase absorption spectrum shows that also CH_4 (3016 cm^{-1}) is present in the plasma gas phase. The infrared absorption intensities measured are equivalent to hydrocarbon flows of 1 sccs to 2 sccs for each individual species. The presence of CH_4 is another indication that methyl groups are removed from the precursor in one piece. The presence of C_2H_y however shows that the removed methyl groups react again with another methyl group [57], with an HMDSO molecule, with one of its dissociation products, or with the deposited film surface, abstracting another methyl group forming C_2H_y species. The presence of these kind of abstraction reactions in the gas phase results in less carbon rich deposition species. Due to recirculation the stable hydrocarbon species will re-enter the plasma beam close to the arc exit. This will result in dissociation of these species in such a way that they can contribute to the deposition process. Nevertheless, during deposition, there is a steady state concentration of these stable hydrocarbon species, which has a positive influence on the oxygen consumption. No significant change in C_2H_2 , C_2H_4 , and CH_4 production has been observed as function of the injected molecular oxygen flow. This forms an indication that oxygen radicals have no interaction with these stable monomers and that these stable monomers are not produced under the presence of oxygen radicals. The study of

the plasma gas phase also showed that there is no or at least no detectable amount of polymerisation of the precursor.

5.5 Conclusions

It has been shown that by means of remote plasma, created by using a thermal argon plasma, it is possible to make silicon oxide like films with good optical properties at a high deposition rate. It has been demonstrated that deposition rates of more than 60 nm/s can be obtained without degeneration of the film quality.

The films that have been deposited all contain carbon that is in the film in the form of methyl groups, just as it is present already in the precursor. Methyl groups are removed from the precursor in the gas phase on charge exchange of the HMDSO molecule with an argon ion. Bonded methyl groups that reach the surface and form a film are etched by oxygen radicals present in the plasma. However, the etch rate is too low to remove all the methyl groups from the film (see also [34]). Both the HMDSO flow and the oxygen flow have to be adjusted to maintain the same film quality at a higher deposition rate.

The HMDSO is dissociated in the plasma by means of an interaction with argon ions and electrons or by an interaction with oxygen radicals. The rate of dissociation is the strongest due to the interaction with argon ions and electrons. The oxygen radicals have the largest contribution at the surface, where they will etch the carbon, which has not been removed by the precursor dissociation process, from the film. After charge exchange of the HMDSO molecule with an argon ion the generated ion will dissociatively recombine with an electron. The dissociation of the generated ion will most likely dominantly take place at the Si-O bond in the ion. This behaviour is different to what has been found for other plasma sources like RF discharges where the methyl groups are removed first due to an electron impact reaction. The fact that the HMDSO molecule is broken at the Si-O bond eliminates one of the advantages of using HMDSO with respect to e.g. TEOS. Although the Si-O-Si bond is present in the precursor, the Si-O-Si bonds present in the film need to be produced at or in the film.

Although has not been the purpose of this research to produce pure silicon dioxide films, it seems possible to obtain carbon free silicon dioxide films at high growth rates by means of a remote thermal argon plasma in combination with HMDSO and oxygen. For this the plasma parameters have to be tuned. The highest probability of obtaining pure silicon dioxide films is at low HMDSO flow rates and high oxygen flow rates. This is a condition at which the deposition rate does significantly decrease with respect to the one obtained at 'standard' conditions. It cannot be guaranteed that the deposited film will be void free at these conditions.

Acknowledgements

The authors would like to thank Wim Arnold Bik of the University of Utrecht for performing the ERDA experiments. The skilful technical assistance of M.J.F. van de Sande, A.B.M. Hüsken, and H.M.M. de Jong is greatly appreciated.

References

- [1] M.L. Hitchman and K.F. Jensen, *Chemical Vapor Deposition-Principles and Applications*, Academic Press, London (1993)
- [2] W.S. Rees Jr. *CVD of Nonmetals*, Weinheim (1996)
- [3] N. Benissad, C. Boisse-Laporte, C. Vallee, A. Granier, and A. Goullet, *Surf. Coat. Technol.* **116-119** (1999) 868
- [4] M. Walker, K.M. Baumgärtner, J. Fiechtinger, M. Kaiser, A. Schulz, and E. Räuchle, *Vacuum* **57** (2000) 387
- [5] K.H.A. Bogart, N.F. Dalleska, G.R. Bogart, and E.R. Fisher, *J. Vac. Sci. Technol. A* **13** (1995) 476
- [6] S.C. Deshmukh and E.S. Aydil, *Appl. Phys. Lett.* **65** (1994) 3185
- [7] J.W.A.M. Gielen, P.R.M. Kleuskens, M.C.M. van de Sanden, L.J. van IJzendoorn, D.C. Schram, E.H.A. Dekempeneer, and J. Meneve, *J. Appl. Phys.* **80** (1996) 5986
- [8] A.J.M. Buuron, J.J. Beulens, G.J. Meeusen, M.C.M. van de Sanden, and D.C. Schram, *J. Appl. Pol. Sci.* **54** (1994) 115
- [9] W.M.M. Kessels, M.C.M. van de Sanden, R.J. Severens, and D.C. Schram, *J. Appl. Phys.* **87** (2000) 3313
- [10] B.A. Korevaar, G.J. Adriaenssens, A.H.M. Smets, W.M.M. Kessels, H.-Z. Song, M.C.M. van de Sanden, and D.C. Schram, *J. Non-Cryst. Solids* **266-269** (2000) 380
- [11] G.M.W. Kroesen, D.C. Schram, and M.J.F. van de Sande, *Plasma Chem. Plasma Proc.* **10** (1990) 49
- [12] K.H.A. Bogart, S.K. Ramirez, L.A. Gonzales, G.R. Bogart, and E.R. Fisher, *J. Vac. Sci. Technol. A* **16** (1998) 3175
- [13] A. Granier, F. Nicolazo, C. Vallee, A. Goullet, G. Turban, and B. Grolleau, *Plasma Sources Sci. Technol.* **6** (1997) 147
- [14] S.M. Han and E.S. Aydil, *J. Vac. Sci. Technol. A* **14** (1996) 2062
- [15] L.-N. He, S. Hasagwa, *Thin Solid Films* **384** (2001) 195
- [16] J.W.A.M. Gielen, M.C.M. van de Sanden, P.R.M. Kleuskens, and D.C. Schram, *Plasma Sources Sci. Technol.* **5** (1996) 492
- [17] J.W.A.M. Gielen, W.M.M. Kessels, M.C.M. van de Sanden, and D.C. Schram, *J. Appl. Phys.* **82** (1997) 2643
- [18] A. de Graaf, *Deposition of CNH Materials; Plasma and Film Characterization*, Ph.D. Thesis, Eindhoven University of Technology (2000)
- [19] J.W.A.M. Gielen, *Plasma Beam Deposition of Amorphous Hydrogenated Carbon*, Ph.D. Thesis, Eindhoven University of Technology (1996)
- [20] D.W. Scott, J.F. Meserly, S.S. Todd, G.B. Guthrie, I.A. Hossenlopp, R.T. Moore, A. Ossborn, W.T. Berg, and J.P. McCullough, *J. Research Natl. Bur. Standards A* **65** (1961) 1321
- [21] K. Fujino, Y. Nishimoto, N. Tokumasu, and K. Maeda, *J. Electrochem. Soc.* **139** (1992) 2282
- [22] H.J. Boer, *Journal de Physique IV* **5** (1995) C5-961
- [23] H.J. Boer, *Solid State Technology* (March 1996) 149
- [24] A.H.M. Smets, D.C. Schram, and M.C.M. van de Sanden, *J. Appl. Phys.* **88** (2000) 6388
- [25] R.M.A. Azzam and N.M. Bashara, *Ellipsometry and Polarized Light*, North-Holland Publishing Co., Amstersdam (1977)

- [26] R.J. Bell, *Introductory Fourier Transform Spectroscopy*, Academic Press, New York (1972)
- [27] A.E. Martin, *Infrared Interferometric Spectrometers*, editor J.R. During, Elsevier Scientific Publishing Company, Amsterdam (1980)
- [28] L.C. Feldman, and J.W. Mayer, *Fundamentals of Surface and Thin Film Analysis*, North-Holland, New York (1986)
- [29] J. L'Ecuyer, C. Brassard, C. Cardinal, and B. Terreault, *Nucl. Instrum. Methods* **149** (1978) 271
- [30] R. Groleau, J.F. Currie, M.R. Wertheimer, J.E. Klemberg-Sapieha, and W. Ke-Ming, *Thin Solid Films* **136** (1986) 85
- [31] M.F.A.M van Hest, J.R. Haartsen, M.H.M. van Weert, D.C. Schram, and M.C.M. van de Sanden, *Analysis of the argon-oxygen plasma gas phase*, to be published; Chapter 4 of this thesis
- [32] J.J. Beulens, M.J. de Graaf, G.M.W. Kroesen, and D.C. Schram, *Proc. Mat. Res. Soc.* **190** (1990) 311
- [33] C. Vallée, A. Granier, K. Aumaille, C. Cardinaud, A. Gouillet, N. Coulon, and G. Turban, *Appl. Surf. Sci.* **138-139** (1999) 57
- [34] M.F.A.M. van Hest, A. Klaver, D.C. Schram, and M.C.M. van de Sanden, *Argon-oxygen plasma treatment of deposited silicon oxide like films*, to be published; Chapter 6 of this thesis
- [35] G.M.W. Kroesen, D.C. Schram, and M.J.F. van de Sande, *Plasma Chem. Plasma Proc.* **10** (1990) 49
- [36] M. Creatore, M.F.A.M. van Hest, J. Benedikt, and M.C.M. van de Sanden, *Expanding thermal plasma deposition of silicon dioxide-like films for microelectronic devices*, to be published in the MRS proceedings 2002
- [37] M.R. Alexander, F.R. Jones, and R.D. Short, *Plasmas and Polymers* **2** (1997) 277
- [38] A.M. Wróbel, M. Kryszewski, and M. Gazicki, *J. Macromol. Sci. Chem.* **A20** (1983) 583
- [39] J.A. Thiel, J.G. Brace, and R.W. Knoll, *J. Vac. Sci. Technol.* **A 12** (1994) 1365
- [40] A.M. Wróbel, *J. Macromol. Sci. Chem.* (1985) 1089
- [41] Silica Glass (SiO₂) Data Sheet, Crystan Ltd, Dorset, United Kingdom
- [42] M. Meier and A. von Keudell, *J. Chem. Phys.* **116** (2002) 5125
- [43] A. Zangwill, *Physics at Surfaces*, Cambridge University Press, Cambridge (1986)
- [44] H. Kersten and G.M.W. Kroesen, *J. Vac. Sci. Technol.* **8** (1990) 38
- [45] A.J.M. Buuron, D.K. Otorbaev, M.C.M. van de Sanden, and D.C. Schram, *Phys. Rev. E* **50** (1994) 1383
- [46] M.C.M. van de Sanden, J.M. de Regt, and D.C. Schram, *Phys. Rev. E* **47** (1993) 2792
- [47] J.W.A.M. Gielen, M.C.M. van de Sanden, P.R.M. Kleuskens, and D.C. Schram, *Plasma Sources Sci. Technol.* **5** (1996) 492
- [48] W.M.M. Kessels, *Remote Plasma Deposition of Hydrogenated Amorphous Silicon-Plasma Process, Film Growth, and Material Properties*, Ph.D. Thesis, Eindhoven University of Technology (2000)
- [49] W.M.M. Kessels, C.M. Leewis, M.C.M. van de Sanden, and D.C. Schram, *J. Appl. Phys.* **86** (1999) 4029
- [50] M.C.M. van de Sanden, R.J. Severens, W.M.M. Kessels, R.F.G. Meulenbroeks, and D.C. Schram, *J. App. Phys.* **84** (1998) 2426

- [51] P. Gaucherel and B. Rowe, *Int. J. of Mass Spectrom. Ion Phys.*, **25** (1977) 211
- [52] J.B. Hasted, *Physics of Atomic Collisions* Butterworths, Washington (1964)
- [53] G.J.H. Brussaard, *Remote Arc Generated Plasma in Diatomic Gases*, Ph.D. Thesis, Eindhoven University of Technology (1999)
- [54] J.W.A.M. Gielen, M.C.M. van de Sanden, W.M.M. Kessels, and D.C Schram, in *Thin Films: Stresses and Mechanical Properties VI*, ed. W.W. Gerberich, H. Hao, and J.-E. Sundgren, *Mat. Res. Soc. Proc.* (1996) 287
- [55] A.M. Wróbel, M. Kryszewski, and M. Gazicki, *J. Macromol. Sci.-Chem.* **A20** (1983) 583
- [56] J. Schwarz, M. Schmidt, and A. Ohl, *Surf. Coat. Technol.* **98** (1998) 859
- [57] M.F.A.M. van Hest, A. de Graaf, M.C.M. van de Sanden, and D.C. Schram, *Plasma Sources Sci. Technol.* **9** (2000) 615; Appendix to chapter 2 of this thesis

Chapter 6

Argon-oxygen plasma treatment of deposited silicon oxide like films

M.F.A.M. van Hest, A. Klaver, D.C. Schram, and M.C.M. van de Sanden

Abstract

Silicon oxide like films deposited from hexamethyldisiloxane and oxygen by means of an expanding thermal plasma have been exposed to an argon-oxygen plasma using the same plasma source as used for deposition of the films. From this it is possible to obtain more information of the reaction mechanism between oxygen radicals in the plasma and the deposited films. It has been shown that the carbon content of the deposited films, present in the form of methyl groups, can be almost fully removed. Therefore the deposited films need to have a significant porosity. The oxygen from the exposing plasma is also incorporated into the films forming Si-O-Si and Si-OH bonds. The dependencies of the various bonding types present in the film as function of exposure time and as function of the oxygen content of the exposure plasma are in agreement with two simple models; one for the plasma gas phase and one for the film. For the dependencies as function of exposure time the diffusion rate into and reaction rate in the film are important. For the dependencies as function of oxygen content in the plasma the difference between the atomic oxygen diffusion coefficient and the ambipolar argon ion diffusion coefficient is important. It has been shown that as function of the oxygen content in the plasma a maximum is observed in the change of the film.

6.1 Introduction

In a previous publication it has been shown that by means of an expanding thermal plasma it is possible to deposit silicon oxide like films from hexamethyldisiloxane (HMDSO, $(\text{CH}_3)_3\text{-Si-O-Si-(CH}_3)_3$) and oxygen at rates over 60 nm/s [1]. Although the deposited films contained carbon they showed good optical properties. To get a better insight in the surface and bulk reaction processes during deposition, the deposited film have been exposed to an argon-oxygen plasma. In this way a better understanding of the influence of oxygen in the deposition plasma can be obtained. Also more knowledge about the diffusion of oxygen into the film will be obtained by exposing the deposited films to an argon-oxygen plasma. The argon-oxygen plasma was created using the same plasma source and plasma reactor as has been used for the deposition of the silicon oxide like films. An extensive description of the deposition setup can be found in literature [1,2,3,4,5].

Table 6.1: *The plasma parameters used for silicon oxide like film deposition.*

Parameter	Value
Argon flow	25 sccs
Oxygen flow	5.0 sccs
HMDSO flow	2.0 sccs
Arc current	50 A
Vessel pressure	11 Pa
Deposited film thickness	0.75 μm
Substrate temperature	50 $^\circ\text{C}$

Table 6.2: *The plasma parameters used for the plasma treatment.*

Parameter	Value time series	Value oxygen series
Argon flow	100 sccs	100 sccs
Oxygen flow	1, 5, and 17 sccs	0, 1, 2, 3, 4, 5, 6, 8, 10, 12, 14, and 17 sccs
Treatment time	0.5, 1, 2, 5, 15, 30, and 60 minutes	15 minutes
Arc current	75 A	75 A
Vessel pressure	30 Pa	30 Pa
Substrate temperature	50 $^\circ\text{C}$	50 $^\circ\text{C}$

For the study of the influence of the argon-oxygen plasma on the deposited silicon oxide like films different experiments have been performed. First the effect of the exposure time has been studied. This has been done by selecting one plasma condition and changing the exposure time of a sample with a deposited silicon oxide like film. Second the effect of changing the oxygen concentration in the plasma has been studied. This is done by selecting one exposure time and expose a sample to a plasma containing different oxygen concentrations. All experiments have been done on films deposited under identical conditions as given in Table 6.1. Keeping all the plasma parameters the same for every deposition

experiment will in principle result in identical films. Verification by means of *ex situ* FTIR transmission absorption spectroscopy measurements [6,7] revealed that all deposited films were indeed identical. The various conditions used for the argon-oxygen plasma treatment are shown in Table 6.2. No film has been treated more than once.

6.2 Definitions

Before and after every treatment the films were analysed using *ex situ* FTIR transmission absorption spectroscopy. Figure 6.1 shows a typical transmission absorption spectrum of a silicon oxide like film before and after an argon-oxygen plasma exposure. Table 6.3 shows the absorption peaks found for silicon oxide like films deposited from HMDSO and oxygen. The CH₃ absorption peak at 2960 cm⁻¹, and the Si-CH₃ absorption peak at 1260 cm⁻¹ have been used to monitor the amount of methyl bonds present in the deposited film. The oxygen incorporation in the film has been monitored by means of the Si-OH absorption band at 3000-3600 cm⁻¹ and the Si-O_x absorption band at 430-350 cm⁻¹. From the Si-H band at 2100-2300 cm⁻¹ the Si-H bond content of the film material has been determined. The Si-O-Si absorption band at 1020-1070 cm⁻¹ has not been used to monitor the film because this band overlaps with the Si-O-C band. Overlap is also reason why the absorption peaks in the band 800-850 cm⁻¹ were ignored.

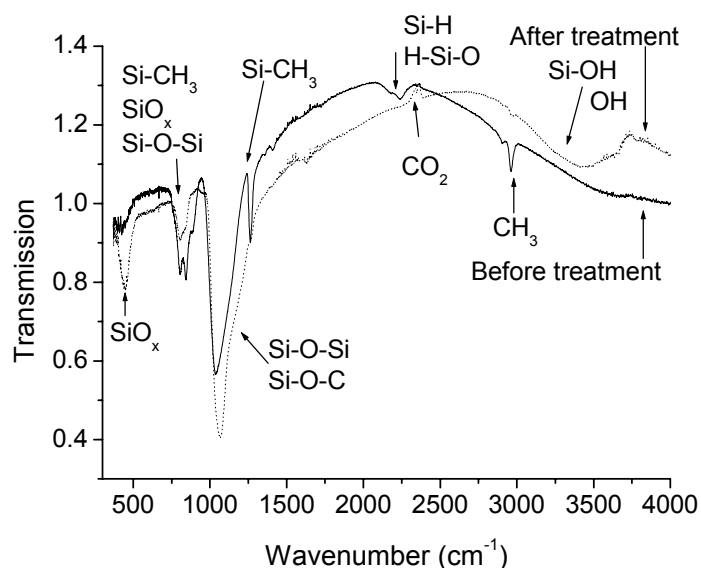


Figure 6.1: Typical FTIR transmission absorption spectrum before and after argon-oxygen plasma treatment.

In Figure 6.1 it can clearly be seen that exposing the deposited films to the argon-oxygen plasma changes the film significantly. The argon-oxygen plasma treatment decreased the methyl density and increase the oxygen density in the film. It can be seen that oxygen is incorporated in Si-O_x bonds as well as in Si-OH bonds. In Figure 6.1 it can also be seen that both the Si-H density and Si-CH₃ density are clearly reduced by the argon-oxygen plasma exposure.

Table 6.3: Absorption peaks measured for silicon oxide films deposited from HMDSO.

Bond type	Location absorption peak
Si-H	2100-2300 cm^{-1} [8,9]
Si-OH, OH	3000-3600 cm^{-1} [9,10,11]
Si-CH ₃	1260 cm^{-1} [8,9,12], 800-850 cm^{-1} [9,12,13]
CH _x	2960 cm^{-1} [8,11,13,14]
Si-O-Si	1020-1090 cm^{-1} [8,9,11,12,13], 800-850 cm^{-1} [11,13]
Si-O-C	1020-1090 cm^{-1} [8,11]
Si-O _x	430-450 cm^{-1} [8,9,10,11], 800-850 cm^{-1} [11,13]

To study the behaviour of the different absorption peaks as function of treatment time and as function of the oxygen flow, the changes in the different absorption peaks have been measured. The absorption intensity has been quantified by integrating the absorption intensity. For this purpose a baseline has been fitted and the difference between this baseline and the absorption intensity as function of the wavenumber has been integrated. However, for the Si-O_x absorption peak 430-450 cm^{-1} this integration method has not been used. The reason for this is the fact that this absorption peak is at the edge of the infrared spectrum measured by the FTIR transmission absorption spectroscope. Due to this part of the absorption peak cannot be measured accurate enough to obtain reliable integrated values of the absorption peak. However, the absolute absorption intensity can be measured accurately and therefore this is used for the Si-O_x absorption peak. The absolute absorption intensity is defined as the maximum difference between the absorption intensity and its baseline. The baseline has been constructed by extrapolating part of the spectrum from 500-750 cm^{-1} , which can be done because in this range no absorption is observed.

During the argon-oxygen plasma treatment, as well as during deposition, the samples were monitored by means of *in situ* ellipsometry [15,16]. In Figure 6.2 a typical Ψ - Δ trajectory of the film deposition and argon-oxygen plasma treatment is shown. The Ψ - Δ trajectory of the deposition of the silicon oxide like film can be modelled as one homogeneously growing film with one refractive index. The deposited film is therefore a homogeneous film. The Ψ - Δ trajectory obtained during the argon-oxygen plasma treatment of the deposited films have not been simulated. If no extra information of the film composition during treatment is known, the simulation of the spectrum has a large degree of freedom, and the simulation becomes a mathematical exercise with no physical relevance. Instead of using the ellipsometry data, the FTIR transmission absorption data has been used to obtain the optical thickness (refractive index times film thickness) of the treated films. The optical thickness is measured, because it is a parameter for which no detailed information about the homogeneity of the film is needed.

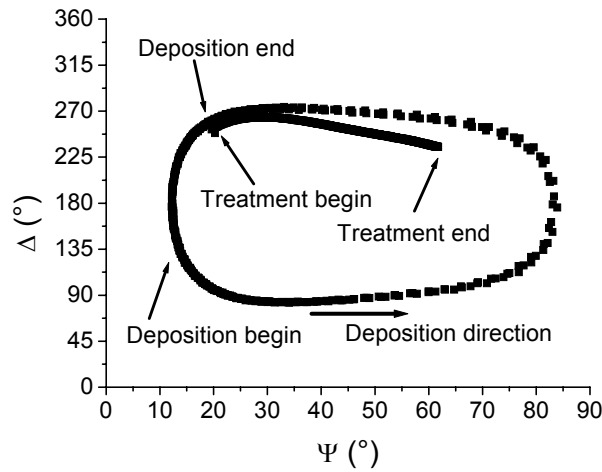


Figure 6.2: A typical ellipsometric Ψ - Δ trajectory obtained in situ of the film deposition and argon-oxygen plasma treatment.

6.3 Results

6.3.1 Exposure time

In Figure 6.3 the relative optical thickness of the treated films as function of treatment time for three different oxygen flows is shown. The relative optical thickness is the optical thickness after exposure to the argon-oxygen plasma relative to the optical thickness before plasma treatment. It can be seen in Figure 6.3 that the optical thickness is decreasing due to the interaction of the argon-oxygen plasma with the deposited silicon oxide film. It can also be seen that the change in optical thickness is time dependent. At first it looks like the time dependency is an exponential decay with the largest change for an oxygen flow of 5 sccs. The oxygen dependency will be discussed later.

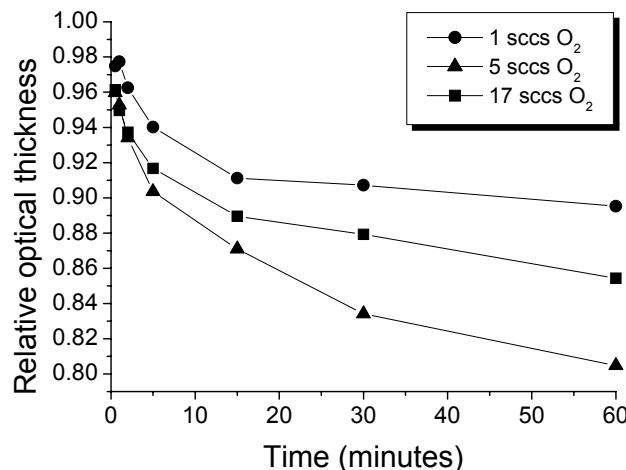


Figure 6.3: The relative optical thickness as function of the treatment time.

The change in optical thickness of the film is expected to be due to a change in the refractive index of the film. A physical reduction of the film thickness is unlikely because pure silicon dioxide films show no etching behaviour when exposed to the used argon-oxygen plasma. This indicates that oxygen is not capable of etching the silicon oxide matrix in the deposited film, leaving the film thickness to be unchanged. The only change due to etching of the films that can be obtained by the argon-oxygen plasma concerns the carbon and hydrogen atoms present in the film. Also attachment of oxygen at free sites present in the film is possible. These changes will only lead to a change in the refractive index and a change in optical thickness will therefore be proportional to the change in refractive index.

To see what exactly is changing in the film when the film is being exposed to an argon-oxygen plasma, the changes in the various infrared absorptions have been analysed. In Figure 6.4 the relative absorption of the carbon related absorption peaks (CH_3 and Si-CH_3) is shown as function of treatment time for three different oxygen flows. The relative absorption is the integrated absorption intensity after treatment relative to the integrated absorption intensity before treatment. In Figure 6.4 it can be seen that the carbon presence in the form of methyl groups reduces significantly and that the change is similar for the CH_3 absorption as well as for the Si-CH_3 absorption. The reduction shows the same trend as function of time as the optical thickness and also the biggest change is observed for an oxygen flow of 5 sccs. The maximum decrease of the carbon related absorptions is almost 90 %, which shows that treatment of a deposited silicon oxide like film with an argon-oxygen plasma is capable of removing almost all the carbon in the film. This means that also the carbon which is situated deep in the film close to the substrate is also removed, which can only be done when oxygen is able to penetrate the film totally. This is only possible when the film is porous. If the film would not be porous the penetration depth of oxygen present in an argon-oxygen plasma is limited to approximately 10 nm [17,18].

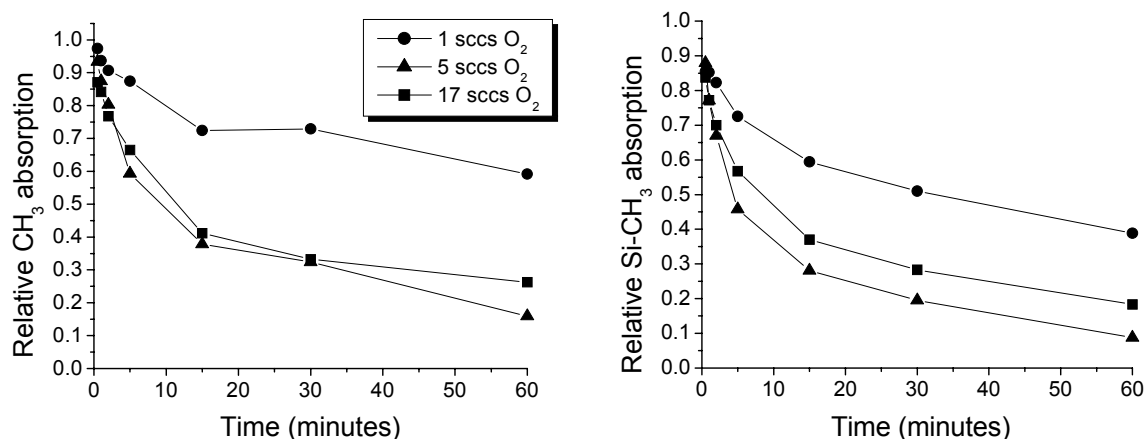


Figure 6.4: Relative absorption of CH_3 and Si-CH_3 .

Not only the CH_3 and Si-CH_3 absorption intensities are decreasing, but also the Si-H absorption intensity is decreasing as function of time during argon-oxygen plasma treatment of the deposited film. In Figure 6.5 the relative Si-H absorption intensity is given as function of time for three different oxygen flows. It can be seen that the decrease is similar to that of CH_3 and Si-CH_3 and that the largest decrease is observed at 5 sccs. For the Si-H also a significant change is observed when the film is only treated for one minute. This can be due to

the fact that the CO₂ absorption (cf. Figure 6.1) has a small overlap with the Si-H absorption. This can influence the accuracy of the absorption peak integration, however the uncertainty introduced will be small and can be positive as well as negative. Although this uncertainty is introduced it can therefore still be said that the response of the Si-H bond in the film to the argon-oxygen plasma treatment is faster than for CH₃ and Si-CH₃ bonds.

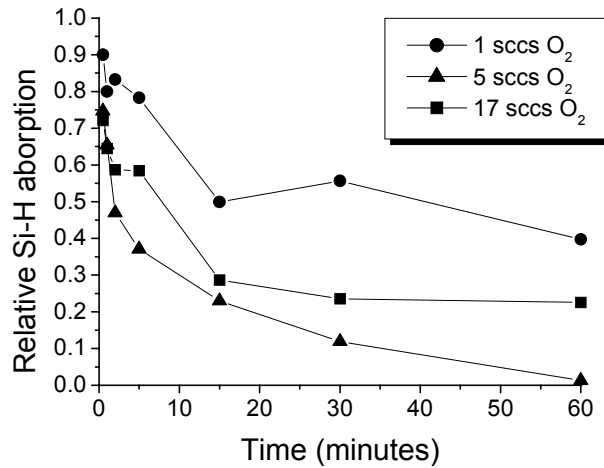


Figure 6.5: Relative absorption of Si-H.

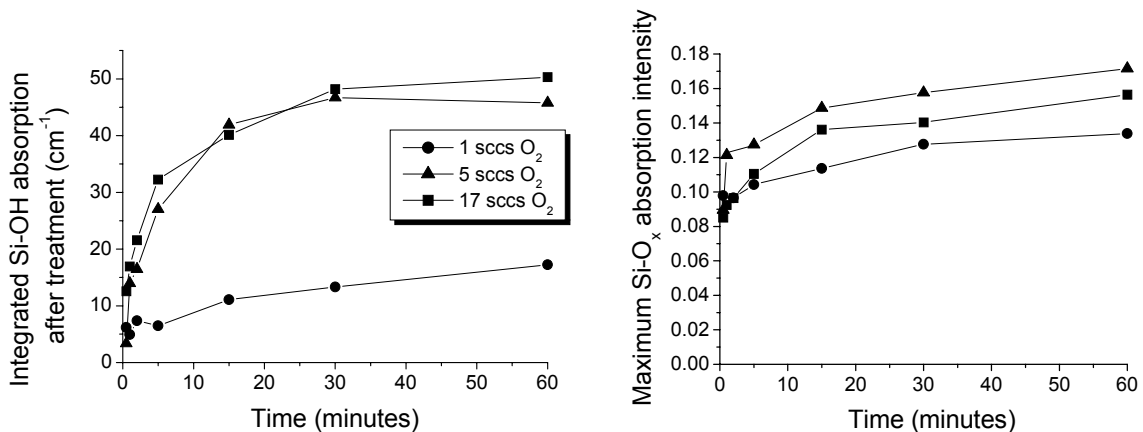


Figure 6.6: Integrated area of the Si-OH absorption peak and the maximum absorption intensity of the Si-O_x absorption peak.

Apart from absorption peaks that decrease during the argon-oxygen plasma treatment there are also absorption peaks that show an increase in absorption intensity. In Figure 6.6 the integrated absorption intensity of the Si-OH absorption peak is shown as function of the treatment time and again for three different oxygen flows. For this absorption peak it is not possible to look at the relative absorption intensity because the peak is almost not present in the film as deposited (cf. Figure 6.1). It can be seen in Figure 6.6 that the Si-OH absorption increases rapidly as function of the treatment time. The difference between using 5 sccs and 17 sccs of oxygen is very small.

In Figure 6.6 also the maximum absorption of the Si-O_x absorption peak is shown. As explained before this peak can not be integrated and therefore the maximum absorption

intensity is shown. As can be seen from Figure 6.6 the number of Si-O_x bonds increases with treatment time. Just as for all the other absorption peaks the biggest change is observed at an oxygen flow of 5 sccs. It can be seen that the change has a similar trend than that of the Si-OH absorption peak. Unlike the Si-OH absorption the difference in absorption intensity between 5 sccs and 17 sccs for the Si-O_x absorption is significant.

Looking more careful at the behaviour of the various bonding types, they can be divided into two different categories. The first category shows a significant difference in the change of the absorption obtained at 5 sccs and the absorption obtained at 17 sccs. The second category does not show this difference. The Si-CH₃, Si-H and Si-O_x bonds are part of first category and the CH₃ and Si-OH bond are part of the second category. Looking at the categories shows that in each category there is at least one bond that is removed as function of time and one bond that is created as function of time during the argon-oxygen plasma treatment. From this it could be derived that the removed bond is replaced by the created bond. To get a better insight the behaviour of the different absorption peaks has been analysed as function of the oxygen flow.

6.3.2 Oxygen flow variation

In Figure 6.3 it has already been shown that changing the oxygen flow changes the effect of the argon-oxygen plasma on the different bonds present in the deposited film. In Figure 6.7 the relative optical thickness as function of the oxygen flow is shown. All samples have been treated for 15 minutes by the argon-oxygen plasma. For this treatment time still a significant fraction of the carbon and hydrogen related bonds is remaining. In Figure 6.7 it can be seen clearly that the optical thickness does not change uniformly with a change in the oxygen flow. At a value around 5 sccs the change has a maximum value, after which an increase in oxygen flow results in a decrease in the change of the optical thickness.

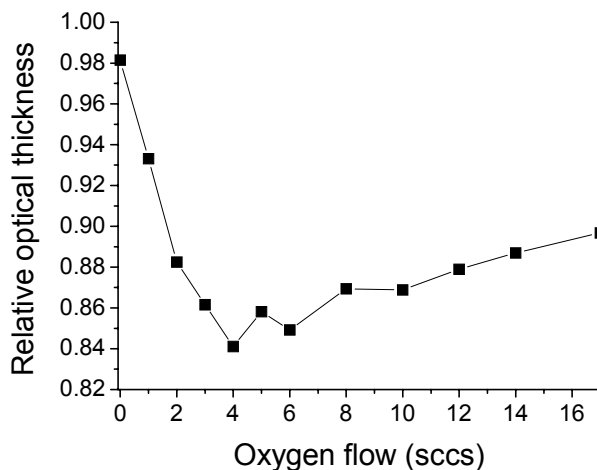


Figure 6.7: Relative optical thickness as function of the oxygen flow.

It can be seen that also without the addition of oxygen to the plasma still a small change in the optical thickness is observed. This can be due to different effect. First it can be a real change in the film properties. Second it can be due to the fact that the FTIR transmission absorption measurement, from which the optical thickness is derived, has been performed *ex*

situ. Therefore the samples had to be transported through air which may lead to a small change in the film properties due to interaction with the particles present in the air. A third effect responsible for the small change in the optical thickness when no oxygen is added to the treatment plasma is a change in film properties after deposition due to cross linking of free bonds. This third effect is expected to occur on a shorter time scale than the time scale needed to perform the *ex-situ* FTIR transmission absorption measurements. Therefore this effect is likely to be negligible.

Also the behaviour of the different absorption intensities as function of the oxygen flow, for a 15 minutes treatment, has been studied. In Figure 6.8 the relative absorption intensities for the Si-CH₃, CH₃ and the Si-H bonds are shown. It can be seen from this figure that the trend observed for these absorption peaks is similar to the trend observed in the optical thickness. It can also be seen that the strongest relative change is observed for the Si-H bond. A maximum reduction of the CH₃, Si-CH₃ and Si-H bond types can be observed when approximately 5 sccs of oxygen is added to the post deposition treatment plasma.

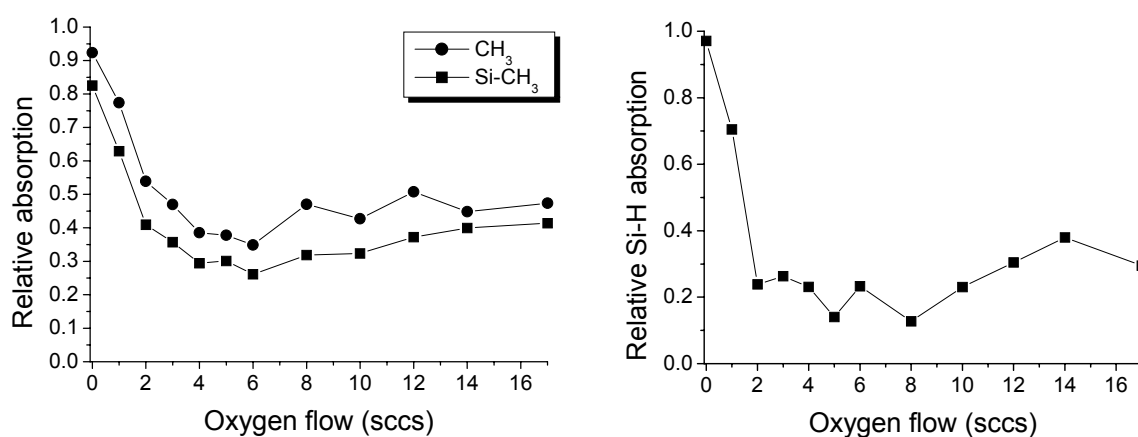


Figure 6.8: Relative absorption of CH₃, Si-CH₃ and Si-H as function of the oxygen flow.

A change in the absorption intensity is also observed for sample treated by a pure argon plasma (0 sccs oxygen), which indicates that the amount of carbon and hydrogen present in the film is reduced by the argon plasma. Therefore the observed change in optical thickness cannot be caused by cross linking of bonds, because this would lead to an increase in the measured absorption intensity. Therefore it has to be caused by either argon plasma induces reactions at the sample surface or by the influence of the air exposure while performing the *ex situ* FTIR transmission absorption measurement. It is likely that the argon plasma will only have an effect at the surface of the film, because the ions and electrons will neutralize at the surface as the ion energy and electron temperature are low (a few tenths of eV). Therefore an interaction of the sample with ambient air is more likely the cause of the change. Although measurement of the FTIR transmission absorption spectrum of an untreated film just after deposition and a couple of weeks after the deposition show no significant change in the transmission absorption spectrum.

In Figure 6.9 the integrated absorption intensity of the Si-OH bond is shown. It can be seen that the change is strongly dependent on the oxygen flow for oxygen flows up to 5 sccs. For oxygen flows higher than 5 sccs the influence on the Si-OH bond is almost independent on the oxygen flow, which explains why there was almost no difference between the absorption intensities as function of time measured for 5 sccs and 17 sccs (cf. Figure 6.6).

Notice that this is not caused by saturation. The absorption intensity can still increase with an increase in exposure time (cf. Figure 6.6). In Figure 6.9 also the maximum absorption intensity of the Si-O_x absorption peak as function of the oxygen flow is shown. It can be seen that the absorption intensity increases for oxygen flow up to 5 sccs, for higher oxygen flows the absorption intensity decreases slightly. The relative change for Si-OH is clearly higher than that for Si-O_x.

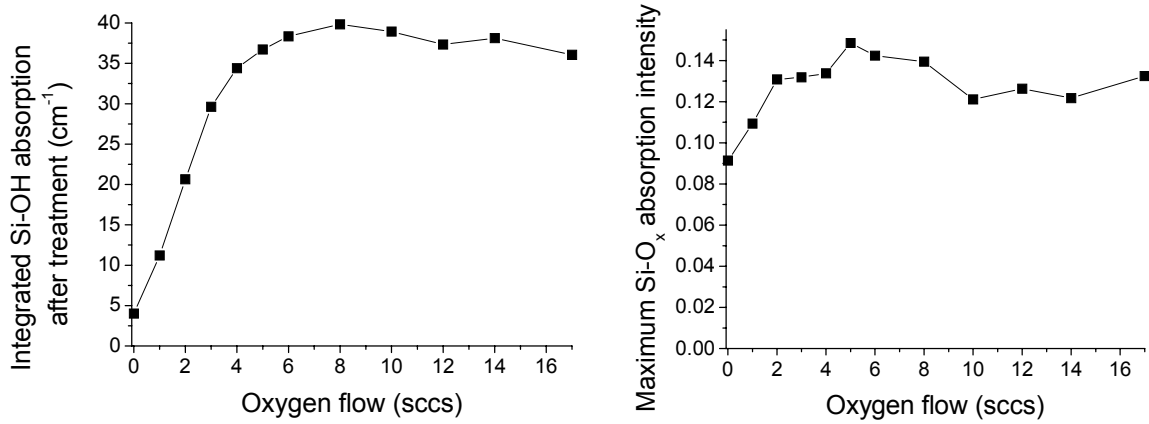


Figure 6.9: *Integrated area of the Si-OH absorption peak and the maximum absorption intensity of the Si-O_x absorption peak.*

6.4 Discussion

6.4.1 Exposure time

To obtain information on the argon-oxygen plasma modification process the time dependencies of the various bonds need to be analysed in more detail. Assume that the process of etching carbon species and the addition of oxygen to the film can be described by one simple reaction equation:



where the ‘reaction site’ is any carbon species or any site to which oxygen can attach. A ‘neutral site’ is a site at which no reaction is possible anymore. It is assumed that only oxygen radicals are responsible for the reactions in the film. The reaction rate (α) is assumed to be constant. Before a reaction can take place at a specific site, the reacting species need to diffuse into the film. The film is deposited homogenously and therefore the diffusion coefficient (D_o) is assumed to be constant. During the diffusion process, also the reacting species can recombine and become non-reacting species. The rate of this loss process depends on the reacting species density with a reaction rate β .

The time dependency (t) of the density of reacting species ($n_o(t, d)$) at a specific depth (d , $d=0$ is at the surface) can then be written as:

$$\frac{\partial n_o(t, d)}{\partial t} = -\alpha n_o(t, d) n_s(t, d) - \beta n_o(t, d) + D_o \frac{\partial n_o(t, d)}{\partial d} \quad (6.2)$$

The time dependency change of the reaction site density ($n_s(t, d)$) can be written as:

$$\frac{\partial n_s(t, d)}{\partial t} = -\alpha n_o(t, d) n_s(t, d). \quad (6.3)$$

The boundary conditions of this system of differential equations are given by:

$$\begin{aligned} n_o(t, 0) &= N_o \\ n_s(0, x) &= N_s(0) \end{aligned} \quad (6.4)$$

where N_o is the initial reacting species density in the film at the surface which is assumed to be equal to the maximum reacting species density possible in the film. $N_s(0)$ is the density of the reacting sites in the film as deposited. For comparison of the model with the infrared absorption measurements the reactive site density has to be integrated over the thickness of the film (D) to obtain the line density, i.e. the total number of reactive sites present in the film per unit of the surface ($N_s(t)$):

$$N_s(t) = \int_0^D n_s(t, \xi) d\xi \quad (6.5)$$

It is not possible to solve the system of differential equations analytically and therefore the system has been solved numerically. From this numerical analysis it has been derived that there are three different solutions. The first solution is in the case that the reaction rate is high enough to keep up with the diffusion. In this case a reaction front is formed which moves through the film. The film can be seen as having two parts, the top of the film without and the bottom of the film with reaction sites. As a result of this the total number of reactive sites will have a close to exponential decrease. The second solution is in the case that the diffusion is much faster than the reaction rate, which results in a gradient of the reaction sites which goes from top to bottom of the film. As a result of this the total number of reaction sites again decreases close to exponential. The third solution is obtained when both the reaction rate and diffusion rate are of the same order. The observed changes in the various absorption intensities cannot be fitted by means of an exponential function. Therefore in Figure 6.10 simulations are given for the last case. The constants indicated in Figure 6.10 are constants used in the differential equation when the densities are normalized for the initial (N_s) or either the final value (N_o). It can be seen in Figure 6.10 that the change of the number of reaction sites as function of time is similar to the change measured for the different absorption intensities correlated with carbon species (cf. Figure 6.4).

In Figure 6.10 it can also be seen that changing the density of reacting species at the surface with a factor of five results in change similar to that observed in the measurements (cf. Figure 6.4). Changing the reaction rate results in a similar change as observed for the Si-CH₃ and the CH₃ bonds. Besides calculating the number or reaction sites, also the number of reacted sites can be calculated. This results in a picture similar to the increase in the Si-OH

bonds density observed (cf. Figure 6.6). Therefore it can be concluded that the chosen model for the post treatment process is in good agreement with reality.

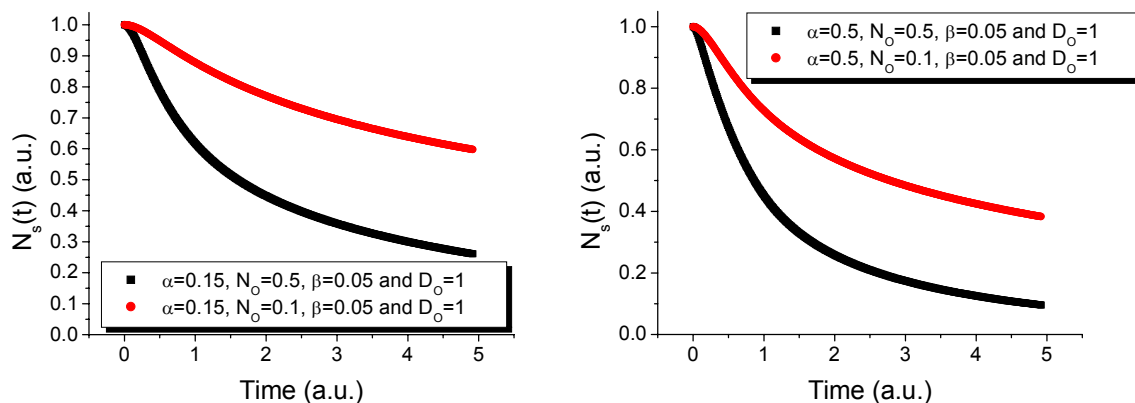


Figure 6.10: Simulated number of reaction sites as function of time for different parameters.

The model can now be used to calculate the various reaction rates for the various bonds, however the calculations with the model have been performed on relative densities and that makes the resulting rates non-comparable to normal reaction rates. Also when calculating the reaction rates it is assumed that there is only one kind of reacting site present, which is not the case in the deposited films because Si-H is different from Si-CH₃. To include all different bonds which are present with their specific reaction rate means that for every bond type a term has to be added to the model. This will introduce many more variables, which will result in multiple solutions for the various reaction coefficients when fitting the measured data.

When using the model without taking these considerations into account it is possible to get some quantitative information. From comparison of the simulations shown in Figure 6.10 and the measurements shown in Figure 6.4 it can be seen that the reaction rate for Si-CH₃ bond elimination is approximately a factor 3 higher than for CH₃ bond elimination. This shows that CH₃ groups are more easily removed as a complete group than partly on interaction with oxygen radicals. This is in agreement with the results from a previous study on the properties of the deposited films presented in reference [1].

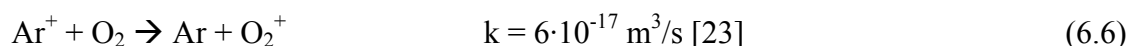
6.4.2 Oxygen flow variation

The maximum observed in the change of various bonds as function of the oxygen flow has been observed before. A similar effect is found with reactive ion etching (RIE) [19] and reactive sputter etching (RSE) [20] experiments on organic polymers (C_xO_y material) using an argon-oxygen gas mixture. In these plasmas the reactive particle with the polymer is atomic oxygen or ionic oxygen (O₂⁺). The effect is only observed at low pressures (10 to 100 Pa) and is contributed to the ions. With ion assisted etching the damage in the lattice caused by the ions reduces the activation energy. Therefore the rate constant of the chemical reaction is increased. With an increase in the oxygen content, more atomic and ionic oxygen is created but at the same time the energy of the ions (T_i) is decreased. The lower energy is a result of the lower voltage drop at the plasma sheath. This results in a lower energy flux to the surface.

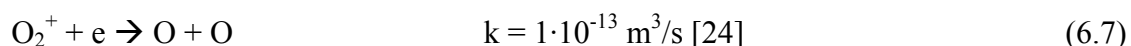
The increase in oxygen atoms and the decrease in ion energy then results in a maximum for the etch rate as function of the oxygen flow.

With the expanding thermal plasma used in this research this scenario is rather unlikely. Although the pressure in the reactor is of the same order, there are also significant differences. The expanding thermal plasma used is a remote plasma, whereas the plasma used for the polymer etching are active plasmas. The remote plasma used has a small ion energy (couple of tenths of eV [21,22]). Therefore there is no ion induced damage and the energy flux to the sample will be smaller, due to which the enhancement of etching by ions will be lost. The total molecular oxygen ion flux towards the surface will be smaller because the used plasma is a remote plasma and these ions can dissociatively recombine with an electron in the gas phase. Moreover when ion assisted etching would occur the ion assisted etching will be limited to the surface of the deposited film and will not have a contribution in the whole film.

First of all the plasma generated with the cascaded arc is an argon plasma which contains mainly argon atoms, argon ions and electrons. The oxygen is injected close to the plasma inlet. The molecular oxygen will charge exchange with argon ions and form molecular oxygen ions:



after which the molecular oxygen ions will dissociatively recombine with an electron, resulting in two oxygen atoms:



This dissociative recombination step is very fast in comparison with the charge exchange step and therefore it is allowed to say that the dissociative step will occur almost instantaneously with the charge exchange reaction. Only the molecular oxygen ions generated close to the substrate will reach the substrate, and thus the ionic molecular oxygen density will indeed be low and with this also the resulting energy flux to the substrate.

A more likely explanation of the measured effect has been given by Brussaard [25]. Although an increase in the oxygen flow increases the production of oxygen atoms, it could also decrease the flux of oxygen atoms to the substrate. The oxygen atom flux to the substrate does not only depend on the creation of the oxygen atoms, but also on the transport of these atoms to the substrate. When the oxygen flow is low, the creation of oxygen atoms is low. When increasing the oxygen flow, more oxygen ions will be formed more close to the oxygen injection point and less argon ions will be present close to the substrate. The oxygen atom production downstream drops and the production becomes more concentrated near the oxygen inlet. In this case the oxygen atoms will have more time to diffuse out of the plasma beam towards the wall and less oxygen atoms will reach the substrate. This is only true when the diffusion coefficient of the oxygen atoms is larger than the ambipolar diffusion coefficient of the argon ions. In first approximations the diffusion coefficient will be inversely proportional to the square root of the masses and thus the oxygen atom diffusion coefficient will be about 1.6 times larger than the argon ion ambipolar diffusion coefficient.

In the model used by Brussaard it was assumed that the diffusion coefficient of the atomic oxygen could be taken much larger than the ambipolar diffusion coefficient 400 m^{-1} and 4 m^{-1} respectively. With the model the normalized atomic oxygen flow at the substrate as function of the atomic oxygen flow can be calculated using the following equation:

$$n_{O_2}(z) = 2n_{Ar^+}(0)k_{ce} \frac{1}{v_d} \int_0^z \frac{\exp(-n_{O_2})k_{ce} \frac{1}{v_d} z'}{\frac{4D_{O_2}}{v_d(\rho(o))^2}(z-z') + \frac{4D_{Ar^+}}{v_d(\rho(o))^2}(z'-1)} dz' \quad (6.8)$$

$$n_{O_2} = \frac{\phi_{O_2}}{\phi_{tot}} \frac{p}{kT} \quad (6.9)$$

where k is the Boltzman constant and the other parameters are described in Table 6.4. Also the typical values of the various parameters are given in this table.

It can be seen in the model that when the ambipolar diffusion coefficient of argon ions is larger than the diffusion coefficient of oxygen atoms, the normalized atomic oxygen flow will always increase with increasing oxygen flow. It can also be seen that in the case the diffusion coefficients of atomic oxygen and ionic argon are equal the atomic oxygen flow at the substrate will saturate. However, the diffusion coefficient of atomic oxygen is larger than the ambipolar diffusion coefficient of ionic argon. In that case the oxygen flux at the substrate will show a maximum value as function of the oxygen flow injected.

Table 6.4: Parameters used in Eq. (6.8).

Parameter	Description	Value
$n_{Ar^+}(0)$	Normalized argon ion flux from arc	1
k_{ce}	Charge exchange rate	$10^{-16} \text{ m}^3/\text{s}$
v_d	Plasma drift velocity*	400 m/s
n_{O_2}	Molecular oxygen flow rate	Given by Eq. (6.9)
z	Distance from arc to substrate	0.6 m
$\frac{4D_{O_2}}{v_d(\rho(o))^2}$	Atomic oxygen diffusion coefficient	6.4 m^{-1}
$\frac{4D_{Ar^+}}{v_d(\rho(o))^2}$	Argon ambipolar diffusion coefficient	4.0 m^{-1}
$\frac{\phi_{O_2}}{\phi_{tot}}$	Fraction oxygen flux to total gas flux	0/100 to 17/117
p	Reactor pressure	28 Pa
T	Gas temperature	1500 K

Table 6.4 shows typical values for the various parameters in Eq. (6.8). Some parameters have been chosen as being constant, but they are not constant in reality, e.g. drift velocity and temperature. However, the exact values are not known and therefore it is hard to use this model to fit the measured data. In Figure 6.11 an example is given of a calculation of

* Average value from Laser induced fluorescence measurements.

the normalized atomic oxygen flux, using the values given in Table 6.4. It can clearly be seen in this figure that the trend of the normalized atomic oxygen flux is similar to the argon-oxygen treatment trends measured. It can also be seen that a weak maximum for the normalized atomic oxygen flow is obtained at an oxygen flux of 5 sccs. This forms an indication that the used values are close to the real values and that the model is a good representation of reality. It is therefore valid to say that the dominant particle responsible for the change in the deposited films in the argon-oxygen treatment is atomic oxygen.

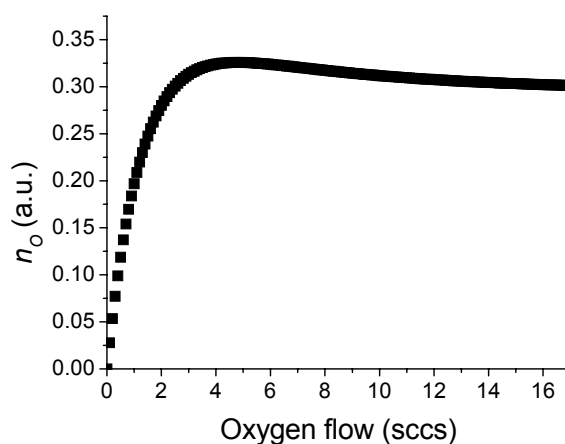


Figure 6.11: Atomic oxygen flux as function of the molecular oxygen flow.

6.4.3 Reaction mechanism

So far it has been shown that the post treatment process is a combination of diffusion of reacting particles into the film and reactions in this film creating oxygen related bonds and removing carbon related bonds. It has also been shown that the reacting particle is most likely the oxygen radical. Using this in combination with the various dependencies measured it is now possible to deduce a reaction mechanism for oxygen radicals with the film.

When looking at the various dependencies as function of time it can be seen that the increase in the Si-OH bond (Figure 6.6) is similar to the decrease in the CH₃ bond (Figure 6.4). Also it can be seen that the decrease in the Si-CH₃ bond (Figure 6.4) as well as the decrease in the Si-H bond (Figure 6.5) is similar to the increase in the Si-O_x bond (Figure 6.6). This latter correlation is less clear because the Si-O_x bond is already present before starting the argon-oxygen plasma post treatment. However when looking more careful at the time dependence and the changes using different oxygen flows it can be seen that the trend is of the same kind. The fact that different bonds show a similar time dependency during an argon-oxygen plasma treatment indicates that the bond of which the density is decreasing is transformed into the bond that shows the similar increasing density behaviour. However this transformation does not have to be a single step reaction. The reacting particle can first break the bond and remove a species and then in a next reaction the reacting particle could attach and form the new bond. When the attaching step is much faster than the removal step, the process could occur as if happening in one single reaction and therefore it is still hard to derive the exact reaction mechanism for the various transitions observed.

It is likely that the first step in the reaction mechanism for Si-CH₃ to Si-O_x is given by:



The formation of formaldehyde ($\text{O}=\text{CH}_2$) has been observed before in different processes involving silicon oxide like film deposition [26,27]. In the argon-oxygen plasma treatment process of the deposited silicon oxide like film this molecule has to diffuse out of the film. Measurement of the infrared gas phase absorption measurement did not show the presence of this particle. However the density is expected to be low because during the diffusion out of the film this particle can react with oxygen radicals diffusing into the film. Such reactions lead to the formation of carbonmono- and dioxide and water. In the first reaction between $\text{Si}-\text{CH}_3$ and oxygen radicals $\text{Si}-\text{H}$ bonds are formed, which is being converted into $\text{Si}-\text{O}_x$ by two more reactions with oxygen radicals:



The second reaction is assumed to be a fast reaction, because a silicon atom with a free bond in the film will easily form a bond with a radical in the close vicinity of this atom. Note that this second part of the reaction process for the conversion of $\text{Si}-\text{CH}_3$ bonds to $\text{Si}-\text{O}_x$ bonds is the same reaction process as for the conversion of $\text{Si}-\text{H}$ bonds to $\text{Si}-\text{O}_x$ bonds. As the $\text{Si}-\text{H}$ bond is weaker than the $\text{Si}-\text{CH}_3$ bond, this second step is faster than the first step. Therefore the $\text{Si}-\text{H}$ bond density in the film should be proportional with the $\text{Si}-\text{CH}_3$ bond density when the $\text{Si}-\text{H}$ bonds present in the deposited film are converted to $\text{Si}-\text{O}$ bonds. Looking carefully to Figure 6.4 and Figure 6.5 shows that the $\text{Si}-\text{H}$ bond density decreases rapidly in the first 5 minutes after which it follows the trend of the $\text{Si}-\text{CH}_3$ bond density corroborating the shown reaction mechanism. Notice that the OH radical formed in the first reaction of Eq. (6.11) could reattach to the film generating $\text{Si}-\text{OH}$ bonds.

The formation of $\text{Si}-\text{OH}$ bonds from CH_3 bonds is also a two step process. The first step is given by:



Also here formaldehyde is formed, but as said before this particle will react with a second oxygen radical to form carbonoxides and water. The produced hydrogen atoms will react with $\text{Si}-\text{O}$ bonds which have a free bond by:



leading to the formation of $\text{Si}-\text{OH}$ bonds in the film. Notice that the hydrogen atoms can also react with silicon atoms which have a free bond forming $\text{Si}-\text{H}$.

Exposing the deposited silicon oxide like films to the argon-oxygen plasma for a much longer time than used in the shown measurements will eventually lead to a decrease of the $\text{Si}-\text{OH}$ bond density because this bond will again react and loose its hydrogen content. However, the film will most probably not become 100 % hydrogen free silicon oxide, because the deposited films have a significant porosity [1]. Therefore it is impossible to form a full silicon oxide network. As a matter of fact it is due to the porosity that it is possible to make carbon free silicon oxide films by argon-oxygen plasma treatment of the deposited films.

Not all the mentioned reactions with oxygen will also occur during deposition of a silicon oxide like film from HMDSO and oxygen, because then there is a competition between deposition particles and oxygen radicals. When on interaction of the film and an

oxygen radical a free reaction site (dangling bond) is created, a deposition particle can attach to this site. This results in film growth. Therefore the reactions for which multiple oxygen radicals are needed to obtain the end product (e.g. Eq. (6.11)) are unlikely to occur in a deposition plasma. For the same reason the Si-OH bond will be present in very low concentrations in the film at high deposition rates, which is in agreement with measurements [1].

6.5 Conclusions

Silicon oxide like films have been deposited at high rates by means of an expanding thermal plasma in combination with HMDSO and oxygen as precursors. It has been shown that these films contain a significant amount of carbon, which can be removed by treating the deposited films with an argon-oxygen plasma. Measurements clearly show that these initially carbon containing silicon oxide like films can be made carbon free. The process of removing the carbon is slow and it will take a long time compared to the deposition time to remove all the carbon. It is therefore not a solution for producing carbon free silicon oxide films at high deposition rates. The possibility of full removal of the carbon is mainly due to the porosity of the deposited silicon oxide films, which makes it possible for particles from the plasma to penetrate the whole film.

The process of removal of the carbon from the films is dominated by diffusion of oxygen radicals into the film which etch away the carbon content. The oxygen radicals also form new bonds with the film leading to the incorporation of oxygen in the film. The removal of the carbon content from the film is a non linear process in time, but by a simple model the time dependency of the carbon removal from the film can be simulated. The shown model is in good agreement with the observed time dependent changes of the carbon density in the argon-oxygen plasma treated films. The amount of carbon removed from the film per unit of time is dominated by the flux of oxygen radicals at the surface.

The total flux of oxygen radicals at the substrate level of the plasma reactor is not only dependent on the total power input and the amount of oxygen injected in the plasma, but it is also dependent on the reactor geometry. Oxygen molecules injected in the plasma will react with the plasma and form oxygen radicals in a two step reaction process. Due to the fact that the outward diffusion of oxygen radicals is faster than that of argon ions, an increase in oxygen input can result in smaller atomic oxygen flux to the substrate surface. The larger the distance between the molecular oxygen injection point and the substrate the stronger the effect will be.

A fairly simple reaction mechanism is suggested for the reaction between atomic oxygen radicals and the deposited silicon oxide like film. The changes in the films by the argon-oxygen plasma treatment can be described with this mechanism. Although the mechanism holds for argon-oxygen plasma treatment of deposited silicon oxide like films from HMDSO and oxygen, not all the reactions will occur while a silicon oxide like film is being deposited using HMDSO and oxygen as a precursor. Just as in the argon-oxygen plasma treatment, oxygen radicals will cause the formation of free reaction sites in the film that is being deposited. Instead of reacting again with oxygen radicals these sites are more likely to react with the deposition species in the deposition plasma, resulting in film growth. To be able to deposit pure silicon dioxide films with the expanding thermal plasma, the deposition rate needs to be decreased or either the carbon etch rate at the film surface needs to

be enhanced by means of e.g. ion bombardment. This can be done by applying an RF bias to the substrate.

References

- [1] M.F.A.M. van Hest, B. Mitu, D.C. Schram, and M.C.M. van de Sanden, *Deposition of silicon oxide like films using a remote thermal plasma*, to be published; Chapter 5 of this thesis.
- [2] G.M.W. Kroesen, D.C. Schram, and M.J.F. van de Sande, *Plasma Chem. Plasma Proc.* **10** (1990) 49
- [3] J.W.A.M. Gielen, M.C.M. van de Sanden, P.R.M. Kleuskens, and D.C. Schram, *Plasma Sources Sci. Technol.* **5** (1996) 492
- [4] J.W.A.M. Gielen, W.M.M. Kessels, M.C.M. van de Sanden, and D.C. Schram, *J. Appl. Phys.* **82** (1997) 2643
- [5] A. de Graaf, *Deposition of CNH Materials; Plasma and Film Characterization*, Ph.D. Thesis, Eindhoven University of Technology (2000)
- [6] R.J. Bell, *Introductory Fourier Transform Spectroscopy*, Academic Press, New York (1972)
- [7] A.E. Martin, *Infrared Interferometric Spectrometers*, editor J.R. During, Elsevier Scientific Publishing Company, Amsterdam (1980)
- [8] K. Kashiwagi, Y. Yoshida, and Y. Murayama, *Jap. J. Appl. Phys.* **30** (1991) 1803
- [9] J.A. Thiel, J.G. Brace, and R.W. Knoll, *J. Vac. Sci. Technol. A* **12** (1994) 1365
- [10] M. Nakamura, Y. Mochizuki, and K. Usima, *Solid State Comm.* **50** (1984) 1079
- [11] K. Sano, S. Hayashi, S. Wickramanayaka, and Y. Hatanaka, *Thin Solid Films* **281-282** (1996) 397
- [12] S.H. Lee and D.C. Lee, *Thin Solid Films* **325** (1998) 83
- [13] K.H.A. Bogart, N.F. Dalleska, G.R. Bogart, and E.R. Fisher, *J. Vac. Sci. Technol. A* **13** (1995) 476
- [14] B. Dischler, A. Bubenzer, and P. Koidl, *Solid State Comm.* **48** (1983) 105
- [15] A.H.M. Smets, D.C. Schram, and M.C.M. van de Sanden, *J. Appl. Phys.* **88** (2000) 6388
- [16] R.M.A. Azzam and N.M. Bashara, *Ellipsometry and Polarized Light*, North-Holland Publishing Co., Amsterdam (1977)
- [17] J. Peeters and L. Li, *J. Appl. Phys.* **73** (1993) 2477
- [18] H. Shindo, T. Koromogawa, T. Fuji, K. Kusaba, and Y. Horiike, *Surface and Coatings Technol.* **116-119** (1999) 618
- [19] M. Sugawara, *Plasma Etching - Fundamentals and Applications*, Oxford University Press (1998)
- [20] C. Steinbrüchel, B.J. Curtis, H.W. Lehmann, and R. Widmer, *IEEE Transactions on Plasma Sci.* **14** (1986) 137
- [21] M.F.A.M. van Hest, J.R. Haartsen, M.H.M. van Weert, D.C. Schram, and M.C.M. van de Sanden, *Analysis of the argon-oxygen plasma gas phase*, to be published; Chapter 4 of this thesis
- [22] J.J. Beulens, M.J. de Graaf, G.M.W. Kroesen, and D.C. Schram, *Proc. Mat. Res. Soc.* **190** (1990) 311
- [23] P. Gaucherel and B. Rowe, *Int. J. of Mass Spectrom. Ion Phys.*, **25** (1977) 211
- [24] J.B. Haster, *Physics of Atomic Collisions*, Butterworths, Washington (1964)

- [25] G.J.H. Brussaard, *Remote Arc Generated Plasma in Diatomic Gases*, Ph.D. Thesis, Eindhoven University of Technology (1999)
- [26] D. Magni, Ch. Deschenaux, Ch. Hollenstein, A. Creatore and P. Fayet, *J. Phys. D* **34** (2001) 87
- [27] C. Courtielle, D. Magni, Ch. Deschenaux, P. Fayet, A.A. Howling, and Ch. Hollenstein, 41st Annual Technical Conference Proceedings, Society of Vacuum Coaters (1998)

Chapter 7

The reaction mechanism of HMDSO in an expanding thermal argon plasma

M.F.A.M. van Hest, D.C. Schram, and M.C.M. van de Sanden

Abstract

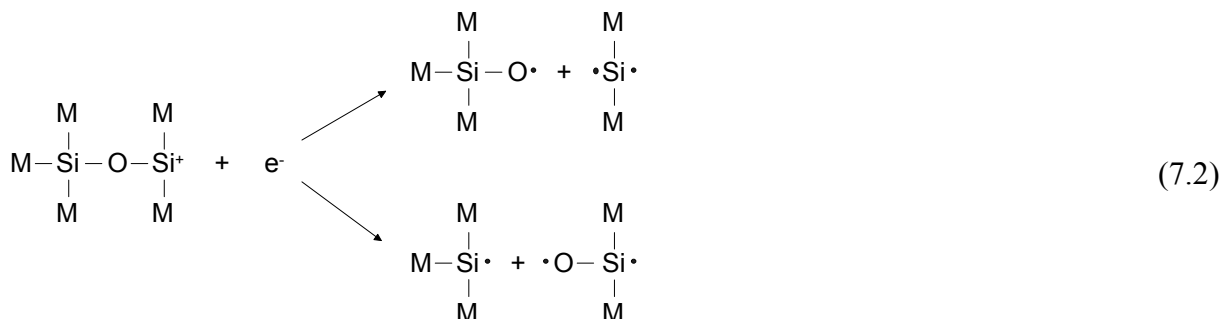
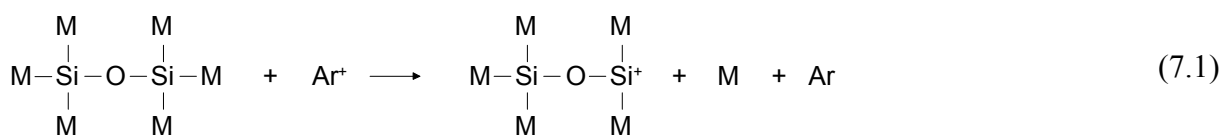
A possible dissociation mechanism as well as a possible deposition mechanism has been derived for hexamethyldisiloxane (HMDSO) injected into an expanding thermal argon-oxygen plasma. This has been done by using the properties (refractive index, infrared absorption, and chemical composition) of films deposited by means of this plasma. Also the properties of films deposited by means of tetramethylsilane (TMS) have been used to obtain a better understanding of the mechanism. Qualitatively the sticking probabilities of various species generated in the HMDSO plasma could be derived from the inclusion of the TMS deposition study. It is found that the sticking probability of $\text{O-Si-(CH}_3)_x$ species is much higher than that of $\text{Si-(CH}_3)_x$ species. The most dominant species responsible for film growth from HMDSO and oxygen is produced by the reaction at which the HMDSO molecule breaks at the Si-O bond. For deposition of silicon oxide like films using HMDSO, oxygen is needed to eliminate methyl groups from the deposition surface to obtain the appropriate film stoichiometry. When using TMS as a deposition precursor, oxygen is needed for the same purpose, but also for the creation of free surface reaction sites.

7.1 Introduction

Silicon oxide like films can be deposited by means of plasmas using various organosilicon precursors and a variety of plasma sources [1,2,3,4,5]. Hexamethyldisiloxane (HMDSO; $(\text{CH}_3)_3\text{-Si-O-Si-(CH}_3)_3$) is one of the precursors becoming more popular in the recent years [6,7,8]. Combination of this precursor with an expanding thermal plasma which is generated by a cascaded arc makes it possible to deposit silicon oxide films at rates over 60 nm/s [9]. In literature possible gas phase reactions in an HMDSO deposition plasma have been given by various authors [10,11,12]. However, they mainly focus their reaction mechanism on polymerisation of the precursor in the gas phase and neglect surface reactions. Also they use a plasma source in which electron impact ionisation and dissociation are dominant processes. However, in a remote expanding thermal argon plasma electron impact ionisation and dissociation are negligible processes due to the low electron temperature [13,14]. In these kind of plasmas charge exchange reactions with ions and dissociative recombination reactions with electrons are dominant. This difference will change the reaction mechanism and plasma chemistry in the gas phase significantly.

In this chapter a deposition mechanism for silicon oxide films from HMDSO in an expanding thermal plasma will be proposed. Gas phase reactions as well as surface reactions will be discussed and based on properties of the deposited films the likeliness of the reaction will be given. Previous findings will be used as a basis for the reaction mechanism. Additional information will be obtained from the use of another deposition precursor. Aside from the pure HMDSO depositions, also reactions occurring in an HMDSO oxygen environment will be shown.

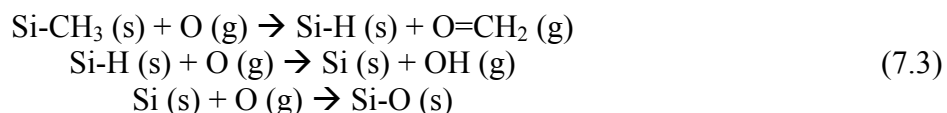
Previously it has been derived that HMDSO which is injected into an expanding thermal argon plasma first charge exchanges with an argon ion after which the resulting ion dissociatively recombines with an electron [9]. It has been suggested that most likely the dominant dissociation channel is the breaking of the Si-O bond in the HMDSO molecule, even though a Si-C bond is less strong (Si-C: 4.7 eV and Si-O: 8.3 eV). The suggested reactions are given by:



where M indicates a methyl group and a dot indicates a free bond. In the charge exchange reaction between argon and HMDSO a methyl group is separated from the HMDSO molecule, which is characteristic for methylsiloxanes [12,15]. The Si-O bond on the non

ionised side will be the weakest of the two Si-O bond due to the absence of a methyl group on the ionised side. Therefore the second dissociative recombination channel in Eq. (7.2) will be the most probable reaction.

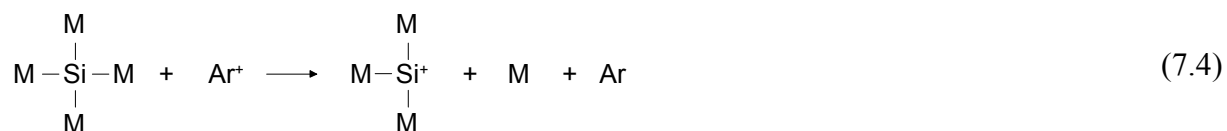
It has been shown, by means of post deposition treatment of silicon oxide like films with an argon-oxygen plasma, that methyl groups are etched from the film and oxygen is incorporated into the film [16,17]. The reaction mechanism for stripping of methyl groups from the film and incorporating oxygen into the film is given by [16]:



During film deposition, when oxygen is added to the deposition plasma, oxygen radicals reduce the number of methyl groups present in the film, but oxygen radicals can also be incorporated in the film resulting in a higher oxygen density than present in the original precursor [9]. Adding oxygen to the deposition plasma obviously also changes the gas phase reaction mechanism which will be addressed further on.

By taking the shown reaction steps, Eqs. (7.1), (7.2), and (7.3), as a basis for the reaction mechanism of HMDSO in an expanding thermal argon-oxygen plasma, the dominant mechanism for the deposition of silicon oxide films will be hypothesized. Although Eq. (7.2) might suggest which species are probably the dominant reaction products, knowledge about surface reactions during film growth is also needed. For example, the sticking probability of the various species is essential in the understanding of the film formation process.

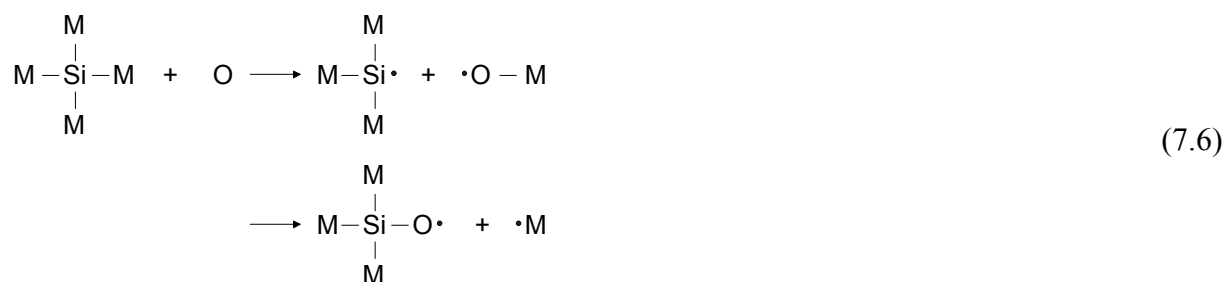
The main particles which can lead to deposition are, according to Eq. (7.2), Si-M₃ and O-Si-M₂. Analysis of the deposited film showed that the ratio of silicon to oxygen in the film is approximately equal to one when no oxygen is added to the plasma. From this it can be tentatively assumed that O-Si-M₂ is contributing dominantly to the film growth. [9]. Such a mechanism would require that the Si-M₃ particle has a very low sticking probability with respect to O-Si-M₂ as Si-M₃ and O-Si-M₂ are produced in equal quantities. It is possible to verify this by performing deposition experiments using tetramethylsilane (TMS; Si-M₄) as a precursor. The injected TMS will charge exchange with an argon ion followed by a dissociative recombination reaction with an electron. The most probable reaction mechanism is given by:



Similar to the HMDSO ion the TMS molecular ion is unstable and therefore a methyl group is separated during charge transfer or directly afterwards [18]. In the dissociative recombination reaction most likely another methyl group is removed from the Si-M₃⁺ ion, because this is the smallest unit which can be split off under the assumption that methyl groups are removed fully. As can be seen from the reaction Eqs (7.4) and (7.5), injecting TMS

in the expanding thermal argon plasma will not result in the formation of Si-M₃ radicals, but in the formation of Si-M₂ and free methyl radicals. Although the most probable reaction product is different, it is still possible to use TMS to obtain useful information on the sticking probability of the Si-M₃ radical. The sticking probability of a Si-M₂ radical will most probably be higher than that of a Si-M₃ radical, because Si-M₂ has one extra free bond with respect to Si-M₃. From literature it is known that the sticking probabilities of Si-H₂ and C-H₂ are higher than that of Si-H₃ and C-H₃ respectively [19,20,21], which supports this assumption.

Notice that the sticking probability does not only depend on the depositing particle, but also on the deposition surface composition. Therefore also information is needed on the change in deposition rate when the deposition surface composition is changed. One way of changing the deposition surface is by adding oxygen to the expanding thermal argon plasma. It is being assumed that the effects at the surface will be similar to a film deposited from HMDSO. However, addition of oxygen to the expanding thermal argon plasma into which TMS is injected will also result in a change in the reaction mechanism for TMS in the gas phase. Besides the reaction with argon ions also reactions with oxygen radicals, created by interaction of argon ions with oxygen molecules, will start to occur. The possible reactions with atomic oxygen are given by:



In this reaction mechanism it is assumed that one oxygen radical will strip a full methyl group, leaving a free bond, and not a part of it. In the deposition of silicon oxide like films from HMDSO in combination with oxygen in an expanding thermal plasma, it has been found that methyl groups are removed fully [9], therefore it is not unlikely that this will also happen with TMS on interaction with oxygen radicals.

In the first reaction with TMS molecules and oxygen radicals the Si-M₃ radical is created, which is exactly equal to the first reaction product of the most likely reaction in the dissociation of HMDSO (Eq. (7.2)). In the second reaction a species is formed which is similar to the second dissociation product of HMDSO (O-Si-M₂). The O-Si-M₃ will likely have a sticking probability which is smaller but still close to that of O-Si-M₂ because they are alike. Therefore introducing oxygen to a TMS argon plasma will result in an insight in the sticking probability of either the O-Si-M₂ particle or the Si-M₃ particle. Apart from this by adding oxygen information is obtained on the dissociation mechanism of TMS by means of oxygen radicals. When the deposition rate is not changed significantly by introducing oxygen to the TMS argon plasma the first reaction in Eq. (7.6) is the dominant reaction, but when the deposition rate does increase significantly then the second reaction is the dominant reaction because the sticking probability of O-Si-M₂ is expected to be significantly higher than that of Si-M₃. It is very likely that the interaction between oxygen radical and HMDSO molecules will be similar to the interaction between oxygen radicals and TMS molecules. Therefore the

information obtained from TMS experiments in combination with oxygen will result in more understanding of the interaction process between oxygen radicals and HMDSO molecules.

In this chapter first a study will be made of the deposition using TMS and oxygen as a precursor, after which the results of this study will be transferred to the more complex deposition using HMDSO and oxygen as a precursor. From the study of the TMS deposition a possible reaction mechanism will be hypothesized. Therefore also information will be given which is of no relevance to the HMDSO reaction mechanism, but it will be included for the sake of completeness. In the transfer from the TMS reaction mechanism to the HMDSO reaction mechanism it is a key assumption that the interaction between oxygen radicals and TMS molecules is similar to the interaction between oxygen radicals and HMDSO molecules. Nevertheless also alternative interactions will be looked upon. These alternatives will be discussed on basis of energetical arguments to get insight in their likelihood.

7.2 Experimental setup

The experimental setup has been described before extensively [22,23,24]. Therefore a short description of the main characteristics will suffice here. The reactor consists of a stainless steel cylindrical vessel (diameter 36 cm, length 100 cm) which is positioned vertically. On top of the vessel a cascaded arc [25] has been mounted. A temperature controlled substrate holder is situated at the bottom of the vessel. The distance between the arc exit and the top of the substrate holder chosen equal to 65 cm. The temperature of the substrate holder can be varied in a range of - 50 °C to 300 °C with an accuracy at the substrate surface of $\Delta T \approx 10$ °C [26]. The reactor vessel is connected to a pump stack with one rotary piston pump (Edwards: 240 m³/hr) and two mechanical booster pumps (Edwards EH2600: 2600 m³/hr; Edwards EH500A: 500 m³/hr) which generates a base pressure of 10⁻⁴ mbar. Overnight the reactor is pumped by a turbo molecular pump (Leybold Turbovac 1500: 90 m³/hr) which keeps the reactor pressure at 10⁻⁶ mbar. Samples are transferred by means of a load lock system (10⁻⁶ mbar).

To get more insight in the reaction mechanism of TMS in the gas phase and at the surface, depositions have been done varying some of the deposition parameters. Therefore 'standard' conditions have been defined. During every experiment only one parameter has been varied with respect to the other parameters. The 'standard' conditions together with the ranges in which they can be varied are given in Table 7.1. The parameters have been chosen in such a way that they are close or equal to the 'standard' conditions used for deposition of silicon oxide like films from HMDSO [9].

TMS is just as HMDSO a liquid precursor. In the case of HMDSO deposition a Bronckhorst controlled evaporation module (CEM, type W-202) in combination with a Bronckhorst Liqui-Flow® meter (type L2C2) [27,28] has been used for controlling and evaporating the HMDSO precursor gas flow. Using TMS in combination with this CEM unit is not possible because of its high vapour pressure at room temperature [29] and low boiling temperature [30]. At room temperature a large amount of vapour is generated on top of the liquid in the TMS reservoir. Therefore for TMS a much simpler system can be used. Between the top of the TMS reservoir and the reactor a gas line is connected into which a regular gas flow controller has been installed to control the TMS vapour flow. Verification of the vapour flow shows it is stable and no liquid is transferred through the gas flow controller. The fact that the gas flow controller is connected to vacuum makes it possible to use it to control

vapours of gasses that have at least a higher vapour pressure than the pressure in the vacuum chamber.

Table 7.1: Overview of the plasma parameters and their ranges as well as the ‘standard’ conditions for TMS depositions

Parameter	Range	‘Standard’ condition
Ar flow	15 – 100 sccs	25 sccs
O ₂ flow	0 – 17 sccs	5 sccs
TMS flow	0 – 12 sccs	6.5 sccs
Arc current	25 – 90 A	50 A
Arc pressure	0.2 – 0.6 bar	0.2 bar
Vessel pressure	10 – 45 Pa	11.0 Pa
Substrate temperature	-50 – 300 °C	50 °C

The rest of the setup is identical to the setup used for HMDSO deposition [9]. This means that the oxygen is injected in the nozzle of the cascaded arc and that the TMS is injected by means of a punctured ring situated approximately 5 cm from the arc exit. Film deposition has been done on silicon substrates (2.5 x 2.5 cm²), and has been monitored by means of an *in situ* single wavelength ellipsometer (He-Ne 632.8 nm). The film growth rate and the film refractive index are determined by fitting the ellipsometric values obtained during deposition of the film. After deposition the film have been analysed using *ex situ* Fourier transform infrared (FTIR) transmission absorption spectroscopy, and information on the various bond types present in the deposited films is obtained.

7.3 TMS deposition results

The first parameter that has been varied is the TMS flow. This variation has been done using three different oxygen flows (0, 5, 10 sccs). The deposition rate and the refractive index of the deposited films are shown in Figure 7.1. It can be seen that the deposition rate increases with increasing TMS flow and with increasing oxygen flow. The absolute value of the deposition rate in the case no oxygen is added is at least one order of magnitude lower than the deposition rate for deposition using HMDSO as a precursor in similar quantities (couple of tens of nm/s). This clearly suggest that the Si-M₂ radical has a low sticking probability with respect to the O-Si-M₂ radical formed in the dissociation reaction of HMDSO (Eq. (7.2)). When adding oxygen to the TMS deposition plasma the deposition rate does not change dramatically and therefore the reaction between oxygen radicals and TMS molecules is most probably an abstraction reaction of a methyl group by oxygen (cf. Eq. (7.6)) resulting in the formation of Si-M₃ radicals.

The refractive index shown in Figure 7.1 shows different trends for different oxygen flows. When no oxygen is added to the deposition plasma the refractive index decreases as function of the TMS flow. Addition of 5 sccs or 10 sccs of oxygen results in an increase of the refractive index as function of the TMS flow. This change is due to the fact that when adding oxygen to the deposition plasma the reaction mechanism in the plasma changes due to which the dominant particle responsible for deposition becomes different as has been shown. Also

the reaction mechanism at the deposition surface will change with the addition of oxygen to the deposition plasma.

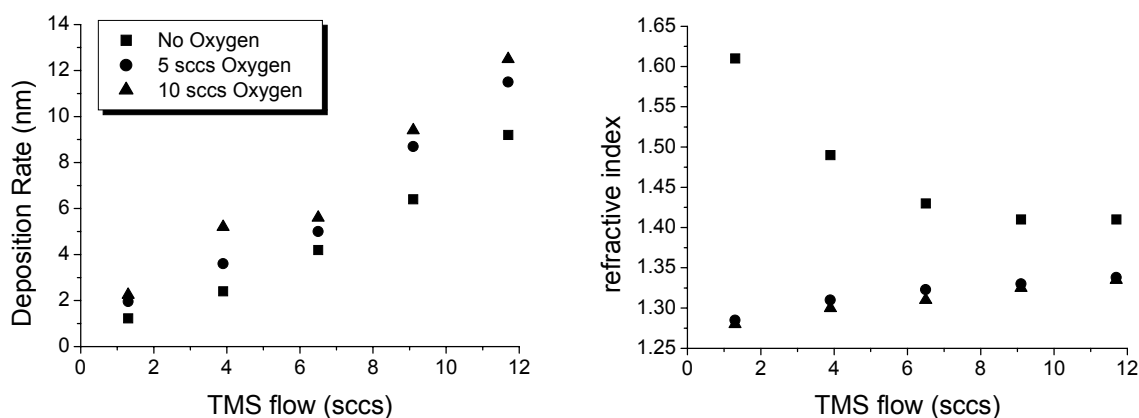


Figure 7.1: Deposition rate and refractive index as function of the TMS flow for different oxygen flows. Other parameters at 'standard' conditions.

The increase of the refractive index as function of TMS flow (cf. Figure 7.1), with addition of oxygen to the deposition plasma, is caused by the fact that increasing the TMS flow at fixed oxygen flow results in a lower oxygen to TMS ratio in the plasma. This results in a lower oxygen to carbon ratio in the plasma and therefore the carbon content of the film will increase resulting in a higher refractive index. When no oxygen is added to the plasma the deposited films will therefore contain the largest carbon content. From the deposition of silicon oxide films from HMDSO and oxygen it is known that a higher refractive index indicates a higher carbon content in the film or a decreased void density [9]. Therefore the refractive index of the films deposited from TMS without the addition of oxygen indicate that the carbon density is decreasing or that the void density is increasing as function of the TMS flow. The increase in void density is most likely, because the deposition rate increases and for HMDSO it has been shown that an increase in deposition rate correlates with an increase in the void density [9]. When looking at the value of the refractive index for the films deposited with the addition of oxygen it can be seen that it has a value which is much lower than the value for pure silicon dioxide films ($n=1.457$), even though the film is not carbon free (cf. Figure 7.4), which causes the refractive index to increase. This is a clear indication that the deposited films have a significant void density.

For higher TMS flows (> 5 sccs) the refractive index of the deposited film seems to reach a constant level. A similar phenomenon has been observed for HMDSO; however there the levelling of the refractive index is observed at 2 sccs [9]. This value is equivalent with the argon ion flow emitted by the cascaded arc for the used plasma parameters [31]. For HMDSO the levelling is due to the fact that the HMDSO molecules can only react once with the argon ions for flows above 2 sccs. So why the levelling occurs at a higher flow for TMS than for HMDSO is not known. One of the reasons could be polymerisation, but it is not possible to derive this from the obtained data.

In Figure 7.2 the deposition rate and refractive index as function of the oxygen flow for fixed TMS flow (6.5 sccs) are shown. It can be seen that the film deposition rate is increasing slightly with an increase in the oxygen flow. This change is most probably caused by a small increase in the reactor vessel pressure. As indicated in the introduction this result

suggests that oxygen does not cause the formation of the second species (O-Si-M₃) shown in Eq (7.6). Analysis of the refractive index as function of the oxygen flow shows that addition of a small amount of oxygen causes the refractive index to drop by a significant amount, which indicates that the properties of the deposited film are indeed altered. Comparison of Eq. (7.5) and Eq. (7.6) shows that the deposition species due to the addition of oxygen to the plasma does change from only Si-M₂ to a mixture of Si-M₂ and Si-M₃. This change would rather result in an increase of the refractive index than a decrease, because of an increase of the carbon content of the film. Therefore the decrease of the refractive index has to occur due to reactions at the deposition surface. As shown by argon-oxygen plasma treatment of deposited silicon oxide like films, oxygen radicals at the surface are capable of etching methyl groups leading to less methyl groups in the film [16]. This results in a lower refractive index. Increasing the molecular oxygen flow in the deposition plasma will lead to an increase of the oxygen radical density at the film surface resulting in a decrease of the methyl group density in the deposited films and thus also to a decrease of the refractive index. A part of the decrease of the refractive index can also be caused by an increase in void density in the film. Due to addition of oxygen the deposition species become larger and therefore it is not unlikely that this will cause a larger void density in the film.

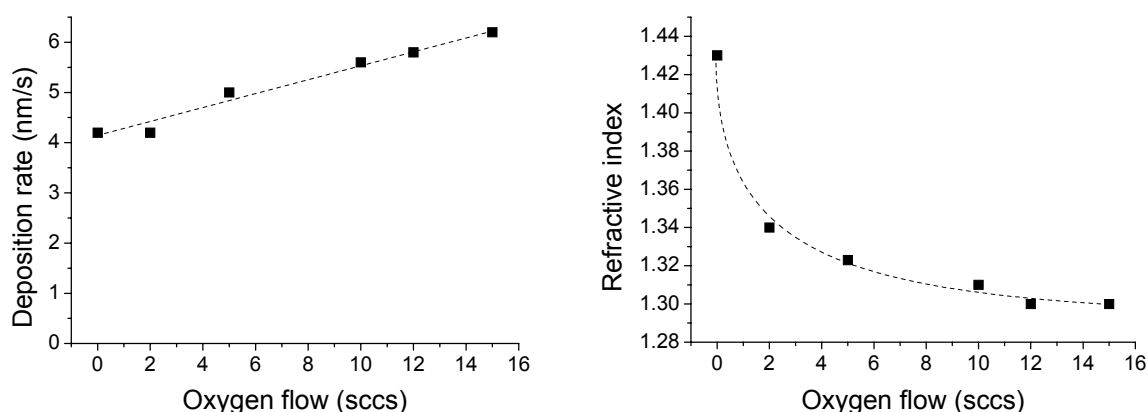


Figure 7.2: Deposition rate and refractive index as function of the oxygen flow for fixed TMS flow (6.5 sccs). Other parameters at 'standard' conditions.

When only looking at the deposition rate and the refractive index already some information about the TMS reaction mechanism is obtained. By means of infrared transmission absorption spectroscopy more information can be obtained and a better understanding of the TMS reaction mechanism can be given. In Figure 7.3 a part of a typical infrared transmission spectrum is shown. Two spectra are shown obtained at two different times, one measured immediately after deposition and one measured approximately two months later. It can be seen that the spectrum does change in the oxygen related absorption peak (Si-O-Si, 1020-1090 cm^{-1}). This change is due to the exposure of the sample to air. The film spontaneously reacts with the molecules present in ambient air, resulting in the incorporation of oxygen in the film. It can be seen in Figure 7.3 that the non oxygen related absorptions (i.e. Si-CH₃ at 1267 cm^{-1}) are not influenced by the exposure to air. Although, due to aging, the oxygen absorption peaks are less reliable for the analysis of the film, they will still be used here. Since the absolute values cannot be trusted it is assumed that the trends in the absorption peak intensities can still be used.

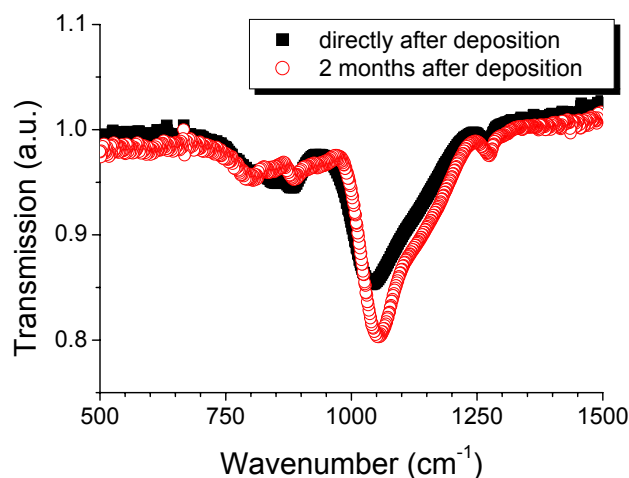


Figure 7.3: Part of the infrared transmission absorption spectrum of a film deposited using TMS as a precursor. No oxygen and other parameters at 'standard' conditions.

To analyse the various trends of the different bonds, the transmission absorption peaks have been integrated and corrected for film thickness. The corrected integrated absorption intensity of the Si-CH₃ absorption peak as function of the TMS flow is shown in Figure 7.4. In Figure 7.4 it can be seen that the Si-CH₃ intensity is increasing with increasing TMS flow when a fixed oxygen flow is added to the deposition plasma. As already discussed before this is due to the fact that at a higher TMS flow less oxygen per TMS molecule is available and therefore less methyl can be removed from the film by the oxygen present in the plasma. When no oxygen is added, the Si-CH₃ intensity is almost constant. It shows a weak minimum in intensity with increasing TMS flow, which could be caused by fact that at low TMS flows multiple reactions with argon ions can occur. It can also be seen in Figure 7.4 that the absorption intensity is the same for measurement just after deposition and for measurements two months after deposition. This indicates that the amount of methyl present in the film is not affected by exposure of the sample to air.

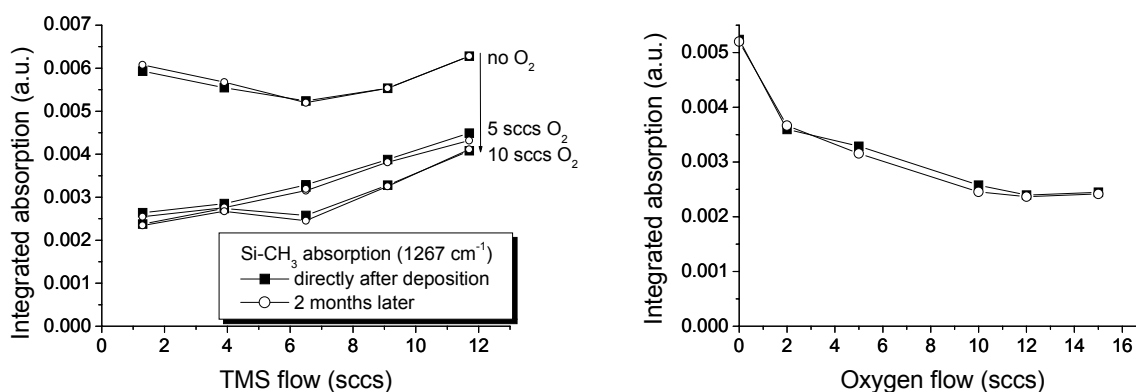


Figure 7.4: Corrected integrated Si-CH₃ absorption intensity as function of the TMS flow for different oxygen flows and as function of the oxygen flow at fixed TMS flow (6.5 sccs). Other parameter at 'standard' conditions.

In Figure 7.4 also the corrected integrated absorption intensity of the Si-CH₃ bond as function of the oxygen flow for fixed TMS flow (6.5 sccs) is shown. It can be seen that there is a negative correlation between the absorption intensity and the oxygen flow. This is as expected because when more oxygen is present more methyl groups can be removed from the film surface. The decrease of the Si-CH₃ absorption intensity as function of the oxygen flow is in good agreement with the change of the refractive index (cf. Figure 7.2). From all data shown in Figure 7.4 it can be concluded that no carbon free silicon oxide like films have been deposited using TMS as a precursor.

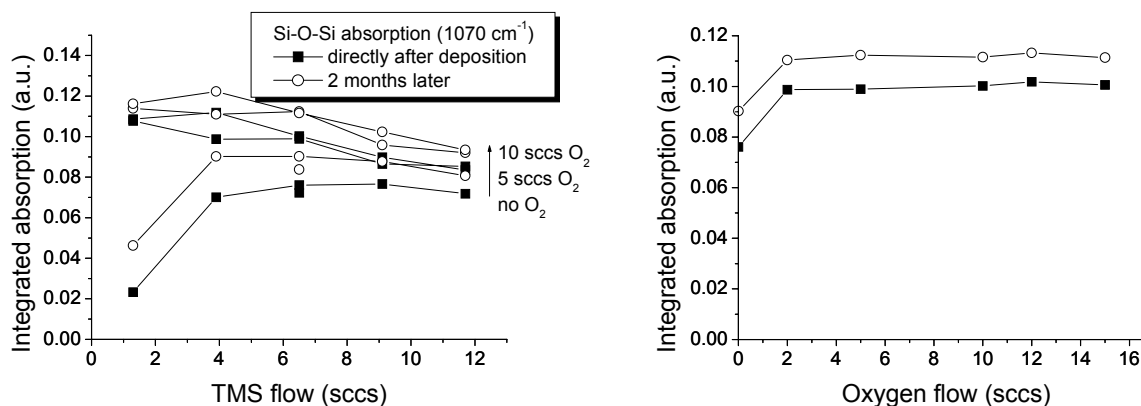


Figure 7.5: Corrected integrated Si-O-Si absorption intensity as function of the TMS flow for different oxygen flows and as function of the oxygen flow at fixed TMS flow (6.5 sccs). Other parameter at 'standard' conditions.

In Figure 7.5 the corrected integrated Si-O-Si absorption intensity as function of the TMS flow and as function of the oxygen flow is shown. It appears that when no oxygen is used in the plasma still the amount of Si-O-Si bonding in the film is significant. It is of the same order as when oxygen is used in the plasma. This oxygen has to be build into the film by exposure of the film to ambient air. The fact that the amount has such a high value shows that this process is fast and throughout the film, indicating once more that the film is very porous. For HMDSO deposition it was found that an increasing deposition rate also increases the amount of voids present in the film. This can also be observed for TMS deposition when looking at the no oxygen deposition. For a low TMS flow (1.6 sccs) the amount of Si-O-Si present in the film just after deposition is small compared to all other values measured, indicating that in this situation the reactivity of the film with ambient air, and thus the void density, is lower.

The Si-O-Si absorption intensity in the case oxygen is added to the deposition plasma decreases as function of the TMS flow. This is again due to the decrease of the oxygen to TMS ratio in the deposition plasma, which is the same reason why the Si-CH₃ density increases with increasing TMS flow. An increase in the void density will also contribute to a decrease of the Si-O-Si bond density.

The Si-O-Si absorption intensity as function of the oxygen flow shows a peculiar behaviour. It increases when adding a little oxygen, but the level remains constant and becomes independent of the oxygen flow when adding more oxygen to the deposition plasma. The increase due to addition of oxygen is small and notice that also in the case when oxygen is added to the deposition plasma, exposure to air will still result in an incorporation of more oxygen in the films. Therefore the small addition is likely due to the oxygen added to the

plasma, suggesting that the deposition process is not changed dramatically by the introduction of oxygen to the plasma. This corroborates again the assumptions that Si-M₃, and not O-Si-M₂, is formed in the reaction between oxygen radicals and TMS molecules.

The TMS flow injected into the plasma is higher than the amount of argon ions and electrons emanating from the plasma source. Therefore a TMS molecule can only react once with an argon ion when no oxygen is added to the plasma. When oxygen is added the argon ions will react with the oxygen molecules forming two oxygen radicals which can react at the surface and in the gas phase. As shown, reaction of oxygen radicals with TMS molecules in the gas phase will result in the formation of Si-M₃ radicals which are similar to the Si-M₂ radicals dominantly created in the reaction between argon ions and TMS molecules. Therefore addition of oxygen to the deposition plasma will not result in dramatic changes to the plasma gas phase and thus surface reactions of oxygen can only change the deposited film properties. It has been observed that the presence of oxygen does change the Si-CH₃ bond density but it does not change the Si-O-Si bond density. This suggests that oxygen at the surface is only responsible for abstraction of methyl groups and does not significantly contribute to incorporation in the film in the Si-O-Si bond stoichiometry.

Comparison of the integrated Si-O-Si absorption intensity obtained immediately after deposition with the ones obtained two months after deposition shows that the measured integrated intensities increase slightly. This increase is almost identical for all measured absorptions. As can be seen in Figure 7.3 the change is a real change and is caused by the interaction between the deposited film and ambient air.

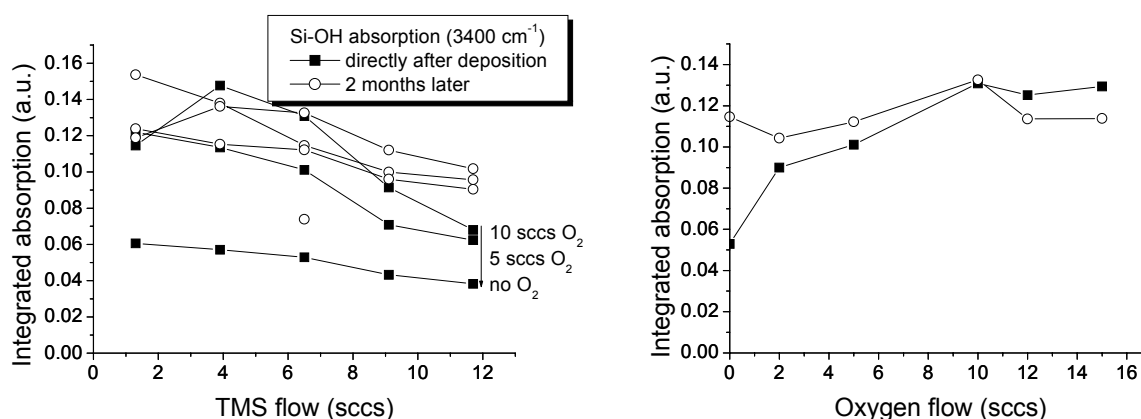


Figure 7.6: Corrected integrated Si-OH absorption intensity as function of the TMS flow for different oxygen flows and as function of the oxygen flow at fixed TMS flow (6.5 sccs). Other parameter at 'standard' conditions.

A third absorption peak that has been analysed is the Si-OH absorption peak. This absorption peak, which is not shown in Figure 7.3, is a broad absorption peak located between 3000 cm⁻¹ and 3300 cm⁻¹. In Figure 7.6 the integrated absorption intensity for this peak has been plotted as function of the TMS flow for different oxygen flows and as function of the oxygen flow for fixed TMS flow. It can be seen that for the Si-OH bond there is a significant difference between the case no oxygen is added and the case oxygen is added to the deposition plasma. In Figure 7.6 it can be seen that the Si-OH density does in general decrease with increasing TMS flow at fixed oxygen flow, which is caused by the changing TMS to oxygen ratio in the plasma. If no oxygen is added the decrease of the Si-OH density

could be caused by an increased void density in the film, due to which less reaction sites per volume are available to form Si-OH bonds when the film is exposed to air. Also in the case oxygen is used in the deposition plasma a part of the Si-OH bonds present in the film will be due to the exposure to air. This can clearly be seen in the difference between the Si-OH absorption intensity measured directly after deposition and the measurements done two months later.

7.4 Discussion

The deposition experiments done using TMS as a precursor provides information on the reaction mechanism of TMS with the argon plasma and with oxygen radicals. The dominant species in the gas phase of the TMS deposition plasma have been deduced. Therefore first the different reactions at the film surface will be addressed in the case that TMS is added to the expanding thermal argon plasma. The results will be used to hypothesize the growth mechanism of silicon oxide like films from a HMDSO containing expanding thermal argon plasma.

Table 7.2: Overview of the various diatomic bonds and their binding energies.

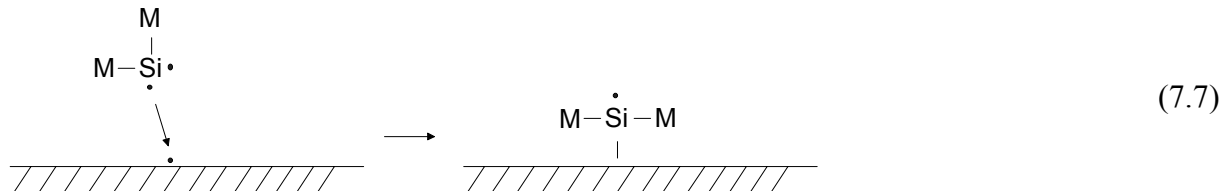
Bonding	E_{bond} (eV)	Bonding	E_{bond} (eV)
Si-Si	3.39	C-O	11.17
Si-C	4.69	C-H	3.51
Si-O	8.30	O-O	5.17
Si-H	≤ 3.11	O-H	4.44
C-C	6.30	H-H	4.53

A requirement for a reaction to occur is that it is energetically feasible. For this the bond strengths are needed to check if the reactions are exothermic. In Table 7.2 an overview is given of the various diatomic bonds that could possibly be formed with silicon, carbon, oxygen and hydrogen atoms. Also their corresponding binding energy (E_{bond}) is given in Table 7.2 [32]. The binding energy is dependent on the configuration and bond types of the other covalent bonds that are connected to an atom. Notice that the binding energies given are determined for well defined molecules, therefore slight differences with silicon oxide like films could exist.

As mentioned the electron temperature is low (a couple of tenths of eV) in an expanding thermal argon plasma [13,14]. The ion temperature is approximately equal to the electron temperature. Bias energies at the substrate are 1 eV at maximum. Therefore there will be no energetic ion bombardment at the film surface. Because no new argon ions and electrons are created downstream of the cascaded arc exit, the ion and electron density will decrease as function of the distance to the arc exit due to the expansion of the plasma. When a precursor is injected into the argon plasma the argon ions and electrons in the plasma will be consumed causing a further decrease of the number of ions and electrons arriving at the film surface [31]. So when ion bombardment or chemical energy of ion-electron recombination at the film surface will have a contribution to film growth it will become less important for increasing deposition precursor gas flows.

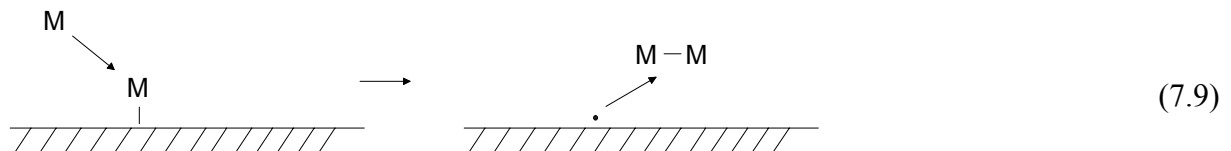
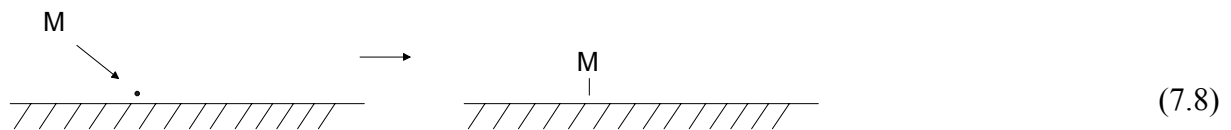
7.4.1 TMS

When no oxygen is added to the deposition plasma the TMS molecules will react with an argon ion followed by a reaction with an electron according to Eq. (7.4) and Eq. (7.5). This results in the formation of Si-M₂ species. A possible mechanism for a Si-M₂ particle to react at the surface is given by:



where the dot indicates a free surface site or a free bond in the gas phase species. As can be seen the reaction is in such a way that a immediately a free surface site is available for further reactions at the surface.

In the gas phase two methyl groups are separated from the TMS precursor gas molecule. These methyl groups are also transported to the surface and have a contribution to the film. Based on binding energy two reactions can occur at the surface:

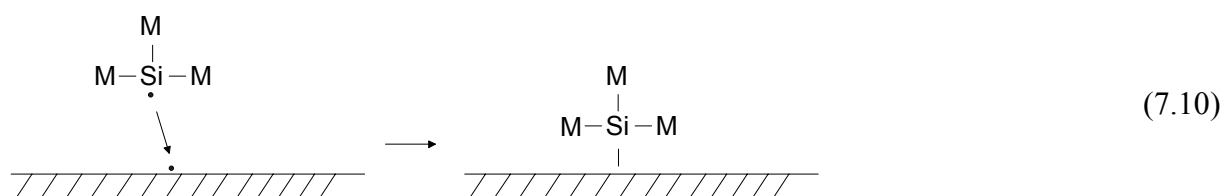


The first reaction is known to occur in the deposition of hydrogenated amorphous carbon and it is found that methyl has a low sticking probability (10^{-4} - 10^{-2} but is dependent on the surface composition [19]). However, in that case the methyl will form a C-C bond at the surface. In the case of deposition of silicon oxide like films also other bonds can be formed and thus the sticking probability of methyl in this case might be different. The binding energy of the C-C bond is higher than the binding energy of the Si-C bond (cf. Table 7.2) and therefore it is very likely that the sticking probability of methyl in the case of TMS deposition without the addition of oxygen will be lower than the reported values in literature [19].

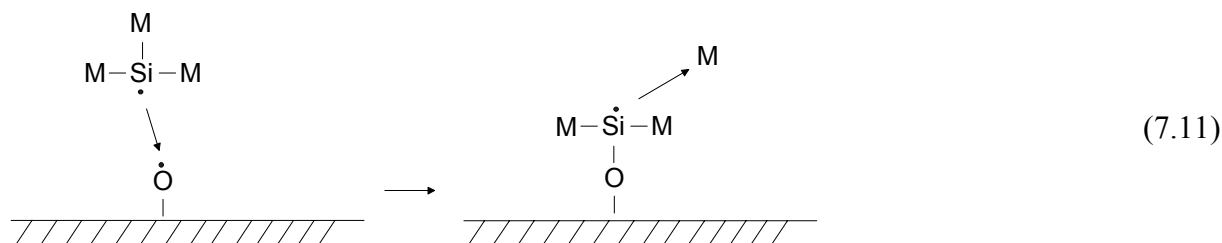
The reaction given by Eq. (7.9) is only possible energetically because the C-C binding energy is significantly higher than the Si-C binding energy. The species indicated by M-M could also have been a ethylene or acetylene in combination with molecular hydrogen. Due to interaction of methyl groups at the surface the number density of free bonds can be decreased by the reaction given by Eq. (7.8) and increased by the reaction given by Eq. (7.9). The former reaction is however the most likely one, because for that reaction there is no threshold energy, whereas there is a threshold energy for the latter reaction. Therefore the number density of free bonds will decrease due to the presence of free methyl groups in the plasma gas phase, which will have a negative influence on the deposition rate.

When the argon ion flux is higher than the TMS flow then also a second reaction between argon ions and the dissociation product of TMS can occur. This results in smaller fractions arriving at the substrate surface. Smaller deposition particles arriving at the substrate surface could result in less voids in the deposited film, because small particles fill up small gaps at the surface and do not cover them leaving a void. Note that stripping of more methyl groups from the TMS molecule in the gas phase automatically results in a higher flux of methyl groups at the substrate surface which also contribute to film growth. Although the sticking probability of the various species is different the films deposited at low TMS flow will still have a fairly high density of methyl groups. The small decrease observed for the Si-CH₃ bond density for increasing TMS flow up to 6.5 sccs when no oxygen is added to the deposition plasma (cf. Figure 7.4) could therefore be due to an increase in the void density. For flows above 6.5 sccs the Si-CH₃ bond density weakly increases with flow. This needs to be caused by an absolute increase in methyl groups in the film.

In reaction Eq. (7.6) two possible deposition particles are given in the case TMS and oxygen are used together in the plasma. With the first particle generated (Si-M₃) oxygen radicals strip of a methyl group from the TMS molecule and with the second particle (O-Si-M₃) oxygen radicals exchanges position with a methyl group in the TMS molecule. As shown from the difference in the deposition rate obtained using TMS and HMDSO as a precursor it can be deduced that the sticking probability of a O-Si-M_x radical is much higher than that of a Si-M_x radical. When oxygen is added to the TMS deposition plasma no significant increase in the deposition rate is measured and from this it can be concluded that O-Si-M₃ is not or almost not produced in a reaction with oxygen radicals and TMS. The most probable surface reaction of the dominant particle (Si-M₃) produced in the reaction between oxygen and TMS is given by:



This reaction can occur when the free bond at the surface is at a silicon site. In that case no free bond is generated automatically and therefore new free bond has to be produced by interaction of oxygen radicals with the surface or by interaction of methyl groups with the surface as indicated by Eq. (7.9). When the free bond at the surface is at an oxygen site it might be possible to generate a free bond on interaction with the surface:



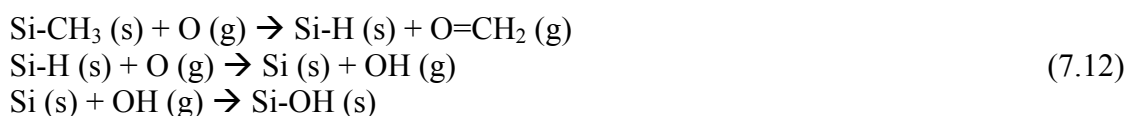
This is because the Si-O binding energy is much higher than the Si-C binding energy so that the generated bond has a surplus energy enough to break a Si-C bond. Even though there is a large energy surplus in this reaction it is not a very likely one because the step of sticking and

splitting has to occur simultaneously. However, when occurring the emitted methyl group could redeposit or abstract another methyl group as indicated by Eq (7.8) and Eq. (7.9).

At the surface oxygen is able to strip methyl groups. The reactions with oxygen radicals occurring at the surface of a film deposited using TMS as a precursor will be similar to the reactions with oxygen radicals occurring at the surface that has been deposited using HMDSO as a precursor. It has been shown before by argon-oxygen plasma treatment [16] that oxygen radicals react at the surface and in the film stripping a methyl group and leaving a Si-H bond. This Si-H bond can then further react with oxygen to become an Si-O bond, but as an intermediate step a silicon atom with a free bond is created (Eq. (7.3)). This occurs when the film is exposed to an argon-oxygen plasma because then oxygen is the only reacting particle and the oxygen radical density at the film surface is high. However in a situation that the film is being deposited at the same time it is less likely to happen because the reaction time is less and the penetration depth of the oxygen radicals will also be less. Generated free bonds will also be used as reaction sites for film growth. When the reaction to form Si-O will occur, the rate will also be lower than in a pure argon-oxygen plasma because a part of the oxygen radicals are consumed by the TMS gas in the gas phase.

If a Si-O bond is generated then still a second reaction needs to occur to form a Si-O-Si bond. Because the film is being deposited and is very porous it is very likely that such a second reaction cannot occur because there is no other silicon atom with a free bond in the vicinity of the created another Si-O bond. Therefore it is conceivable that the Si-O bond will be terminated by hydrogen which is present in the gas phase resulting in an Si-OH bond, which explains also why the Si-OH bond density is dependent on the oxygen flow and the Si-O-Si bond is not. The hydrogen present in the gas phase is e.g. produced by reactions of oxygen radicals with methyl radicals. Although there is a possibility that during deposition an Si-O is terminated by a hydrogen radical, the free bond can also be used as a deposition site for further film growth and therefore the Si-OH density will remain relatively small compared to other bond types.

As shown in the formation of the Si-O bond from an Si-CH₃ bond as an intermediate step Si-H is created. When this reacts with an oxygen radical a silicon atom with a free bond is produced and one OH radical. When this OH radical is not created at the surface of the film, it has to diffuse out of the film which means that it will collide many times on the way out. It is very likely that the OH radical will then encounter a silicon atom with a free bond to which it can easily stick forming a Si-OH bond. Because both the stripping of the methyl group and the production of the OH radicals is oxygen dependent, the produced Si-OH bond density is also oxygen dependent. The depicted process is almost identical to the process given by Eq. (7.3). Only the last reaction is different and the total reaction mechanism is given by:



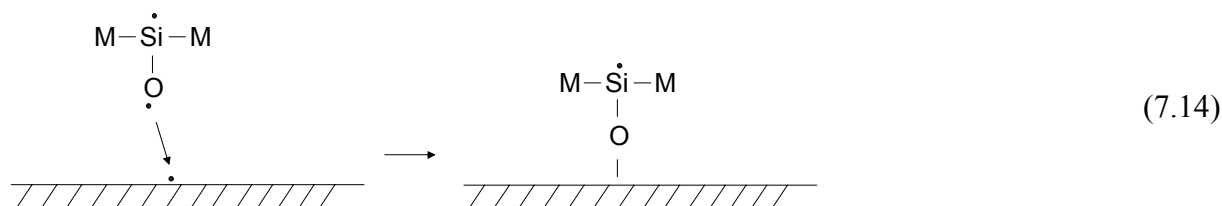
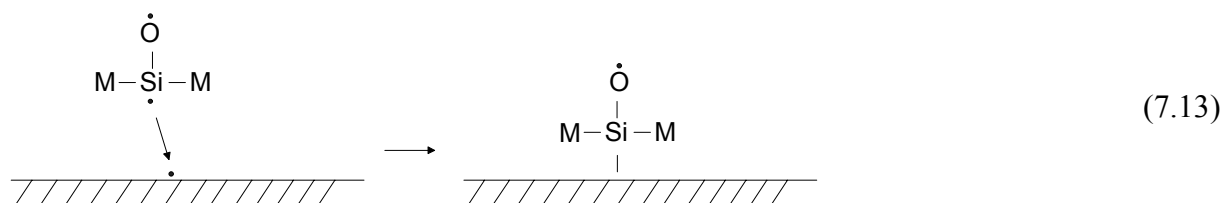
where the silicon atom created in the second reaction does not necessarily have to be the same as the silicon atom consumed in the third reaction.

It has been shown that films deposited using TMS as a precursor react with ambient air. There are two possible reactions, one with molecular oxygen and one with water. Since the film is very porous the reactions will not only occur at the surface but throughout the

whole film. This is the main reason why the influence can be measured by a fairly easy analysis technique as FTIR transmission absorption spectroscopy. When the reactions would only occur at the surface the influence would most likely not have been noted. Based on the bonding energy it is possible for molecular oxygen to generate Si-OH and Si-O bonds. For water it is possible to generate Si-OH bonds, but it is also possible for water to get physisorbed to the film. In that case also a kind of Si-OH bond is generated which will show an infrared absorption in the same area as a chemical Si-OH bond. It is therefore likely that a change in Si-OH density is caused by physisorbed water. The generation of Si-O-Si bonds cannot be caused by physisorbed species and therefore a chemical reaction is needed. When after deposition still silicon atoms with free bonds are present in the film then these sites will be the easiest sites at which molecular oxygen can react, followed by the Si-H bonds which are present in the deposited films. A third possibility is that atomic oxygen will react with a Si-Si bond to form a Si-O-Si bond by inserting an oxygen atom in the network.

7.4.2 HMDSO

The interaction of HMDSO with argon ions in a pure argon plasma is already known and is given by Eq. (7.1). This is followed by dissociative recombination with an electron (Eq. (7.2)) which can result in two different reaction pathways. The second pathway is the most likely because that reaction has the lowest activation energy. Therefore the dominant deposition species in the plasma gas phase are Si-M₃ and O-Si-M₂. From the TMS reaction mechanism in combination with the HMDSO deposition rate it is derived that the Si-M_x radical has a low sticking probability at the surface in comparison to a O-Si-M_x radical. Therefore the most likely deposition precursor is the O-Si-M₂ radical. This radical has two dangling bonds and therefore it can react in two different ways at the surface:

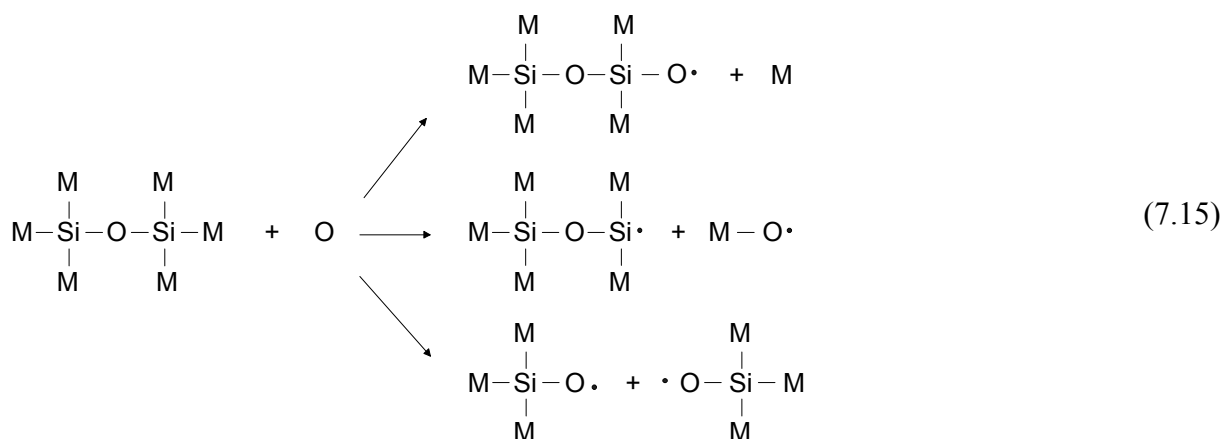


Both reactions can occur on a surface silicon atom with a free bond as well as on a surface oxygen atom with a free bond. It is most likely that the reaction will occur in such a way that an Si-O bond is created, because this has the highest bonding energy and the highest reaction probability. Investigation of both reactions shows that the binding energy excess when a Si-O bond is formed is enough to break a Si-C bond and therefore it is possible that on interaction with the surface a methyl group is removed and emitted into the gas phase. This emitted methyl group can redeposit or abstract another methyl group as indicated by Eq. (7.8) and Eq. (7.9). Not all the emitted methyl groups will redeposit and therefore this extra

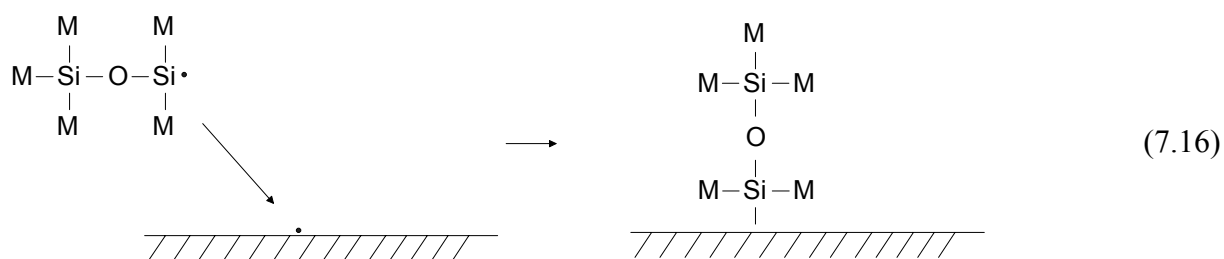
removal of a methyl group can result in an increase of surface free bonds and a decrease in methyl groups in the deposited film. Notice that when a Si-Si bond is created during deposition of the O-Si-M₂ radical the excess energy is too small to remove a methyl group.

When the HMDSO flow injected into the deposition plasma is smaller than the argon ion flux emanating from the arc, then the HMDSO molecules can react more than once with the argon ions, resulting in smaller fractions of the HMDSO molecule arriving at the surface of the film. Further dissociation of Si-M₃ and O-Si-M₂ results in the production of more free methyl groups in the gas phase. This production of free methyl radicals will terminate surface free bonds as shown in Eq. (7.8). This results in a more methyl rich composition of the film when the injected HMDSO flow is smaller than the argon flux emitted by the arc in comparison to the case in which the HMDSO flow is larger than the ion flux from the arc. In the latter case, when polymerisation reactions are excluded, the ratio of the various deposition radicals, O-Si-M₂, Si-M₃ and methyl, arriving at the surface will be constant and independent of the HMDSO flow. Therefore the film properties will not change with an increase in HMDSO flow. This is in agreement with the observed film properties [9].

When oxygen is added to the HMDSO argon plasma, oxygen radicals are produced and these will react with the HMDSO molecules. From the TMS experiments it has been derived that most probably oxygen strips of one methyl group from the TMS molecule. So it is fair to assume that the same will occur in the case of HMDSO. However in the case of HMDSO there is also one extra reaction possibility. The HMDSO molecule is not a linear molecule, but for clarity it has been drawn linear in the reaction equations. In reality it is a dipole molecule similar to water. When the oxygen radical approaches the HMDSO molecule at the oxygen atom, then it is possible to break the molecule at the Si-O bond and form another Si-O bond with the oxygen radical. This is a energy neutral reaction and when the oxygen radical is an excited one, this reaction is exothermic. In short the reactions between HMDSO and oxygen are given by:



As mentioned from the first two reactions the second is the most likely one. Interaction of the species created in this reaction with the deposition surface is given by:

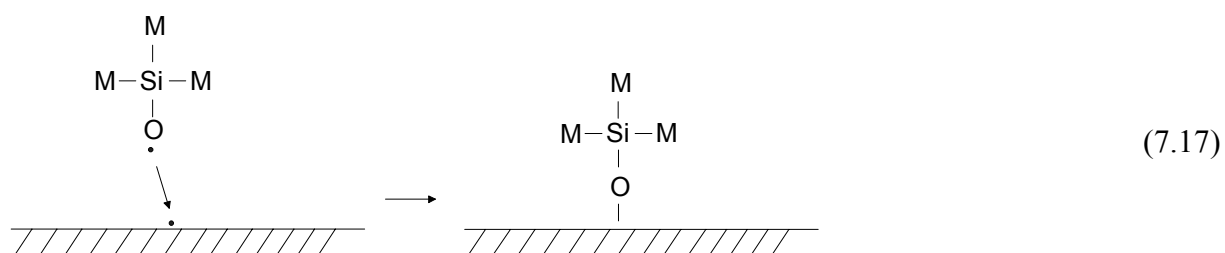


Depending on what is the surface species to which the Si_2OM_5 radical is connecting there will be enough exothermic binding energy to remove some parts of the radical. This could be a methyl group, but it could even be a break at one of the Si-O-Si bonds when the bond formed at the surface is an Si-O bond. However this reaction is neutral in energy and thus less likely.

The deposition reaction shows that addition of oxygen to the deposition plasma will result in an increase of the Si-CH₃ density for low oxygen flows. This has also been observed by infrared transmission absorption spectroscopy (not shown) for HMDSO deposited films at constant background pressure (for oxygen flows <2 sccs). At the same time a continuous increase of the Si-O-Si bond density is observed on addition of oxygen to the deposition plasma, which is caused by the fact that part of the depositing species already have a Si-O-Si bond (Eq. (7.16)). If no oxygen is added, this bond has to be formed at the surface interaction because it is broken in the plasma gas phase. From the trend observed by infrared transmission absorption spectroscopy it can tentatively be concluded that the Si_2OM_5 radical is not likely to break at the Si-O-Si bond at the surface. However the removal of a methyl group on interaction of the Si_2OM_5 radical at the surface is not excluded by this. Splitting of a methyl group is beneficial for the growth rate, because then no new surface site has to be created by an interaction with gas phase species.

Addition of large amounts of oxygen will result in stripping of methyl groups at the surface, similar to TMS depositions. However, for HMDSO no formation of Si-OH bonds has been observed when the film is exposed to air, which indicates that the HMDSO deposited film is probably less porous than the film deposited using TMS as a precursor. On the other hand argon-oxygen plasma treatment of silicon oxide like films deposited from HMDSO shows that the film can be altered over the full thickness [16], which indicates that it has a significant porosity.

At an equivalent silicon atom flow and similar other plasma conditions the deposition rate using HMDSO is at least one order of magnitude higher than when using TMS as a precursor. This is a clear indication that the dominant deposition species in the case of HMDSO deposition is different from that of TMS deposition. Although the first reaction product shown in the second reaction of Eq. (7.16) is about twice the size of the dominant reaction product in the case TMS is used as a precursor (Si-M_3) this alone could not lead to an increase of the deposition rate by at least one order of magnitude. This suggests that in the reaction between oxygen radicals and HMDSO molecules the dominant deposition has a higher sticking probability than Si-M_3 . The most probable species is generated in the third reaction (O-Si-M_3) of Eq. (7.16). The reaction at the film surface of this species is given by:



One oxygen molecule will be dissociated in two oxygen radicals and therefore two HMDSO molecules can be dissociated per oxygen molecule. On interaction with HMDSO and oxygen radicals two of the dominant deposition species are produced (O-Si-M_3). Which suggest an increase of the deposition rate by a factor four is possible when assuming the sticking probability of O-Si-M_2 is similar to that of O-Si-M_3 . However no serious increase of the deposition rate has been observed when adding oxygen to the deposition plasma. This may be caused by the absence of free bonds after deposition of the O-Si-M_3 radicals. Therefore first free bonds have to be generated before deposition can continue. For this generation of free bonds oxygen is needed. On interaction of the O-Si-M_3 molecule with the surface however a part of the radicals will split off a methyl group, which is energetically possible, and therefore the deposition rate will initially increase on addition of oxygen to the HMDSO deposition plasma. Notice that with the addition of small amounts of oxygen the dominant dissociation for HMDSO will still be by interaction between argon ions rather than oxygen radicals.

Opposite to the case of pure HMDSO deposition, addition of oxygen to the argon-HMDSO deposition plasma will stop the production of free methyl groups in the gas phase. This will cause the deposition rate to remain at a high level or even to increase. For high oxygen flows (>5 sccs) and at constant pressure it has been observed that the deposition rate does decrease with an increase of oxygen flow (not shown). A similar maximum has been observed at the same oxygen level in argon-oxygen plasma treatment of silicon oxide like films deposited from HMDSO [16]. There it has been shown that the oxygen radical density does decrease at the surface for increasing oxygen flow above 5 sccs. Addition of HMDSO to an argon-oxygen plasma does change the plasma chemistry and therefore this process does not have to apply for a deposition plasma. However adding HMDSO to an argon-oxygen plasma automatically decreases the oxygen radical flux arriving at the substrate surface because oxygen radicals react with the HMDSO molecules in the gas phase. Nevertheless this does not automatically mean that the trend of the oxygen radical density as function of the injected oxygen flow is changed. At large oxygen flows the oxygen radical reactions with HMDSO molecules are dominant and thus oxygen radicals are needed at the surface to create free surface sites. If the oxygen radical density decreases with increasing oxygen flow then also the deposition rate will decrease, which is in agreement with the observations.

7.5 Conclusions

Using TMS and oxygen as precursors for the deposition of silicon oxide films in combination of an expanding thermal plasma does result in silicon oxide like films with high porosity. Also the films show a high reactivity with ambient air. Although the films contain a significant amount of carbon the refractive index of the films is significantly lower than that of pure silicon dioxide (1.3 vs. 1.46). Comparison of the deposition rate using TMS as a

precursor with the deposition rate using HMDSO as a precursor for equivalent silicon atom flows shows that the deposition rate using TMS is at least one order of magnitude lower. This indicates that the deposition species generated in the plasma when TMS is used as a precursor has a low sticking probability which is at least an order of magnitude lower than that of the most dominant deposition species in the case that HMDSO is used as a precursor.

From the measurements using TMS as a precursor a first picture of the deposition mechanism can be given. Although the shown deposition mechanism is by far complete, it can explain the variations in the film properties as function of conditions. Based on this information it can be qualitatively indicated which reactions are more important than others. For additional information on relevant reaction rates, more data needs to be obtained by additional experiments, e.g. gas phase absorption spectroscopy and mass spectrometry [33]. Combination of such additional experiments and modelling of the reaction mechanism could result in refinement of the deposition mechanism. However then it should be kept in mind that sticking probabilities of various species could also depend on the state and composition of the surface to which they will stick. When the plasma parameters are changed, this may change the film properties caused by a change in deposition species composition but probably also by a change in sticking probability of the various depositing species.

The study of the TMS deposition mechanism tentatively shows that oxygen atoms and methyl groups do not exchange upon interaction in the gas phase. Therefore it can be assumed that in the case HMDSO is used as a precursor, oxygen atoms will also not be able to exchange with a methyl group. From this it can therefore be derived that HMDSO molecules need to have a different interaction with oxygen radicals in the gas phase. Otherwise the deposition rate would become less with addition of oxygen compared to no addition of oxygen, as a deposition species is generated with a lower sticking probability than the species that is produced in the absence of oxygen. A large fraction of the HMDSO molecules is assumed to dissociate on a Si-O bond by the interaction with argon ions and also by the interaction with oxygen radicals.

Although high deposition rates (>20 nm/s) can be obtained easily with the expanding thermal plasma, the deposited silicon oxide films have a high porosity which makes the films probably less suitable for use as protective coatings in the packaging industry. The films can however easily be used as optical coatings, especially because a large diversity in refractive indices can be obtained (1.28 to 1.60). Due to the high porosity the films could maybe also be used for catalytic purposes. The mechanical properties of the films have not been analysed and therefore nothing can be said about the scratch resistance of the films. The presence of a significant amount of methyl groups in the film and an amorphous structure makes it likely that the films show a large elasticity.

References

- [1] C. Bourreau, Y. Catherine, and P. Garcia, *Plasma Chem. Plasma Proc.* **10** (1990) 247
- [2] K. Fujino, Y. Nishimoto, N. Tokomasu, and K. Maeda, *J. Electrochem. Soc.* **139** (1992) 2283
- [3] K. Aumaille, C. Vallee, A. Granier, A. Gouillet, F. Gaboriau, and G. Turban, *Thin Solid Films* **359** (2000) 188
- [4] K. Sano, S. Hayashi, S. Wrickramanayaka, and Y. Hatanaka, *Thin Solid Films* **281-282** (1996) 397

- [5] K.H.A. Bogart, S.K. Ramirez, L.A. Gonzales, G.R. Bogart, and E.R. Fisher, *J. Vac. Sci. Technol.* **A 16** (1998) 3175
- [6] N. Benissad, C. Boisse-Laporte, C. Vallee, A. Granier, and A. Gouillet, *Surf. Coat. Technol.* **116-119** (1999) 868
- [7] D. Hegemann, U. Vohrer, C. Oehr, and R. Riedel, *Surf. Coat. Technol.* **116-119** (1999) 1033
- [8] M. Walker, K.M. Baumgärtner, J. Fiechtinger, M. Kaiser, A. Schulz, and E. Räuchle, *Vacuum* **57** (2000) 387
- [9] M.F.A.M. van Hest, B. Mitu, and M.C.M. van de Sanden, *Deposition of silicon oxide like films using a remote thermal plasma*, to be published; Chapter 5 of this thesis
- [10] M.R. Alexander, F.R. Jones, and R.D. Short, *Plasmas and Polymers* **2** (1997) 277
- [11] M.R. Alexander, F.R. Jones, and R.D. Short, *J. Phys. Chem. B* **101** (1997) 3614
- [12] A.M. Wróbel, M. Kryszewski, and M. Gazicki, *J. Macromol. Sci.-Chem.* **A20** (1983) 583
- [13] J.J. Beulens, M.J. de Graaf, G.M.W. Kroesen, and D.C. Schram, *Mater. Res. Soc. Proc.* **190** (1990) 311
- [14] M.C.M. van de Sanden, J.M. de Regt, and D.C. Schram, *Phys. Rev. E* **47** (1993) 2792
- [15] J. Schwarz, M. Schmidt, and A. Ohl, *Surf. Coat. Technol.* **98** (1998) 859
- [16] M.F.A.M. van Hest, A. Klaver, D.C. Schram, and M.C.M. van de Sanden, *Argon-oxygen plasma treatment of deposited silicon oxide like films*, to be published; Chapter 6 of this thesis
- [17] C. Vallee, A. Granier, K. Aumaille, C. Cardinaud, A. Gouillet, N. Coulon, and G. Turban, *Appl. Surf. Sci.* **138-139** (1999) 57
- [18] S. McGinnis, K. Riehl, and P.D. Haaland, *Chem. Phys. Letters* **232** (1995) 99
- [19] M. Meier and A. von Keudell, *J. Chem. Phys.* **116** (2002) 5125
- [20] H. Kojima, H. Toyoda, and H. Sugai, *Appl. Phys., Lett.* **55** (1989) 1292
- [21] W.M.M. Kessels, M.C.M. van de Sanden, R.J. Severens, and D.C. Schram, *J. Appl. Phys.* **87** (2000) 3313
- [22] J.W.A.M. Gielen, M.C.M. van de Sanden, P.R.M. Kleuskens, and D.C. Schram, *Plasma Sources Sci. Technol.* **5** (1996) 492
- [23] J.W.A.M. Gielen, W.M.M. Kessels, M.C.M. van de Sanden, and D.C. Schram, *J. Appl. Phys.* **82** (1997) 2643
- [24] A. de Graaf, *Deposition of CNH Materials; Plasma and Film Characterization*, Ph.D. Thesis, Eindhoven University of Technology (2000)
- [25] H. Mäcker, *Z. Naturforsch.* **11** (1956) 457
- [26] J.W.A.M. Gielen, *Plasma Beam Deposition of Amorphous Hydrogenated Carbon*, Ph.D. Thesis, Eindhoven University of Technology (1996)
- [27] H.J. Boer, *J. de Physique IV* **5** (1995) C5-961
- [28] H.J. Boer, *Solid State Technology* (March 1996) 149
- [29] TRCVP, *Vapor Pressure Database, Version 2.2P*, Thermodynamic Research Center, Texas A&M University, College Station
- [30] Schumacher, *Material Safety Data Sheet 1315-0057 E* (2000)
- [31] M.F.A.M. van Hest, J.R. Haartsen, M.H.M. van Weert, D.C. Schram, and M.C.M. van de Sanden, *Analysis of the argon-oxygen plasma gas phase*, to be published; Chapter 4 of this thesis

Chapter 7

- [32] D.R. Lide, Editor-in-chief, CRC Handbook of Chemistry and Physics 79th edition, CRC Press, New York (1999)
- [33] M.F.A.M. van Hest, A. de Graaf, M.C.M. van de Sanden, and D.C. Schram, Plasma Sources Sci. Technol. **9** (2000) 615; Appendix to Chapter 2 of this thesis

Chapter 8

ZnSn_xO_y deposition: A combinatorial approach*

M.F.A.M. van Hest, J.D. Perkins, and D.S. Ginley

Abstract

In the search of new transparent conducting oxides a large material phase space needs to be investigated. This can be done by using the combinatorial approach, which makes it possible to investigate a large part of the material phase space with a relatively small amount of deposition runs. So called binary ZnSn_xO_y combinatorial libraries have been deposited by means of sputtering of solid ZnO, Sn and SnO₂ targets. The deposited libraries have a high resistivity ($>10^5 \Omega\text{cm}$) when deposited. The resistivity becomes reasonable for various compositions ($<1 \Omega\text{cm}$) when the libraries are annealed in a nitrogen atmosphere. An increase in the annealing temperature results in a decrease of the resistivity. The lowest value for the resistivity is obtained for a Sn/Zn ratio close to 0 and a Sn/Zn ratio of approximately 1. This suggest that the best conductivity is obtained for Sn doped ZnO or the ZnSnO₃ stoichiometry. Including indium in the combinatorial deposition process to form a ternary ZnSn_xIn_yO_z combinatorial library results for specific film composition in a reduction of the resistivity. Also the resistivity becomes less dependent on the film composition.

* This is an overview of a part of the work which is the result of a two month visit to the National Renewable Energy Laboratory (NREL) in Golden, Colorado (USA).

8.1 Introduction

In the thin film industry transparent conducting oxides (TCO) are becoming increasingly important due to their wide range of applications. TCOs can be used in e.g.: thin film photovoltaics (solar cells) and flat panel displays, and exist generally as n-type material. Traditional TCO materials are ZnO doped with Al or F, SnO₂ doped with F, and InSnO_x doped with F. Due to the increasing demand for TCOs there is a growing need for new materials with improved properties. Beside the basic properties which are important, i.e. high conductivity and good optical transparency, many other criteria are becoming equally important e.g. crystallinity, stability, hardness, and toxicity.

One of the current dilemmas for the development of TCOs is that while improved carrier concentrations can be obtained, the result is not always an increased conductivity. Rather both the transparency in the infrared and the conductivity can suffer due to free electron absorption and an increase in defects. Nevertheless one of the main objectives in current TCO research is finding higher mobility materials. To obtain this, new exotic binary and ternary TCO materials are being investigated e.g. Cd₂SnO₄ [1,2], Zn₂In₂O₅ [3,4], and In_{2-2x}Sn_xZn_xO₃ [5,6]. To date, these complex materials are generally alloys of the simpler established transparent conducting metal oxides such as ZnO, SnO₂, In₂O₃, CdO, and Ga₂O₃ [7].

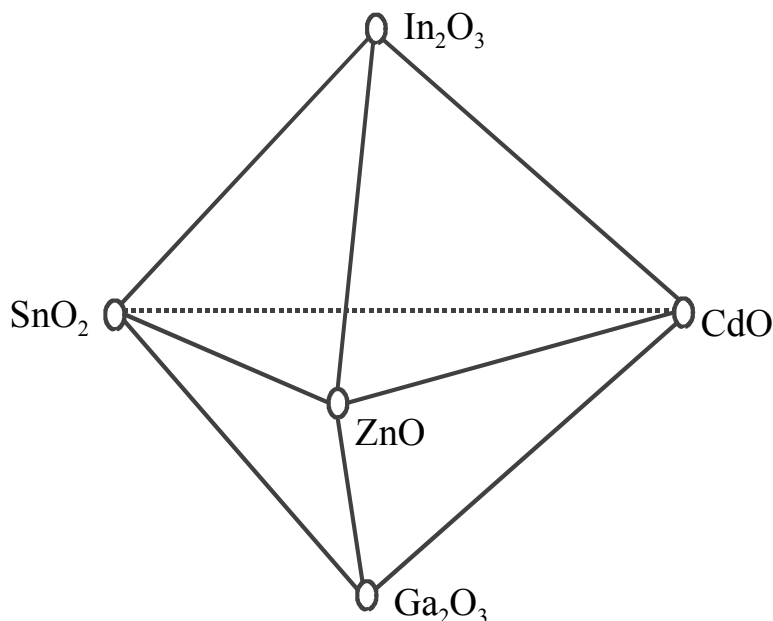


Figure 8.1: Pictorial representation of the complex composition phase space which is currently investigated formed by ZnO, SnO₂, In₂O₃, CdO, and Ga₂O₃.

No complete theory exists to predict the behaviour of these complex materials. Therefore a large compositional phase space is being explored. When using the five mentioned metal oxides this results in a compositional phase space as given in Figure 8.1. A full exploration of the compositional phase space represented in Figure 8.1 can only be done realistically by a combinatorial approach [e.g. 8,9,10]. In this approach each sample, called a library, spans a range of material compositions and processing conditions.

In addition to this empirical approach of optimising the performance of TCOs, full exploration of the composition phase space will result in new insights into the basic material science and solid state physics of TCOs. Also the full exploration will yield unanticipated domains of promising new TCOs, because many different crystalline phases will be encountered, e.g. along the simple binary ZnO-SnO₂ line already at least four distinct crystalline phases exist: SnO₂, ZnSnO₃, Zn₂SnO₄, and ZnO.

The application of combinatorial approaches to the development of TCOs requires not only the development of appropriate deposition tools, but also rapid automated characterization and analysis or data mining tools. Because each combinatorial library consists of a large number of effective samples, mining the data is a real challenge, even for moderately sized combinatorial libraries. Therefore, while one of the strengths of combinatorial approaches is the fact that they can take a large slice of the phase space without much prior discrimination, one of the potential weaknesses is the need to develop appropriate analytical approaches and data analysis schemes to actually produce the desired end result.

Even with the use of the combinatorial approach investigation of the entire phase space represented in Figure 8.1 is a large operation. Therefore in this work the investigation of the compositional phase space is limited to the binary ZnO-SnO₂ line with a small step into the ternary ZnO-SnO₂-In₂O₃ plane as shown in Figure 8.2. Of the produced libraries for this work the resistivity and the chemical composition have been determined. The libraries are analysed immediately after deposition ('as deposited') and after they have been annealed in a nitrogen atmosphere. From the obtained data some interesting features can be derived.

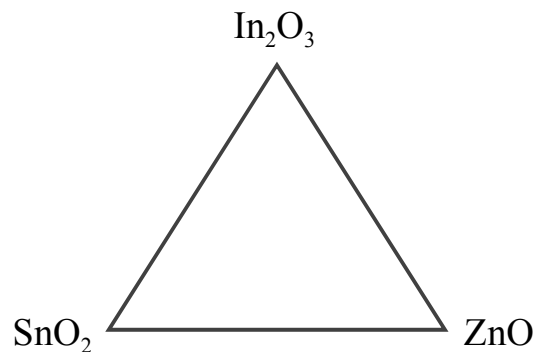


Figure 8.2: Pictorial representation of the compositional phase space investigated in this work.

Generally the deposition of combinatorial libraries is focussed on two kind of libraries, compositional spread and multiple composition. In the first type the composition is continuously varied over the entire library with gradients defined by the deposition source positions and fluxes. In the second type the same approach is used but the sample is masked before and after deposition to establish small areas with approximately discrete compositions. In the work presented here a sputter based deposition system has been used to generate compositionally graded libraries.

8.2 Experimental setup

The method used for deposition of compositionally graded combinatorial libraries of TCO is co-sputtering from two or three targets of different composition. In Figure 8.3 the

used sputtering system is depicted. The system consists of a substrate holder and three magnetron cathodes (guns). Gun #2 and gun #3 both have a diameter of 2 inch and gun #1 has a diameter of 1 inch. The target in gun #1 is a metallic indium disc and the target in gun #2 is a pressed-powder ZnO disc. In gun #3 the target has been either a metallic tin disc or a pressed-powder SnO₂ disc. The targets are sputtered by applying RF-power to the gun (0-100 W). For the sputtering a continuous flow of argon (20 sccm) and oxygen (0.4 sccm) into the reactor has been used. The sputter deposition is performed at a pressure of approximately 29.5 mTorr in the sputtering tool which is pumped by a cryo pump. The base pressure of the reactor without any gas flow is approximately 10⁻⁵ Torr.

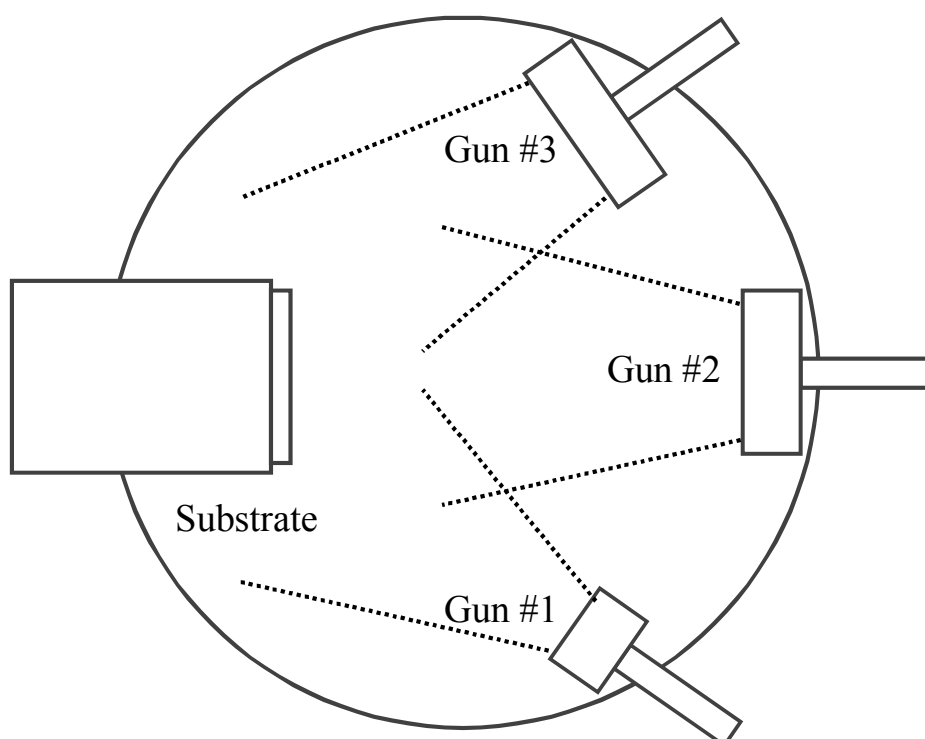


Figure 8.3: Top view of the sputter deposition setup (not to scale).

As substrates 1 mm thick 2-inch-by-2-inch Corning 7059 glass plates have been used. The substrates were mounted to the substrate holder which for all deposition experiments has been heated to a temperature of 250 °C. All deposition experiments lasted for 60 minutes and the deposition conditions were not changed during deposition. The deposited combinatorial samples have been annealed in an oven flushed with pure nitrogen (thus oxygen deficient) at a temperature in the range of 400 °C to 625 °C. For the experiment the temperature is increased at a rate of 200 °C/hour up to the desired temperature, then it is kept constant for 60 minutes, after which the heating is turned off and the sample is cooled down to room temperature.

The deposited combinatorial libraries will have a non-uniform film composition. This is due to the positioning of the three guns. This causes the deposition rate of the separate guns to be inhomogeneous and therefore a gradient in the film composition will occur in the deposited film. To obtain the film properties of the combinatorial libraries the samples have

been virtually divided into 16 elements as is depicted in Figure 8.4[†]. With respect to the presentation of the sample in Figure 8.4 gun #1 is located on the left side, gun #2 head on and gun #3 on the right side.

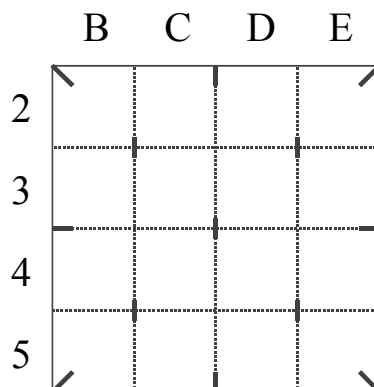


Figure 8.4: *Virtual matrix used for sample analysis.*

Every element on the sample has been analysed after deposition and after thermal anneal. The film thickness has been measured by means of a Dektak step profiler. For this the samples have been marked before deposition (short thick lines in Figure 8.4) by means of a permanent marker. After deposition these marker marks have been removed with ethanol, therewith creating a step, which could be used to measure the film thickness by means of the dektak step profiler. The resistivity of the deposited combinatorial library has been measured in the centre of each combinatorial matrix element by means of a four point probe [11,12]. The chemical composition of the film has been determined by means of electron microprobe analysis (EMPA) [13,14] in the centre of each matrix element. The position at which the thickness has been measured is obviously not the same as the position at which all other parameters have been measured, therefore the data have been interpolated to obtain the thickness at the measuring positions of the other parameters.

8.3 Results

8.3.1 ZnSn_xO_y combinatorial libraries

To determine the resistivity from four point probe data the thickness of the film is needed. An example of the film thickness distribution of one of the combinatorial libraries that has been deposited is given in Figure 8.5. This film has been deposited using two sputter guns (#2 and #3). It can be seen clearly that the deposited film has a gradient, with the largest thickness on the side of gun #3 (cf. Figure 8.3). This indicates that the deposition rate because of sputtering from gun #3 depends on the location on the substrate and that the locations closest to gun #3 have the highest deposition rate. This is exactly what is needed to generate a concentration gradient of zinc and tin in the film so that a large variation in film composition is obtained by performing one single deposition.

[†] Because also 3”-3” substrates are used in the system, the rows are indicated by numbers 2 to 5 and the columns by the letters B to E.

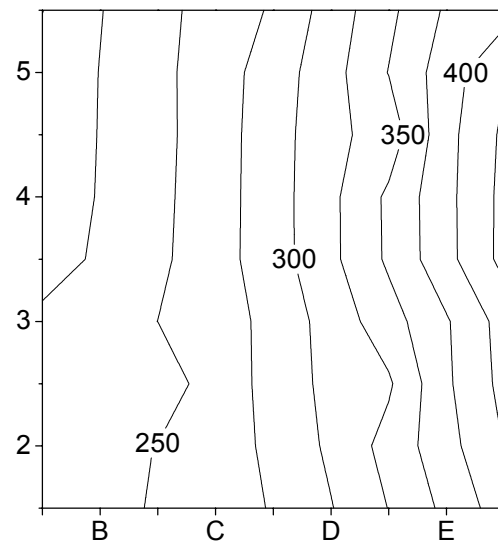


Figure 8.5: Film thickness distribution (in nm) of a $ZnSn_xO_y$ combinatorial library.

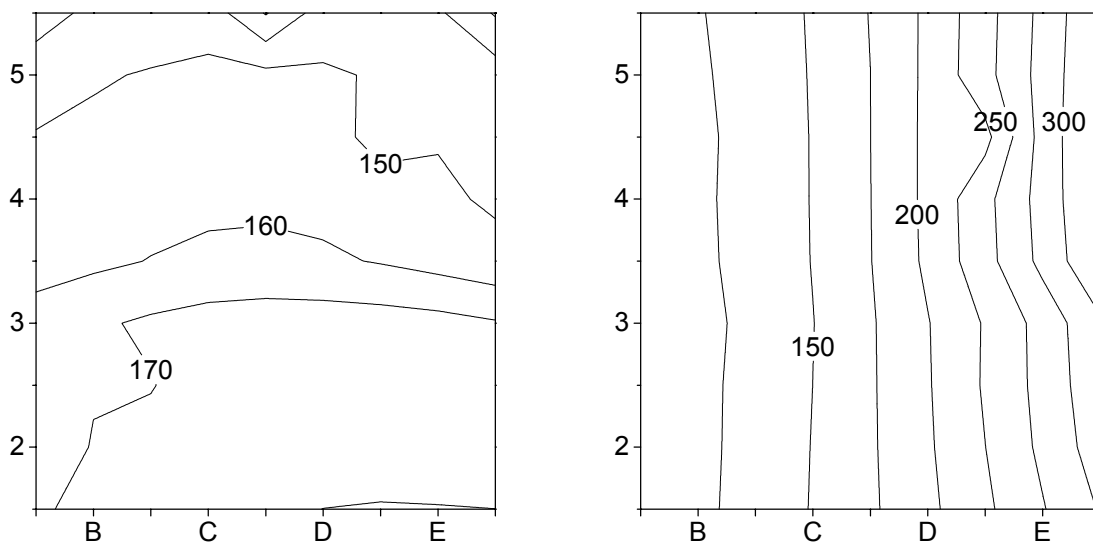


Figure 8.6: Film thickness distribution (in nm) obtained by using gun #2 (ZnO , left) and gun #3 (SnO_2 , right) separately.

If the film thickness distribution is equal to the sum of the film thickness distributions obtained by using the two sputtering guns individually, then measuring the film thickness distribution is an easy way of obtaining information on the Zn-Sn composition distribution. In Figure 8.6 the film thickness distribution as obtained using the two guns separately is given. From comparison of Figure 8.5 and Figure 8.6 it can be seen that unfortunately the film thickness distribution is not equal to the sum of the individual film thickness distributions. Therefore the Zn-Sn composition distribution needs to be obtained by different means. The technique employed here is electron microprobe analysis (EMPA).

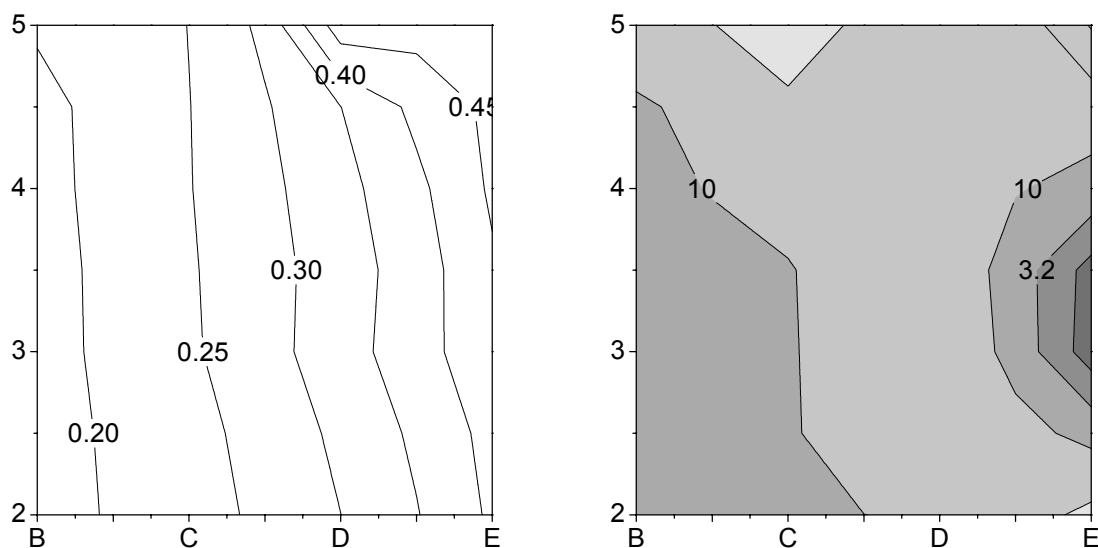


Figure 8.7: Sn/Zn ratio distribution (left) and corresponding resistivity distribution in (Ωcm , right). Annealing temperature 625 °C.

The film resistivity has been measured by means of a four point probe. It has been found that before annealing almost all films that have been deposited using a ZnO and a SnO₂ sputtering targets had a resistivity which was too high ($>10^5 \Omega\text{cm}$) to be measured with the four point probe. After annealing the samples in a nitrogen atmosphere at a temperature of 625 °C the resistivity decreased to a measurable value. Therefore all resistivity data shown are from annealed samples. In Figure 8.7 the resistivity distribution of the film, as well as the measured Sn/Zn ratio distribution by means of EMPA, are shown for the same library of which the thickness distribution is depicted in Figure 8.5. It can be seen that the resistivity has a maximum for Sn/Zn ratios of approximately 0.3. The lowest value for the resistivity are obtained for the smallest and largest values of the Sn/Zn ratios present in this sample. Therefore more samples have been deposited which extend the Sn/Zn range to lower as well as to higher values. Notice that the lines of equal resistivity do not coincide with the lines of equal Sn/Zn ratio. This is due to the fact that the resistivity is not only determined by the Sn/Zn ratio, but also the amount of oxygen in the film and the crystallinity of the film influences this value. Unfortunately the oxygen content cannot be measured by means of EMPA.

The Sn/Zn ratio distribution of a library with values for the Sn/Zn ratio below 0.3 is shown in Figure 8.8 together with its corresponding resistivity distribution. It can be seen that for a decrease in the Sn/Zn ratio the resistivity is also decreasing. At the lowest values of the Sn/Zn ratio the film can best be considered as Sn doped ZnO. Comparison of the resistivity at this point shows that the resistivity of pure ZnO film sputtered from a ZnO target in the same system has a similar value.

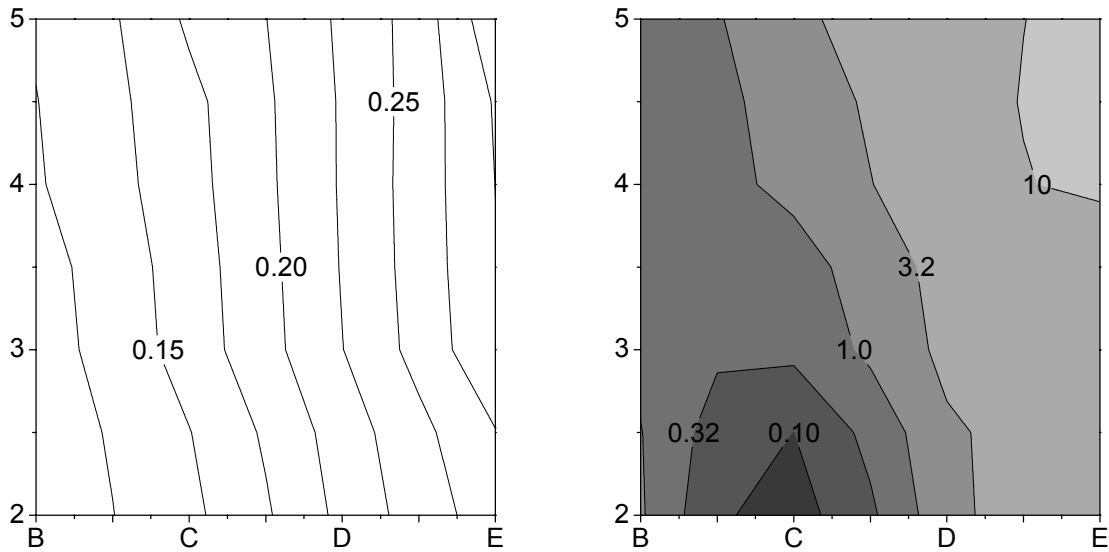


Figure 8.8: Sn/Zn ratio distribution (left) and corresponding resistivity distribution (in Ωcm , right). Annealing temperature $625\text{ }^\circ\text{C}$.

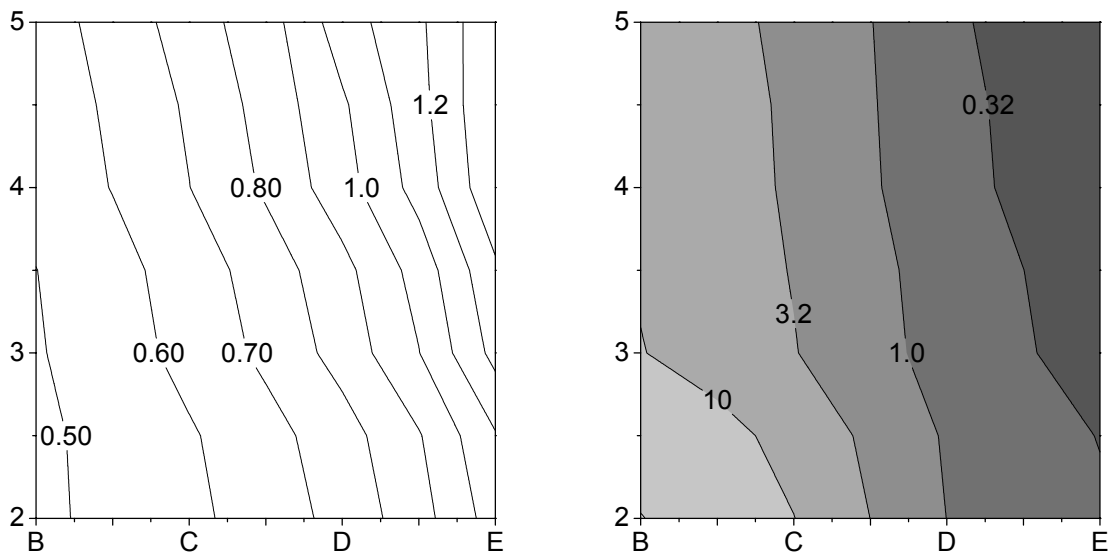


Figure 8.9: Sn/Zn ratio distribution (left) and corresponding resistivity distribution (in Ωcm , right). Annealing temperature $625\text{ }^\circ\text{C}$.

In Figure 8.9 the Sn/Zn ratio distribution and corresponding resistivity distribution of a library with Sn/Zn ratios of 0.5 and higher is given. The resistivity does continuously decrease with an increase of the Sn/Zn ratio from 0.5 to 1.4. Combining the data from Figure 8.7, Figure 8.8, and Figure 8.9 shows that the lowest value for the resistivity is obtained at a Sn/Zn ratio slightly higher than 1 or close to 0. Although the oxygen content is unknown, this indicates that on the binary ZnO-SnO₂ line the TCO with the lowest resistivity is pure ZnO or ZnSnO₃. The highest value for the resistivity is obtained at a value for the Sn/Zn ratio of 0.5, which corresponds to the Sn/Zn stoichiometry in Zn₂SnO₄. Notice that also a relative low resistivity ($<1\ \Omega\text{cm}$) was observed in Figure 8.7 for a Sn/Zn ratio close to 0.5. This indicates

that for specific conditions (oxygen content and anneal process) the Zn₂SnO₄ stoichiometry can also result in low resistivity.

8.3.2 Anneal temperature

The Sn/Zn compositional properties of a library does not change during annealing, but the resistivity does change significantly. For the libraries shown so far an annealing temperature of 625 °C has been used. To study the influence of the annealing temperature two more libraries have been made similar to the library shown in Figure 8.9, using the same deposition conditions and time. These two libraries have been annealed individually at a temperature of 400 °C and 500 °C respectively. From the thickness distributions, which is almost identical for the three libraries, it can be assumed that the film composition distribution is similar for the three libraries. In Figure 8.10 the resistivity distributions for the libraries annealed at 400 °C and 500 °C are depicted. From comparison of the three resistivity distribution it can be seen that annealing at a higher temperature does decrease the resistivity for high values of the Sn/Zn ratio. This indicates that a higher annealing temperature results in a lower resistivity. At a higher temperature the crystallization process in the film is faster and therefore the crystallinity of the sample annealed at 625 °C will be the highest. Therefore it can be concluded that crystalline material has the lowest resistivity for a Sn/Zn ratio of approximately 1. Notice that the temperature of the annealing oven is increased linearly in time up to the maximum temperature and that the maximum temperature is always kept for 60 minutes. This results in a longer annealing time for the highest temperature, due to which the library annealed at the highest temperature will even be more crystalline. For the lowest value of the Sn/Zn ratio depicted in Figure 8.9 and Figure 8.10 (approximately 0.5) the library annealed at 400 °C shows the lowest resistivity. This indicates that for this Sn/Zn ratio and oxygen content (which is unknown) probably the amorphous state has a lower resistivity than the crystalline state.

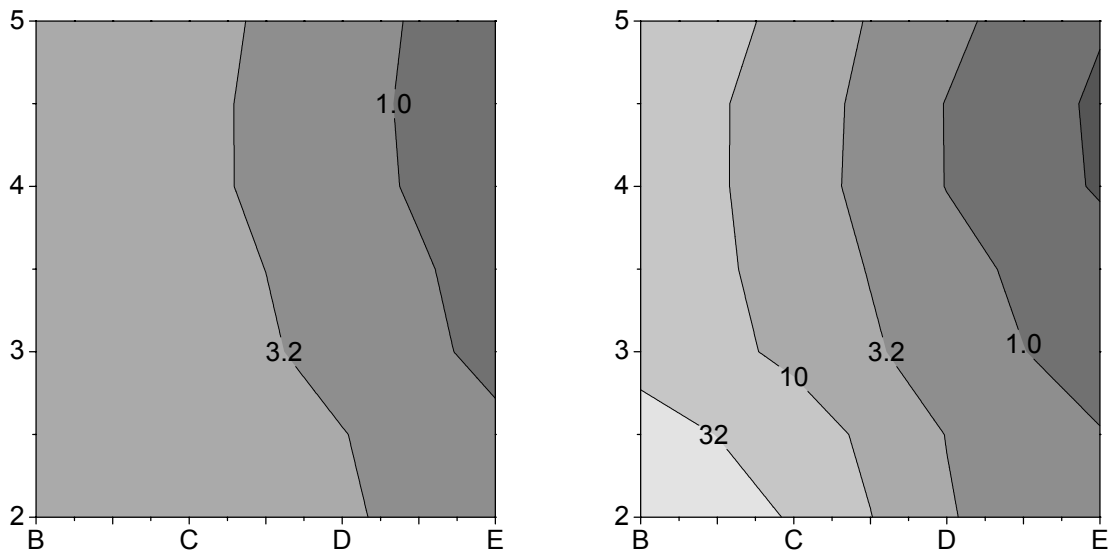


Figure 8.10: Resistivity distribution (in Ωcm) of an identical library as shown in Figure 8.9 but at an annealing temperature of 400 °C (left) and 500 °C (right).

8.3.3 ZnSn_xIn_yO_z combinatorial libraries

Now the resistivity of the binary ZnO-SnO₂ line is known, a brief inspection of the ternary ZnO-SnO₂-In₂O₃ plane will be discussed. For this purpose a ZnSn_xIn_yO_z combinatorial library has been deposited. For the incorporation of indium into the film a metallic indium target has been used. In Figure 8.11 the film thickness distribution and its corresponding resistivity distribution, after annealing, is shown of a deposited ternary ZnSn_xIn_yO_z library. The film thickness distribution is more homogeneous than the distribution shown in Figure 8.5 for the binary ZnSn_xO_y library, which clearly indicates that a significant amount of indium is incorporated into the film.

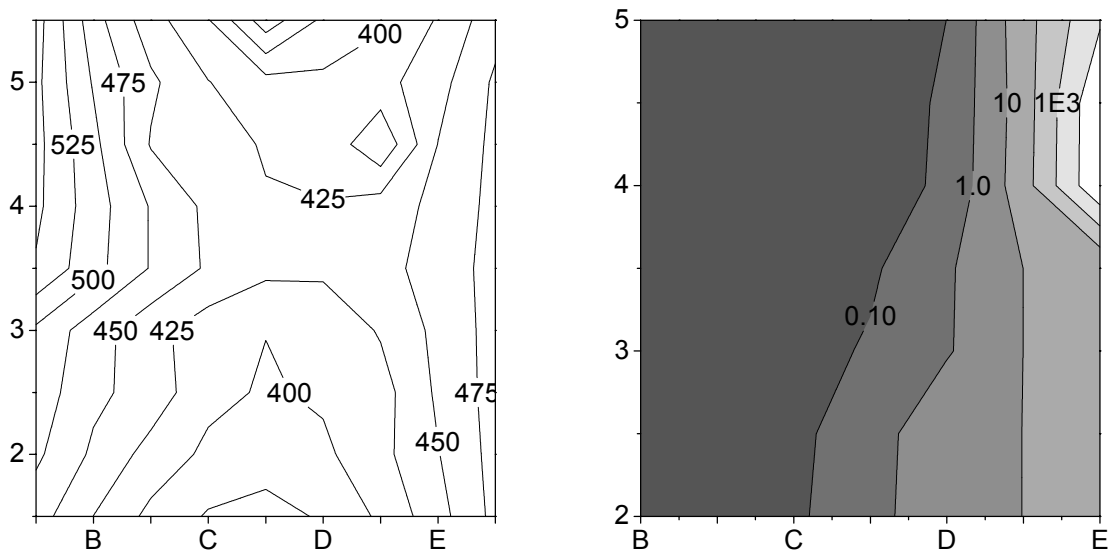


Figure 8.11: Thickness distribution (in nm, left) and the corresponding resistivity distribution (in Ωcm , right).

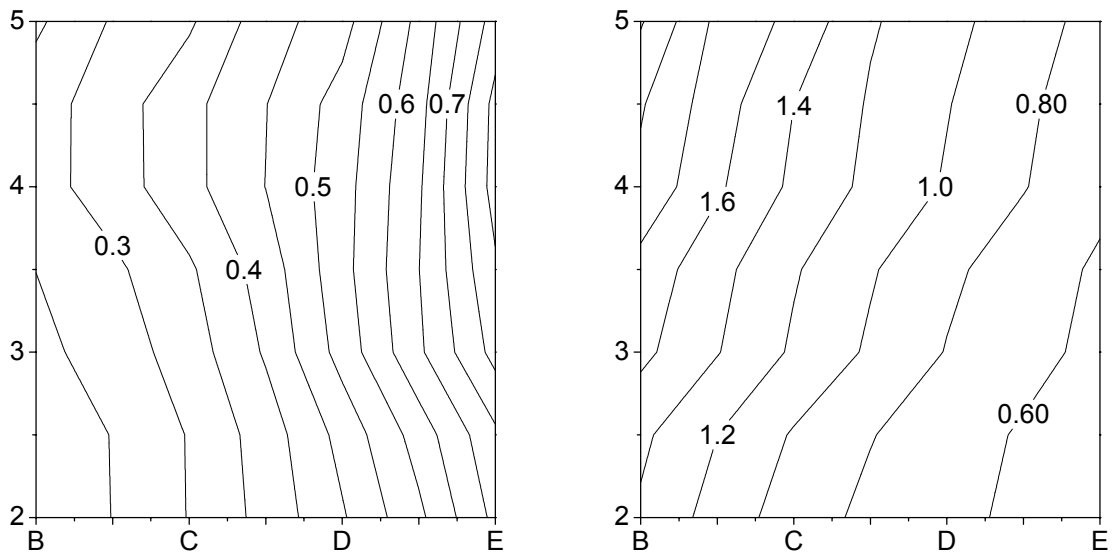


Figure 8.12: Sn/Zn ratio distribution (left) and In/Zn ratio distribution (right).

The composition of the film has been determined by means of EMPA and the Sn/Zn ratio and In/Zn ratios are depicted in Figure 8.12. Comparison of the Sn/Zn ratio and the In/Zn ratio with the resistivity as shown in Figure 8.11 shows that the lowest resistivity is obtained for the Sn/Zn ratio smaller than 0.5 and a In/Zn ratio higher than 1. The range in which the resistivity has a low value ($<0.10 \Omega\text{cm}$) is quite large in comparison to the binary ZnSn_xO_y libraries. Also the lowest value obtained for the resistivity is smaller, by approximately a factor 2, than the lowest value obtained in the binary ZnSn_xO_y libraries.

8.4 Conclusions

From the various combinatorial libraries which have been deposited it can be seen that the combinatorial approach is capable of exploring large parts of the phase space by a single deposition. The analysis technique EMPA is used to obtain the film composition. Such a technique is needed because it has been shown that it is not possible to derive the composition of the deposited combinatorial libraries from the individual sputter gun deposition rates.

For the ZnO-SnO₂ binary system resistivities as low as $0.1 \Omega\text{cm}$ have been obtained. This low resistivity is obtained for small values of the Sn/Zn ratio (<0.3) or for values of the Sn/Zn ratio close to 1. This means that the film should be either close to the ZnSnO₃ stoichiometry or Sn doped ZnO. For Sn/Zn ratios close to 0.4, which is close to the Zn₂SnO₄ stoichiometry, the worst resistivity is found ($>10 \Omega\text{cm}$).

By changing the anneal temperature, the resistivity does also change. When annealing under a nitrogen atmosphere, a higher anneal temperature results in a lower resistivity for the Sn/Zn ratios at which the absolute lowest resistivity is obtained. This is due to an increase in crystallinity of the film with an increase of the anneal temperature. A similar result might be obtained by increasing the anneal time at lower temperature. For a Sn/Zn ratio approximately equal to 0.5 the lowest resistivity is found for an anneal of $400 \text{ }^\circ\text{C}$, which suggests that in this case the amorphous phase is a better conductor.

Going from the ZnSn_xO_y binary system to the ZnSn_xIn_yO_z ternary system results in a decrease of the resistivity by approximately a factor 2 for the lowest value. Also a lower resistivity is obtained in a much larger slice of the phase space, which is good for industrial application, because the resistivity depends less critical on the deposition parameters.

The lowest resistivity obtained for binary and ternary system is significantly larger than the values obtained for metallic doped ZnO ($10^{-4} \Omega\text{cm}$ [15]) and ZnSn_xIn_yO_z as found by Minami *et al.* ($3\text{-}4 \cdot 10^{-4} \Omega\text{cm}$) [5]. This is probably due to the combination of deposition method and annealing method. Annealing the films in e.g. an oxygen atmosphere could decrease the resistivity to more comparable levels. Therefore further investigation on these kind of promising libraries is needed to obtain device quality material.

References

- [1] T.J. Coutts, D.L. Young, and X.N. Li, MRS Bulletin **25** (2000) 58
- [2] T.J. Coutts, D.L. Young, X. N. Li, W.P. Mulligan, and X. Wu, J. Vac. Sci. Technol. **A** **18** (2000) 2646
- [3] T. Minami, H. Sohohara, T. Kakumu, and S. Takata, Jap. J. Appl. Phys. Lett. **34** (1995) L971

- [4] J.M. Phillips, R.J. Cava, G.A. Thomas, S.A. Carter, J.Kwo, T. Siegrist, J.J. Krajewski, J.H. Marshall, W.F. Peck Jr., and D.H. Rapkine, *Appl. Phys. Lett.* **67** (1995) 2246
- [5] T. Minami, T.Kakumu, K. Shimokawa, and S. Takata, *Thin Solid Films* **317** (1998) 318
- [6] G.B. Palmer, K.R. Poepelmeier, and T.O. Mason, *Chem. Mater.* **9** (1997) 3121
- [7] T. Minami, *MRS Bulletin* **25** (2000) 38
- [8] L. Laversenne, A. Kairouani, Y. Guyot, C. Coutaudier, G. Boulon, and M.Th. Cohen-Adad, *Optical Mater.* **19** (2002) 59
- [9] R. Cremer, K. Reichert, and D. Neuschütz, *Surf. Coat. Technol.* **142-144** (2001) 642
- [10] R. Cremer and D. Neuschütz, *Surf. Coat. Technol.* **146-147** (2001) 229
- [11] I. Shiraki, F. Tanabe, R. Hobarra, T. Nagao, and SA. Hasegawa, *Surf. Sci.* **493** (2001) 633
- [12] R.J. Pollard, S.E. McCartney, and R. Atkinson, *J. Phys. D* **32** (1999) 1553
- [13] J.F. Watts, *An Introduction to Surface Analysis by Electron Spectroscopy*, Oxford University Press (1990)
- [14] R.F. Egerton, *Electron Energy-Loss Spectroscopy in the Electron Microscope*, 2nd edition, Plenum Press, New York (1996)
- [15] B.M. Ataev, A.M. Bagamadova, V.V. Mamedov, A.K. Omaev, and M.R. Rabadanov, *J. Crystal Growth* **198-199** (1999) 1222

Chapter 9

General conclusions

The main objective of the study presented in this thesis has been the deposition of silicon oxide like films from hexamethyldisiloxane (HMDSO) by means of an expanding thermal plasma. However, it has not been the purpose of this thesis to optimise the plasma deposition parameters in such a way that pure silicon oxide films are produced. Instead the deposition plasma and the deposition processes have been investigated to obtain a better insight. The various investigations have been presented as separate chapters in this thesis. Most of these chapters are written as separate journal papers with their own conclusions. Here an overview of the main conclusions of the various investigations is given.

Silicon oxide like film deposition

(chapter 5, 6 and 7)

- Silicon oxide like films with good optical properties can be deposited at high rates (>60 nm/s) by means of an expanding thermal plasma and HMDSO as a precursor. The deposited films do however contain a significant amount of voids as well as a significant amount of carbon which is present in the form of methyl groups. The deposition rate has a negative dependency with substrate temperature which is highly beneficial for various applications.
- The HMDSO molecules are dissociated in an expanding thermal argon plasma by means of a charge exchange reaction followed by a dissociative recombination reaction. When oxygen is added to the plasma the HMDSO molecules can also be dissociated on interaction with oxygen radicals. In the first process the HMDSO molecule is dominantly broken at one of the two Si-O bond present in the HMDSO molecule. On interaction of HMDSO with oxygen radicals it is likely that the HMDSO molecule will also break at the Si-O bond.
- The Si-O-Si structure needed for the pure silicon oxide films which is present in HMDSO needs to be generated at the film surface during deposition of the film. Although the HMDSO molecule has a Si-O-Si chain, the fact that the HMDSO molecule is being dissociated at the Si-O bond cancels this main advantages of using HMDSO as a precursor with respect to the more conventionally used tetraethoxysilane (TEOS).
- During deposition oxygen radicals have a dominant contribution in the removal of carbon (present in methyl groups) from the film surface. By removal of methyl groups new free surface reaction sites are generated at which deposition species from the plasma gas phase can attach.
- All carbon present in the deposited silicon oxide like films can be removed by means of argon-oxygen plasma treatment of deposited films. Therefore the deposited films need to have a significant porosity which enable the oxygen radical present in the plasma gas phase to diffuse into the deposited film up to the substrate-film boundary. By means of a model it has been shown that the rate at which the carbon is removed from the deposited films is mainly determined by the total oxygen flux that arrives at the film surface. The porosity of the deposited films causes the diffusion of oxygen atoms into the film to be fast.
- On interaction of oxygen radicals with an as deposited silicon oxide like film oxygen is incorporated into the film and Si-O-Si and Si-OH bonds are generated. The formation of these bonds has been depicted by means of a simple reaction mechanism. Due to the porosity it is not possible to generate a perfect silicon dioxide network.

- The number of oxygen radicals to the substrate surface in an argon-oxygen plasma is not only dependent on the total amount of molecular oxygen injected, but is also dependent on the reactor geometry. In the plasma gas phase oxygen radical will diffuse faster than argon ions and molecular oxygen and therefore the radicals are more easily lost at the reactor wall. This results in a maximum in the oxygen radical density at the substrate as function of the amount of molecular oxygen injected into the expanding thermal argon plasma.
- By means of a small deposition study using tetramethylsilane (TMS) as a precursor it has been found the sticking probability of $\text{Si}-(\text{CH}_3)_x$ is negligible in comparison to the sticking probability of $\text{O-Si}-(\text{CH}_3)_x$ radicals. The deposition rate using TMS as a precursor is at least one order of magnitude lower than the rate obtained using HMDSO as a precursor. This is because the species responsible for film growth when TMS is used as a precursor have a lower sticking probability than the species generated in a plasma into which HMDSO is injected as a precursor. In the case of deposition using TMS also free surface reaction sites need to be generated by interaction of species in the plasma gas phase and the film surface. This is because a negligible amount of free surface sites is generated when deposition species, produced from dissociation of TMS molecules, attach at the deposition surface. Aside from oxygen radical also methyl radicals can cause the formation of free surface reaction sites.

Fast infrared spectroscopy

(chapter 3)

- Due to the high deposition rates obtained by means of an expanding thermal plasma in combination with HMDSO as a precursor it is no longer possible to use conventional Fourier transform infrared reflection absorption spectroscopy to analyse the film growth *in situ* during deposition at monolayer sensitivity. Therefore a new analysis tool has been developed. The new analysis tool is based on conventional grating technology in combination with an optical scanner and a high intensity infrared light source (cascaded arc).
- The sensitivity of the new setup is dependent on the amount of light collected by the detector and on the interaction length of the light with the absorbing medium. One infrared reflection spectrum (single scan) can be obtained in a time as short as 1.3 ms. When using the setup in single scan single reflection mode absorptions of $1 \cdot 10^{-2}$ and up can be detected. The minimum sensitivity can be improved by using an attenuated total reflection (ATR) crystal. When using the setup in single scan ATR mode the minimum absorption intensity which can be detected drops to $1 \cdot 10^{-3}$. One way to increase the sensitivity is by improving the optical components of the setup.
- The absorption sensitivity of the new setup in single scan ATR mode is not enough to make the setup monolayer sensitive for the strongest absorber in silicon oxide like films (Si-O-Si). To reach monolayer sensitivity for the strongest bond a minimum sensitivity of $2 \cdot 10^{-4}$ is needed. This sensitivity can be reached by averaging several absorption spectra. This however worsens the time resolution of the setup.

Plasma gas phase

(Chapter 4)

- Analysis of the argon-oxygen plasma showed that the electron and ion temperature in the downstream plasma are low (couple of tenths of eV). Addition of oxygen causes the temperature to increase with respect to a pure argon plasma due to the exothermic reaction between molecular oxygen and the argon plasma. The interaction of oxygen molecules and the argon plasma mainly occurs at the edge of the plasma beam.
- The ion diffusion profile is mainly dependent on the background pressure in the expansion vessel and the arc current. Increasing the arc current will cause the ion diffusion to occur faster and increasing the background pressure will reduce the plasma beam diameter. Changing the argon gas flow in the arc does not change the diffusion profile when the background pressure is kept constant.
- Pitot probe measurements show experimentally the presence of a recirculation cell in the expanding thermal plasma. Pitot probe measurements cannot provide quantitative information on the particle velocity of the particles in the plasma beam, because due to the low pressure and the plasma temperature viscous effects are no longer negligible and the traditional compressible Pitot probe theory is no longer valid.
- The reverse flow in the recirculation cell is at least of the same order as the total gas flow used in the plasma source. The driving force of the recirculation cell is mainly caused by the charged particles present in the plasma beam.
- The total ionisation degree of the plasma is dependent on the arc current and on the argon flow used in the plasma source. The energy transfer efficiency from plasma source to gas does increase with increasing argon flow used in the plasma source. However there is an optimum in the energy transfer efficiency because no more ions are produced once a critical argon flow is reached.
- In a pure argon plasma there is a negligible loss of ions and electrons due to recombination of argon ions and electrons. The only loss of ions and electrons is at the wall. On addition of oxygen to the plasma the ion density does decrease due to interaction of ions and electrons with the oxygen molecules.

Transparent conductive oxides

(chapter 8)

- Deposition of libraries using a combinatorial approach is an useful technique for exploring large parts of the phase space by one single deposition experiment. This can be used in the search for new transparent conductive oxides (TCO).
- In the ZnO-SnO₂ binary system the lowest film resistivity has been found for films that are close to the ZnSnO₃ stoichiometry as well as for Sn doped ZnO. When annealing the deposited libraries in a nitrogen atmosphere the resistivity is dependent on the film anneal temperature. The lowest value for the resistivity is found at the highest anneal temperature. Addition of indium to the ZnO-SnO₂ binary system causes the resistivity to decrease.

Summary

In this thesis the deposition process of silicon oxide like thin films, deposited by means of an expanding thermal argon plasma into which hexamethyldisiloxane (HMDSO) and oxygen are injected as deposition precursors, has been investigated. Silicon oxide and silicon oxide like films have numerous applications, due to their specific optical, electrical, and mechanical properties. To reduce the production cost of these films a high growth rate is highly beneficial. By conventional deposition techniques, such as chemical vapour deposition (CVD) and traditional plasma enhanced CVD, in general deposition rates of up to 1 nm/s can be obtained. In this thesis it has been shown that by means of the expanding thermal plasma technique, for silicon oxide like films deposition rates of over 60 nm/s can be obtained.

The silicon oxide like films deposited under various plasma conditions have been studied. The refractive index, growth rate, chemical composition and various chemical bond types of the film have been studied. The refractive index of the deposited films is a function of the silicon oxide, carbon, and void content of the film. A refractive index above that of pure silicon dioxide indicates the presence of carbon and a refractive index below that of pure silicon oxide is the result of a void content. Elastic recoil detection analysis revealed the chemical composition and infrared transmission absorption spectroscopy has been used to determine the chemical bond types. Combination of these two techniques revealed that the carbon present in the deposited films is present in the form of methyl. This is the same form as in the deposition precursor. The chemical composition of the deposited films revealed that the most likely bond at which the HMDSO molecule is dissociated is one of the Si-O bonds. This is different from the dissociation process in a plasma dominated by electron kinetics.

The silicon oxide like film deposition process has been investigated in the plasma gas phase as well as at the substrate surface. The plasma gas phase of the argon plasma into which oxygen has been injected has been studied by means of a double Langmuir probe and a Pitot probe. The Langmuir probe measurements provide information on the ion density and temperature distribution in the downstream plasma. The ion density profile is mainly determined by the pressure in the expansion vessel and the total number of ions emanating from the plasma source. Addition of oxygen results in a decrease of the ion density at the edge of the plasma beam, which shows that reactions mainly occur at that position. Information on the flow pattern of the gas in the plasma reactor is obtained by the Pitot probe measurement. The presence of a recirculating flow pattern in the downstream reactor has been shown experimentally. Due to the conditions in the plasma reactor, viscous effects begin to play an important role in the measured stagnation pressure, due to which the conventional Pitot probe theory cannot be applied. A combination of the two techniques has been used to calculate the total ion flux generated by the cascaded arc plasma source. The ion flux is mainly dependent on the total power input and for low gas flow (<50 sccs) also on the gas flow in the plasma source.

Summary

The deposition process at the substrate surface has been investigated by means of post deposition argon-oxygen plasma treatment of deposited silicon oxide like films. This is done in order to obtain more information on the interaction between oxygen and the film surface during deposition. The argon-oxygen treatment plasma is capable of removing all the carbon from the film, which indicates that the deposited films are porous. Also oxygen is incorporated into the film, where Si-O-Si and Si-OH bonds are generated. A simple model based on diffusion of oxygen into the film and reaction of oxygen in the film has been proposed for the removal of the carbon content and the oxidation process. This model is in good agreement with the observed changes. A reaction mechanism for atomic oxygen in the film has also been proposed.

To obtain a better understanding of the interaction process between the plasma gas phase and the film surface, deposition experiments using tetramethylsilane (TMS) and oxygen as deposition precursors have been performed. This showed that the sticking probability of an Si-(CH₃)_x radical is negligible when compared to that of an O-Si-(CH₃)_x radical. From the combination of all data obtained, the dominant deposition species as well as the deposition mechanism for deposition of silicon oxide like films from HMDSO and oxygen has been proposed.

In situ diagnostics are able to provide even more information on the deposition process. However, the high deposition rates obtained with the expanding thermal plasma deposition technique pushes the common *in situ* infrared absorption spectroscopes to their limits. Therefore a new *in situ* infrared reflection absorption spectroscopy tool has been developed. The new tool is based on conventional grating technology in combination with a fast optical scanner. Infrared reflection absorption spectra in the range 700 cm⁻¹ to 1400 cm⁻¹ can be obtained at a time resolution of 1.3 ms and a spectral resolution of 24 cm⁻¹. The absorption sensitivity obtained is 10⁻² when the setup is used in single reflection mode. The sensitivity can be improved to 10⁻³ by using the attenuated total reflection technique. This sensitivity is close to monolayer sensitivity for the Si-O-Si absorption bond in the infrared absorption spectrum of silicon oxide like film. Further improvement of the sensitivity can be obtained by averaging multiple spectra, however this will cause the time resolution to decrease.

In this thesis aside from the work on the deposition of silicon oxide like films, work resulting from a two month visit to the National Renewable Energy Laboratory in Golden, Colorado (USA) is also presented. This work involves the deposition of transparent conductive oxides (TCO). In search for new TCO materials a large phase space needs to be explored. For doing this the combinatorial approach has been used. In a sample, called a library, a compositional gradient is created by which multiple chemical compositions can be studied by performing one single deposition experiment. Investigation of binary ZnSn_xO_y combinatorial libraries, showed that the lowest values for resistivity are obtained when films are deposited in either a Sn doped ZnO or a ZnSnO₃ stoichiometry. Annealing the films in a nitrogen atmosphere reduces the resistivity. Including indium in the combinatorial deposition process to form a ternary ZnSn_xIn_yO_z combinatorial library results in a reduction of the resistivity for a specific film composition. The resistivity also becomes less dependent on the film composition.

Samenvatting

In dit proefschrift is het depositieproces onderzocht van siliciumoxideachtige dunne lagen, welke gedeponereerd zijn door middel van een expanderend thermisch plasma waarin hexamethyldisiloxane (HMDSO) en zuurstof zijn geïnjecteerd. Siliciumoxide en siliciumoxideachtige lagen hebben, dankzij hun specifieke optische, elektrische en mechanische eigenschappen, een talrijk aantal toepassingen. Een hoge depositiesnelheid maakt het mogelijk om de productiekosten van dit type lagen te verlagen. Met behulp van conventionele depositietechnieken, zoals chemische damp depositie (CVD) en klassieke plasma ondersteunde CVD, kunnen in het algemeen depositiesnelheden tot 1 nm/s worden bereikt. In dit proefschrift is het aangetoond dat met behulp van de expanderende thermische plasma techniek het mogelijk is om voor siliciumoxideachtige lagen depositiesnelheden van meer dan 60 nm/s te bereiken.

De siliciumoxideachtige lagen gedeponereerd onder verschillende plasma condities zijn bestudeerd. De brekingsindex, groeisnelheid, chemische samenstelling en de verschillende chemische binding types van de lagen zijn onderzocht. De brekingsindex van de gedeponereerde lagen is een functie van de hoeveelheid siliciumoxide, koolstof en lege ruimte in de lagen. Een brekingsindex hoger dan die van puur siliciumoxide geeft de aanwezigheid van koolstof aan en een brekingsindex lager dan die van puur siliciumoxide is het gevolg van de aanwezigheid van lege ruimte in de laag. Nucleaire analyse en infrarood transmissie absorptie spectroscopie is gebruikt om de chemische samenstelling en de chemische binding typen te bepalen. Combinatie van deze twee technieken geeft aan dat het koolstof aanwezig in de lagen gebonden is in de vorm van methylgroepen, net zoals in de depositieprecursor. De chemische samenstelling van de gedeponereerde lagen laat zien dat de dissociatie van HMDSO meest waarschijnlijk plaatsvindt op een van de Si-O bindingen. Dit is verschillend van het dissociatieproces in meer conventionele plasma.

Het siliciumoxideachtige lagen depositieproces is onderzocht in zowel de plasmagasfase als aan het substraatoppervlak. De plasmagasfase van het argon plasma waarin zuurstof is geïnjecteerd is bestudeerd door middel van een dubbele Langmuirsonde en een Pitotsonde. De Langmuirsonde metingen geven informatie over de ionendichtheid en temperatuur-verdeling in de plasmaexpansie. De ionendiffusie is hoofdzakelijk bepaald door de druk in het expansievat en de hoeveelheid ionen geproduceerd door de plasmabron. Toevoeging van zuurstof resulteert in een afname van de ionendichtheid aan de rand van de plasma bundel. Dit laat zien dat de reacties hoofdzakelijk op die positie gebeuren. Informatie met betrekking tot het stromingspatroon van het gas in de plasmareactor is verkregen door middel van Pitotsonde metingen. De aanwezigheid van een recirculatiepatroon in de reactor is experimenteel waargenomen. Door de condities in de plasmareactor kan de viscositeit niet worden verwaarloosd en kan de traditionele Pitotsonde theorie niet worden toegepast. Combinatie van de twee technieken is gebruikt om de hoeveelheid ionen gecreëerd in de

cascadeboog te berekenen. De hoeveelheid ionen is hoofdzakelijk afhankelijk van het elektrische vermogen en voor een lage argongastoevoer (<50 sccs) ook van deze parameter.

Het depositieproces aan het substraatoppervlak is bestudeerd door middel van nabehandeling van de gedeponeerde siliciumoxideachtige lagen met een argon-zuurstof plasma. Dit verschaft meer informatie over de interactie van zuurstof met het laagoppervlak tijdens depositie. Het argon-zuurstof plasma is in staat om alle aanwezig koolstof uit de laag te verwijderen, wat er op duidt dat de gedeponeerde lagen poreus zijn. Zuurstof is ook ingebouwd in de lagen, waar Si-O-Si en Si-OH bindingen worden gegenereerd. Voor het verwijderen van het koolstof en het inbouwen van zuurstof is er een eenvoudig model, gebaseerd op diffusie van zuurstof de laag in en reactie van zuurstof in de laag, geponeerd. Dit model is in overeenstemming met de waargenomen veranderingen. Ook is er een potentieel reactiemechanisme voor atomair zuurstof in de film afgeleid.

Om een beter inzicht te krijgen in het interactieproces tussen de plasmagasfase en het laagoppervlak zijn er depositie experimenten met tetramethylsilane (TMS) en zuurstof als precursor verricht. Dit experiment liet zien dat de aanhechtingswaarschijnlijkheid van Si-(CH₃)_x radicalen verwaarloosbaar is ten opzichte van O-Si-(CH₃)_x radicalen. Gebruikmakend van alle data heeft geleid tot een voorstel voor de dominante depositiedeeltjes en het depositiemechanisme voor depositie van siliciumoxideachtige lagen uit HMDSO en zuurstof.

In situ diagnostieken zijn in staat om nog meer informatie omtrent het depositieproces te geven, waardoor het mogelijk is om het depositieproces in meer detail af te leiden. Echter de hoge depositiesnelheden, verkregen door het gebruik van de expanderend thermisch plasmadepositietechniek, zorgen ervoor dat de limieten van de huidige *in situ* infrarood absorptiespectroscopen worden gebruikt. Daarom is er een nieuwe *in situ* infrarood reflectie spectroscop ontwikkeld. De nieuwe spectroscop is gebaseerd op conventionele rooster-technologie in combinatie met een snelle optische scanner. Infrarood reflectie-absorptiespectra van 700 cm⁻¹ tot 1400 cm⁻¹ kunnen worden verkregen in een tijdschaal van 1.3 ms en een spectrale resolutie van 24 cm⁻¹. De bereikte absorptiegevoeligheid is gelijk aan 10⁻² voor het gebruik in enkele reflectie en kan worden verbeterd tot 10⁻³ door het gebruik van de geattenuerde totale reflectie techniek. Deze gevoeligheid is ongeveer gelijk aan de gevoeligheid nodig om monolaag gevoeligheid te krijgen voor de Si-O-Si absorptieband. Verbeteringen van de gevoeligheid kunnen worden bereikt door het middelen van spectra, echter dit heeft een verslechtering van de tijdsresolutie tot gevolg.

In dit proefschrift is naast het werk aan de deposite van siliciumoxideachtige lagen ook werk gepresenteerd wat het resultaat is van een twee maanden durend bezoek aan het National Renewable Energy Laboratory in Golden, Colorado (USA). Dit werk heeft betrekking op het deponeren van transparante geleidende oxides (TCO). In de zoektocht naar nieuwe TCO materialen is het noodzakelijk om een grote faseruimte te onderzoeken. Om dit te kunnen doen is gebruik gemaakt van de zogenaamde combinatoriale aanpak. Hierbij wordt in tijdens een depositie een compositionele gradient aangebracht in de gedeponeerde laag, waardoor het mogelijk is om meerdere chemische samenstellingen te analyseren door een enkel depositie experiment. Onderzoek aan het binaire ZnSn_xO_y systeem resulteerde in de laagste weerstand voor lagen welke overeenkomen met Sn gedoteerde ZnO of de ZnSnO₃ stoichiometry. Het uitstoken van de lagen in een stikstof omgeving verminderd de weerstand. Vorming van een ZnSn_xIn_yO_z systeem door toevoeging van indium in het combinatoriale depositieproces resulteert voor specifieke laagcomposities in een vermindering van de weerstand. Ook wordt de weerstand minder afhankelijk van de filmcompositie.

Dankwoord/Acknowledgements

Bij deze wil ik graag iedereen die een directe of indirecte bijdrage heeft geleverd bij het tot stand komen van dit proefschrift bedanken. Een aantal mensen wil ik echter in het bijzonder bedanken.

Richard van de Sanden wil ik graag bedanken voor de mogelijkheid die hij mij heeft gegeven om mijn promotieonderzoek binnen de vakgroep ETP uit te voeren. Ook wil ik hem bedanken voor zijn begeleiding en de werk gerelateerde discussies. Daan Schram wil ik graag bedanken voor zijn steun en met name voor de discussies met betrekking tot de Pitot sonde.

I would like to thank General Electric for their Financial support. At General Electric I would like to thank all people who are related to the project, and in special: James Johnson and Marc Schaepkens for being the primary contact.

Een significant gedeelte van de gegevens in dit proefschrift is mede te danken aan de inzet van een aantal studenten. Ik wil daarom ook als eerste de afstudeerder Arjen Klaver bedanken voor zijn bijdrage (*Je werk is de basis geweest voor twee hoofdstukken in dit proefschrift.*). Daarnaast wil ik de stagairs bedanken in volgorde van verschijning: Bogdana Mitu (*Thanks for the helping with the first silicon oxide like film deposition experiments.*), Jurgen Schoonus (*Mooi werk, helaas is het geen onderdeel van dit proefschrift geworden.*), Maarten van Weert en Jaap Haartsen (*Goed team, begonnen als een 'zomerstage'. Het duurde echter wat langer en daarom ook terecht beloond als een reguliere stage.*) en Joris Vorselaars (*Harde werker, schrijven van een verslag kost meer tijd dan je denkt.*).

Van mijn naaste collega's wil ik met name de mensen binnen Depo I bedanken: Ariël, Karine, Jan en Adriana (bedankt, merci, dēkuji, grazie). Echter ook de technische ondersteuning van Ries, Jo, Bertus en Herman was onmisbaar, evenals de hulp van duizendpoot en secretaresse Jeanne. Mijn kamergenoten: Marco, Stéphane en Jean-Pierre, wil ik bedanken voor hun aanwezigheid en hun bijdrage bij het oplossen van (kleine) probleempjes. Vaak was luisteren naar wat het probleem was al voldoende om tot een oplossing te komen. Ook wil ik Joost van der Mullen bedanken voor zijn (bijna) dagelijkse verschijning in de kamer en zijn 'Joostse' opmerkingen waarop ik altijd op soortgelijke wijze heb geprobeerd te reageren. Verder wil ik de collega's bij ETP die nog niet zijn genoemd bedanken. Bas, Arno, Erwin, Iain, Edward, Johan, Roland, Greg, Eugen, Alain, Peter, Junegie, Richard E., Maarten, Colin, Karel, Jan van D., Ger, Bart, Harm en de enkele die ik vast vergeten ben. Allemaal bedankt.

At the National Renewable Energy Laboratory in Golden (CO, USA) I would like to thank: Dave Ginley, John Perkins, Jeff Alleman, Carole Allman, Tanya Rivkin, and Bobby To for their hospitality and the pleasant time during my two month working visit over there.

Voor hun indirecte bijdrage aan het tot stand komen van dit proefschrift, door middel van zinnige en onzinnige maar ontspannende discussies, wil ik mijn vrienden van het 'donderdagavond' clubje bedanken. (*Trouwens, er zit een fout in de tekening op de placemat bij de Chinees!!!*)

Als laatste wil ik mijn ouders, mijn zus en mijn vriendin Fenna bedanken voor de nodige afleiding tijdens en hun onvoorwaardelijke steun en vertrouwen bij het tot stand komen van dit proefschrift.

Curriculum vitae

- January 2, 1974 Born in Tilburg, The Netherlands
- 1986-1990 St. Norbertusmavo, Tilburg
- 1990-1993 Pauluslyceum, Tilburg
- 1993-1998 Student Applied Physics, Eindhoven University of Technology
- Internal traineeship in the group Physics of Surfaces and Boundary Layers
 - External traineeship (six months) in the group of Prof. G. S. Oehrlein at the State University of New York at Albany
 - Master thesis project in the group Equilibrium and Transport in Plasmas.
- 1998-2002 Ph.D. student, in the group Equilibrium and Transport in Plasmas, Center for Plasma Physics and Radiation Technology, Department of Applied Physics, Eindhoven University of Technology
- Two month (fall 2001) working visit to the group of Dr. D. S. Ginley at the National Renewable Energy Laboratory, Golden, Colorado

Stellingen

behorende bij het proefschrift

**High Rate Plasma Deposition
of Silicon Oxide Like Films**

door

Maikel van Hest

Eindhoven, 27 augustus 2002

I

De aanhechtingswaarschijnlijkheid van deeltjes aan een oppervlak wordt vaak ten onrechte onafhankelijk verondersteld van de fysische en chemische gesteldheid van het oppervlak.
(dit proefschrift)

II

In de zoektocht naar hogere depositiesnelheden is het noodzakelijk om snellere *in situ* oppervlakteanalysemethoden te ontwikkelen.
(dit proefschrift)

III

Voor een correcte interpretatie van Pitot-sondemetingen aan een bij lage druk expanderend thermisch plasma ter bepaling van de deeltjessnelheid is het niet toegestaan om de effecten veroorzaakt door viscositeit te verwaarlozen.
(dit proefschrift)

IV

Het verhogen van het argongasdebiet in een cascadeboog zal, in tegenstelling tot het verhogen van de boogstroom, niet automatisch leiden tot een toename in de productie van argon-ionen.
(dit proefschrift)

V

Met de “cavity ring down” techniek is het mogelijk om de dichtheid van “open bindingen” aan het oppervlak van dunne lagen te bepalen.

VI

Een ‘vol is vol’ politiek kan beter worden toegepast als oplossing voor het huidige fileprobleem dan als oplossing voor de immigratieproblematiek.

VII

Geneesmiddelen waarvan de fabrikant beweert dat ze een proces op natuurlijke wijze laten verlopen, zijn niet meer dan een sigaar uit eigen doos.

VIII

De globalisering van de economie en de daarmee gepaard gaande fusies van en overnames door bedrijven beperkt de toetreding van nieuwe spelers op het economische toneel.

IX

Het aantrekkelijker maken van een beroep door het verhogen van de financiële vergoeding heeft niet automatisch tot gevolg dat daarmee naast de kwantiteit ook de kwaliteit van de geleverde diensten toeneemt.

X

Er moeten grote vraagtekens worden geplaatst bij de conclusies die getrokken worden uit de resultaten van een rampenoefening indien alle betrokken instanties van tevoren op de hoogte waren van de oefening.

XI

Het inwerken van nieuw gekozen politici door ervaren politici heeft als gevolg dat de nieuwe politiek niet veel zal verschillen van de oude.

XII

Soms is het beter niet alles te weten.